

**THE MAGNETIC AND TRANSPORT PROPERTIES OF
TEMPLATE-SYNTHESIZED
CARBON-BASED AND RELATED
NANOMATERIALS**

A dissertation presented

By

Adam Louis Friedman

Submitted in partial fulfillment
of the requirements for the degree of
Doctor of Philosophy
in the field of
Physics
in the Graduate School of Arts and Sciences

Northeastern University
Boston, Massachusetts
February 2009

**THE MAGNETIC AND TRANSPORT PROPERTIES OF
TEMPLATE-SYNTHESIZED
CARBON-BASED AND RELATED
NANOMATERIALS**

By

Adam Louis Friedman

ABSTRACT OF DISSERTATION

Submitted in partial fulfillment of the requirements for the degree of
Doctor of Philosophy in the field of Physics in the Graduate School of Arts and
Sciences of Northeastern University, February 2009

The Magnetic and Transport Properties of Template-Synthesized Carbon-Based and Related Nanomaterials

Abstract

The porous alumina template-assisted method of nanoscale materials preparation provides a simple, relatively inexpensive, yet highly controllable and repeatable process for nanomaterial synthesis. Various nanostructures can then be made utilizing the porous structure as a scaffold. In this dissertation we study the porous alumina anodization process, the synthesis of porous alumina-assisted materials, and the basic physical properties of these materials, primarily concentrating on the magnetic and transport properties. First, we study the porous alumina formation process as a function of anodization voltage, acid type, and acid concentration. We find that while acid type strongly affects the growth characteristics of porous alumina, pH does not. We also study the stability of pore formation. We characterize the two- and three-dimensional stability of the growth process. We find that in three dimensions, an unstable formation region as a function of pH and voltage will cause the formation of dendrite structures. Next, we study the synthesis of materials in the porous alumina templates. Through chemical self-assembly, electrodeposition is able to make a wide variety of nanowires and nanotubes and we seek to optimize this process. Third, we study the optical properties Au and Ag nanowire arrays embedded in porous alumina. We find that such materials have use as negative index metamaterials owing to the existence of both transverse and longitudinal surface plasmon resonances. Next, we study the basic magnetic properties of new PANi-ferromagnet composite nanostructures and compare these properties to the magnetic properties of the nanotubes and the nanowires alone. We find the high dielectric properties of the PANi to strongly shield the ferromagnetic nanowires from magnetostatic interactions. Fifth, we make devices out of

carbon nanotubes synthesized by CVD in the alumina templates. We investigate the transport properties of these carbon nanotubes. Further, we find that the contact resistances, which are normally on the order of mega-ohms for these tubes, can be lowered to the order of kilo-ohms by annealing in H_2/Ar atmosphere. We find that the disorder in these carbon nanotubes allows for the uptake of H during the annealing process. These H-complex hydrogen impurities, along with C and H adatoms, induce ferromagnetism in the carbon nanotubes. We carry out a magnetic study on the annealed carbon nanotubes. Moreover, the ferromagnetism of the carbon nanotubes results in hysteric magnetoresistance. We study this effect, attributing it to strong magneto-viscosity effects and anisotropic magnetoresistance. We also study the transport and magnetotransport properties of the annealed carbon nanotubes as a function of temperature and inner diameter. We find that there is an order-disorder transition that occurs at lower temperatures that resembles behavior predicted in disordered carbon fibers by the Bright model. We also find that the nanotubes behave as one-dimensional Luttinger liquids. Finally, as a means of comparison, we fabricate and study the properties of monolayer graphene devices.

Acknowledgements

There are many people that helped me a great deal in completing the work for this dissertation and I will try my best to thank as many of them as I can: First, I would like to thank my advisor, Prof. Latika Menon, for her constant support, direction, and mentoring. I thank my committee members, who all also helped me with various parts of this work. I thank Prof. Yung Joon Jung (and his students Hyunkyung Chun and Myung Gwan Hahm) for performing the CVD of the carbon nanotubes, Raman spectroscopy, and greatly helping me to understand carbon nanotube transport. I thank Prof. Sergey Kravchenko (and his student Anish Mokashi) for teaching me all about low temperature physics, dilution refrigerators, and collaborating with the graphene measurements. I thank Prof. Jeffery Sokoloff for his many helpful and encouraging discussions. I also thank Prof. Don Heiman (and his student Steve Bennett) for his help with magnetic measurements, allowing me to use his equipment extensively, and for many, many helpful discussions and collaborations. I thank Prof. Srinivas Sridhar and his group members Dattatri Nagesha and Evin Gultepe for many helpful discussions, and Didier Casse and Wen-Tao Lu for their collaboration with the metamaterial applications of metal/alumina arrays. I thank Prof. Laura H. Lewis for her help with the MPMS SQUID oven measurements and helpful comments. I thank my labmates Eugen Panaitescu, Zhen Wu, Christiaan Richter, and Sucharita Saha for many helpful and interesting discussions and collaborations. I thank the Kostas Center and CHN for their help in device fabrication. In particular, many thanks go to Sivasubramanian Somu, Scott McNamara, Rich DeVito, David McKee, Juan Aceros, and Peter Ryan, who trained me on every piece of equipment I used for fabrication. I thank Peter Blake of the University of Manchester for his collaboration and helpful discussions on graphene transport. I thank the people who trained me on microscopic methods: Bill Fowle of the

Biology department (SEM) and Richard Schalek of Harvard University (FIB). I thank the undergraduates and summer students who worked on various projects related to the work. In particular, many thanks to Jesse Silverberg for the bifurcated nanowires and nanotube device fabrication, for which he spent many very, very late nights and holidays working with me in the lab and Derrick Brittain for the alumina, PANi, and graphene device fabrication, for which he was forced to make hundreds of samples. I also thank Wael Al-Sawai for being my study partner in getting through the graduate classes and qualifying exam and Daniel Feldman for his advice and offering some interesting distractions. And, most importantly, I thank my family: my wife, Caroline, and my parents for their unending support, help, and understanding.

Contents

Abstract	3
Aknowledgments	5
List of Figures	10
1. Introduction	16
1.1. Motivation.....	16
1.2. Outline of Thesis.....	19
2. Porous Alumina	21
2.1. Introduction.....	21
2.2. Dimensional Growth.....	23
2.2.1. Electrochemical Models.....	23
2.2.2. The Parkhutik and Shershulsky Model.....	26
2.2.3. The Thamida and Chang Model for Dimensional Growth.....	30
2.2.4. Experimental Results.....	32
2.3. Stability of Growth.....	39
2.3.1. The Thamida and Chang Model for Stability Growth.....	39
2.3.2. The Singh Model.....	40
2.3.3. Experimental Results	43
2.3.4. Dendrite Formation.....	49
2.4. Other Structures.....	54
2.4.1. Nanonoodles.....	54
2.4.2. Y-Shaped and Bifurcated Pores.....	60
3. Growth of Nanowires and Nanotubes in Porous Alumina	62
3.1. Nanowire Growth by Electrodeposition.....	62
3.1.1. Introduction.....	62
3.1.2. Metallic Nanowires.....	67
3.1.3. PANi Composites.....	76
3.1.4. Filled Carbon Nanotubes.....	80
3.2. Growth of Carbon Nanotubes.....	81
3.2.1. Introduction.....	81
3.2.2. CVD Growth.....	83
4. An Application of Nanowire/Alumina Arrays in Metamaterials	88
4.1. Introduction and Theory.....	88
4.2. Preparation of Samples.....	90
4.3. Experimental Results.....	91
5. Magnetic Properties of Template Synthesized Nanostructures	96

5.1. Introduction.....	96
5.2. Nanowire Arrays.....	96
5.2.1. Theory.....	96
5.2.2. Bifurcated Nanowires.....	102
5.2.3. PANi Composite Nanowires.....	110
5.3. Carbon Nanotube Magnetism.....	120
5.3.1. Theory.....	120
5.3.2. Experimental Results.....	123
6. Fabrication of Nanoscale Devices for Nanotubes, Nanowires, and Graphene Flakes	130
6.1. Introduction.....	130
6.2. Preparation of Template Synthesized Materials.....	130
6.3. Preparation of Graphene Flakes.....	135
6.4. Lithography.....	143
6.4.1. Photolithography.....	143
6.4.2. Electron Beam Lithography.....	145
6.4.3. Focused Ion Beam Lithography.....	152
6.5. Plasma Etching.....	156
6.6. Deposition Techniques.....	159
6.7. Other Treatments.....	166
6.7.1. Lowering Contact Resistances of CNT Devices.....	166
6.7.2. Dielectrophoresis.....	171
6.7.3. Graphene Annealing.....	173
6.7.4. Wire Bonding.....	174
7. Transport Properties of Template Synthesized Carbon Nanotubes	178
7.1. Introduction.....	178
7.2. Room Temperature V-I Sweeps and Contact Resistances.....	185
7.3. Luttinger Liquids.....	188
7.3.1. Theory of Transport in Luttinger Liquids.....	188
7.3.2. Experimental Results.....	190
7.4. Magnetoresistance.....	198
7.4.1. Theory.....	198
7.4.2. Hysteretic Magnetoresistance.....	204
7.4.3. Temperature Dependence of Magnetoresistance.....	210
8. Transport Properties of Graphene	214
8.1. Introduction and Theory.....	214
8.2. Temperature Dependence of the Quantum Hall Effect.....	218
8.3. Parallel Field.....	223
9. Conclusion	225
9.1. Restatement of Major Results.....	225
9.2. Outlook for Future Work.....	228

Appendix A. The Quantum Design SQUID MPMS Oven	232
Appendix B. Princeton Measurements Corp. AGM	235
Appendix C. Cryogenics, Ltd. Cryo-free Superconducting Magnet System with Cryo Industries Variable Temperature Insert	239
Bibliography	244

List of Figures

Figure 2.1: SEM image of pores formed by anodization of aluminum.....	21
Figure 2.2: A typical experimental set-up for porous alumina growth.....	22
Figure 2.3: A schematic drawing of the field assisted diffusion of aluminum and oxygen ions.....	25
Figure 2.4: A typical current vs. time curve for anodization.....	25
Figure 2.5: Graphs of average pore diameter vs. voltage for some acids.....	33
Figure 2.6: Graphs of average interpore separation.....	34
Figure 2.7: Graph of average pore length vs. voltage for three different acids.....	35
Figure 2.8: Graph of average interpore separation vs. pH for three acids.....	36
Figure 2.9: Graph of average interpore separation vs. pH for one acid.....	37
Figure 2.10: Graph of average pore length vs. pH.....	39
Figure 2.11: Pore formation stability graphs calculated from the Singh model.....	43
Figure 2.12: Images of pores made by the 3 different acid types.....	45
Table 2.1: Summary of stability results for oxalic acid.....	47
Figure 2.13: SEM images showing the evolution of two-dimensional stability of pore growth.....	48
Figure 2.14: Pore diameter as a function of voltage.....	49
Figure 2.15: SEM profile view of 5% phosphoric acid templates.....	50
Figure 2.16: Samples with and without dendrites.....	51
Table 2.2: Summary of 5% phosphoric acid stability.....	52
Figure 2.17: Sample anodized for a long time where dendrites are clearly seen.....	53
Figure 2.18: Current vs. time graphs in different stability regions.....	54
Figure 2.19: Average pore diameter vs. time.....	55
Figure 2.20: SEM image of nanonoodles.....	56
Figure 2.21: SEM image of alumina nanonoodles formed by etching.....	57

Figure 2.22: Dependence of average wall thickness as a function of etching time.....	58
Figure 2.23: Pictorial model demonstrating the formation of nanonoodles.....	58
Figure 2.24: SEM image showing branched pore structures of alumina.....	61
Figure 3.1: Porous alumina template with metal contact.....	63
Figure 3.2: Schematic of the electrodeposition apparatus.....	64
Table 3.1: A list of materials deposited by AC electrodeposition.....	65
Figure 3.3: Current vs. time for deposition of Fe nanowires.....	68
Figure 3.4: Average fill rate vs. pH.....	71
Figure 3.5: Average fill rate vs. applied voltage.....	71
Figure 3.6: Average fill rate vs. frequency.....	72
Figure 3.7: Coercivity vs. frequency.....	73
Figure 3.8: Squareness ratio vs. frequency.....	73
Figure 3.9: Gold nanowires grown in alumina.....	75
Figure 3.10: SEM images and layout of branched bifurcated Co nanowires.....	76
Figure 3.11: Chemical structure of polyaniline.....	76
Figure 3.12: Current vs. Time deposition curve to form filled PANi nanotubes.....	78
Figure 3.13: SEM images of PANi nanotubes.....	79
Figure 3.14: TEM images showing a bundle of carbon nanotubes where the cavities are not clear.....	81
Figure 3.15: TEM images of Ni filled carbon nanotubes.....	81
Figure 3.16: Drawing of graphene sheet and single and multiwalled carbon nanotubes.....	82
Figure 3.17: Schematic of the CVD set-up to grow MWCNTs in alumina templates.....	84
Figure 3.18: MWCNTs in alumina templates grown for 60 minutes.....	84
Figure 3.19: MWCNTs in alumina grown for 100 minutes.....	85

Figure 3.20: Graph of inner diameter vs. deposition time and inner diameter as % of total MCNT vs. time.....	86
Figure 3.21: TEM image showing disorder in CVD MWCNT.....	87
Figure 4.1: Theoretical absorption spectra.....	89
Figure 4.2: Experimental set up for optical experiments.....	91
Figure 4.3: Transmission and absorbance spectra for Ag nanowires.....	92
Figure 4.4: Transmission and absorbance spectra for Au nanowires.....	94
Figure 4.5: Spectra of gold nanowires with different diameters/fill ratios.....	95
Figure 5.1: Hysteresis curves for straight, bifurcated, and thin-film samples.....	104
Figure 5.2: Coercivity as a function of anodization time for 1:2:1 bifurcated nanowires.....	106
Figure 5.3: Coercivity as a function of anodization ratio.....	107
Figure 5.4: ZFC Moment vs. temperature for straight and bifurcated nanowires.....	108
Figure 5.5: Room temperature hysteresis loops for filled PANi nanotubes as compared to nanowires.....	111
Figure 5.6: Coercivity vs. diameter graphs for filled PANi nanotubes as compared to nanowires.....	112
Figure 5.7: Magnetic viscosity vs. demagnetizing field.....	115
Figure 5.8: Graph showing interwire interactions.....	116
Table 5.1: Summary of α data.....	117
Figure 5.9: Coercivity vs. temperature for a variety of diameters of Co nanowires and Co filled PANi nanotubes.....	118
Figure 5.10: Moment vs. temperature for a magnetic field of 5000 Oe.....	119
Figure 5.11: Demonstration of hydrogenation of a zigzag CNT.....	121
Figure 5.12: Hysteresis loops at 2 K for nanotubes annealed in H ₂ /Ar, Ar only, and the substrate material.....	125
Figure 5.13: Moment as a function of temperature.....	126
Table 5.2: Summary of annealing results.....	128

Figure 5.14: Moment/mass as a function of inner diameter.....	129
Figure 6.1: Bundle of cobalt nanowires released onto Si/SiO ₂ and a carbon nanotube film released onto Si/SiO ₂	135
Figure 6.2: Graph of silicon dioxide color vs. thickness at 0 degree angle.....	136
Figure 6.3: Optical images of graphene on silicon dioxide.....	138
Figure 6.4: SEM image showing graphene layers.....	139
Figure 6.5: Raman spectroscopy of various points on a multiplayer sample of graphene.....	140
Figure 6.6: Quintel 4000-6 photolithography aligner.....	143
Figure 6.7: Patterns made by photolithography.....	145
Figure 6.8: Square EBL raster pattern.....	146
Figure 6.9: EBL exposure patterns.....	147
Figure 6.10: EBL dosage test.....	148
Figure 6.11: Diagram showing how a chip is positioned in the SEM before EBL.....	149
Figure 6.12: Angled SEM image of contacts placed onto a carbon nanotube by EBL.....	151
Figure 6.13: Graphene devices prepared by EBL.....	152
Figure 6.14: Drawing of the FIB system.....	153
Figure 6.15: Photolithography/FIB devices with Pt wires.....	155
Figure 6.16: South Bay Technologies RIE-2000 reactive ion etcher.....	156
Figure 6.17: RIE calibrations for PMMA and S1813 photoresist.....	158
Figure 6.18: Graphene flake contacted by EBL defined contacts and patterned by oxygen plasma etching.....	159
Figure 6.19: Drawing of the sputtering process and the MRC 8667 sputtering system.....	160
Figure 6.20: Device created by sputtering where lift off did not occur.....	162
Figure 6.21: Drawing of a thermal evaporator the Sharon Vacuum thermal evaporation system.....	163

Figure 6.22: Drawing of an electron beam evaporator the Kostas Center electron beam evaporation system.....	164
Figure 6.23: CNT device where sonication has destroyed part of the device.....	165
Figure 6.24: I-V curve of a CNT device before and after electron beam soldering.....	168
Figure 6.25: I-V curve before and after annealing a CNT device.....	170
Figure 6.26: TEM images of nanotubes.....	171
Figure 6.27: Carbon nanotubes deposited and aligned between two contacts by the dielectrophoresis method.....	173
Figure 6.28: H ₂ /Ar annealing tests.....	174
Figure 6.29: MEI 1204B Hybrid Ball Binder.....	175
Figure 6.30: SEM images of the successful bonding of a CNT device.....	176
Figure 6.31: Optical image of unsuccessful wire bonding due to poor adhesion.....	177
Figure 7.1: Theoretical plot of weak localization magnetoresistance.....	184
Figure 7.2: A 4-probe carbon nanotube device.....	185
Figure 7.3: SEM image of a 2-probe CNT device of the kind used in the experiments.....	186
Table 7.1: Example of a contact resistance test for a CNT 4-probe device.....	186
Figure 7.4: Current vs. voltage for a 75 minute CVD device for which a great applied voltage broke the first nanotube and another nanotube began to conduct.....	187
Figure 7.5: Resistance vs. temperature for hydrogen annealed CNTs.....	191
Figure 7.6: Resistance vs. temperature for argon annealed CNTs.....	193
Figure 7.7: Conductance vs. Voltage curves as a function of temperature.....	194
Figure 7.8: Close up of the conductance singularity.....	195
Figure 7.9: Luttinger scaling plots fit with Mathematica.....	196
Table 7.2: Luttinger parameters for a variety of samples.....	197
Figure 7.10: Hysteretic magnetoresistance in CNTs.....	205
Figure 7.11: Graphs showing the rate dependence of the magnetoresistance.....	206

Figure 7.12: Graph showing the sweeping up magnetoresistance minus the sweeping down magnetoresistance for H ₂ /Ar annealed CNTs at 6 K.....	207
Figure 7.13: Relaxation time constant.....	209
Figure 7.14: Temperature dependent magnetoresistance in CNTs.....	210
Figure 7.15: Mobilities calculated as parameters of the Bright model.....	213
Figure 8.1: SEM images of a destroyed graphene device.....	217
Figure 8.2: Temperature dependence of the resistance of graphene.....	219
Figure 8.3: R_{xx} as a function of the back-gate voltage.....	220
Figure 8.4: SdHO at $V_g = -10$ V at 6 K.....	221
Figure 8.5: Temperature dependence of the QHE in graphene.....	222
Figure 8.6: Temperature dependence of the width of hall peak.....	222
Figure 8.7: Gate voltage sweep for graphene in a parallel field at 5 K.....	223
Figure 8.8: Resistance vs. field at various gate voltages for a graphene sample in a parallel magnetic field.....	224
Figure A1: The Quantum Designs MPMS SQUID.....	232
Figure A2: The top end of the oven and the bottom end of the transport rod.....	233
Figure A3: A picture of an aluminum sample holder.....	233
Figure B1: Picture of the MicroMag AGM.....	235
Figure C1: The magnet system.....	239
Figure C2: Cryo Industries CoolPower Lab4.2.....	241

Chapter 1: Introduction

1.1 Motivation

The study of nanoscale systems has been ongoing for decades, but recent breakthroughs in high resolution imaging techniques such as scanning electron microscopy (SEM), transmission electron microscopy (TEM), atomic force microscopy (AFM), and scanning tunneling microscopy (STM) have enabled researchers to see and work with materials smaller than anything ever experimented with before. In addition, the evolution of modern computing and electronics to ever smaller transistors, microchips, and devices has fueled a booming industrial search for new materials and their novel applications. Additionally, the recent decoding of the human genome has led medical researchers too seek nano-sized particles that can interact with the DNA itself to cure diseases. And, medical researchers are actively seeking to develop new nano-medicines that can interact only locally with tumors and diseases without affecting other cells in the body. They have demonstrated that one way to do this is with drug-coated nanoparticles controlled by magnetic fields. Indeed, the nanoscale scientific revolution has hardly just begun, and there are many important and exciting basic physical properties that must be understood regarding various nanoscale materials, and scientific challenges that must be overcome before nanomaterials can be applied to the world's problems.

In particular, one problem with nanoscale materials is that fabrication can be expensive, resource hungry, and time consuming. Materials must be able to be manufactured on a large scale at a low cost. One way to do this is by using the bottom up technique of chemical self-assembly. Here, constituent materials assemble themselves by acting as building blocks under the influence of some external stimulus (like an

electric field). However, very little research has been done on the basic physics of such methods, both the fabrication of the materials and on the basic physical properties of bottom up synthesized materials themselves.

The boom in nanoscale science gives us a fantastic opportunity to explore the many fascinating and bizarre physical properties of nanoscale materials. These properties include electron transport that does not obey normal 3-dimensional laws, but rather acts as a 1- or 2-dimensional quantum system, and magnetic characteristics that are unlike any in macroscopic bulk materials due to the unique ordering of magnetic domains, various anisotropies, and strong magnetic coupling of one magnetic structure to its neighbors.

A cheap, simple, and reliable way to fabricate nanostructures is by utilizing anodic porous alumina as a scaffold for growth. Both porous alumina formation and nanowire growth are self-assembly methods that are electric field assisted. Although there are existing models that attempt to explain the behavior of porous alumina growth, they are not complete. In addition, no complete, systematic study has been done to better understand the process of porous alumina growth. The same is true for the electrodeposition of nanostructures into the porous alumina templates.

The formation of ferromagnetic materials in porous alumina in well-aligned arrays allows a perfect opportunity to explore the magnetic properties of nanoscale ferromagnets in more depth. Although there has been much work on nanoscale ferromagnets, there is still much that needs to be done to understand the physics of such structures. In addition, electrodeposition into porous alumina allows us to create many interesting shapes and composites that have yet to be studied and can reveal much about the nature of nanoscale magnetism.

In addition, there may be many interesting and important applications of porous alumina and metal-electrodeposited nanowires as metal-dielectric lenses for superlensing and negative index of refraction metamaterials. The bottom-up method provides a very quick and simple method for making such samples, and it would be an easy way to mass produce lenses for negative refraction.

Carbon nanotubes can also be fabricated inside porous alumina templates. The majority of carbon nanotube studies have been carried out on very well ordered carbon nanotubes. However, nanotubes made by chemical vapor deposition into porous alumina templates are very disordered. There has been very little work to date on such disordered nanotubes. Disordered nanotubes can shine much light on the nature of interactions on the nanoscale that are not easily observed in well-ordered nanotubes. In addition, as we will find, disordered carbon nanotubes can be very easily made ferromagnetic by annealing them in an atmosphere containing hydrogen. Because these ferromagnetic nanotubes are entirely new, there is much exciting physics yet to be discovered.

Carbon nanotubes are composed of concentric circles of graphene layers. Graphene is a single monolayer of carbon atoms packed into a two-dimensional hexagonal honeycomb lattice. Theoretically, graphene has been studied for over sixty years as the basic constituent of bulk graphite, but graphene itself was long considered to be of purely academic interest because monolayers were thought to be thermodynamically unstable and hence unobservable in nature. Recently, it was shown that monolayers of graphene could be stabilized on suitable surfaces, and experiments have demonstrated many remarkable properties predicted by theory. Also, because the discovery of graphene is so new, there is very little experimental data available. Plus,

because graphene is the basic constituent of carbon nanotubes, it is interesting to compare their many diverging characteristics.

1.2 Outline of Thesis

In chapter 2, we discuss the work done on porous alumina. The results led to the publication of [1-4]. We were the first to perform a systematic study of the growth process of porous alumina templates. This study showed that the prevailing models on pore growth and stability formation erred in their initial assumptions involving the nature of dissolution during the anodization reaction. Furthermore, we were the first to notice the formation of dendrites in the alumina, which are a signal of instability in the growth. We were also the first to characterize the formation of “nanonoodles” caused by over-etching of the alumina. These nanonoodles have given new insight into the role of dissolution during anodization.

Chapter 3 discusses the fabrication of nanomaterials in porous alumina. This work led to the publication of 2 review articles [4, 5] and the research article in ref. [6], which was republished in the Virtual Journal of Nanoscience. Our main results were that we optimized the deposition of magnetic nanowires. We also showed that we could create filled polyaniline nanotubes by a highly repeatable and successful three step anodization method that has never before been used.

Chapter 4 discusses an application of metal dielectric arrays. This led to the publication of the paper listed in ref. [7], which was also republished in the Virtual Journal of Nanoscience and received mention in the October issue of the Materials Research Society Bulletin. Here, our main results were to show that the bottom-up electrodeposition method can create metal-dielectric arrays that exhibit the necessary surface plasmon resonances characteristic of negative index of refraction materials.

In Chapter 5, we discuss the magnetic properties of nanowires, nanotubes, and composites. This work led to 3 papers. One has been accepted and two are currently under review [8-10]. We were the first to create and measure the magnetic properties of bifurcated nanowires. We also were the first to perform a comprehensive magnetic study on ferromagnetic filled polyaniline nanowires. Also, and most importantly, we are the first to experimentally demonstrate ferromagnetism in carbon nanotubes caused by H₂ annealing.

In Chapter 6, we discuss methods to make devices out of template-synthesized nanostructures. In doing this work, a review article was published, cited in ref. [11].

Chapter 7 deals with transport phenomena in template-synthesized carbon nanotubes, and has led to 2 papers, both currently under review and cited in refs. [9, 12]. Our main results were to show that despite previous research on disordered carbon nanotubes that show weak localization as the dominating behavior, our carbon nanotubes act as Luttinger liquids. Furthermore, we demonstrate the never before seen phenomena of field sweep rate dependent hysteretic magnetoresistance in carbon nanotubes, which we attribute to strong magneto-viscosity effects and anisotropic magnetoresistance, and a temperature dependent transition in the magnetoresistance, which we attribute to a Bright model order-disorder transition.

Chapter 8 deals with the 2 dimensional, or unrolled carbon nanotube structure graphene. We present the first results, to the best of our knowledge, of transport taken in an in-plane magnetic field. We also study the temperature dependent transport, which has also never been accomplished.

Chapter 9 is a conclusion.

Chapter 2: Porous Alumina

2.1 Introduction

The anodic growth of alumina has been studied for quite some time and has been used by industry as a protective coating on aluminum objects. However, in the last few decades, due to the invention of high resolution scanning electron microscopy (SEM) and other imaging methods that allow visualization at the micron and sub-micron scale, it has been discovered that under certain conditions, a film of hexagonally ordered porous structures can be grown anodically in alumina [13-16]. **Figure 2.1** displays an SEM image of such a porous structure. The top image is a profile view that shows the pores extending down to a curved “barrier layer” of alumina which sits on the aluminum substrate. The bottom image shows a top view of the hexagonally ordered pores.

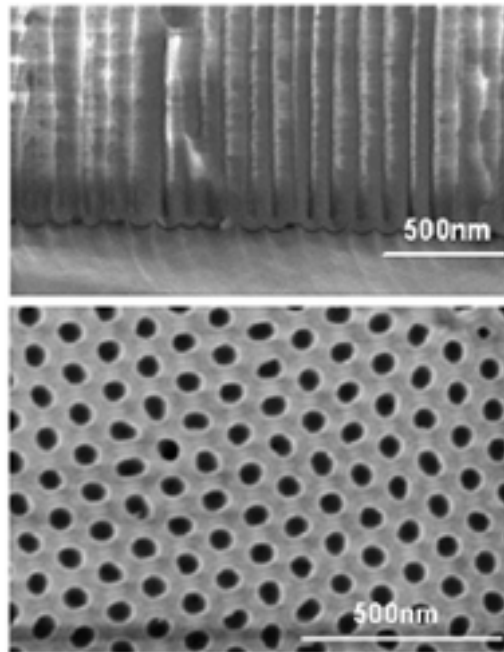


Figure 2.1: SEM image of pores formed by anodization of aluminum at 40 V DC with 3% oxalic acid. The upper image is a profile view. The curved barrier layer is easily seen at the bottom of the pores. The lower image shows a top view of the hexagonally ordered pores.

A typical set up for the growth of porous alumina templates is shown in **Figure**

2.2.

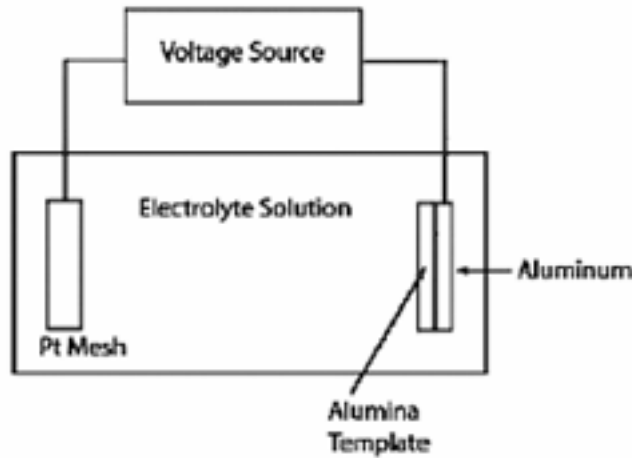


Figure 2.2: A typical experimental set-up for porous alumina growth.

The process of porous alumina growth is quite complex, and it involves the formation and shaping of an electric field at the interfaces of the sample, which accelerates various ions into the reaction (as discussed in the upcoming sections). In general, it is a function of the type of electrolyte (or acid) used, the *pH* of the electrolyte, the temperature of the electrolyte (affecting the speed of the reaction only), the composition of the counter electrode, the amount of foil exposed to the reaction, the separation distance between electrode and counter electrode, and the voltage or current applied. Anodization can be carried out in any beaker. However, for our experiments we use a specially designed cell composed of quartz and Teflon. Therefore, the amount surface area of aluminum exposed to the electrolyte is kept at a constant $0.25\pi \text{ cm}^2$ and the electrode-counter electrode separation distance is a constant 11 cm. The amount of exposed aluminum mainly affects the current density; more exposed aluminum results in a smaller current density. The separation distance controls the strength of the electric field generated at the various interfaces of the sample. We do not investigate these two variables in our

experiments. Many different materials can be used for a counter electrode including C, Au, Ag, Cu, and In. However, for our experiments we use a rectangular Pt mesh. By changing the shape and material of the counter-electrode, the uniformity and strength of the electric field can be changed. The rectangular Pt mesh is chosen because it gives a good uniformity of electric field over the entire area of the aluminum foil. We are also not concerned with this variable in our experiments. The reaction can be carried out under either constant current or constant voltage conditions (DC). In our set up, we use a constant voltage. In what follows, we investigate the effect of changing the electrolyte type, electrolyte pH, and applied voltage.

Contrary to the growth mechanism, the experiments to create porous templates are quite simple. Templates are made in either two ways: 1-step or 2-step anodization. In 1-step anodization, a piece of aluminum foil is placed in the anodization cell, an electrolyte is chosen and poured into the cell to cover the foil, and a voltage is applied for a set amount of time. The resulting template is removed and washed of acid. In 2-step anodization, first a 1-step anodization is performed for a longer time. After which, the template is removed and placed in an acid bath containing a 1:1 mixture of 5% chromic acid and 5% phosphoric acid heated to 150° C for approximately 2 hours or left to sit in the unheated solution overnight. This removes the pores leaving only the formed barrier layer. The etched template is then placed back in the anodization cell and re-anodized for a time that is shorter than the initial anodization. A 2-step anodization often results in a better ordered structure, as is discussed in section 2.3.

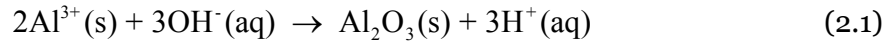
2.2 Dimensional Growth

2.2.1 *Electrochemical Models*

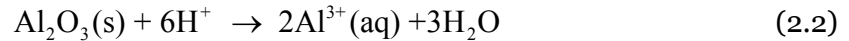
Electrochemically, researchers have hypothesized that the porous alumina formation occurs during two separate processes: oxidation of the aluminum substrate

and dissolution of the oxide layer [17-20]. When aluminum is placed in an electrolyte bath with a counter electrode and a current or voltage is applied, an electric field focuses at the interfaces of the aluminum, which draws OH⁻ ions to oxidize the aluminum. Concurrently, the aluminum reacts with available protons, which creates free aluminum ions, which diffuse across the barrier layer to become oxidized by the hydroxyl ions. The alumina nucleates at the oxide/electrolyte interface during this process and pores etch downward towards the barrier layer, or metal/oxide interface. However, the process may be done by more than one chemical pathway. It could be a combination of oxidation of the aluminum and concurrent dissolution of the alumina. Or, rather than dissolution, the aluminum can be protonated to create the observed aluminum cations. This is summarized by the following chemical formulas [13, 14, 21]:

Oxidation of Aluminum to form Alumina:



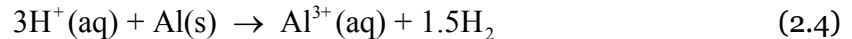
Dissolution of the Alumina:



Aside from dissolution, the diffusion of Al³⁺ may also be due to:



Or



In this way, the two interfaces are in constant motion. **Figure 2.3** shows a schematic of this chemical process.

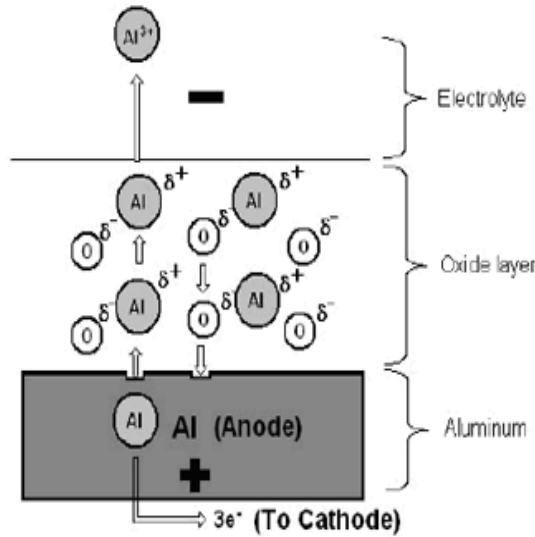


Figure 2.3: A schematic drawing of the field assisted diffusion of aluminum and oxygen ions. The diagram shows the pathway of dissolution of aluminum ions into the electrolyte according to the mechanism of the reaction in equation (2.3). Oxidation of alumina occurs at the oxide layer-aluminum interface.

A graph of current vs. time for a typical anodization process is displayed in

Figure 2.4. By analyzing this graph, the various components of the reaction can be better understood.

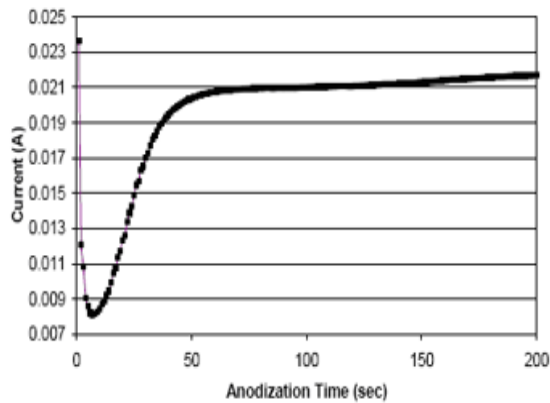


Figure 2.4: A typical current vs. time curve for anodization in 3% oxalic acid at 40 V DC.

In the first part of the process, the voltage is switched on and the barrier layer begins to form, causing a sudden drop in measured current. Then, the nucleation and formation of the porous structures causes a rise in the measured current. During these two parts of the reaction, due to widely varying chemical conditions and focal point of the electric field at the interfaces, the reaction is unstable. Eventually, though, as the pores begin to grow, the reaction stabilizes and a steady state current is reached. These current vs. time curves were modeled using chemical assumptions, such as ion concentration, notably, by the group of Singaraju, et al. in [22, 23]. However, their observations differed significantly from those of the most ubiquitous physical model by Parkhutik and Shershulsky [17] (also the model on which most of the other models are based). Primarily, Singaraju, et al. noticed the opposite curvature for their experimental studies (an almost $1/x$ dependence rather than the almost $x^{1/2}$ dependence of **Figure 2.4**). This discrepancy will be further discussed in Section 2.3.4.

2.2.2 The Parkhutik and Shershulsky Model

There are several competing and sometimes complementary physical models for porous aluminum oxide growth. Each is not without its fundamental problems. The oldest, and perhaps most widely cited theoretical model for porous alumina oxide growth is that of Parkhutik and Shershulsky [17, 24-26]. The model seeks to describe the motion of the two interfaces, aluminum-alumina and alumina-electrolyte. This model begins by assuming that the applied voltage creates an electric field in the alumina. The electric field in the alumina is given by Laplace's equation:

$$\nabla^2\Phi = 0. \tag{2.5}$$

The boundary conditions are given at the interface of the alumina and the aluminum (subscript AA) and the alumina and the electrolyte (subscript AE):

$$\begin{aligned}\Phi_{AA} &= U_A \\ \Phi_{AE} &= 0\end{aligned}\quad (2.6)$$

All other electric fields, including the field in the electrolyte, are ignored. The current in the alumina found using the continuity equation:

$$\nabla \cdot J = 0. \quad (2.7)$$

So,

$$J = \mu(E)nE. \quad (2.8)$$

Here, $\mu(E)$ is the ionic mobility, given by the equation:

$$\mu(E)E \approx \sinh(cE). \quad (2.9)$$

This allows us to write the electric current at the alumina-electrolyte surface as:

$$J_{AE} = -\left[A e^{k_d E_{AE}} - B e^{k_o E_{AE}} \right] \hat{n}_{AE}, \quad (2.10)$$

where, \hat{n}_{AE} is a unit vector normal to the alumina-electrolyte interface. A is a dissolution reaction factor and B is an oxidation reaction factor. Furthermore, the proton concentration information is contained in these coefficients by

$$A = A_0 10^{-\eta p^H}. \quad (2.11)$$

Here, η can be either 0 or 1; 1 for protons supplied by the electrolyte and 0 for the dissociation of water molecules at the alumina surface. Therefore, for the dissolution process, it is set to 1. The coefficients k_o and k_d are functions of temperature and describe the alumina molecular structure. E is the electric field in the oxide and is proportional to the electric field in the electrolyte by the proportionality factor

$$k = \frac{\epsilon_{ox}}{\epsilon_{el}}, \quad (2.12)$$

where ϵ_{ox} and ϵ_{el} are the dielectric constants of the respective materials.

During the reaction, it is assumed that the alumina-electrolyte interface shifts due to dissolution of the surface and subsequent conversion of aluminum into alumina. The rate at which the interface shifts is given by

$$\frac{d\mathbf{R}_{AE}}{dt} = \left[\alpha A e^{k_d E_{AE}} - \beta B e^{k_o E_{AE}} \right] \cdot \hat{\mathbf{n}}_{AE} . \quad (2.13)$$

\mathbf{R}_{AE} is the radius vector of a point on the interface, α and β are coefficients related to the currents and alumina growth and dissolution.

The interface between the alumina and the aluminum also shifts, and its shifting rate is given by

$$\frac{d\mathbf{R}_{AA}}{dt} = -\gamma \mathbf{J}_{AA} . \quad (2.14)$$

Using (2.10) we can relate the two currents [17]:

$$\mathbf{J}_{AA} = J_{AE} \frac{E_{AA}}{E_{AE}} . \quad (2.15)$$

It now remains to transform (2.13) and (2.14) into Cartesian coordinates. This gives

$$\begin{aligned} \frac{\partial y_{AE}}{\partial t} &= -V_{AE} \left[1 + (\nabla y_{AE})^2 \right]^{1/2} \\ \frac{\partial y_{AA}}{\partial t} &= -V_{AA} \left[1 + (\nabla y_{AA})^2 \right]^{1/2} , \end{aligned} \quad (2.16)$$

where, the V 's are the rates of interface shifting,

$$\begin{aligned} V_{AE} &= \alpha A e^{k_d E_{AE}} - \beta B e^{k_o E_{AA}} \\ V_{AA} &= \gamma J_{AA} . \end{aligned} \quad (2.17)$$

This can be simplified by focusing our attention only on the growth of the bottom of the pores. We know that

$$V_{AA} - V_{AE} = 0 . \quad (2.18)$$

Also, the constancy of the curvature equations is described by

$$\begin{aligned}\frac{dG_{AA}}{dt} &= \frac{\partial}{\partial t} \left(\frac{\partial^2 y_{AA}}{\partial x^2} \right) = - \left(\frac{\partial V_{AA}}{\partial E} \frac{\partial^2 E_{AA}}{\partial x^2} + G_{AA}^2 V_{AA} \right) = 0 \\ \frac{dG_{AE}}{dt} &= \frac{\partial}{\partial t} \left(\frac{\partial^2 y_{AE}}{\partial x^2} \right) = - \left(\frac{\partial V_{AE}}{\partial E} \frac{\partial^2 E_{AE}}{\partial x^2} + G_{AE}^2 V_{AE} \right) = 0\end{aligned}\quad (2.19)$$

Rewritten in polar coordinates where, $x = R_{AE} \sin \theta_{AE}$:

$$\frac{\partial^2 E_{AE}}{\partial \theta^2} = -V_{AE} \left(\frac{\partial V_{AE}}{\partial E} \right)^{-1} \quad (2.20)$$

Then,

$$V_{AE} \left(\frac{\partial V_{AE}}{\partial E} \right)^{-1} = \frac{1}{k_d} \frac{1 - \frac{\beta B}{\alpha A} e^{[(k_o - k_d)E_{AE}]}}{1 - \frac{\beta B k_o}{\alpha A k_d} e^{[(k_o - k_d)E_{AE}]}} \quad (2.21)$$

In order for pore growth to be sustained, the electric field must always be at a maximum at the bottom of the pores, therefore the partial derivative in (2.20) should be less than zero. Then large shifts in the interface should leave the electric field unchanged. This allows us to write,

$$E_{AE} = \frac{1}{k_o - k_d} \ln \left(\frac{k_d \alpha A}{k_o \beta B} \right) \quad (2.22)$$

From (2.18) we can write,

$$\frac{E_{AA}}{E_{AE}} = \frac{\alpha(1 - k_d / k_o)}{\gamma(1 + \alpha k_d / \beta k_o)} \quad (2.23)$$

The shapes of the boundaries are hemispheres, which yields the solutions,

$$\frac{E_{AA}}{E_{AE}} = \frac{1}{1 + L / R_{AE}} \quad (2.24)$$

With $L = R_{AA} - R_{AE}$. The 2-dimensional solutions for the electric fields at the boundaries are:

$$\begin{aligned}
E_{AE} &= \frac{-U_a G_{AA}}{(1-G_{AA}L)\ln(1-G_{AA}L)} \\
E_{AA} &= \frac{-U_a G_{AA}}{\ln(1-G_{AA}L)}
\end{aligned} \tag{2.25}$$

And, the 3 dimensional solutions are:

$$\begin{aligned}
E_{AE} &= \frac{U_a / L}{1-G_{AA}L} \\
E_{AA} &= \frac{(1-G_{AA}L)U_a}{L}
\end{aligned} \tag{2.26}$$

Where U_a is the applied voltage. Substituting these into (2.23) and rewriting, we get

$$\begin{aligned}
R_{AA} &= \frac{-U_a / E_{AE'}}{(1-\kappa_2)\ln(1-\kappa_2)} \quad 2D \\
R_{AA} &= \frac{U_a / E_{AE'}}{\kappa_3(1-\kappa_3)} \quad 3D
\end{aligned} \tag{2.27}$$

The model also predicts a dependence of pore radius on pH. Substituting (2.11) into (2.27), we arrive at

$$R_{AA} = \frac{R_{AAo}}{1 - 2.3\eta pH \left[\ln \left(\frac{\alpha k_d A_o}{\beta k_o B} \right) \right]^{-1}}, \tag{2.28}$$

where, R_{AAo} is the pore radius extrapolated to pH=0.

2.2.3 The Thamida and Chang Model for Dimensional Growth

The second physical model to appear was that by Thamida and Chang [20]. They note several exceptions with the Parkhutik model. First, by choosing a hemispherical geometry in their model, Parkhutik and Shershulsky have allowed for a radially directed electric field at the bottom of the pores, which would increase the pore diameter as a

function of time. Plus, Thamida and Chang argue, Parkhutik and Shershulsky have oversimplified the problem altogether.

Thamida and Chang begin with the interfacial speed of the alumina-electrolyte boundary given by equations (2.11) and (2.13):

$$u_{AE} = \alpha A_0 10^{-pH} e^{k_d E_{AE}} - \beta B e^{k_o E_{AE}}. \quad (2.29)$$

Likewise, the speed at which the alumina-aluminum boundary shifts is given by equations (2.10), (2.14), and (2.15):

$$u_{AA} = \frac{E_{AA}}{E_{AE}} \left[\gamma A_o 10^{-pH} e^{k_d E_{AE}} + \gamma B e^{k_o E_{AE}} \right]. \quad (2.30)$$

The same boundary conditions as Parkhutik and Shershulsky are used, given in (2.22) and (2.23). Thamida and Chang then assume that the thickness of the alumina increases until both interfacial speeds are equal. Also, they assume that:

$$E_{AE} = E_{AA} = E_{AE'} = \frac{U_a}{d}, \quad (2.31)$$

where, d is the oxide thickness. This makes the base state electric field different from that of equation (2.22):

$$E_{AE} = \frac{1}{k_o - k_d} \ln \left[\frac{(1 - \gamma / \alpha) \alpha A_0 10^{-pH}}{(1 + \gamma / \beta) \beta B} \right]. \quad (2.32)$$

Thamida and Chang also find that there is a critical value of $pH_c=1.77$. They predict that beyond this pH no porous structures will grow because the electric field, as predicted by their model, vanishes. Moreover, they also find that the pore diameter is directly proportional to voltage. They calculate that the barrier layer thickness is given by

$$d_b = \frac{U_a}{2.31 - 1.19 pH} \quad (2.33)$$

by inserting the necessary constants into equations (2.31) and (2.32). Then, they pick a dimensional wave number that would maximize the growth rate of the alumina, k_{max} .

This allows them to estimate the wavelength of the pores at 2.96 in dimensional units, or the wavelength is 2.96 times the barrier layer thickness. So, the diameter of each alumina crystal cell, which they equate to the wavelength and interpore separation is

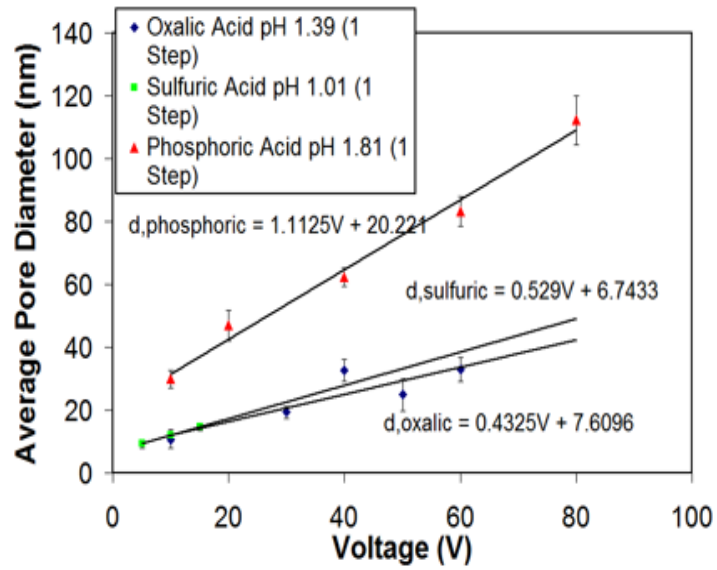
$$d = \frac{2.96U_a}{2.31 - 1.19pH}. \quad (2.34)$$

2.2.4 Experimental Results

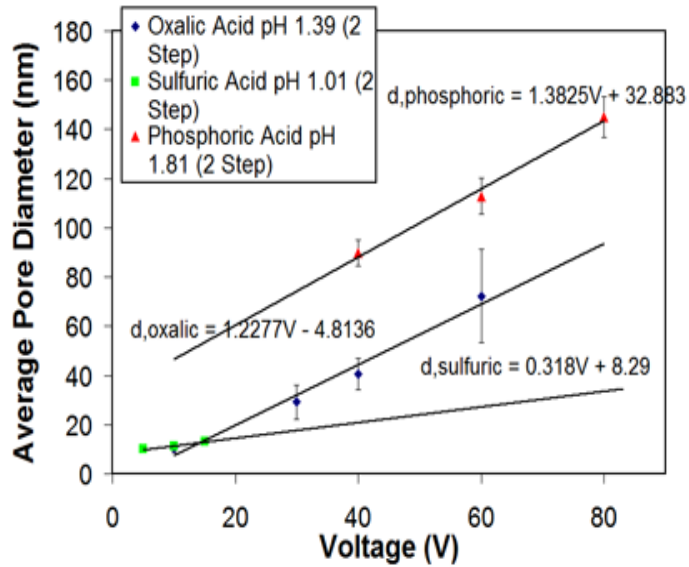
For the experiments that follow, unless otherwise noted, anodization was carried out in the cell described in Section 2.1. 1-step anodization samples were anodized for 30 minutes. 2-step anodization was carried out by anodizing first for 2 hours, followed by an overnight etch in 5% phosphoric/5% chromic acid, and a second anodization for 15 minutes. Pore dimensions are found by taking an arithmetical mean of approximately 50 measurements and the quoted error is the standard deviation.

Figure 2.5 displays average pore diameter as a function of voltage for a selected group of constant pH values for oxalic, sulfuric, and phosphoric acids for 1- and 2-step anodization. Trend lines have been placed on the data by the method of least squares. It is clear that the behavior is linear for both the 1- and 2-step cases. **Figure 2.6** displays interpore spacing as a function of voltage for both 1- and 2-step anodization for a selected pH for oxalic and phosphoric acids. The behavior predicted by the Thamida and Chang model is also graphed along with the experimental results. From **Figures 2.5** and **2.6**, it is evident that both Parkhutik and Shershulsky and Thamida and Chang have accurately predicted the linear dependence of pore diameter (or interpore spacing) on voltage. However, when Parkhutik and Shershulsky suggested in their model that an experimentalist pick the parameters of the model to fit the data [17], they are requiring their model to fit appropriately. Therefore, any linear set of data can be fit using this model. This means that the model lacks a necessary preciseness. Also, it is clear that the

model presented by Thamida and Chang, although it is indeed linear in voltage, does not fit the data well.

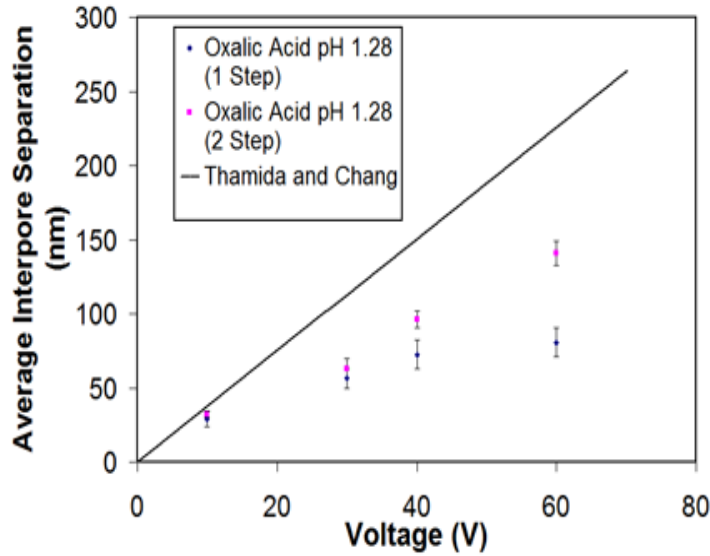


(A)

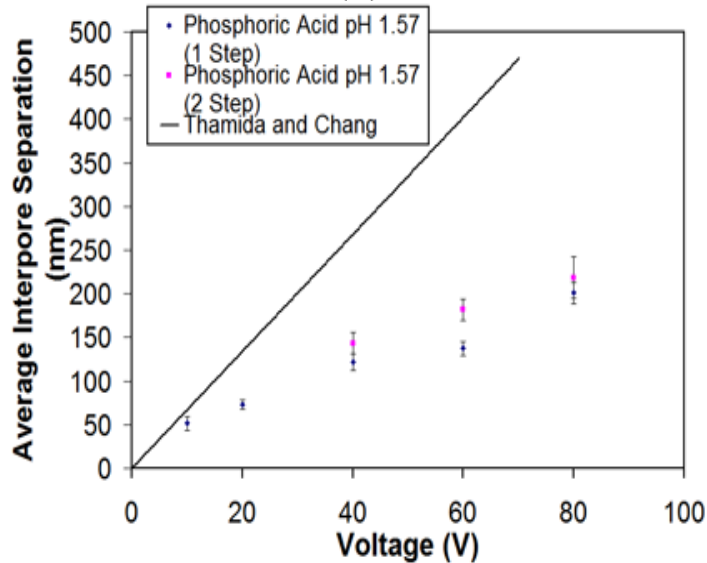


(B)

Figure 2.5: Graphs of average pore diameter vs. voltage for some acids for (A) 1-step anodization and (B) 2-step anodization. The pore diameter is directly proportional to the voltage.



(A)



(B)

Figure 2.6: Graphs of average interpore separation for 1- and 2-step anodization compared to the predicted curves of the Thamida and Chang model [20] for (A) oxalic acid with a pH of 1.28 and (B) phosphoric acid with a pH of 1.57. We see that although the linear dependence on voltage was correctly predicted, the model does not fit the data well.

Figure 2.7 displays pore length as a function of voltage for the three acid types for a selected pH. As expected, the pores get longer as the voltage increases. At higher voltages, more energy is available in the system causing the reaction to happen faster,

thus giving longer pores. The exponential increase for higher voltages could be due to higher voltages causing a slight heating of the solution, thus leading to an even more efficient growth.

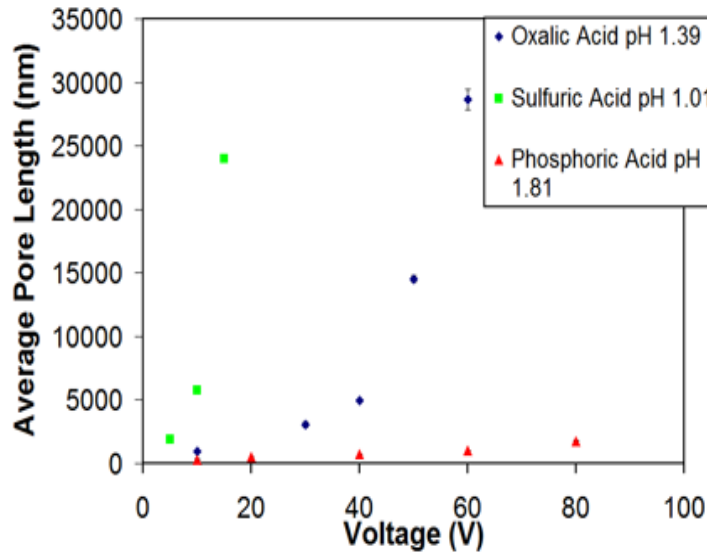


Figure 2.7: Graph of average pore length vs. voltage for three different acids. As the pH increases, the length is longer for equal time reactions.

Figure 2.8 displays a graph of interpore spacing vs. *pH* for all three acid types at 10 V. The formula derived by Thamida and Chang (equation (2.34)), which also expressed the $1/(1-pH)$ behavior predicted by Parkhutik and Shershulsky (equation (2.28)) is graphed along with the data. Each acid type is denoted by a different symbol. At a first glance, it would appear that the data somewhat fits the curve because all of the points lie somewhat on the line, however, if one looks closely, one will see that, on the contrary, the data does not fit at all because each group of points is for a completely different acid type. In fact, the interpore spacing remains relatively constant over the range of *pH* values for each different acid type. This would suggest that there is more of a dependence of interpore spacing (thus pore diameter, as well) on acid type rather than on *pH*. This constancy of interpore separation is seen again in **Figure 2.9**, this time

much more acutely when only one acid is used. **Figure 2.9** displays a graph of pore diameter vs. pH for oxalic acid at 40 V. The formula derived by Thamida and Chang, which also expressed the behavior predicted by Parkhutik and Shershulsky is graphed along with the data.

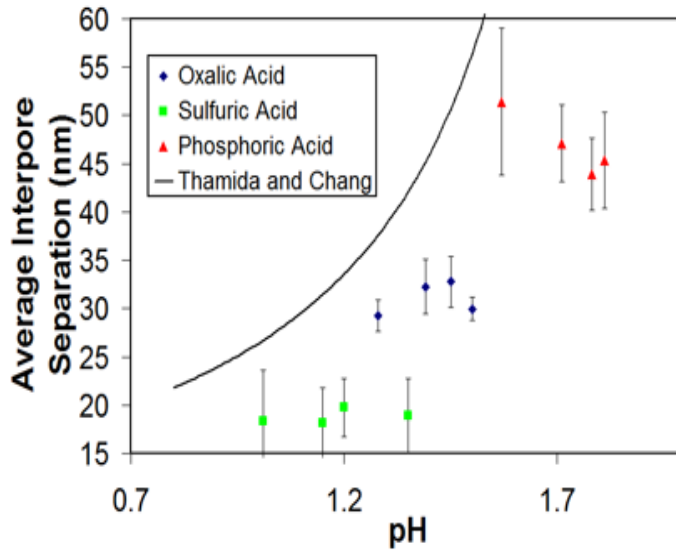


Figure 2.8: Graph of average inter pore separation vs. pH for three different acids for an anodization voltage of 10 V as compared to the behavior predicted by the model of Thamida and Chang and Parkhutik and Shershulsky [17, 20]. Although the total behavior roughly follows the shape of the curve, each group of points symbolizes a completely different acid, so the dependence is non-existent. We also see that pores formed after the $pH_c=1.77$ of Thamida and Chang.

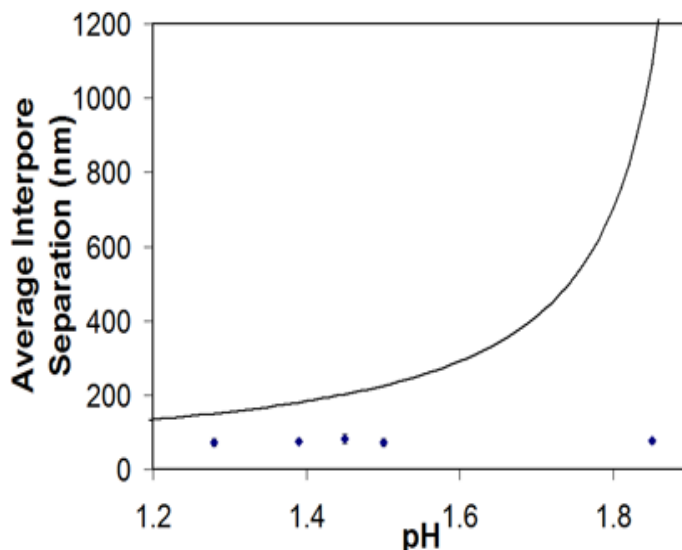


Figure 2.9: Graph of average interpore separation vs. pH for oxalic acid at 40 V as compared to the behavior predicted by Thamida and Chang and Parkhutik and Shershulsky [17, 20]. We see that, indeed, as the pH increases, the pores size stays constant. We also see that pores formed after the $pH_c=1.77$ of Thamida and Chang.

Indeed, the pore diameter (and interpore spacing) is constant in pH . The models predict in their assumptions that the pH comes into the picture in equation (2.13) in the form of the dissolution factor given by equation (2.11). This assumes that the dissolution and oxidation processes compete with each other with somewhat equal weight during the anodization process. Obviously, if this was the case, no pores would form at all. The authors account for pore formation by arguing that small energy perturbations and holes in the aluminum or oxide will lead to pores under certain circumstances (discussed in Section 2.3). However, this seems to be an error. In ref. [21], an experiment performed by our colleagues found that dissolution accounts for a negligible part of the process, or that, chemically, the process does not follow the pathway of equation (2.2). This was done by quantifying the amount of material present at the beginning of the reaction, at the end of the reaction, and also noting the presence of dissolved aluminum in the electrolyte. It was found that the amounts of material present before and after are the

same, so nothing could have dissolved. Rather, the chemical process must follow equations (2.3) or (2.4). Therefore, the oxidation and dissolution do not equally compete with one another, and it would seem that some form of weighting factor is necessary to be included in the models to account for this discrepancy.

We suggest that this weighting factor should be related to the amount of time that the anodization process occurs. In the simplest case, it could be a step function of reaction time. In ref. [21], where dissolution was found to have a negligible role, all the processes were carried out for a relatively short period of time (less than 2 h), which is commonly the case for aluminum anodization, owing to propensity of the aluminum to be entirely consumed for longer reactions. However, we have also discovered that in the process of anodization of titanium, which is similar to the aluminum anodization process, dissolution may have a role in long-time anodizations (greater than 10 hours) [3]. In short-time reactions, there is simply not enough time for the acid to dissolve any of the alumina and thus the proposed weighting factor would be set to 0. This would eliminate the dissolution factor in equation (2.13), which would change all later equations that calculate the pore size as a function of pH to be constant in pH . For longer time reactions, a simple version of the proposed weighting factor could have a value of 1, which would reinstate the pH dependence. However, a more accurate weighting factor would need to take into account the time scale of the reaction, thus the speed of the reaction, and include the temperature of the solution and current density in the template.

However, the pH does have an affect on the process, as viewed in **Figure 2.10**, where we can see that the length of the pores steadily increases as a function of the pH . This is readily explained by noting that at higher pH values, the concentration, thus availability, of oxidizing ions is much greater. If the availability of these ions is greater,

the process will happen much faster. Therefore, it is also necessary to add a factor in some way that includes the pH , or, rather, the pOH , to the oxidation term in the models. This might take a form equivalent to the pH factor in equation (2.11), but with the pH replaced by the pOH .

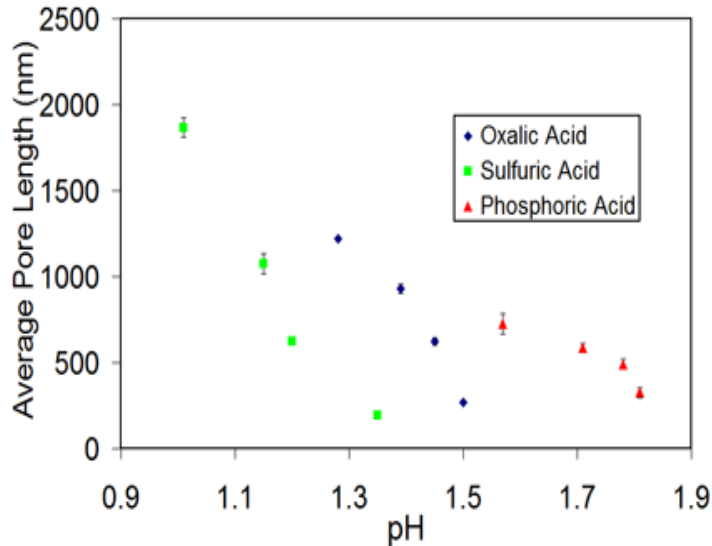


Figure 2.10: Graph of average pore length vs. pH for three different acids at 10 V anodization potential. The pore length increases as a function of pH .

Interestingly, the critical pH value suggested by Thamida and Chang after which no pores will form was surpassed, as evidenced by **Figures 2.4, 2.6, 2.7, and 2.8**, and pores did form properly. In fact, there appears to be no such critical pH value beyond which pores will not form. This further supports the idea that pH plays very little role in the formation of the pores.

2.3 Stability of Growth

2.3.1 *The Thamida and Chang Model for Stability Growth*

Thamida and Chang were the first to introduce the idea of stability regions in the formation of the alumina pores into a physical model [20]. The concept has also been discussed from a more qualitative chemical standpoint notably by the group of Asoh, et

al., for instance, in ref. [27, 28]. Thamida and Chang hypothesized that if small holes, which they refer to as perturbations, form in different surface geometries on the alumina-electrolyte interface, different structures would result. In one instance, the pores will not form at all, rather, the oxide will dissolve and only a barrier layer will form. In another instance, the pores will form as well ordered and, therefore, stable pore structures. Finally, there is the instance where pores will form but do so without the ordering and uniformity in size and shape. This is unstable pore formation. They also map out a stability phase diagram, were they note, although they do not explain (or provide a formula to calculate), how stability is a function of pH [20].

Finally, Thamida and Chang make an argument for the pore shape at the barrier layer being based on a function of pH. They model that for higher pH, the cone at the base of the pore becomes sharper. However, this is very difficult to verify, as a combination of extremely small size and large capacitance effects in the alumina make it difficult to see with SEM with such detail at these necessary sizes.

2.3.2 *The Singh Model*

The most recent model of porous alumina growth was done by Singh, Golovin, and Aranson [18, 19]. In their model, they continue in the way of Thamida and Chang by noting the effect of interface geometry on the initiation of pore growth and final size. However, they argue that one must introduce several more physical mechanisms. They now introduce the effect of pore activation energy on the Laplace pressure, which results due to surface energy at curved geometries. They also consider elastic stress due to volume expansion at the aluminum-alumina interface. This suggestion arises from the fact that it has been found that by cleaning or pre-patterning the surface of the aluminum prior to anodization, the resulting porous templates are more ordered [27]. In addition, we have found that marks left by the regular machining of the aluminum

sheets can lead to regions of instability and also clearly mark off boundaries in the template itself. It is this pre-stress on the aluminum, they argue, that leads to more ordered porous structures.

Using the same boundary conditions as the previous two models, they write an equation for the electric current across the alumina-electrolyte interface as

$$-\sigma \partial_n \Phi = k_+ e^{\alpha\Phi} - k_- e^{-\alpha\Phi}, \quad (2.35)$$

Where, σ is the conductivity in the alumina $k(\pm)$ are coefficients describing either the oxidation or dissolution reactions, respectively, and $\alpha=e/(2k_B T)$. And,

$$\begin{aligned} \partial_n &= \hat{n} \cdot \nabla \\ \hat{n} &= \frac{(-\partial_x X - \partial_y X)}{\left[1 + (\partial_x X)^2 + (\partial_y X)^2\right]^{1/2}} \end{aligned} \quad (2.36)$$

in Cartesian coordinates with X being the position of the interface.

For the Singh model, the velocities of the interface movements are again calculated, except, now, most of the values of the parameters are filled in. $k_d = -k_o = q_e/k_B T = k$, with q_e being the charge on an electron, k_B is the Boltzmann constant, and T is the temperature. Likewise, the pre-exponential coefficients αA and βB are exchanged for

$$k_{\pm} = A_{\pm} \exp \left[\frac{1}{\rho k_B T} (\gamma^{\pm} \kappa + s_{ij}^{\pm} \sigma_{ij}) \right], \quad (2.37)$$

respectively. Here $A_+ = A$, and $A_- = B$ from earlier. κ is the interface curvature, ρ is the oxide number density, σ_{ij} is the stress tensor evaluated at the oxide-electrolyte interface, s_{ij}^{\pm} are the aforementioned elastic strains, and

$$\gamma^{\pm} = \rho \frac{\partial E_a^{\pm}}{\partial \kappa} \quad (2.38)$$

includes the activation energies E_a^{\pm} . The equations are then solved.

The Singh model then predicts what occurs if a small perturbation is applied using a linear stability analysis. For the case in which there are no elastic strains, or for $s_{ij}=0$, they find that there is a critical voltage that defines a stability threshold given by

$$V = \frac{r\sqrt{A_0 B 10^{-pH}} B_{\pm} \Gamma}{\sigma(r b_{+} + b_{-})} + \frac{1}{k} \ln \left(r \sqrt{\frac{B}{A_0 10^{-pH}}} \right). \quad (2.39)$$

Here, we have amended the original notation used in the Singh model papers [18, 19] to be consistent with the Parkhutik model and the Thamida and Chang model, and to condense mathematical expressions containing only constants. Here, r , B_{\pm} , b_{-} , b_{+} are constants. And,

$$\Gamma = \frac{1}{\rho k_b T} (\gamma^{-} - \gamma^{+}). \quad (2.40)$$

For the typical parameters given in [18], this is plotted in **Figure 2.11**. For the case in which there are elastic strains present, or for pre-patterning of the barrier layer, they find,

$$V = r E_s K B_{\pm} \Gamma \left\{ C_1 r \eta K B_{\pm} S - \sigma E_s B (r^2 b_{+} + b_{-}) \exp \left[\frac{C_2 \eta S}{2} \right] \right\}^{-1} + \frac{C_2 \eta S + \ln \left(r^2 B / A_0 10^{-pH} \right)}{2k}, \quad (2.41)$$

where,

$$K = \sqrt{A_0 10^{-pH} B^3} \quad (2.42)$$

and E_s is the steady state electric field given by

$$E_s = \sigma^{-1} \sqrt{A_0 10^{-pH} B^3} (r - r^{-1}) \quad (2.43)$$

And, C_1 , C_2 , η , and S are additional constants. **Figure 2.11** also displays a graph of this equation as a function of pH for the typical parameter values given in [18].

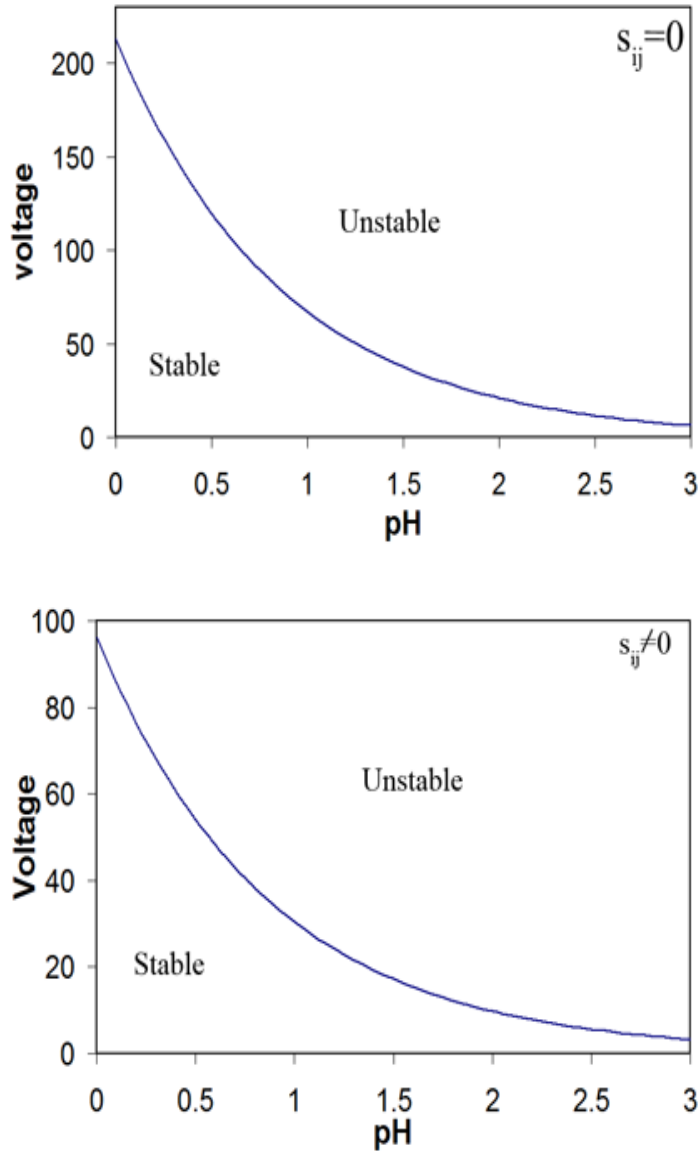


Figure 2.11: Pore formation stability graphs calculated from the Singh model. The upper graph has the stress tensor set to $\mathbf{0}$, or is the case of equation (2.39) with no pre-patterning of the aluminum. The lower graph has the stress tensor set to a some non-zero value, or is the case of equation (2.41) with pre-patterning of the aluminum.

2.3.3 Experimental Results

The dependence of anodization on acid type is evidence in **Figure 2.12** where pores made by oxalic, sulfuric, and phosphoric acids are pictured. The shapes are clearly

different. In one step anodization, **Figure 2.12(A)** shows that the phosphoric acid pores are very close together, almost arranged in a parallelogram and are square in shape. Sulfuric acid pores and oxalic acid pores are arranged in rows and spaced further apart with non-uniform shapes. **Figure 2.12(B)** shows that for 2-step anodization, the oxalic acid and sulfuric acid pores are arranged roughly hexagonally and have a rounded type of shape. Phosphoric acid pores are oddly arranged and shaped. Therefore, there must be some chemical process that occurs as a result of the acid's chemical constituents that adds another variable to the problem.

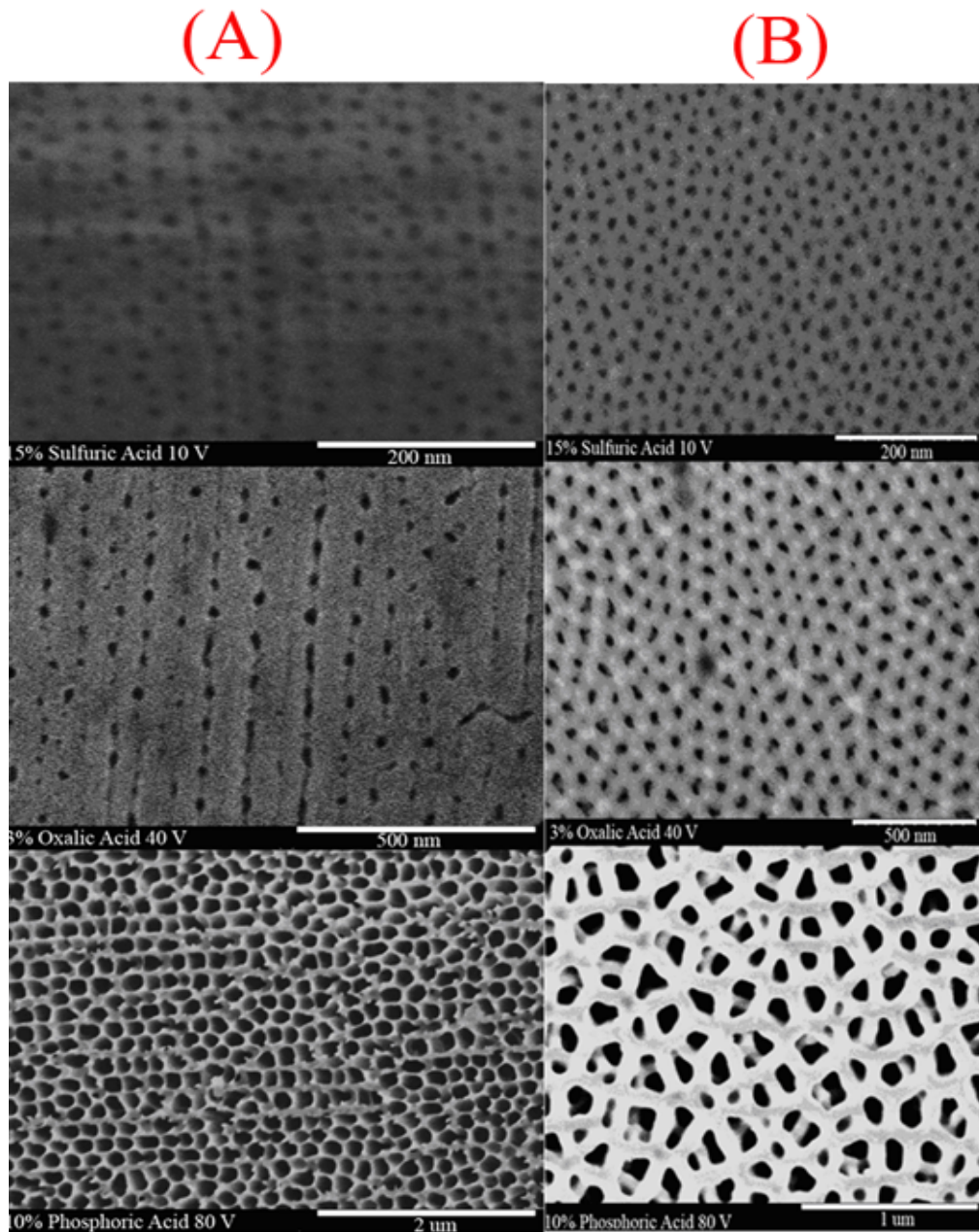


Figure 2.12: Images of pores made by the 3 different acid types for top: 10 V 15% sulfuric acid, middle: 40 V 3% oxalic acid, bottom: 80 V 10% phosphoric acid (A) 1-step anodization and (B) 2-step anodization. Acid concentrations are % by weight. The pore shapes and organizations are different depending on the acid type. The 2-step anodized pores are much better organized due to pre-patterning, or a non-zero stress tensor.

Table 2.1 summarizes the experimental pore formation stability results for oxalic acid and compares them to those predicted by the Singh model [18]. The results for sulfuric acid were similar, but they are not included so as not to be redundant. The Singh model defines 2-dimensional stability to occur when the pores appear to be well-ordered and of uniform size. We also use this definition. As it can be seen, the experimental stability results do not fit the Singh model very well (**Figure 2.11**). There does seem to be a correlation between *pH* and stability. The stable region occurs at a lower voltage for increasing *pH* values. But, rather than a curve that goes like $1/x$, the sample is unstable at low voltage, then stabilizes, then becomes unstable again. Phosphoric acid is somewhat different. For 1 step anodization, it becomes stable at about 80 V, and then remains stable until the voltage becomes too high to perform anodization (a huge current density causes the reaction time scale to become too short and the aluminum is quickly eaten). This was also previously noticed in [28, 29]. However, according to the Singh model, this is the opposite of what should occur. For 2-step anodization, the phosphoric acid samples become stable at about 40 V and remain stable thereafter. This is also contrary to the Singh model. Additionally, the shapes of the stable 1-step and 2-step anodized pores are of a different shape for phosphoric acid, as evidenced in **Figure 2.12**.

Table 2.1: Summary of stability results for oxalic acid.

	pH	Voltage (V)	Stable (Exp.)	Stable (Theory)
1 step	1.28	10	No	yes
		30	No	yes
		40	No	yes
		60	Yes	no
	1.39	10	No	yes
		30	No	yes
		40	Yes	no
		60	No	no
	1.45	10	No	yes
		30	No	yes
		40	Yes	no
		60	No	no
	1.5	10	No	yes
		30	yes	yes
		40	no	no
		60	no	no
2 step	1.28	10	no	yes
		30	yes	no
		40	yes	no
		60	no	no
	1.39	10	no	yes
		30	yes	no
		40	yes	no
		60	no	no
	1.45	10	no	yes
		30	yes	no
		40	yes	no
		60	no	no
	1.5	10	no	yes
		30	yes	no
		40	yes	no
		60	no	no

The evolution of two-dimensional pore stability as a function of voltage can be further seen in **Figure 2.13**. **Figure 2.13** shows top-view SEM images of samples prepared by anodization under varying voltages with 5% Phosphoric Acid and using 1-step anodization. At 20 V we see that the pores vary widely in diameter and they are not

very well organized into rows. We can see that as the voltage increases, the pores become more ordered. At about 100 V the pores become fairly uniform in diameter and also self-organize themselves evenly. This stability is maintained for all higher voltages.

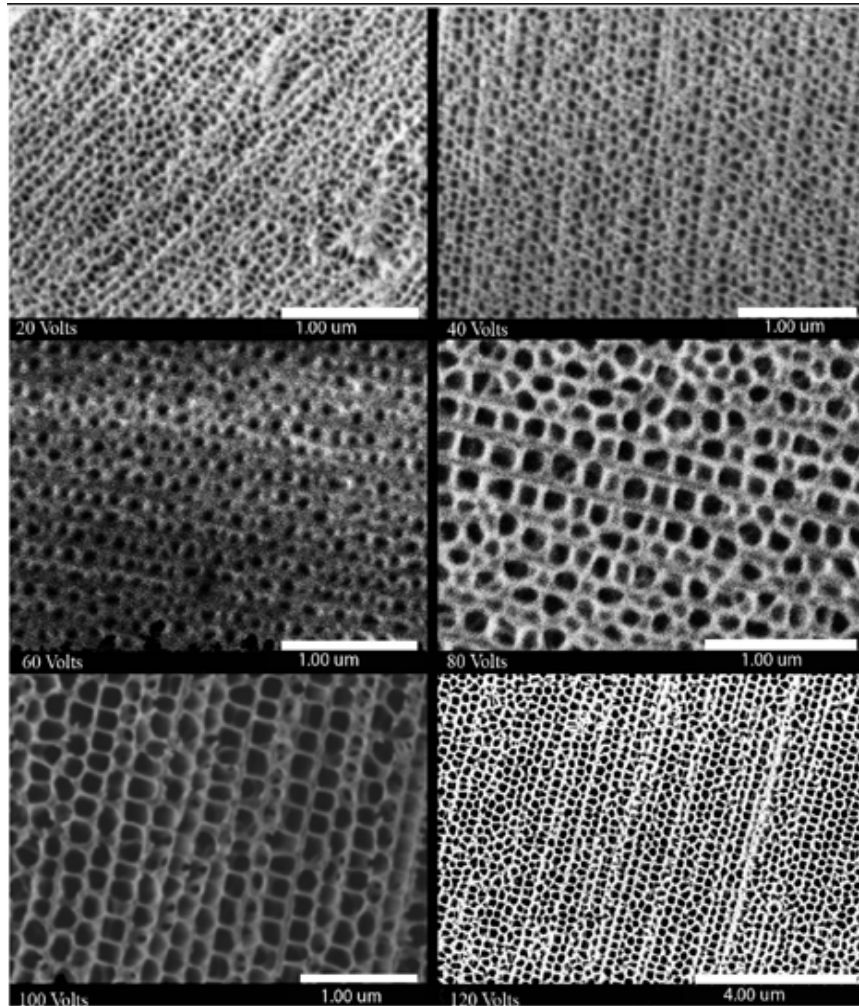


Figure 2.13: SEM images showing the evolution of two dimensional stability of pore growth as seen in 5% Phosphoric acid, 1 step samples. The pores start out unstable, but begin to form more stable, well-ordered rows.

From these images, the pore diameters were determined. **Figure 2.14** shows a plot of pore diameter as a function of voltage. Pore diameters are clearly linear in voltage. As the voltage increases, we can see that the standard deviation of the pore diameters depicted by the error bars becomes a smaller percentage of the total value. Thus, the pores are becoming more uniform and the system is evolving into stability.

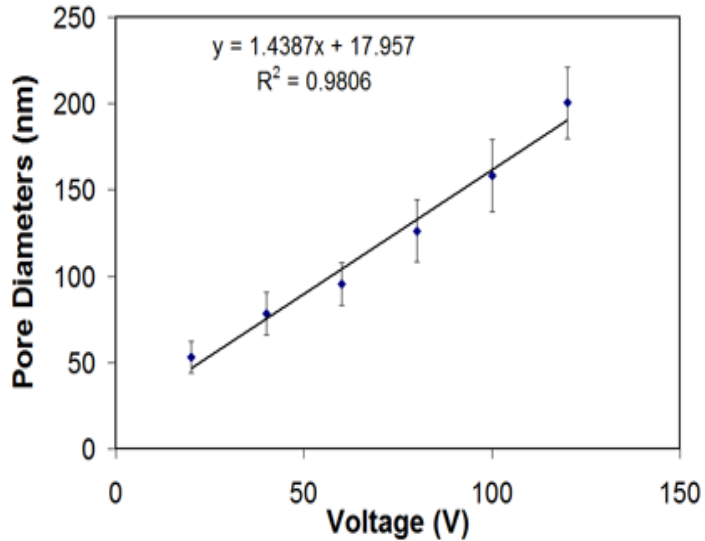


Figure 2.14: Pore diameter as a function of voltage for the samples in Figure 2.13. Higher voltages give standard deviations that are a smaller percentage of the total pore diameter, thus, the pores are more ordered.

2.3.4 Dendrite Formation

While these instabilities and the evolution of the system were studied in depth in the previously mentioned models [18-20], the previous studies only modeled and noticed growth and instabilities in two dimensions. Also, they restricted their analysis to the evolution of the system rather than the pore growth, that is, they focused mainly on the initial stages of pore growth. However, we observe instabilities in the pore growth in three dimensions, that is, also along the axis of the pore. Here instabilities manifest themselves as dendrites. We also find that the regime over which the 3-dimensional stability is observed is not necessarily linked to the 2-dimensional instability.

The corresponding side view SEM images of the samples in **Figures 2.13** and **2.14** are shown in **Figure 2.15**. From these images, it is clear that, at lower voltages, instability in pattern formation is seen in the form of dendrite-like structures that branch outward from the main pore cavities. Galenko, et al. in [30] note that dendrite formation

in material growth is a trademark of non-equilibrium. However, despite the predictions by Galenko we do not observe secondary and continuing branch bifurcations along the dendrites as predicted by many prevailing dendrite growth models, such as the models by Feigenbaum, Galenko, and Zhuravlev, or Hopf [30]. However, this may be due to the resolution restrictions of the SEM rather than an actual absence of such structures.

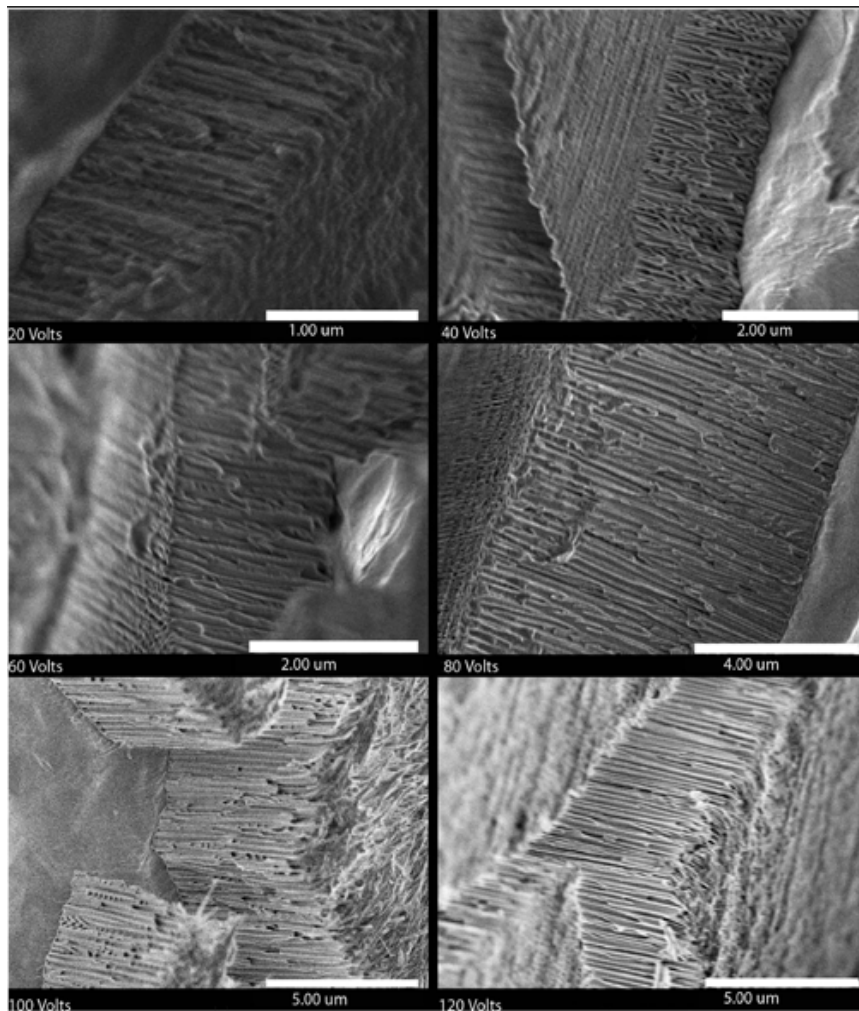


Figure 2.15: The profile view of the 5% phosphoric acid, 1-step samples. 3-dimensional instability is seen in all but the 120 V sample.

As the anodization voltage increases, the dendrite-pattern is seen to slowly diminish and finally disappear. For example, at 120 V no dendrites are observed. To

visually compare samples that contain dendrites to those where dendrites are absent, **Figure 2.16** shows a high-resolution image of a sample with dendrites and another without dendrites. The arrows point to the dendrite structures.

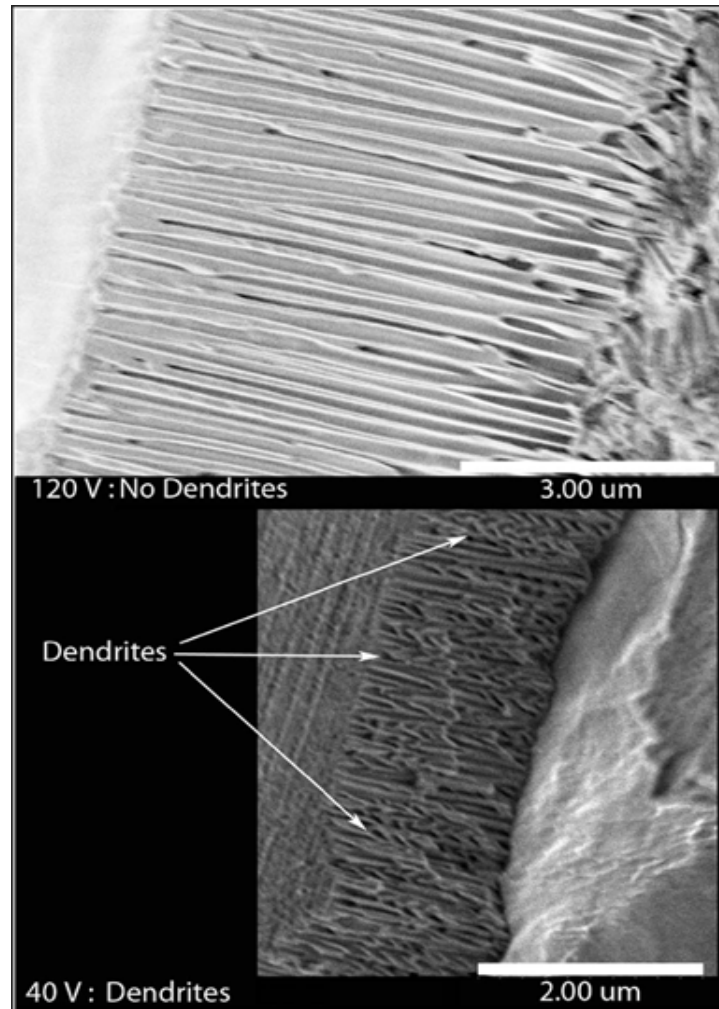


Figure 2.16: Samples with and without dendrites. The arrows point to some dendrite structures.

If we now compare the top view SEM images with the side view images, it is clear that at low voltages there is instability in two dimensions as well as along the third dimension, that is, along the axis of the cylinder. This 3-dimensional instability is seen to continue up to higher voltages. At 100 V, the top view image appears to be somewhat

stable, though there remains some dendrite growth along the cylindrical axis. This means that although the system has reached two-dimensional stability, it has not yet reached three-dimensional stability. Therefore, stability in two and three dimensions are not directly coupled to one another. These findings are summarized in **Table 2.2**.

Table 2.2: Summary of 5% phosphoric acid stability

Voltage (V)	2D Stable?	3D Stable?
20	No	No
40	No	No
60	No	No
80	No	No
100	Yes	No
120	Yes	Yes

It must be added here that in addition to the voltage, the time of anodization may also play a critical role in stabilizing the pore pattern. For example, at the lower voltages with increased anodization time, one would expect the pore patterns to become stable. We anodized several samples at low voltages for long time (16 h). In most of these samples, we continue to observe dendrite-formation along the cylindrical axis. **Figure 2.17** shows a SEM image of a sample anodized for 16 h where the dendrite branching is clearly seen.

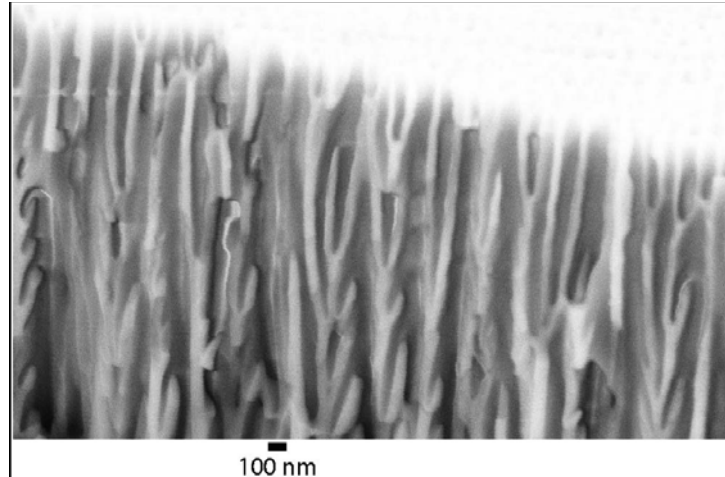
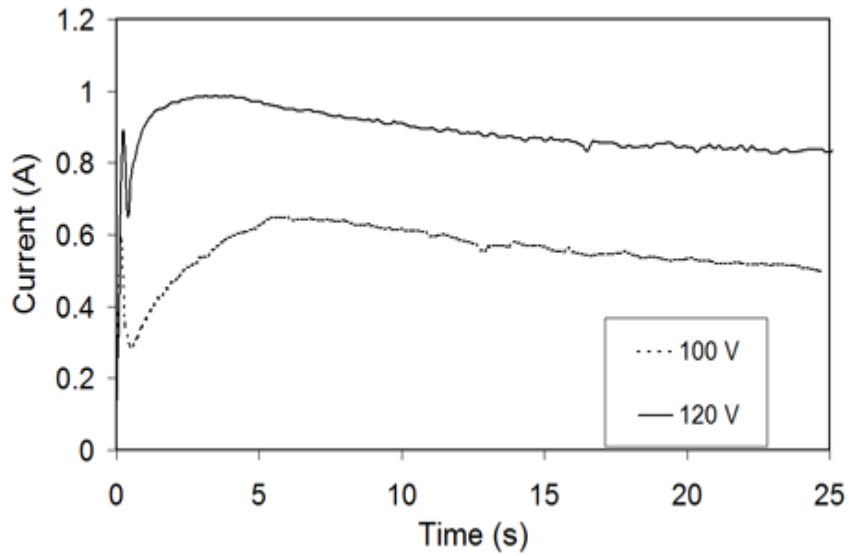
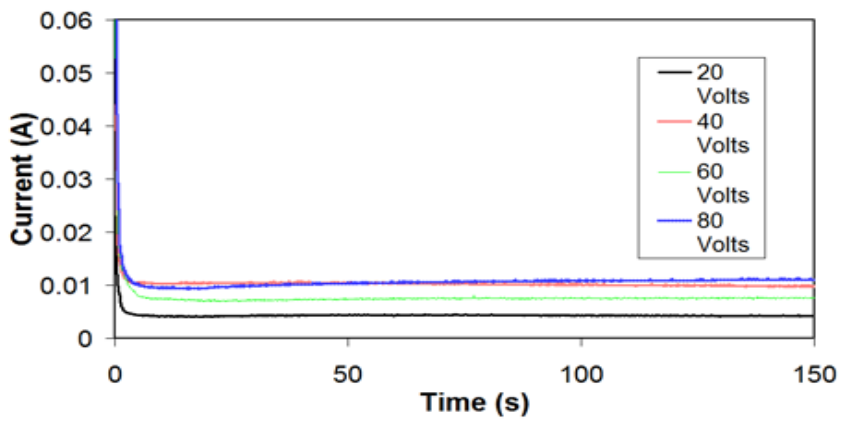


Figure 2.17: Sample anodized for a long time where dendrites are clearly seen.

Further insight into the properties of the system can be gleaned from the anodization current vs. time graphs (see **Figure 2.18 (A)** and **(B)**). It is apparent that during the 2-dimensionally unstable anodization process, the current versus time relationship is very different from that obtained during the 2-dimensionally stable process. However, no insight can be attained from these graphs for the three-dimensional case. Moreover, by comparing **Figure 2.18(A)** to the model put forward by Parkhutik and Shershulsky [17] it appears that their model describes the two-dimensionally stable case. Comparing **Figure 2.18(B)** to the Singaraju model (discussed in Section 2.21) [23], it appears that the Singaraju model describes the 2-dimensionally unstable case. Therefore, although both models seem to predict the correct behavior for each stability regime, neither can be considered a complete model.



(A)



(B)

Figure 2.18: (A) Current vs. time graphs in the stable regime described by Parkhutik and Shershulsky [17], and (B) current vs. time graphs in the unstable regime described by Singarju, et al. [23].

2.4 Other Structures

2.4.1 Nanonoodles

In order to widen and straighten the pores formed by anodization, and to smooth the top surface of the template, the templates can be treated by a post-anodization acid etch. This can be done with a variety of acids at different temperatures. However we find 5% Phosphoric acid at room temperature to give the best results. The templates are simply placed in the acid for a set period of time and the pores are widened. **Figure 2.19** displays pore diameter as a function of etching time for two different anodization voltages.

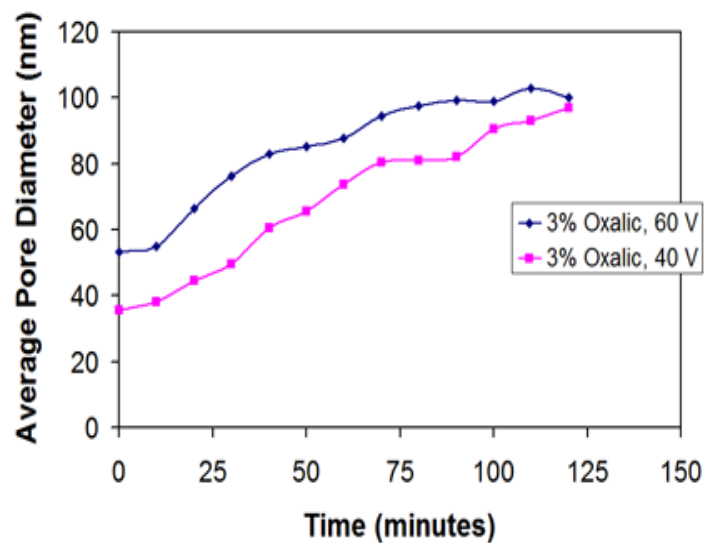


Figure 2.19: Average pore diameter vs. time for 2 different porous alumina templates being etched in 5% phosphoric acid.

By examining **Figure 2.19**, we can see that the pores will slowly widen until they asymptotically approach some maximum widening value. At this critical value an interesting material dubbed “nanonoodles” forms. We actually found two methods to create nanonoodles. In the first method, anodization is carried out in highly acidic electrolytes, for example, 10% oxalic acid, and at very high anodization voltages, typically >60 V. Also, the anodization is allowed to continue until the foil is entirely consumed by the reaction. In the second method, the template is etched in 5% phosphoric as previously described.

Figure 2.20 shows SEM images of nanonoodles formed by rapid anodization (method 1) while **Figure 2.21** shows nanonoodles formed by post-anodization etching (method 2). In general, the nanonoodles form due to thinning of the walls that separate the alumina pores. Eventually, the walls become too thin to support the weight of the column of alumina formed by the intersection of three pores. This column then snaps off, forming the nanonoodle structure.

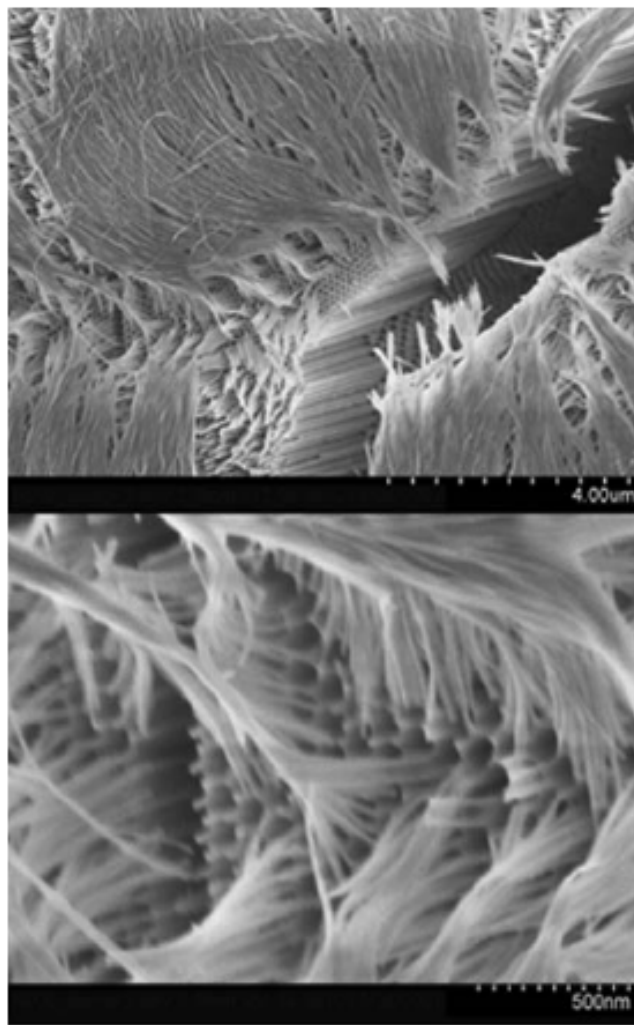


Figure 2.20: SEM image of nanonoodles formed by anodization of aluminum in 10% oxalic acid at 60 V. The bottom figure shows a very high magnification image. The hexagonal pore structure of the template below the nanonoodles can also clearly be seen.

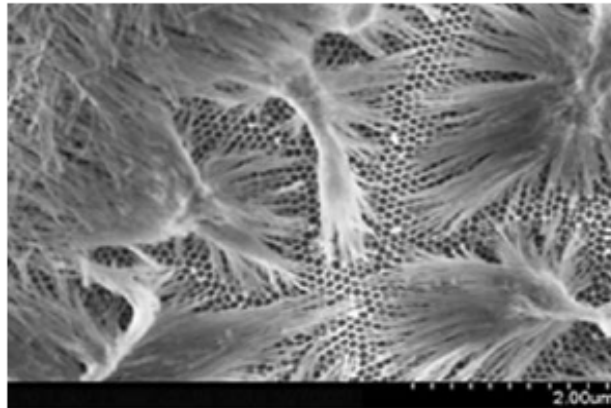


Figure 2.21: SEM image of alumina nanonoodles formed by anodization in 5% phosphoric acid at 80 V followed by 120 minutes etch time in 5% phosphoric acid.

In the case of post-anodization etching, the pores are widened slowly by 5% phosphoric acid. **Figure 2.22** displays a graph of the average pore wall thickness, or the thickness of the wall that separates a pore from its neighboring pore, versus etch time. The pore wall thickness was obtained by measuring the interpore separation and diameters of the pores using high resolution SEM images and then subtracting the average diameter from the average interpore separation. It is evident that the wall thickness decreases gradually until the walls disappear. The formation of the nanonoodles occurred at approximately 100 minutes (or greater) of etch time. In this method, the nanonoodles form because the acid etches (due to a simple chemical dissolution process) the pores radially as well as longitudinally. Since, the length of the pores is several times larger than their diameter, eventually, the pore walls are thinned and the columns snap off to form nanonoodles. This is described pictorially in **Figure 2.23**. The corresponding geometry of the nanonoodles can also be seen in the SEM (bottom) image of **Figure 2.20**.

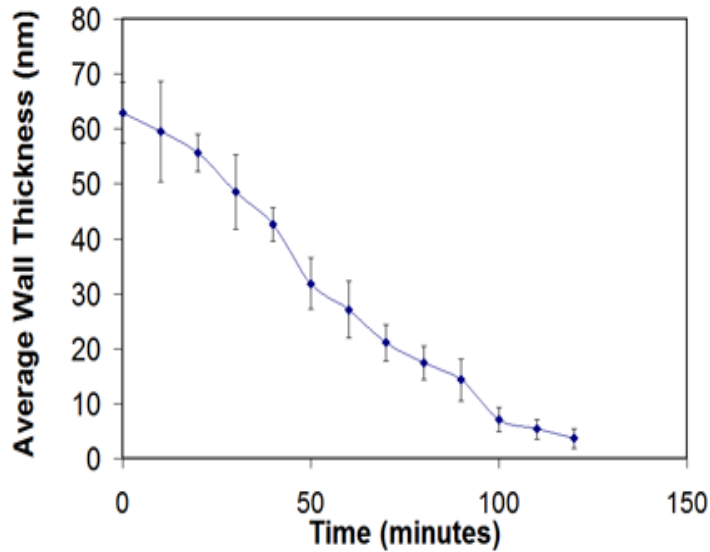


Figure 2.22: Dependence of average wall thickness as a function of etching time. Eventually, the walls disappear.

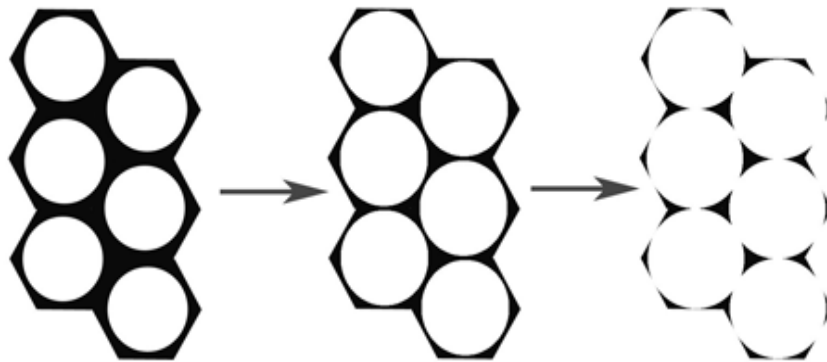


Figure 2.23: Pictorial model demonstrating the formation of nanonoodles from thin pore walls. Etching eats away at the walls from the inside until the columns formed between the pores break off to form nanonoodles.

In the case of anodization, the nanonoodles form for very rapid reactions—that is, when the reaction to convert aluminum into porous alumina occurs very quickly and violently. This can be accomplished either through the use of high acid concentration electrolytes and/or high anodization voltages. Under normal anodization conditions, for example 3% oxalic acid at 40 V (at room temperature or below), the oxidation process occurs slowly, with a small current passing through the cell. The pores

are created with a negligible amount of dissolution, as the reaction is halted before the weak anodization acid can begin to etch them. When the conditions are changed to stronger acids and higher voltages, for example 10% oxalic acid at 70 V, the reaction proceeds with a high current passing through the cell causing the acid to heat up significantly during the reaction. The high current causes the reaction to occur very rapidly and violently. However, this also greatly increases the acid's ability to etch the pores (chemical dissolution), due to the heating of the acid, while at the same time increasing their length. Also, with the increased acid concentration (increased H⁺ availability), the chemical dissolution process is further increased.

For anodization under the previously stated low *pH* and high voltage conditions, increased chemical dissolution with respect to the oxidation is responsible for the formation of nanonoodles. The chemical dissolution is enhanced by the particular reaction conditions. As depicted in **Figure 2.23**, the dissolution process will etch the pores radially much more rapidly than along the length, due to the comparable thicknesses of both areas (the length is orders of magnitude thicker than the walls), thus making the walls very thin. The structurally weakened columns are further weakened by the extreme violence of the reaction. Eventually, the walls snap to form nanonoodles. Finally, it must be mentioned here that even with the increased dissolution, the oxidation reaction continues to dominate the reaction as we reported earlier in Section 2.3.3. If both processes competed equally, only a barrier layer of alumina would remain after the reaction, as the pores would be etched away just as quickly as they were being formed. However, under the rapid reaction conditions reported here, the dissolution reaction is no longer negligible.

We previously showed that dissolution has little effect on the anodization process for short-time anodization (usually less than 2 hours). Additionally, we showed how this

effect has drastic implications for the accuracy of the prevailing models for porous alumina growth. The formation of the nanonoodles and our discovery that they occur by result of etching, or dissolution, suggests that for certain conditions the dissolution process becomes non-negligible and begins to compete with oxidation. Also, we have seen that nanonoodles form during anodization with solutions of low pH, at high anodization voltage, or when etched for long periods of time. In the case of low pH or high voltage (thus high current), it appears that the dissolution is strongly dependent on the availability of H⁺ ions to dissolve the alumina. In the case of etching, however, it appears that the dissolution comes into effect simply as a result of the long reaction time. This new information about the character of dissolution in the anodization process is significant and will help with future attempts to model porous alumina growth. Moreover, the appearance of nanonoodles in titania under similar circumstances [3] shows that the physical processes involved in the growth of porous alumina and porous titania are similar and can be modeled using similar assumptions.

2.4.2 Y-shaped and Bifurcated Pores

By changing the anodization voltage while the anodization process is proceeding, it is possible to make y-shaped, branched porous structures and bifurcated porous structures. **Figure 2.24** shows an example of such branched pore structures.

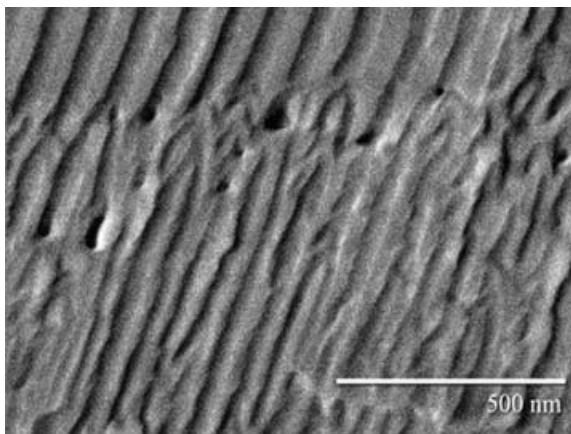


Figure 2.24: SEM image showing branched pore structures of alumina created by changing the anodization voltage during the reaction.

Here, the anodization voltage was initially set at 10 V and then reduced to 7.1 V and subsequently set back at 10 V. The result is 10 nm diameter stems at the two pore ends with 7 nm diameter branches in the mid-section. However, more generally, the selection of branching voltages is based on a simple relation between the stem voltage V_S and the branch voltage V_B given by:

$$V_B = \frac{V_S}{\sqrt{n}}, \quad (2.44)$$

where n is the desired number of branches [31]. Thus, for two branches, the anodizing voltage for the branches turns out to be 7.1 V when the anodizing voltage for the stem is 10 V. Then, these branched templates can be used to create branched nanostructures, as will be discussed in the following chapter.

Chapter 3: Growth of Nanowires and Nanotubes in Porous Alumina

3.1 Nanowire Growth by Electrodeposition

3.1.1 Introduction

Electrodeposition is a fast, easy, and inexpensive way to create nanostructures using porous alumina templates as scaffolding. In general, the electrodeposition process occurs when a positively charged element in an electrolyte is reduced by a flow of electrons, and then, assisted by an applied electric field, the reduced element deposits itself on a substrate. The deposition of nanowires is similar to electroplating found in [32-34]. In order to reduce a given number of moles of a substance, n , a certain amount of electric charge, q , is required. This required charge is given by

$$q = nn_e F , \quad (3.1)$$

where, n_e is the number of electrons and F is Faraday's constant. From basic electrostatics the total charge, q , can be expressed as the integral over time of the current. Now, using this information we can determine the number of moles, n , in terms of the applied current. Then, we can use the density to determine the thickness of the deposited material, which is given by,

$$thickness = \frac{m_a}{A\rho n_e F} \int I dt , \quad (3.2)$$

where, m_a is the atomic mass of the deposited material, A is the area, ρ is the density of the material, and I is the current. As it applies to the electrodeposition of wires, the thickness is synonymous with the length of the wires. And, obviously, the higher the current that is applied, the faster the wires will be grown. There are two different types of electrodeposition: alternating current (AC) and direct current (DC) electrodeposition.

The process may be done both under constant current or constant voltage conditions. However, in our experiments, we use constant voltage conditions solely.

AC electrodeposition takes place in a specially designed cell or in a beaker. The same set up that is used for anodization is commonly the one used for electrodeposition, but with the acidic anodization electrolyte solution replaced by an electrolyte solution containing the desired deposition constituents. One lead of a power supply is attached to a metal mesh. This mesh is made of a metal that is a very good conductor and acts as a counter electrode. Some commonly used metals for this mesh are Pt, Au, Cu, Pd, and Ag. However, there have been cases where conductive non-metals have been used. For instance, graphite was used in [35-38]. As in anodization, the shape and material make-up of the counter-electrode has a strong effect on the shape and strength of the electric field in the cell that causes the field-assisted deposition [39]. The other lead is attached to a contact that is put on the porous alumina either by sputtering, electroplating, or chemical evaporation. The contact may also be aluminum, present from the creation of the porous alumina. Some common contact metals are Au, Ag, and Cu. This is presented pictorially in **Figure 3.1**.

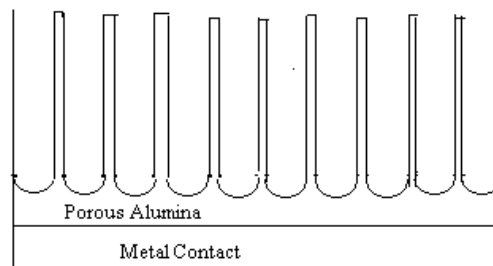


Figure 3.1: Porous Alumina Template with Metal Contact.

The mesh and the template are then immersed in an electrolyte solution which contains the material that one wishes to deposit. Then, an AC voltage is applied to the circuit and deposition begins due to the focusing of an electric field at the bottom of the

pores. Grains of material randomly deposit themselves into the template, eventually filling the pores, creating nanowires. Therefore, the size of the wires depends directly on the dimensions of the pores in the template. **Figure 3.2** shows a schematic of this setup.

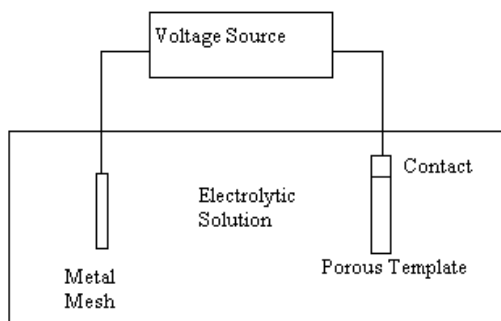


Figure 3.2: Schematic of the electrodeposition apparatus.

As time increases, metals are released from the electrolyte solution and electrochemical processes occur relating to the current passing through the solution. The *pH* will also change due to the oxidation and reduction caused by the flow of electrons and deposition into the template. Sometimes, it is necessary to maintain a certain range of *pH* values in order for the desired deposition to occur. In these cases, the solution must be buffered prior to and during the deposition process. So, an apparatus to monitor the *pH* may be added to the experimental set-up. Common acids used to buffer the solution are boric acid, sulfuric acid, and nitric acid.

AC electrodeposition is an ideal process to use when fabricating nanowires. Many different types of wires can and have been manufactured through the use of AC electrodeposition into porous alumina templates including semimetals, magnetic metals, non-magnetic metals, semiconducting metals, superconducting metals. **Table 3.1** gives a brief summary that is by no means complete. If the authors of the reviewed paper have made a point to mention an optimal temperature or *pH* of the electrolyte solution used, that information is also included.

Table 3.1: A list of materials deposited by AC electrodeposition

Material	Electrolyte Solution	pH, Temperature (°C)	Characterization
Bi nanowires[40-43]	75 g/l bismuth nitrate pentahydrate, 65g/l KOH, 125 g/l glycerol, 50g/l tartaric Acid	pH: 0.9	Magnetic Semimetal/ Semiconductor
Ni nanowires[44, 45]	0.1 M NiSO ₄ *6H ₂ O, 45 g/L boric acid	Temperature: 55	Magnetic
NiPb nanowires[37]	30 g/l Ni(CH ₃ COO) ₂ *4H ₂ O, 6 g/l Pb(CH ₃ COO) ₂ *3H ₂ O 6 g/l, 30 g/l H ₃ BO ₃	pH: 5.5	Magnetic
Fe nanowires[44, 46, 47]	50 g/l FeSO ₄ , 25 g/l Boric Acid		Magnetic
Co nanowires[46-48]	1 M CoSO ₄ [48]; or 30 g/l CoSO ₄ , 25 g/l Boric Acid[46]	pH: 4.0	Magnetic
CoP nanowires[49]	50 g/l CoSO ₄ *7H ₂ O, 30 g/l H ₃ BO ₃	pH: 3.0-4.0 Temperature: 30	Magnetic
CoPt nanowires[50-52]	10 to 1 mixture of CoCl ₂ and PtCl ₂ [50]; or 0.5 g/l PtCl ₄ , 96g/l CoSO ₄ , 42 g/l Boric Acid[51]	pH: 2.8-3[51]	Magnetic
FeS ₂ nanowires[53]	120 g/l FeSO ₄ , 45 g/l boric acid		Magnetic
FePt nanowires[50]	10 to 1 mixture of FeCl ₂ and PtCl ₂		Magnetic
Prussian Blue Nanowires (catera- [MFe ^{II} Fe ^{III} (CN) ₆] with M=Li ⁺ , Na ⁺ , K ⁺ , NH ₄ ⁺) [54, 55]	0.02 M FeCl ₃ , 0.02 M K ₃ Fe(CN) ₆ , 0.6 M Boric Acid, 0.5 M KCl	Temperature: 10	Magnetic Conducting Polymer
Co _{1-x} Fe _x nanowires[35]	45 g/l boric acid, CoSO ₄ , CoCl ₂ , FeSO ₄	Temperature: 37	Magnetic
vanadium iron cyanide nanowires[56]	0.02 M NaVO ₄ , 0.02 M K ₃ Fe(CN) ₆ , 3.6 M H ₂ SO ₄		Magnetic, Carbon based
Fe _{1-x} Ni _x	1 mol FeSO ₄ to 7 mol	pH: 3.0-3.5	Magnetic

nanowires[36]	water, 1 mol NiSO ₄ to 6 mol water, boric acid		
CdS nanowires [44]	0.055M CdCl ₂ , 0.19 M S in dimethylsulfoxide		Semiconducting
CdSe nanowires [44]	0.055 M CdCl ₂ , 0.19 M Se in dimethylsulfoxide		Semiconducting
CdS _x Se _{1-x} nanowires[44]	0.055 M CdCl ₂ , 0.19 M (Se + S) in dimethylsulfoxide		Semiconducting
Cd _x Zn _{1-x} S nanowires[44]	0.055 M (CdCl ₂ + ZnCl ₂), 0.19 M S in dimethylsulfoxide		Semiconducting
GaAs nanowires [44]	Ga(III), As(III)	pH: >2.5	Semiconducting
Sb/Sb ₂ O ₃ nanowires[57]	0.03 M potassium antimonyl tartrate, 0.435 M sodium tartrate dihydrate	pH: 9	Semiconducting
Au nanowires[47]	1 g/l HAuCl ₂ , 20 g/l MgSO ₄ *7H ₂ O	pH: 1.7	Metallic, Non-Magnetic
Ag nanowires[47]	1 g/l AgNO ₃ , 41 g/l MgSO ₄ *7H ₂ O, H ₂ SO ₄	pH: 2	Metallic, Non-Magnetic
Pt nanowires[57]	1 g/l H ₂ PtCl ₆ , 176.4 g/l H ₂ SO ₄	pH: <1	Metallic, Non-Magnetic
Pd nanowires[57]	10 g/l Pd(NH ₂)(NO ₂) ₂ , 100 g/l NH ₄ NH ₂ SO ₃	pH: 8	Metallic, Non-Magnetic
Cu nanowires[47]	35 g/l CuSO ₄ , 20 g/l MgSO ₄ *7H ₂ O, H ₂ SO ₄	pH: 1.2	Metallic, Non-Magnetic
Polyaniline nanotubes[58, 59]	0.3 M aniline, 1 M HCl, 10 ml 0.5 M toluene-p-sulfonic acid sodium salt, 0.12 M ammonium metavanadate		Conducting Polymer

DC electrodeposition takes place using the same type of set-up as in **Figure 3.2** and follows the same type of electrochemical processes described above. However, the anode must be attached to the metal mesh and the cathode must be attached to the contact on the alumina template, as the current never switches polarity. Also, the same rules as far as pH apply to DC electrodeposition as AC electrodeposition. There are two methods for carrying out the DC deposition process. First, the voltage is applied

electrostatically. This method is often used in plating techniques, and is ideal for creating thin films. Alternatively, and frequently, the applied voltage may be pulsed. The process that uses a pulsed voltage is very similar to the AC deposition process. However, now a square wave of unchanging polarity is applied instead of a sine wave that changes polarity. This method is usually used when growing single element nanowires, and can grow many of the same types of wires as AC deposition. Pulsed DC deposition is also ideal for growing multilayered wires, where the wires have layers made of different materials. As the primary method of electrodeposition for this thesis is AC deposition, we will not discuss DC deposition in any more depth.

3.1.2 *Metallic Nanowires*

In order to accurately fabricate nanostructures through electrodeposition, one must understand the optimal process conditions for doing so. Here we undergo a systematic study to understand the effect of the variation of three variables (*pH*, voltage, and frequency) involved in the electrodeposition process on the average nanowire growth rate. Experiments are carried out by depositing iron into porous alumina templates. First, we examine the effect of changing the *pH* of the electrolyte solution on the average growth rate of iron nanowires inside the pores. Then, we vary the magnitude of the applied AC voltage and determine its effect on the deposition rate. Finally, we vary the frequency of the AC voltage to show that there are three unique frequency regions corresponding to distinctly differing electrodeposition rates. These varying parameters have a significant impact on the properties of the nanowires that are deposited inside the template. Using the magnetic properties as an analytical tool, each region is analyzed and the results are discussed.

To do this, we use the AC electrodeposition set-up pictured in **Figure 3.2**. Porous alumina templates are created by anodizing aluminum foil in 15% sulfuric acid at

10 V for 30 min, which creates well ordered alumina pores of approximately 10 nm in diameter and 9380 ± 40 nm in length. The average filling rate is defined as $\Delta L/\Delta t$, the length of the pore divided by the time it takes to fill the pore in units of nanometers/second. The pore is considered to be “filled” when the current vs. time curve ceases to decrease smoothly and suddenly jumps, at which time the pores overflow and a thin film of iron is deposited on the surface of the nanowires as shown in **Figure 3.3**.

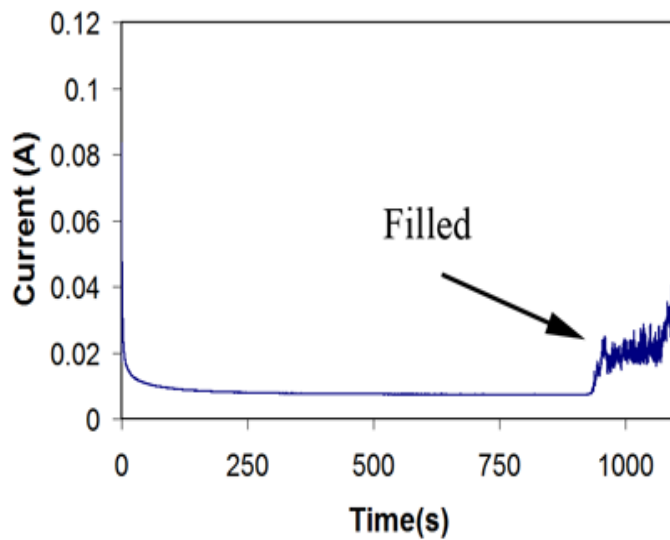


Figure 3.3: Current vs. time for deposition of Fe nanowires showing the jump of current that corresponds to filling of the pores.

For the pH experiments, a standard pH meter is used to measure the pH of the electrolyte solution immediately prior to electrodeposition. The pH is lowered by performing successive depositions using the same electrolyte solution. As current passes through the cell, electrons are donated to the solution, causing the concentration of free protons to increase. Also, the pH is lowered through natural oxidation over time. For the voltage experiments, the magnitude of the AC voltage applied across the cell is varied and deposition continues until the pores have been filled. The current vs. time curve is

analyzed and the time at which the pore becomes filled is recorded. For the frequency experiments, the frequency of the AC voltage is varied, and deposition continues until the pores have been filled. The current vs. time curve is then analyzed and the filling time is recorded.

It is a well-studied phenomenon that in ferromagnets there are preferred alignment directions. It has been noted that the easy axis is along the length of the nanowires. Therefore, we can verify the presence of nanowires in the templates by applying a magnetic field and measuring the magnetization vs. applied field behavior. This is a very good method for the verification of the formation of wires in the templates because oftentimes, due to the wires' small size, good SEM images are very difficult to capture and require much preparation of the sample. In the case of nanowires, one expects a large perpendicular anisotropy, that is, for applied fields along the axis of the nanowires, we expect the magnetic spins to align easily in the direction of the field. In contrast, for applied field perpendicular to the axis of the nanowires, we expect the wires to align less easily in the direction of the applied field. By comparing the coercivity and shape of the hysteresis curves in the two directions, one can get significant information into the nature of the deposited nanowires. We expect a high coercivity when the magnetic field is along the nanowire axis and a low coercivity when the field is perpendicular to the axis of the wires, which would indicate that there is a large perpendicular magnetic anisotropy, thus there are nanowires. Moreover, we can examine the squareness ratio, which can be defined as the ratio of the remnant magnetic field to the saturation magnetization. If there is magnetic anisotropy due to the nanowires, the ratio should be close to 1. These magnetic characterization experiments are done using a Princeton Measurements Corporation MicroMag model 2900

alternating gradient magnetometer (AGM) (See Appendix B). An in-depth discussion of the magnetic properties of nanowires is given in Chapter 5.

The *pH* is an important variable in the deposition process because it could be an indirect measurement of the concentration of iron in the solution that is available to deposit. When voltage is applied across the cell, iron from the electrolyte deposits inside the pores. The current in the cell causes some oxidation and the *pH* increases with increasing deposition time, due to the separation of FeSO_4 into Fe^{2+} (which is reduced by the flow of electrons to Fe) and SO_4^{2-} (commonly known as sulfuric acid). Clearly, as the concentration of iron in the solution decreases due to deposition, the less likely it is for deposition to occur. So, one can ask, is the *pH* of the solution directly related to the likelihood that an iron particle will deposit, and thus is it related to the rate of deposition? **Figure 3.4** shows that within a certain range of *pH* values, the deposition rate is not affected much. As long as one maintains the *pH* of the solution within a certain range of values, one can expect the same results. However, at low *pH* values, the rate of deposition is found to sharply increase. This increase is because the current in the cell is very high when the solution is very acidic. We must therefore conclude that the *pH* of the solution cannot be a good measure of the iron concentration.

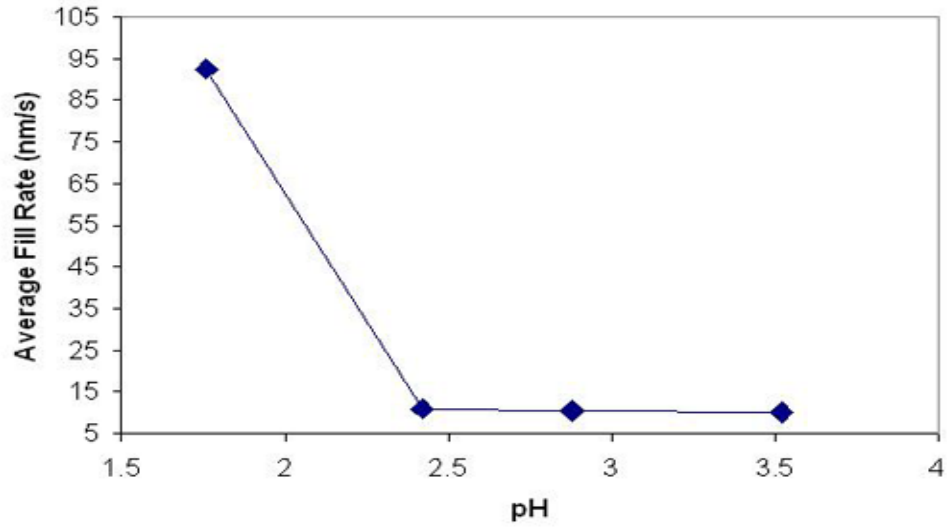


Figure 3.4: Average fill rate vs. pH. In general, the pH does not affect the deposition unless it is very low.

The applied AC voltage takes the form of a sine wave, which oscillates between the magnitude of the applied voltage, V_o . Deposition only takes place during the negative half-cycle. So, we would expect that as V_o increases, the deposition rate would also increase, as the area under the curve would increase. If one inserts Ohm's Law, $V=IR$ into (3.2), this will become evident. **Figure 3.5** shows that this is indeed the case. The relationship between the deposition rate and V_o appears to obey a power law

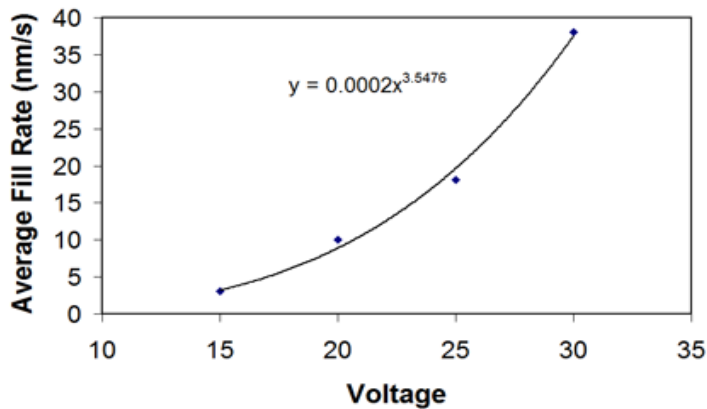


Figure 3.5: Average fill rate vs. applied voltage. The fill rate increases like $x^{3.5}$ as a function of applied voltage.

The frequency (f) dependence of the average fill rate is the most complicated of all the variables studied. Deposition occurs during a half-cycle of the voltage. So, deposition occurs every $1/f$ seconds for a period of $1/(2f)$ seconds. As we increase the frequency, the amount of time for deposition per cycle actually decreases. But, concurrently, the number of deposition periods in a length of time increase. It is difficult to predict how this affects the average deposition rate. **Figure 3.6** displays the results where the voltage is kept at 20 V. To better determine the nature of the samples, we have measured the hysteresis loops using an AGM. The magnetic results are displayed in **Figures 3.7** and **3.8**.

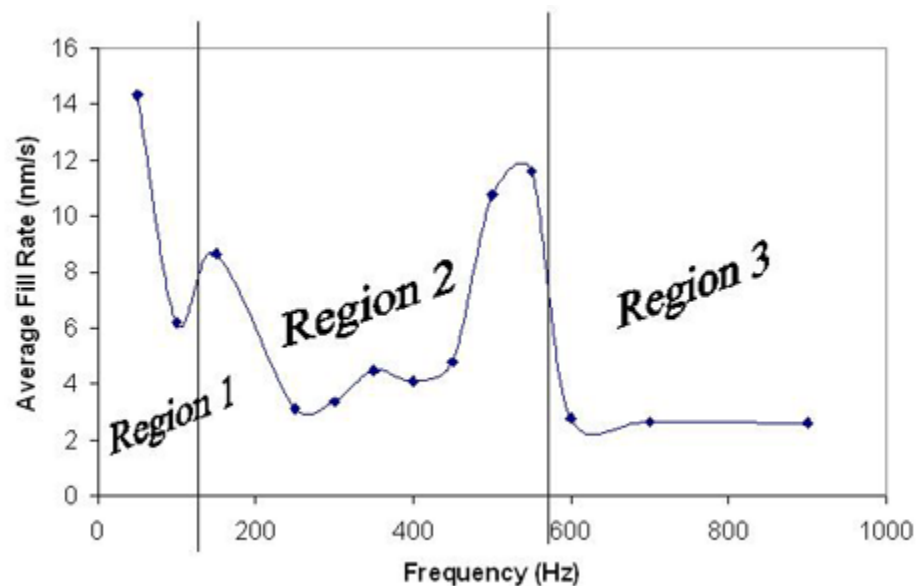


Figure 3.6: Average fill rate vs. frequency showing regions of different filling behavior. In region 1, only a thin film is formed. In region 2, we have optimal deposition. In region 3, the polarity switches too quickly for efficient deposition.

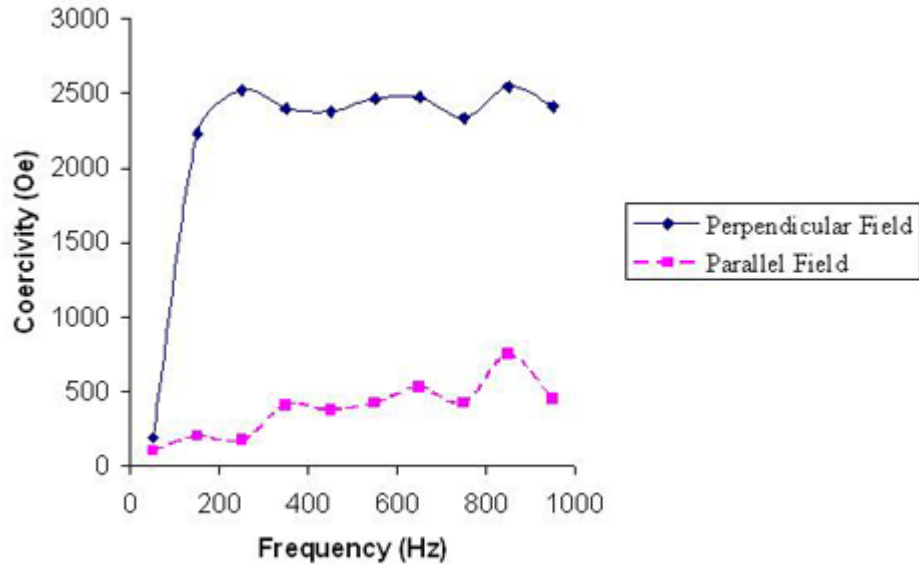


Figure 3.7: Coercivity vs. frequency for parallel and perpendicular fields. This shows that all frequencies result in wires except the lowest frequency, which forms a thin film.

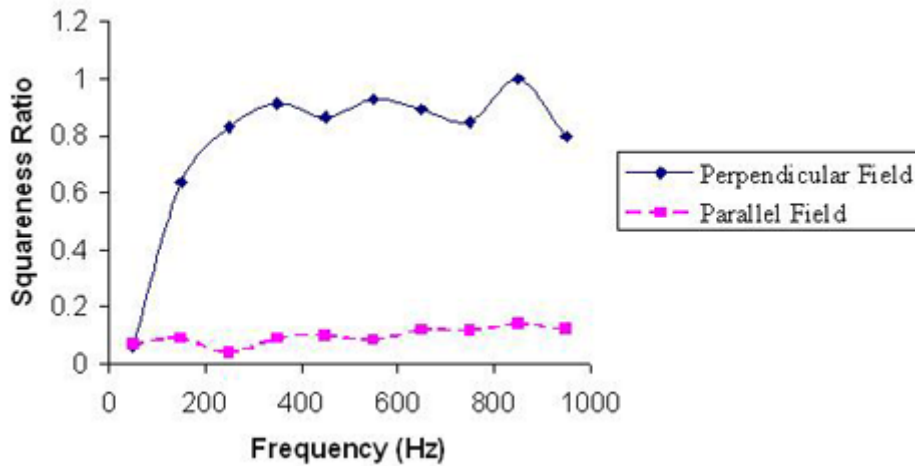


Figure 3.8: Squareness ratio vs. frequency for parallel and perpendicular fields. A squareness close to 1 is expected for materials showing strong magnetic shape anisotropy, such as nanowires. Again, the lowest frequency only forms a thin film.

In **Figure 3.6**, we can see three distinct regions. In the first region, there is no real dependence pattern. Here, the frequency is low. If the frequency is low enough, the

period of deposition per cycle would be very large. This behavior is almost the same as DC deposition. So, in region 1, $1/f$ is relatively large and the deposition acts like DC and very little gets deposited in the pores. Rather, as in DC electrodeposition through a barrier layer, a thin film gets deposited on the surface. The deposition rate appears to be rather high because iron is immediately deposited on the surface of the template, causing the current to jump. This explanation is supported by the magnetic measurements that show that the coercivity and squareness ratio are very small for low frequencies, as is expected for thin-film samples.

In region 3, we see an almost constant, slow rate of deposition. Here, the frequency is too large for efficient deposition. The time interval per cycle is too small for adequate deposition to occur. At high frequency, $1/f$ is relatively small, so, the polarity of the voltage switches very quickly, causing the iron particles to move around a lot but not necessarily deposit, although eventually wires are deposited, as we see in **Figure 3.7** a high coercivity and in **Figure 3.8** a squareness ratio close to 1. However, with such a high frequency, deposition of nanowires proves to be extremely slow.

Region 2 is the ideal region for electrodeposition. Here, one notes a parabolic increase of the deposition rate with frequency. In general, however, one can see an increasing deposition rate with increasing frequency. The existence of nanowires in this region is verified by the magnetic measurements in **Figures 3.7** and **3.8**.

Using this information, we fabricate Fe, Ni, Co, Au, and Ag nanowires to be used in characterization studies later in the dissertation. To make Fe nanowires, we found the best chemical recipe to be 10 g iron sulfate hexahydrate, 2.5 g boric acid, and 250 mL water deposited at room temperature. For Ni nanowires, the best chemical recipe was found to be 10 g nickel sulfate heptahydrate (although, nickel nitrate hexahydrate in the same concentration works just as well), 11.25 g boric acid, and 250 mL water deposited

at 100°C. For Co, we use 10 g cobalt sulfate hexahydrate, 2.5 g boric acid, and 250 mL water deposited at room temperature. The lifetime for Fe deposition solution is approximately 1 day due to its propensity for rapid oxidation. Iron particles quickly react with air to form iron oxide and they precipitate out of the solution and collect in a yellowish-brown film in the bottom of the solution storage bottle. However, once a suitable solution for Ni or Co has been made, it can be continuously used for many weeks. For Au and Ag, 0.25 g of either gold chloride or silver nitrate, respectively are mixed with 1 g of boric acid and 250 mL water. For the best results, gold deposition solution should be deposited and stored in a way to keep it away from light exposure. Both Au and Ag solutions may be reused for a long period of time. **Figure 3.9** displays an SEM picture of Au nanowires.

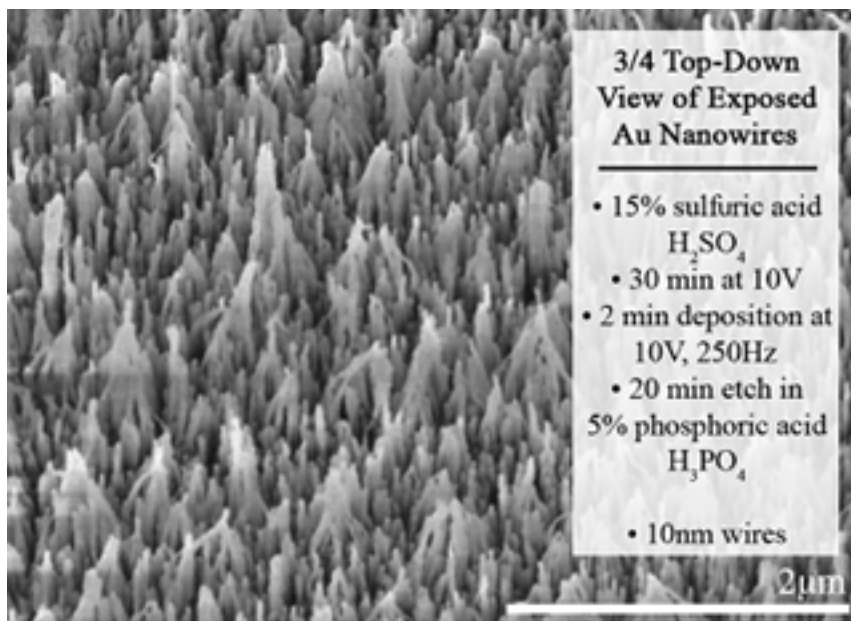


Figure 3.9: Gold nanowires grown in alumina. The template has been etched with phosphoric acid to expose the wires.

It should also be noted that we can grow y-shaped and bifurcated nanowires using the branched templates discussed in Section 2.4.2. **Figure 3.10** shows an SEM

image of a bifurcated wire that has been removed from the template by methods discussed in Section 6.1.

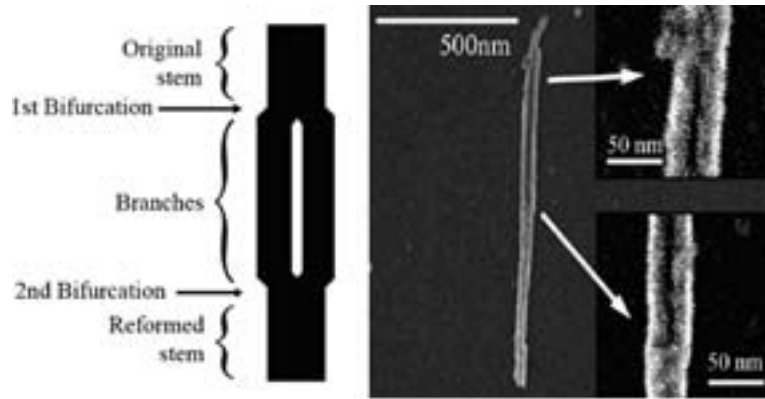


Figure 3.10: SEM images and layout of a branched bifurcated Co wire synthesized by electrodeposition.

3.1.3 PANi Composites

An interesting carbon based structure that can be synthesized via the electrodeposition method is polyaniline (PANi) nanotubes. **Figure 3.11** displays a chemical diagram of polyaniline.

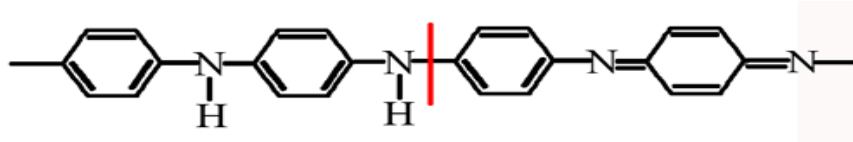


Figure 3.11: Chemical structure of polyaniline. Two isomers are possible, shown to the left and right of the red line. To the left, the first isomer is when nitrogen forms a bond with a hydrogen. To the right, the second isomer is when nitrogen double bonds to the benzene.

This chemical structure allows for many different properties. It is highly dielectric in its undoped state, and can be made conductive through doping. Recently, metal-filled PANi nanotubes have attracted some attention due to their interesting magnetic properties, which includes magnetic shape anisotropy and large coercivities, and their strong dielectric properties [60-63]. Due to the insulating and dielectric properties of PANi and

the conductive properties of the metal, the use of metal-filled PANi structures as coaxial cables has been imagined [64, 65]. However, the process of fabrication of these structures is often complicated, requiring several steps and different processes and fabrication methods [60-63, 66].

The filling of the PANi nanotubes is usually accomplished by electrodeposition. Our process is unique in that one can prepare the entire metal-filled PANi structure in a single cell, simply by changing the electrolyte at each step. We do not have to reposition the alumina template during fabrication. When depositing into a barrier layer, it is very important to ensure that the template is aligned properly. If the template is not aligned, with a small amount of un-anodized aluminum present in the corner of the anodization window, for instance, all of the current during deposition will run through this area. This occurs because aluminum is a much better conductor than alumina. If this happens, the deposition will most likely fail. Because re-aligning the template is a difficult and sensitive process, fabrication techniques that call for re-alignment do not boast high success rates. However, our process is successful almost all of the time because we do not have to realign the template, as it stays in position in the flat cell.

The fabrication of polyaniline nanotubes filled with metallic wires contains three steps. A constant voltage anodization is first carried out in the methods described in Chapter 2. Polyaniline nanotubes can be made into a variety of diameters depending on the dimensions of the template, thus the acids and voltages used. The acids we used were 15% sulfuric (v/v) and 3% oxalic (v/v). A range of voltages were used: 5V, 7.5V, 9V, 10V, 12V and 30V, 40V, 50V, 60V when sulfuric and oxalic acid were used respectively. These voltages are directly proportional to the diameters of the pores formed during the anodization. The anodization time lasted 30 minutes.

These pores are then filled with polyaniline by electrodeposition in the same flat cell. The acid electrolyte is simply removed and an electrolyte solution containing aniline was added. This is an aqueous solution of 10% sulfuric acid and 0.05 M liquid aniline. We found that solutions containing concentrations of aniline greater than 0.5 M do not deposit nanowires. And, it seems that the smaller the amount of aniline, the better the nanotubes deposit. When depositing, an AC voltage was applied. An AC voltage of amplitude 20V and 250 Hz was used when the anodized template was created with sulfuric acid. When oxalic acid was used, an amplitude range of AC voltages from 35V to 50V and frequencies from 350 Hz to 450 Hz were applied depending on the amplitude of the DC anodization voltage. The total deposition time for PANi was three minutes. **Figure 3.12** shows a typical I vs. t curve for this deposition and the entire three step process.

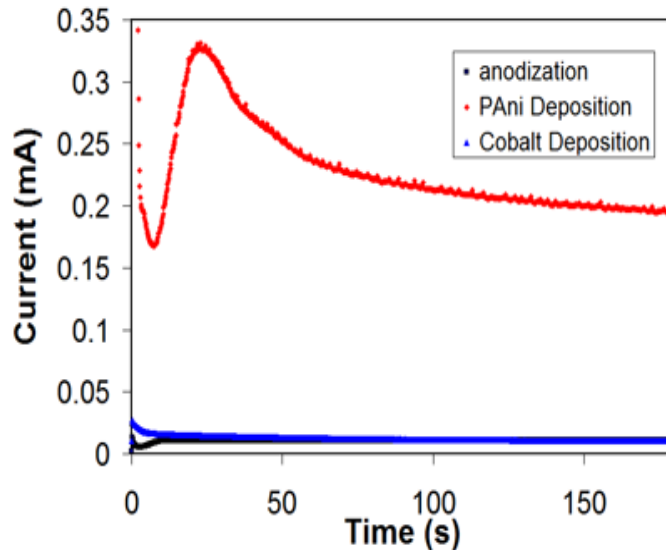


Figure 3.12: Current vs. Time deposition curve for the 3 step deposition process to form filled PANi nanotubes. First, we anodize aluminum foil. Second, we deposit PANi. Third, we deposit metal, which in this case is Co.

From the graph, we see that the current for PANi deposition first drops, then climbs to reach a peak before dropping to a steady state. The peak most likely corresponds to an

energy barrier that must be overcome in order for the polymerization reaction to occur.

Figure 3.13 shows SEM pictures of the deposited PANi nanotubes. It can be seen that the tubes fill the pores completely, with some of them rising far above the surface of the template.

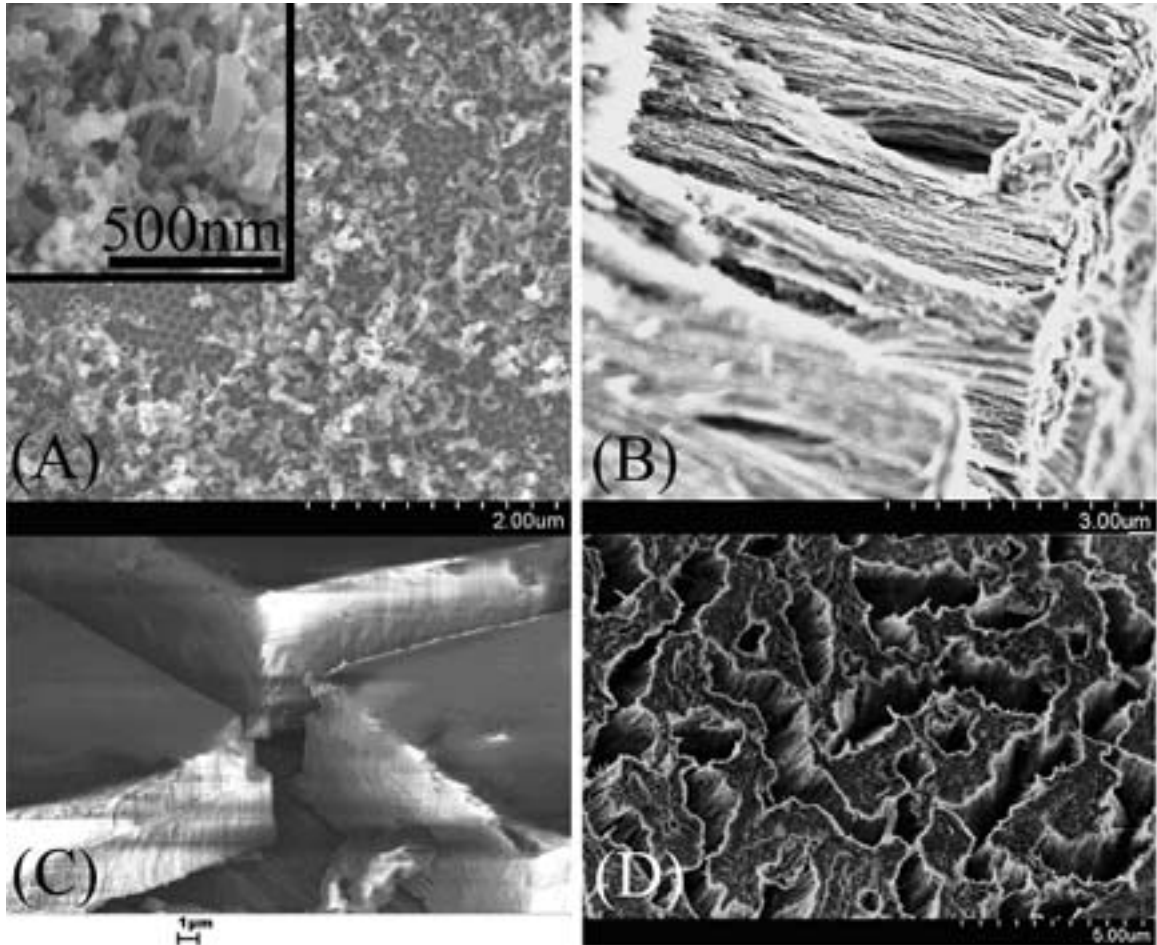


Figure 3.13: SEM images of PANi nanotubes: (A) A partially filled template (B) tubes extending beyond the template (C) A side view of an over filled template with a bundle of PANi tubes (D) A top view of an over filled template showing closed channels with tube bundles.

Once the PANi tubes were successfully deposited within the Al pores, a metal sulfate solution was used as the electrolyte bath and metals were deposited into the PANi nanotubes. The metals we deposited were Fe, Ni, and Co using the electrolyte solutions discussed in the previous section. The applied varying voltages and frequencies used for

deposition were again based on the anodization acid used. When sulfuric acid was used, a voltage of 20 V and 250 Hz was applied. When oxalic acid was used, a voltage range of 35 V to 45 V and a frequency range of 350 Hz to 450 Hz was applied, as the anodization constant current voltages with oxalic acid increased. The deposition time for the metals took 4 minutes. Again, **Figure 3.12** shows I vs. t curves for this metal deposition. Once the process was finished, the pores in the aluminum foil were filled with polyaniline tubes which were filled with Co, Fe or Ni wires. SEM images of the filled pores are in **Figure 3.13**. We can see that once the nanotubes fill, they begin to clump together at the top of the template.

3.1.4 Filled Carbon Nanotubes

Template synthesized carbon nanotubes can also be filled using electrodeposition. The fabrication of such carbon nanotubes is discussed in the next section (Section 3.2). The filling is accomplished in much the same way as with PANi nanotubes. Aluminum foil is anodized to desired dimensions. The template is then removed from the cell for carbon nanotube fabrication. Finally, it is returned to the cell for the deposition of metals. However, because the template must be removed and replaced, proper template alignment becomes an issue. Moreover, because nanotubes deposited in alumina by CVD are extremely disordered (also discussed later), sometimes the cavities are not clear for the full length of the tube, making deposition physically impossible. This is displayed in **Figure 3.14**. Although we were eventually successful with depositing Ni into carbon nanotubes, we found the overall success rate to be too low to warrant continued study. **Figure 3.15** displays transmission electron microscopy images (TEM) of Ni filled carbon nanotubes.

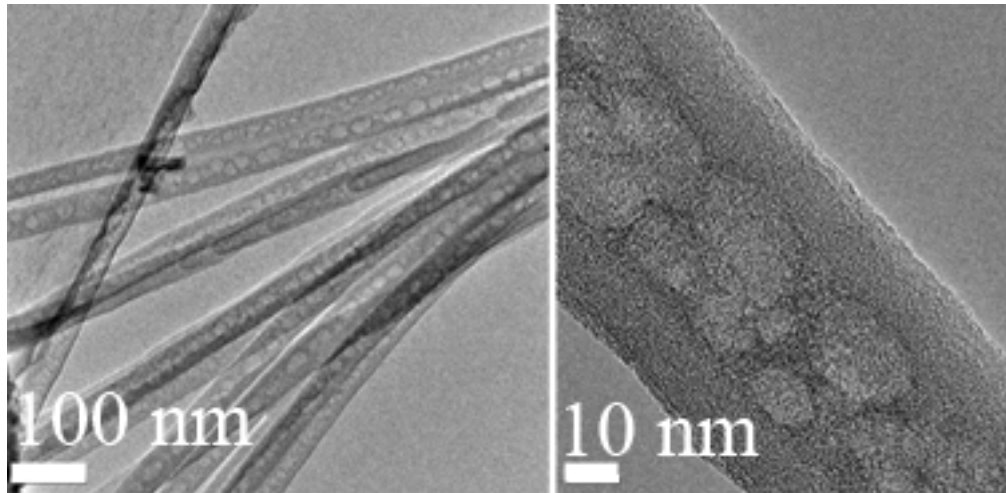


Figure 3.14: TEM images showing a bundle of carbon nanotubes where the cavities have are not clear and a close up of one of those carbon nanotubes.

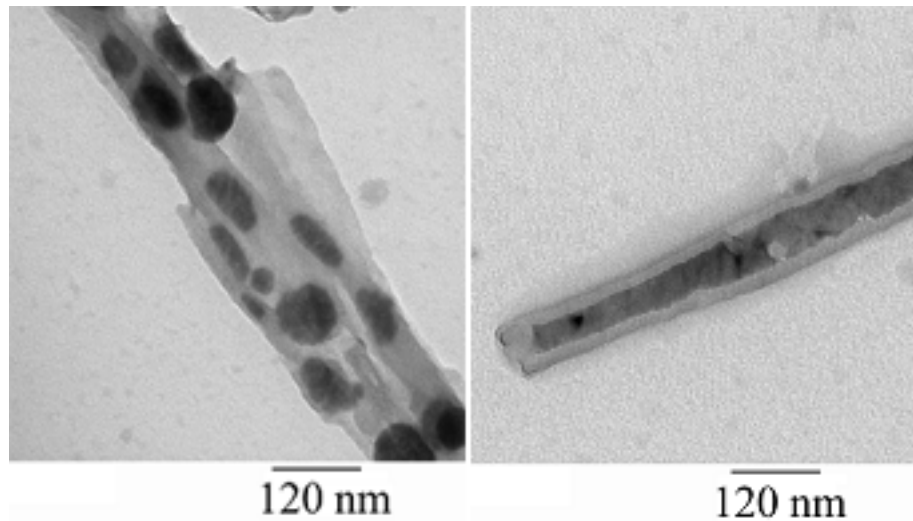


Figure 3.15: TEM images of Ni filled carbon nanotubes. The dark spots are the Ni, whose presence was later confirmed by magnetic studies, exploited the strong magnetic shape anisotropy of nanowires, as in Section 3.1.2.

3.2 Growth of Carbon Nanotubes

3.2.1 Introduction to Carbon Nanotube Structure

Carbon nanotubes (CNTs) consist of cylindrically rolled sheets of monolayer graphite, termed graphene. They are usually less than 100 nm in diameter and can be as

small as a 1 nm in diameter [67]. There are two types of CNTs, single walled carbon nanotubes (SWCNTs), so termed because they are made of a single rolled sheet of graphene, and multiwalled carbon nanotubes (MWCNTs), so termed because they consist of several and sometimes hundreds of concentrically rolled sheets of graphene. We only grow multiwalled carbon nanotubes (MWCNT). This is diagramed in **Figure 3.16**.

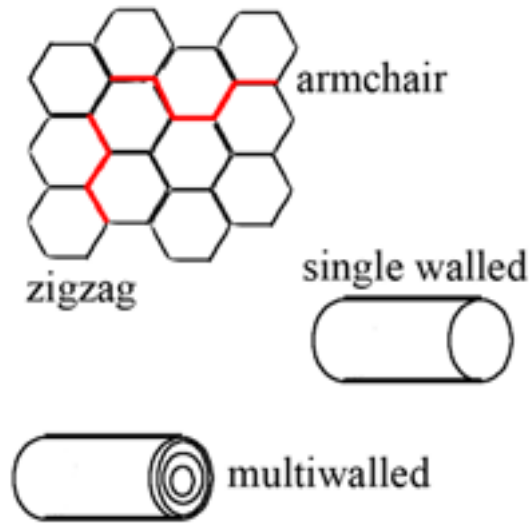


Figure 3.16: Drawing of graphene sheet and single and multiwalled carbon nanotubes. The red highlights the orientations for armchair and zigzag tubes. Depending on how the graphene sheet is rolled, the nanotube can be zigzag, armchair, or a combination.

The graphene sheets are arranged in a hexagonally ordered honeycomb lattice. CNTs are described by a chiral unit vector \mathbf{C} , made up of the unit cell lattice vectors \mathbf{n}_1 and \mathbf{n}_2 given by:

$$\mathbf{C} = a\mathbf{n}_1 + b\mathbf{n}_2. \quad (3.3)$$

There are three possible organizations for the graphene sheets that make up the carbon nanotube (also shown in **Figure 3.16**). First is the “armchair” type, so termed because it looks like an armchair as viewed from the top. Here, $a=b$. Second is the case where

$b=0$, which is termed “zigzag” type due to the zigzag formation of the carbon bonds. For a defect free graphene sheet, either zigzag or armchair is possible depending on how the graphene sheet was rolled into the carbon nanotube. Finally, there is the case where there is a mixture of armchair and zigzag. Depending on the values of the lattice constants, a nanotube can be either metallic or semiconducting. However, all randomly grown MWCNTs are metallic due to the metallic layers dominating the behavior of the semiconducting cylinders.

3.2.2 CVD Growth of Carbon Nanotubes¹

Carbon nanotubes can easily be grown in the pores of the alumina templates using chemical vapor deposition (CVD). And, because the dimensions of the pores (length and diameter) can be chosen easily by varying the template growth conditions, exacting dimensions of carbon nanotubes can be deposited by this method. We grow the carbon nanotubes in the templates without catalyst using a tube furnace, pictured in **Figure 3.17**. Argon acts as a carrier gas to transport gaseous acetylene through the furnace, which is set to 660 °C. The template is placed in the tube furnace. Because the aluminum backing will melt slightly during deposition, we place a piece of copper tape on the back of the template and then mount the template/copper piece on a piece of silicon to help the template stay uncurled. Finally, the acetylene is left to decompose into the template forming carbon nanotubes. These tubes are shown in **Figure 3.18** while still in the alumina.

¹ CNTs are grown in the laboratory of Prof. Yung Joon Jung

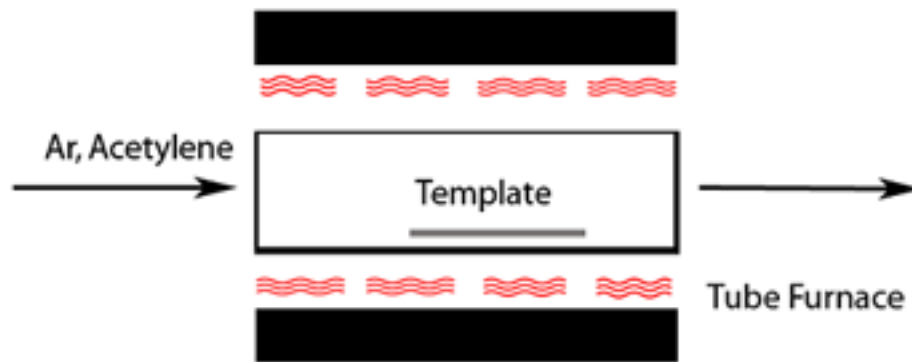


Figure 3.17: Schematic of the CVD set-up to grow MWCNTs in alumina templates. CNTs are formed by decomposition of acetylene gas carried by argon in a tube furnace.

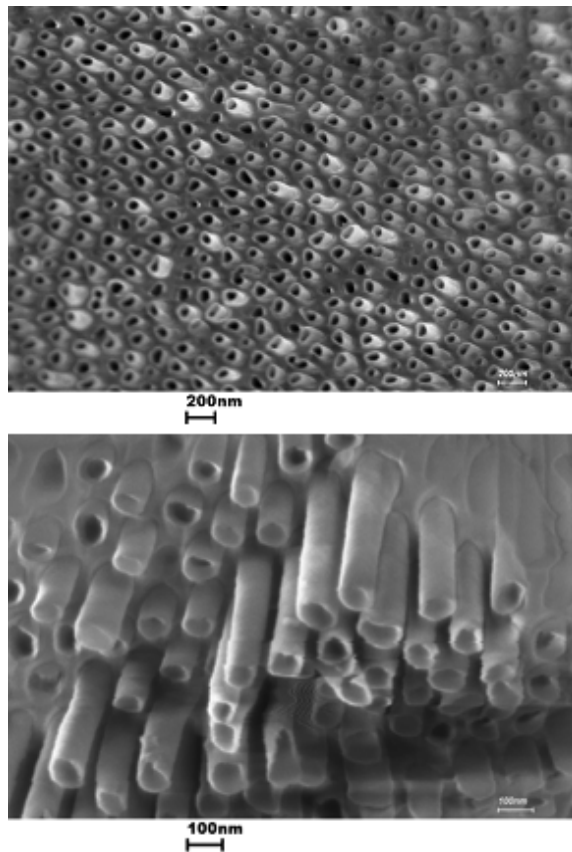


Figure 3.18: MWCNTs in alumina templates grown for 60 minutes. The nanotubes are coming slightly out of the template.

By varying the amount of time that the furnace reaction is left to proceed, tubes of different inner diameters can be grown. Comparing **Figure 3.18** to **Figure 3.19**, where the reaction took 60 minutes and 100 minutes, respectively, we can see that the 100 minute reaction produces carbon nanotubes where the walls are much thicker.

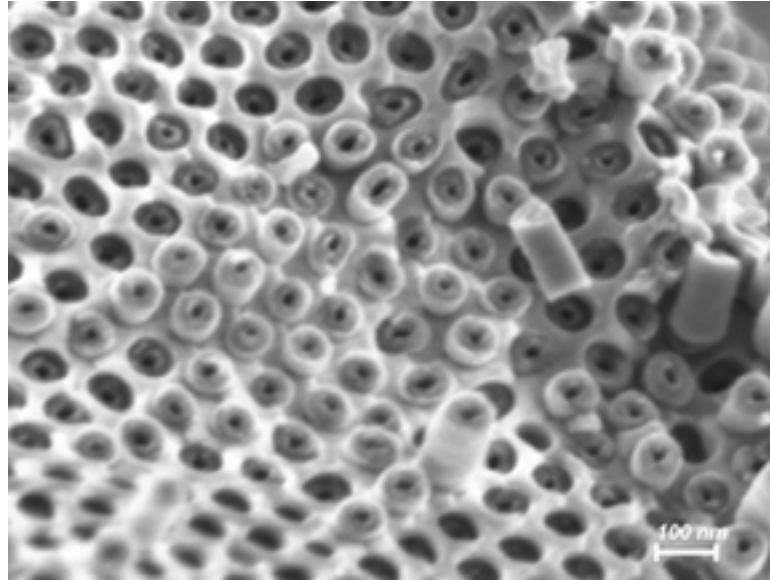


Figure 3.19: MWCNTs in alumina grown for 100 minutes. The inner diameters are visibly much smaller than tubes grown for less time.

Using this, we grow carbon nanotubes of 4 different inner diameters for an outer diameter (pore diameter) of approximately 65 nm. **Figure 3.20** displays a graph of inner diameter vs. growth time and inner diameter expressed a percentage of the overall tube volume vs. growth time. For this graph, inner diameter is calculated by taking the average inner diameter of approximately 50 nanotubes using TEM images and the stated error is the standard deviation.

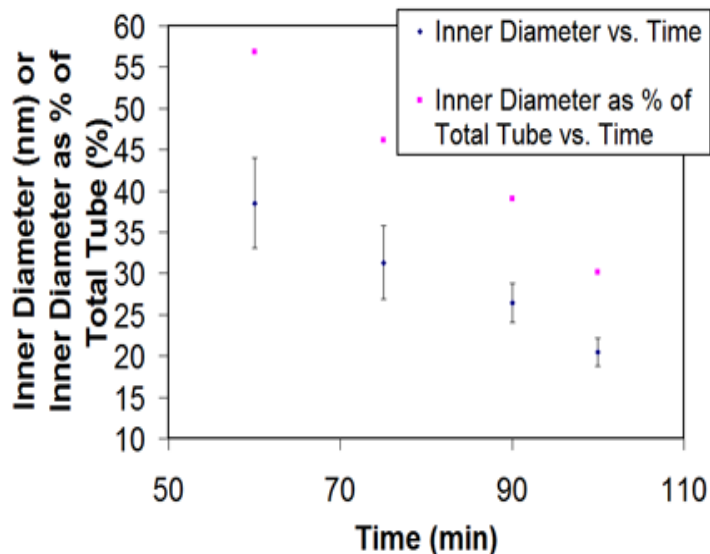


Figure 3.20: Graph of inner diameter vs. deposition time and inner diameter as % of total MCNT vs. time. As the growth time increases, the inner diameter also increases.

The template-assisted method of growing carbon nanotubes has several important advantages to other commonly used growth methods (for instance, laser ablation, arc discharge, or catalytic gas decomposition CVD directly onto a substrate). As stated before, the nanotubes can be tuned to many exacting dimensions, as needed. Also, the produced tubes are made in already aligned arrays, which is perfect for a range of studies and applications. And, due to their confinement in the alumina, the tubes have structural integrity and can easily be transported and stored. However, a possible disadvantage to the template-assisted growth technique is that it is a relatively low temperature growth technique that produces rather disordered structures. A TEM image of the disordered walls is shown in **Figure 3.21**.

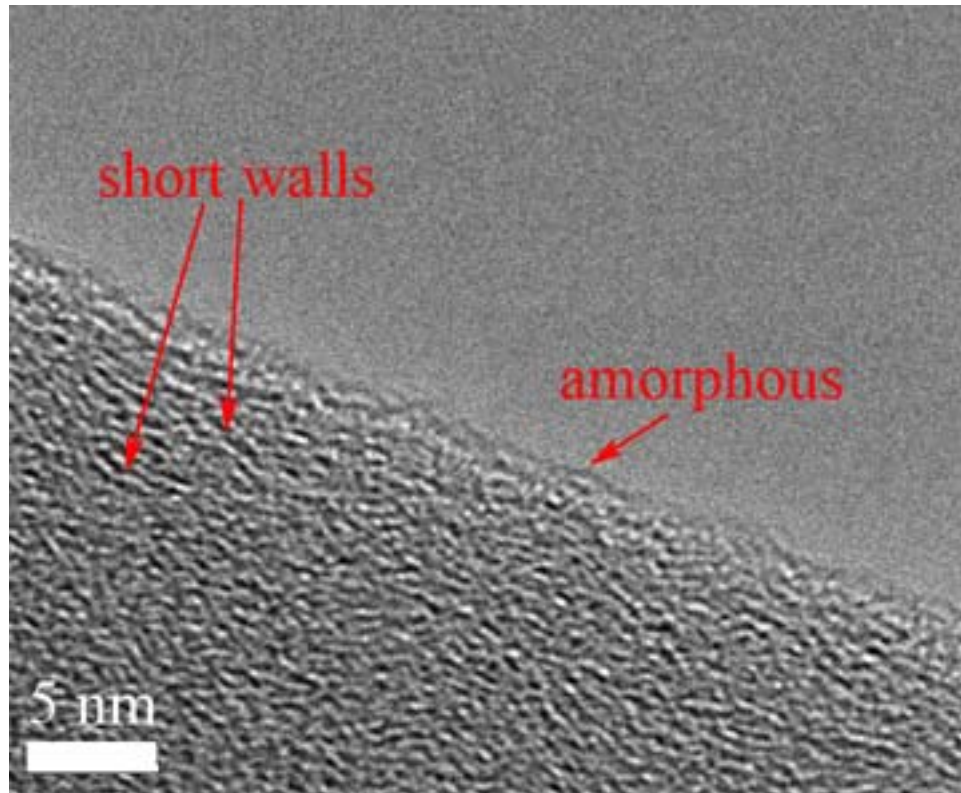


Figure 3.21: TEM image showing disorder in CVD MWCNT. There is an amorphous shell on the outside of the tube, which is common for all nanotubes (including very well-ordered nanotubes), and a highly polycrystalline wall on the inside.

We can see in **Figure 3.21** that there is an amorphous layer of carbon that surrounds the tube. However, this is commonly observed even in very well-ordered CNTs. The inner walls of the tube are made of highly disordered polycrystalline carbon. Rather than neat concentric circles of graphene layers, we see intersecting walls that are no more than 5 nm in length. This is in contrast to MWCNTs made by other methods that produce walls that are highly ordered and can extend for microns. Although these MWCNTs are disordered, and usually, higher order tubes are more desired, very little work has been done on such disordered tubes. The disorder has profound effects on the fundamental physics of the tubes, which will be discussed in Chapters 5 and 7.

Chapter 4: An Application of Nanowire/Alumina Arrays in Metamaterials

4.1 Introduction and Theory

Recently, there has been a great interest in using nanowires embedded in alumina as metal-dielectric lenses due their ability to become negative index of refraction and superlens materials [68-70]. A recently published theory by Lu and Sridhar in ref. [71] shows how, due to the occurrence of two surface plasmon resonances (SPRs), negative refraction can occur.

To model the structure, they begin with Bruggeman's effective medium theory equation in the long wavelength limit [72-74]:

$$0 = f \frac{\epsilon_m - \epsilon_{eff}}{\epsilon_m + D\epsilon_{eff}} + (1-f) \frac{\epsilon_a - \epsilon_{eff}}{\epsilon_a + D\epsilon_{eff}}. \quad (4.1)$$

Here ϵ_m is the permittivity of the nanowires, ϵ_{eff} is the effective permittivity of the composite structure, ϵ_a is the permittivity of the dielectric, D is a measure of the aspect ratio of the nanowires, and f is the ratio of metal vs. dielectric (filling ratio). For a cylinder, $D=1$ and we have the solution:

$$\begin{aligned} \epsilon_{eff} = \epsilon_x = \epsilon_y &= \frac{1}{2} \left(\Delta \pm \sqrt{\Delta^2 + 4\epsilon_a\epsilon_m} \right), \\ \Delta &= (1-2f)(\epsilon_a - \epsilon_m) \end{aligned} \quad (4.2)$$

Also, for our cylindrical geometry, we have

$$\epsilon_z = \epsilon_{eff}(\infty) = f\epsilon_m + (1-f)\epsilon_a. \quad (4.3)$$

So, there exists a minimum filling ratio such that for $f > f_{min}$, $\text{Re } \epsilon_z = \text{Re } \epsilon_{parallel} < 0$ and for $f > 1/2$, $\text{Re } \epsilon_{x,y} = \text{Re } \epsilon_{perpendicular} < 0$:

$$f_{\min} = \frac{\epsilon_a}{\epsilon_a - \text{Re } \epsilon_m}. \quad (4.4)$$

The SPRs arise due to a coupling of the electromagnetic field with the material [75]. Free electrons in the conduction band of the metal occupying energy states near the Fermi level produce surface plasmon bands leading to broad peaks in the absorption and emission spectra. As mentioned, our material gives two such SPRs. The transverse peak occurs when $\text{Re } \epsilon_x = 0$. This occurs when $\text{Re } \epsilon_m \sim -\epsilon_a$. And, this mode is only weakly dependent on the fill ratio, f . f_{\min} corresponds to a specific λ_l , which is the longitudinal SPR. Here, $\text{Re } \epsilon_{\text{parallel}} = 0$. This SPR, according to the Drude model, is strongly dependent on fill ratio. **Figure 4.1** shows modeled absorption spectra for both s and p polarized light showing both SPRs.

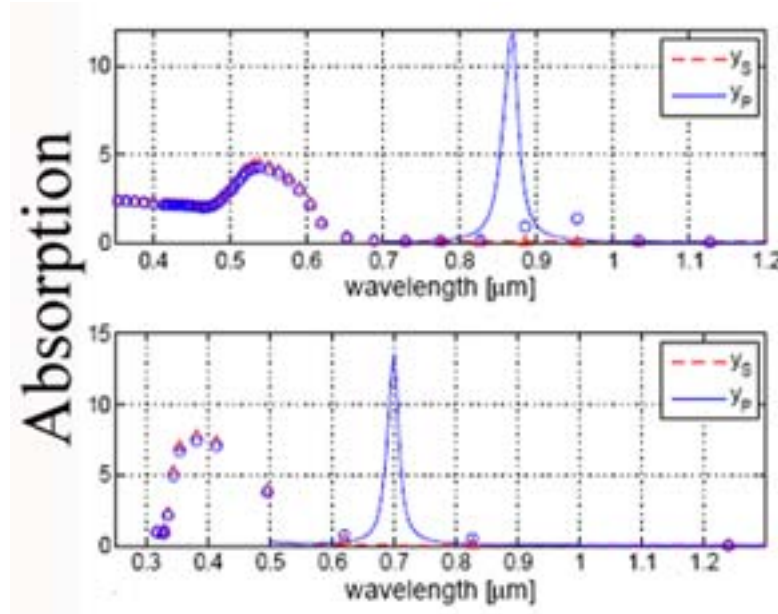


Figure 4.1: Theoretical absorption spectra with both s and p polarized light showing both SPRs. The transverse SPR is the first peak and the longitudinal SPR is the second peak. The top image is for an Au nanowire-alumina array with the light incident at 20 degrees and $f=8\%$. The bottom graph is for an Ag nanowire-aluminum array with the light incident at 20 degrees and $f=10\%$.

We found that the best f , or the one that produces the highest magnitude and most narrow longitudinal SPR to be approximately 10%. For long wavelengths, $\lambda > \lambda_i$, there is a small part of the spectrum where negative refraction will occur with $\text{Re } \epsilon_{\text{parallel}} < 0$ and $\text{Re } \epsilon_{\text{perpendicular}} > 0$.

4.2 Preparation of Samples

There have been several studies made of metal-dielectric composites and their optical properties. These included studies on samples prepared by top-down fabrication techniques [76]. Or, there, wires were grown directly onto substrates using lithographic methods. One advantage to this method is that it produces clean, very well-ordered wires. However, it has a very major disadvantage in that the growth substrates are usually very thick and do not transmit light. So, the angles available for shining the light are very limited, and usually, only perpendicular coupling is allowed. Furthermore, this approach is highly limited in the aspect ratios that it can grow. Thus, the filling ratios cannot be tuned as easily. A second method for optical studies is to use particles suspended in solution [77]. However, there, aspect ratios are, again, rather small and all coupling is purely random. In our study, we use chemical self-assembly, as described in Chapter 3, which is a bottom-up technique. So, although the resulting wires are not as neatly and cleanly fabricated as in top-down methods, we can very easily tune the aspect ratios, filling ratios, and can shine light at many different angles.

For this study, we produce Au and Ag metal-dielectric arrays using the same methods described in Chapter 3. Aluminum foil is anodized in 15% oxalic acid at 10 V, creating pores of diameter approximately 12 nm and in 3% oxalic acid at 40 V, creating pores of diameter approximately 35 nm. The aspect ratio (diameter/length) was approximately 10^3 . Au or Ag was deposited at 20 V and 250 Hz using electrodeposition. Using SEM images to calculate the average diameters of the wires and the alumina pores,

we calculate the fill factors to be ~ 0.05 for the 12 nm pores and ~ 0.20 for the 35 nm pores.

In order to facilitate the optical experiment, the remaining aluminum layer on the back of the template was removed. To do this, the wire side of the template was coated with wood varnish to protect the wires. Then, the template was placed in a bath of mercury chloride for approximately a day. The template was then removed and washed in water before placing it in ethanol to remove the protective varnish coating. The finished sample was placed on a glass slide 1.5 mm thick.

4.3 Experimental Results

Optical experiments were done in the set-up shown in **Figure 4.2**.

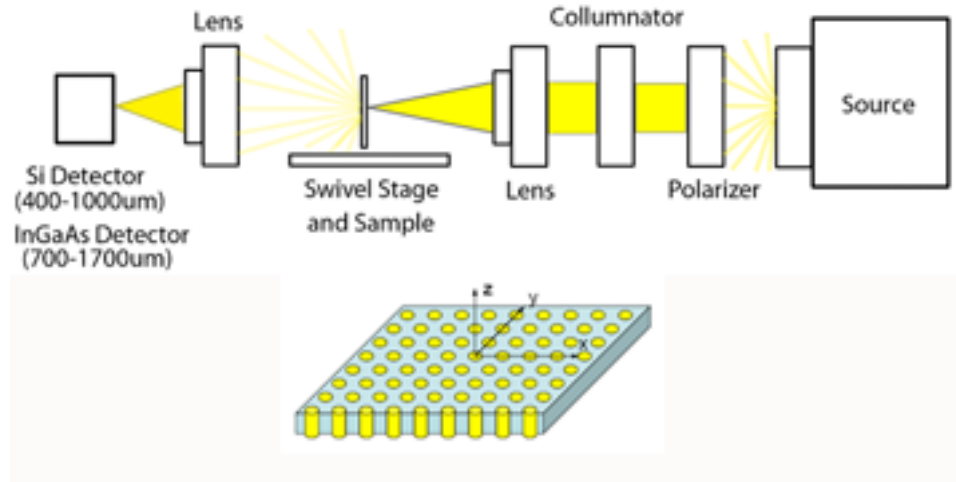


Figure 4.2: Diagram of the experimental set up for optical experiments. Light is shone onto the sample in the z-direction onto the x-y plane as shown.

The sample is placed on a swivel stage and a polarized, collimated, and focused white light source is shone onto the sample. The transmitted (T) light is collected and focused into two detectors. There is a Si detector (400-1000 μm) and an InGaAs detector (700-1700 μm). Absorbance, $-\ln(T)$, is calculated from the transmission.

Figure 4.3 shows the experimental results from the small diameter Ag nanowire-alumina arrays.

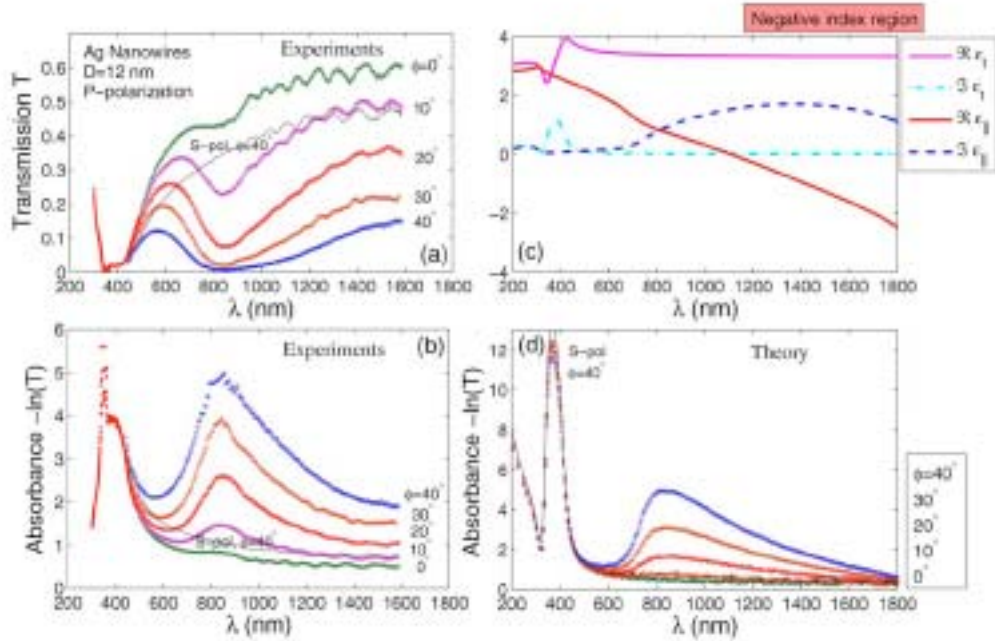


Figure 4.3: Transmission (A) and absorbance (B) spectra for 12 ± 2 nm diameter Ag nanowires in porous alumina for varying angles of incidence (φ) and with P polarization. The solid curve is for S polarization and $\varphi=40$ degrees. The feature at 350 nm is an artifact. The template is modeled as consisting of a layer d_1 of porous alumina without nanowires followed by a layer d_2 of nanowires within alumina. (C) Anisotropic permittivity of the Ag nanowires in alumina with $f=0.055$. The dielectric constant of amorphous alumina is taken to be 2.25. (D) calculated absorbance of an Ag nanotemplate with $d_1=2.9 \mu\text{m}$, $d_2=1.1 \mu\text{m}$.

The predicted transverse SPR is readily seen at approximately 390 nm as a peak in the absorbance and a corresponding minimum in the transmission spectra. We can see that this feature is constant for all angles of incidence and for the S polarized case. As predicted, this SPR does not depend on angle of incidence. The longitudinal SPR is seen at approximately 845 nm. Again, as predicted, it is strongly dependent on angle of incidence and is absent in the S polarized case. The longitudinal SPR disappears for normal incidence and is very small for small angles of incidence, resembling the S

polarized case. For the S polarized wave and for normal incidence, the sample is isotropic with positive ϵ_{eff} , so the conditions for the longitudinal SPR are never realized. For the larger angles of incidence and the P polarized waves, there is a component of the wave that couples parallel to the wire axis, thus satisfying the necessary conditions for the observation of the longitudinal SPR. According to the theory, negative refraction occurs for $\text{Re } \epsilon_{parallel} < 0$, or for $\lambda > 1100$ nm. The wideness of the longitudinal peak as compared to **Figure 4.1** can be attributed to defects and incomplete filling in some of the nanowires in the array, which is a disadvantage to the chemical self-assembly method of fabrication. However, this can be improved in the future, possibly, by annealing the samples at low temperatures prior to performing the investigation.

Figure 4.4 displays similar results for the Au nanowire arrays.

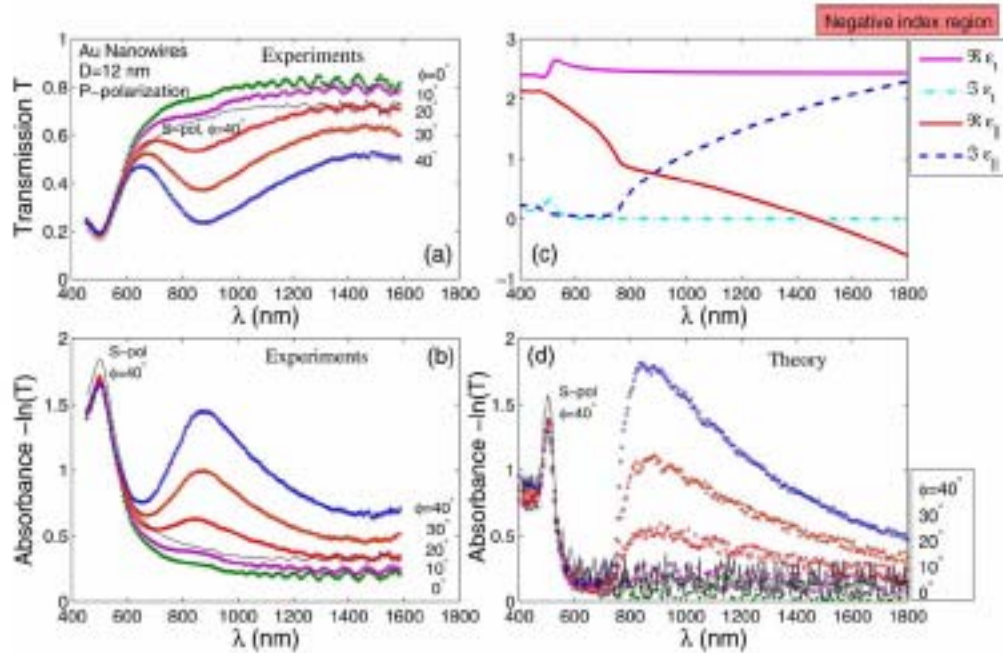


Figure 4.4: Transmission (A) and absorbance (B) spectra for 12 ± 2 nm diameter Au nanowires in porous alumina for varying angles of incidence (φ) and with *P* polarization. The solid curve is for *S* polarization and $\varphi=40$ degrees. The feature at 350 nm is an artifact. The template is modeled as consisting of a layer d_1 of porous alumina without nanowires followed by a layer d_2 of nanowires within alumina. (C) Anisotropic permittivity of the Ag nanowires in alumina with $f=0.04$. The dielectric constant of amorphous alumina is taken to be 2.25. (D) calculated absorbance of an Ag nanotemplate with $d_1=3.5 \mu\text{m}$, $d_2=0.5 \mu\text{m}$.

Here, the transverse SPR is seen at approximately 500 nm and the longitudinal peak is seen at approximately 860 nm. However, in this case there is a small blue shift as a function of increasing angle. According to the theory, negative refraction occurs for $\text{Re } \epsilon_{\text{parallel}} < 0$, or for $\lambda > 1450$ nm.

The model also predicts a strong dependence of the longitudinal SPR on filling ratio. **Figure 4.5** shows spectra of the small Au nanowire arrays as compared to the larger diameter Au nanowire arrays. Here, the larger arrays were found to have a filling ratio of 0.186 ± 0.08 and the smaller arrays were found to have a filling ratio of 0.141 ± 0.058 . These were calculated by averaging the diameters of approximately 50 SEM imaged pores and the error is the standard deviation.

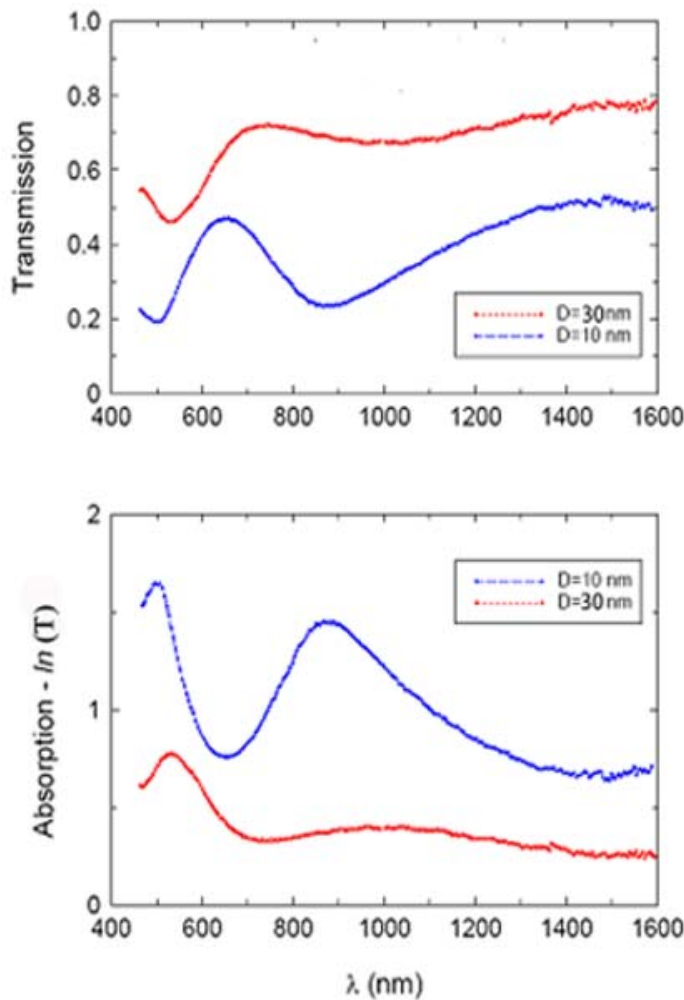


Figure 4.5: Spectra of gold nanowires with different diameters/fill ratios. The longitudinal peak is very strongly dependent on filling ratio.

One will recall that the ideal filling ratio was predicted to be approximately 0.10. From the graph, we can clearly see the appearance of the longitudinal SPR at approximately 875 nm in the smaller diameter/fill ratio sample and that it is, for the most part, absent in the larger diameter/fill ratio sample. Moreover, the theory predicted that the transverse SPR would not be dependent on the fill ratio. From the chart, we can see that this is the case, with the transverse mode visible at approximately 500 nm for both samples. This shows that there is a very good correlation between the model and the experimental results.

Chapter 5: Magnetic Properties of Template Synthesized Nanostructures

5.1 Introduction

Nanostructures have demonstrated many remarkable magnetic characteristics. Because of the extremely small size of nanowires and nanotubes, previously known models of bulk magnetism do not apply, as many different highly contributing magnetic phases can exist inside a single nanostructure (such as ferromagnetism and superparamagnetism). And, the situation becomes remarkably more complicated when one considers arrays of magnetic nanoscale structures due to inter-nanostructure interactions. In addition, magnetism can be used as a probe to learn more about other properties of a nanowire, such as crystal and electronic structure (as already utilized in Chapter 3). In this chapter, we study the magnetic properties of nanowires and carbon nanotubes. We discuss the various types of anisotropy: magnetic shape anisotropy, crystal anisotropy, and magnetoelastic anisotropy that contribute to the magnetic behavior of nanowires. We perform measurements on various types of ferromagnetic nanowire arrays including Fe, Co, Ni, PANi composites, and bifurcated nanowires and discuss what can be learned from these measurements. We also show how H₂ annealing can induce ferromagnetism in template-synthesized MWCNTs.

5.2 Nanowire Arrays

5.2.1 Theory

Ferromagnetic nanowire arrays, in the simplest sense, are interacting arrays of cylindrically shaped ferromagnets. Therefore, in the simplest case, each nanowire can be thought of as a magnetic dipole contributing an electrostatic magnetic field of

$$\mathbf{H}_m = \frac{m}{\left(x^2 + \frac{l^2}{4}\right)^{3/2}}, \quad (5.1)$$

with \mathbf{H}_m being the total magnetic field, l being the length of the wire, and $m=M_sV$ (saturation magnetization times volume) being the dipole moment, and x being some distance away from the wire [78]. So, if an array of these dipoles is immersed in an external magnetic field, they will couple to each other and the magnetic field, giving an observed total magnetic field of

$$\mathbf{H}^T_{i,j} = \mathbf{H} + \mathbf{H}_m \sum_{l \neq i, m' \neq j} \sigma_{l,m'} \mathbf{K}_{lm',ij} \quad (5.2)$$

Here, \mathbf{H} is the applied magnetic field, σ is 1 if the field is oriented parallel to the easy axis and -1 if the field is oriented parallel to the easy axis, \mathbf{K} are the geometric coupling factors which depend on the interwire separation distance, and \mathbf{H}^T is the total observed magnetic field [79, 80].

However, when nanowires are synthesized by electrodeposition, they can often be grainy in their physical structure or incomplete. One pore can contain several smaller wires and separated, but coupled and interacting grains. Some of these grains may not be ferromagnetic, but superparamagnetic, which subtracts from the observed total magnetic field. In addition, the grains in a single wire will interact with each other, greatly affecting the observed magnetic characteristics. So, a more accurate measure of the overall field would include the field due to the dipoles, the field due to the interwire interaction, the external field, and also the intrawire self-interaction due to graininess. To get a better idea of what is occurring in a nanowire array, one needs to discuss the various types of anisotropies that these effects can create.

For anisotropies in ferromagnetic nanowire arrays, we need to consider, shape anisotropy, magnetocrystalline anisotropy, and magneto-elastic anisotropy [78]. Shape

anisotropy leads to the observation of a larger coercivity along a particular orientation of the wire in an external field due to the shape of the nanowires. Magnetocrystalline anisotropy refers to the favoring of magnetization along certain crystal orientations in a nanowire. Magnetoelastic anisotropy refers to the effects of external stress (usually from the surrounding alumina template) causing changes in observed magnetic characteristics of the array.

It has been found that the predominant crystal structures of electrodeposited Fe and Ni nanowires are bcc and fcc, respectively, while the predominant crystal structure of electrodeposited Co nanowires is a mixture of fcc and hcp [81]. Likewise, under SEM imaging, Fe and Ni nanowires appear to be somewhat continuous, while Co nanowires can appear grainy and disjointed. It has been shown that the measured coercivity of a ferromagnetic nanowire array as a function of wire diameter will increase until a certain point and then begin to decrease again [81-84]. Initially, the coercivity is small due to the presence of single domain superparamagnetic particles. But, as the diameter increases, magnetocrystalline anisotropy due to the preferred alignment of the electronic spins in the crystal lattice and shape anisotropy effects become significant. Usually, the easy axis of magnetization is along the length of the nanowire, perpendicular to the area of the array. Due to this preferred easy axis in the nanowire, a majority of the spins will align this way, resulting in a large coercivity and squareness ratio close to 1 if the field is applied parallel to the length of the nanowires. And, the coercivity will be small if the field is applied perpendicular to the length of the nanowires.

As the diameter of the nanowires begins to increase, they begin to contain more crystal cells and magnetocrystalline anisotropy becomes more significant. The coercivity will begin to decrease and approach the bulk material characteristics. The maximum in coercivity is seen to occur at a critical radius, R_c , given by

$$R_c = \left(\frac{kA}{\mu_0 M_s^2} \right)^{1/2}. \quad (5.3)$$

Here, k is an aspect ratio dependent constant, A is the exchange constant, and M_s is the saturation magnetization [78, 83]. For Ni, R_c has been found to be approximately 13 nm in [83]. For Co, due to the presence of graininess and a mixture of 2 crystal states, the coercivity drops much slower and an exact R_c is difficult to discern, but it is most likely near the same value as Ni [81]. However, recent work has shown that for larger nanowire diameters (>50 nm), it is possible to make the easy axis perpendicular to the length of the nanowires [82]. For Fe, R_c has been found to be approximately 16 nm [81].

Magnetoelastic anisotropy mainly contributes due to the fact that the nanowires are still embedded in the porous alumina. As discussed, because of the shape and magnetocrystalline anisotropies, there is a preferred alignment to the spins, which, for small nanowires, is usually along the length of the wire. But, if the matrix in which these wires are embedded is curled, stretched, or otherwise changed in shape, the direction of the moments of the wires in the array will no longer add up in the same direction, which decreases the value of the observed moments and coercivities. This mainly comes into consideration if the template is bent and not flat, and during temperature dependent measurements. Because the thermal and expansion coefficients for alumina are very different than those for the nanowires, thermal compression and expansion of the template will happen at a different rate than for the nanowires. If the template contracts and the wires do not, the overall direction of the moments of some of the nanowires, with respect to a flat template, changes.

Magnetic viscosity effects can also contribute to the observed magnetic behavior of the nanowire array due to the small size of the nanowires, and is a good measure of intrawire interaction. The magnetic viscosity is a measure of the ferromagnet's

resistance to changing its current magnetization in an applied field. The magnetization as a function of applied field and time is given by [85],

$$M(H, t) = M(H, t_0) - S(H) \ln(t/t_0). \quad (5.4)$$

Here, $S(H)$ is the magnetic viscosity, t_0 is some initial time, t is time, and H is the applied field. So, if a nanowire array, which has a spontaneous magnetization is forced to demagnetize in an applied field, the spins will decay in some time t . There is some energy barrier, E_B involved in the reversal process that, for non-interacting grains is given by

$$E_B(H) = K_u V \left(1 - \frac{H}{H_A}\right)^2. \quad (5.5)$$

Here, K_u is a measure of the anisotropy, V is the volume of the grain or nanowire, $H_A = 2K_u/M_s$. Using this, we can define an activation volume V^* for the reversal process:

$$V^* = -\frac{1}{M_s} \left. \frac{\partial E_B(H)}{\partial H} \right|_{H_c(T, V)} = V \left(1 - \frac{H_c}{H_A}\right) = \left(\frac{25k_B T}{K_u V}\right)^{1/2} V. \quad (5.6)$$

However, this is strongly affected by imperfections in the nanowires that can cause pinning and raise or lower the energy barrier required for a reversal [81].

The magnetic viscosity, due to the fact that it considers only non-interacting particles, cannot measure interwire interactions. A good way to measure interwire and interparticle interaction is by using the Henkel method [86, 87]. The parameter α is defined by,

$$\alpha = 2 \int_0^\infty \frac{\Delta M}{M_r} d\left(\frac{H}{H_s}\right), \quad (5.7)$$

where,

$$\Delta M(H) = \frac{M_d(H)}{M_r} - 1 + 2 \frac{M_r(H)}{M_r}. \quad (5.8)$$

Here, $M_d(H)$ is the DC demagnetization remanence, $M_r(H)$ is the isothermal remanence, M_s is the saturation remanence magnetization, and H_s is the saturating field. For α values that are less than zero, it can be said that demagnetization is favored in the interaction due to less particle-particle interaction and smaller activation volume. For α greater than zero, there is a lot of particle-particle interaction and there is a resistance to demagnetization.

Because of the graininess of the nanowires, there may be non-interacting superparamagnetic particles present in the nanowires that have not formed interacting magnetic clusters. Below a certain diameter, given by

$$D_c = \frac{18}{\pi} \frac{\sqrt{AK_u}}{M_s^2}, \quad (5.9)$$

stable magnetic domains will not form [85]. It is expected in electrodeposited nanowires that there are a lot of non-interacting grains and imperfections. However, annealing the wires may remove some of these.

A good way to judge the amount of superparamagnetic particles is by performing temperature dependent measurements. There are many contributing factors when considering the temperature dependence of the magnetism in nanowire arrays. First, as previously stated, magnetoelastic anisotropy contributes due to uneven compression and expansion in the alumina template and in the nanowires themselves. Also, small single domain grains in the nanowires that act at room temperature like superparamagnets will eventually become ferromagnetic and contribute to the overall observed ferromagnetic behavior below their blocking temperature. In general, however, the magnetization is expected to follow the Bloch law in the form of

$$M(T) = M(0)(1 - BT^2), \quad (5.10)$$

with $M(0)$ being the extrapolated zero temperature magnetization B is the Bloch constant and $\lambda = 3/2$ [81, 83].

5.2.2 Bifurcated Nanowires

In this section, we study the magnetic properties of self-assembled bifurcated Co nanowires. The wires were synthesized by electrodeposition using the methods outlined in Chapter 3. Anodization was carried out using a 1-step process with 15% sulfuric acid. For the straight nanowires, a constant voltage of 10 V is applied across the electrodes. Under these conditions, nanoporous alumina forms at the surface with pore diameters of around 10 nm. Electrodeposition is carried out at 20 V and 250 Hz. In order to prepare the bifurcated nanowires, we started with a template consisting of the desired branched pore structure discussed in Chapter 2. During the anodization process the applied voltage was initially set at 10 V and then reduced to 7.1 V and subsequently set back at 10 V. This results in 10 nm diameter stems at the two wire ends with 7 nm diameter branches in the mid-section.

We are only interested in the magnetic properties of the smaller nanowires, which, due to their small size, provide a perfect platform for studying the effect of low magnetic domain materials, as discussed below. For comparison of magnetic properties of the wire samples with thin films, we prepared Co films deposited on commercial Al foil by thermal evaporation of Co (discussed in Chapter 6). Using this method, we created a polycrystalline film whose thickness was approximately 2 μm , which is comparable to the total length of straight and bifurcated nanowires.

Magnetic measurements were subsequently made with a Princeton Measurements Corporation AGM (Appendix B), for room temperature measurements (~ 300 K) and a Quantum Designs Corporation SQUID for variable temperature measurements (4-350 K).

First, we discuss our results on the magnetization versus field curves for the nanowires in both perpendicular and parallel orientations. For clarity, we define the perpendicular alignment to be one in which the field is applied perpendicular to the surface of the template, or parallel to the cylindrical axis of the nanowires. The parallel alignment is defined as one in which the field is applied parallel to the surface of the film or perpendicular to the cylindrical axis of the nanowires.

Typical hysteresis loops are shown in **Figure 5.1** for a typical bifurcated and straight Co nanowire array sample with similar total wire length. In the case of the straight nanowires, the coercivity in the perpendicular direction is around 1000 Oe. In the parallel direction, the coercivity is only around 151 Oe.

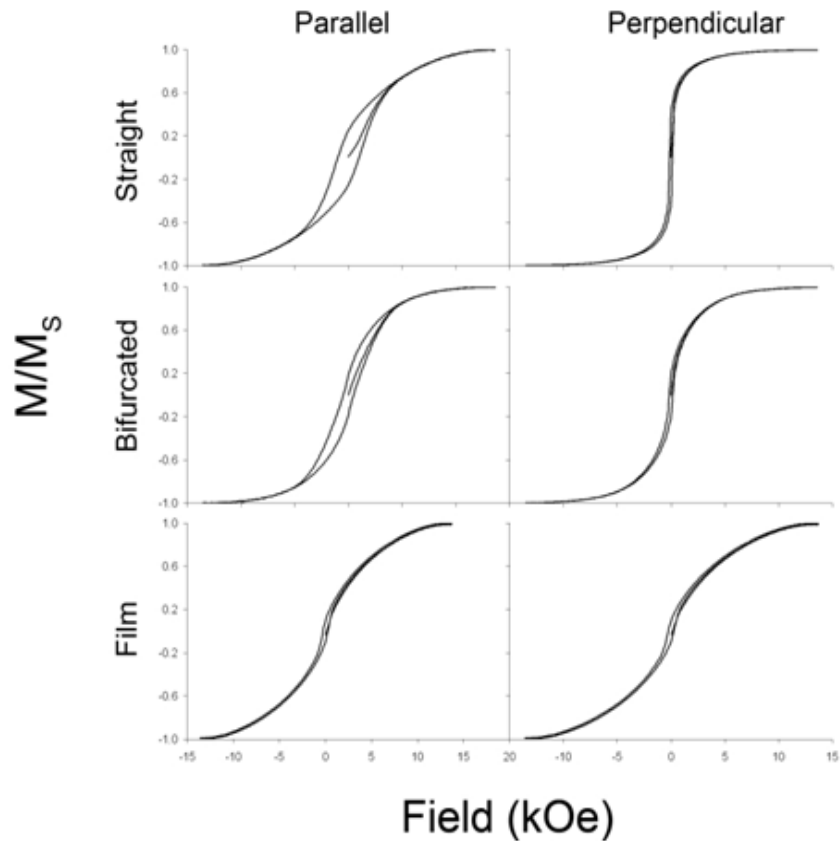


Figure 5.1: Hysteresis curves for perpendicular and parallel orientations of straight, bifurcated, and thin-film samples. The shape anisotropy is observed in straight and bifurcated samples. The coercivity of the bifurcated wires is small due to the branches having radii $< R_c$.

This behavior is typical of magnetic nanowires where the magnetic properties are largely determined by shape anisotropy effects when compared to magnetocrystalline anisotropy, as previously discussed. Also, because of the very large aspect ratio of the nanowires (>100) shape anisotropy effects clearly dominate magnetocrystalline anisotropy effects. For the bifurcated nanowires, the coercivity in the perpendicular orientation is only about 500 Oe (much lower than that for the straight nanowires). This reduced coercivity may be related to the reduced aspect ratio of the nanowires or the fact that the radii in the branches are expected to be very small and $< R_c$.

The bifurcated nanowires can be thought of as consisting of four segments (two at the mid-section and one each at the two ends as seen in **Figure 3.10**) with reduced aspect ratio (~ 30). Here, the magnetic properties are a result of competing shape anisotropy and magnetocrystalline anisotropy. In consistence with this explanation, it may be noted that the coercivity in the parallel direction is reasonable, ~ 150 Oe, as in the case of the straight wires. For comparison, **Figure 5.1** also shows the magnetization versus field curves for polycrystalline thin film samples. Here, the coercivity in the perpendicular and parallel direction is about 250 Oe. In thin films, the magnetization behavior is mostly dominated by magnetocrystalline anisotropy effects.

Additionally, multi-domain effects will also play a significant role in determining the magnetic behavior. By comparing the thin films to the bifurcated and straight nanowires, it is evident that the magnetocrystalline anisotropy effects are only implicated in reducing the observed coercivities of thin films and larger diameter nanowires. In straight nanowires of our size, clearly shape anisotropy dominates. In the bifurcated wires, there appears to be a mixture of shape anisotropy and multi-domain effects caused by the presence of ample defects and separate grains in the branched region of the wires (discussed below).

We have studied the dependence of coercivity as a function of total length of the nanowires and also as a function of branch/stem length ratios of the nanowires. For this, we first prepared the bifurcated templates with specific ratios of branch/stem and also specific total length of the pores. The obtained templates were then completely filled with Co. The anodization times took place in ratio of 1:2:1. For example, one sample was anodized for 2 minutes at 10 V, 4 minutes at 7.1 V and 2 minutes at 10 V at 10/7.1/10 V (a total of 8 minutes). Each sample underwent electrodeposition until signs of overfilling

were present. Electrodeposition was halted before significant portions of the template were made to contain wires linked at the top.

Figure 5.2 shows the coercivity as a function of total anodization time.

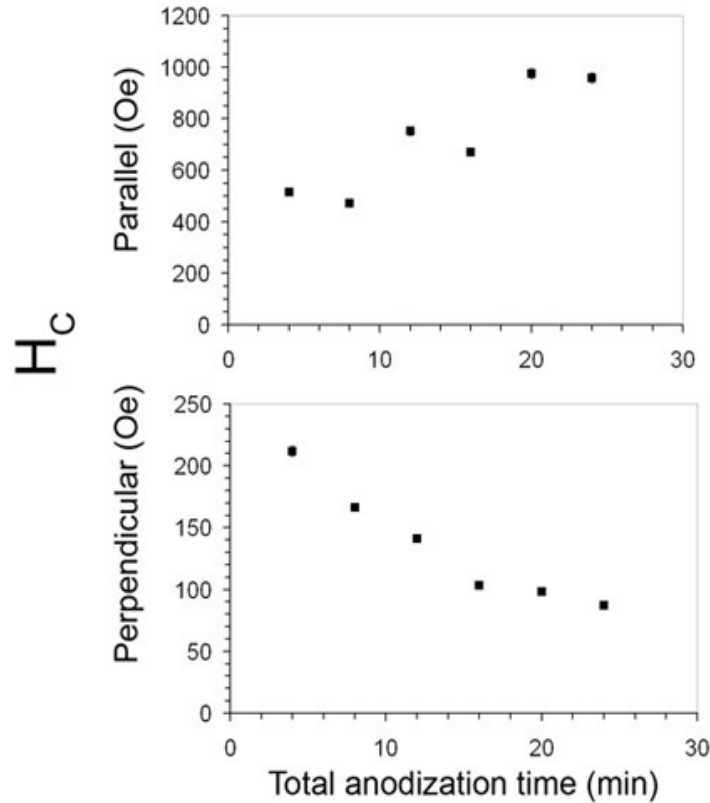


Figure 5.2: Coercivity as a function of anodization time for 1:2:1 bifurcated nanowires.

We see that in the perpendicular alignment the coercivities tend to increase with time and in the parallel alignment the coercivities tend to decrease with time. The reduced coercivity for the wires with shorter anodization time is attributed to the presence of superparamagnetic components in the wires. Thermal fluctuations can reduce the energy barrier for magnetization reversal, which in turn reduces the coercivity.

Interestingly, in **Figure 5.3**, the perpendicular coercivity is found to decrease with increased branch/stem ratio. This is consistent with the previous explanation. Presence

of superparamagnetic components is expected to be higher in the branched sections of the nanowires leading to reduced coercivity for the wires with largest branch lengths.

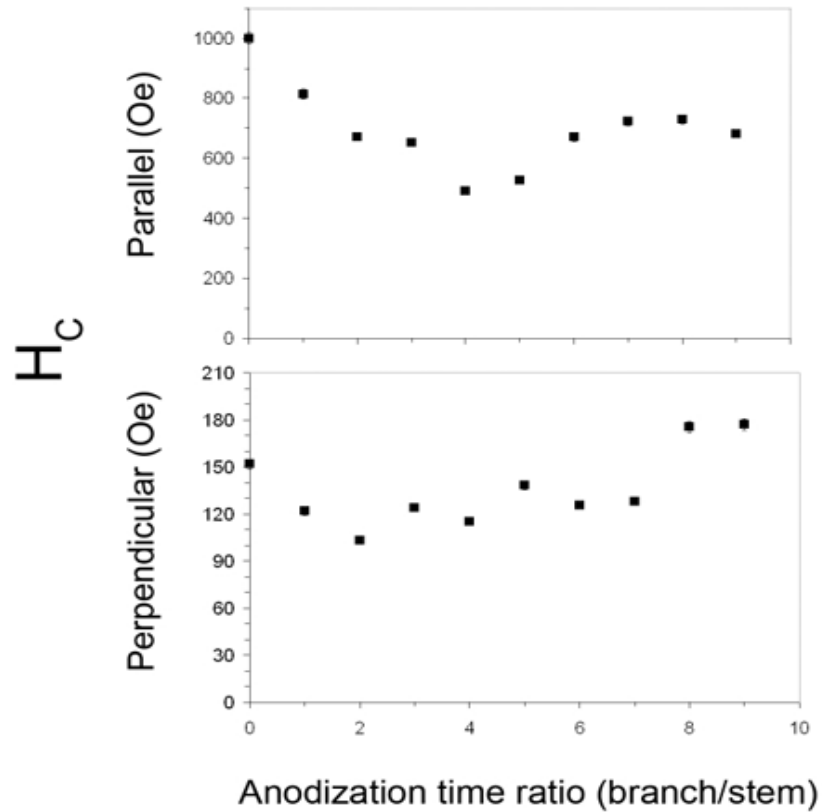


Figure 5.3: Coercivity as a function of anodization ratio for fixed total anodization time of 12 minutes. The anodization ratio is calculated as time spent anodization the branch / time spent anodizing stem.

Finally, we have also studied the temperature dependence of the magnetization of the nanowires. For each type of nanowire and alignment, samples were made as-deposited as well under two different annealing conditions, 200° C and 400° C in air for 3 hours. **Figure 5.4** shows the magnetization versus temperature plots for straight and bifurcated nanowires in both alignments (perpendicular and parallel to applied field of 5000 Oe and zero-field cooled (ZFC). Field-cooled (FC) measurements were also taken (not shown here), however were found not to deviate significantly from the ZFC data.

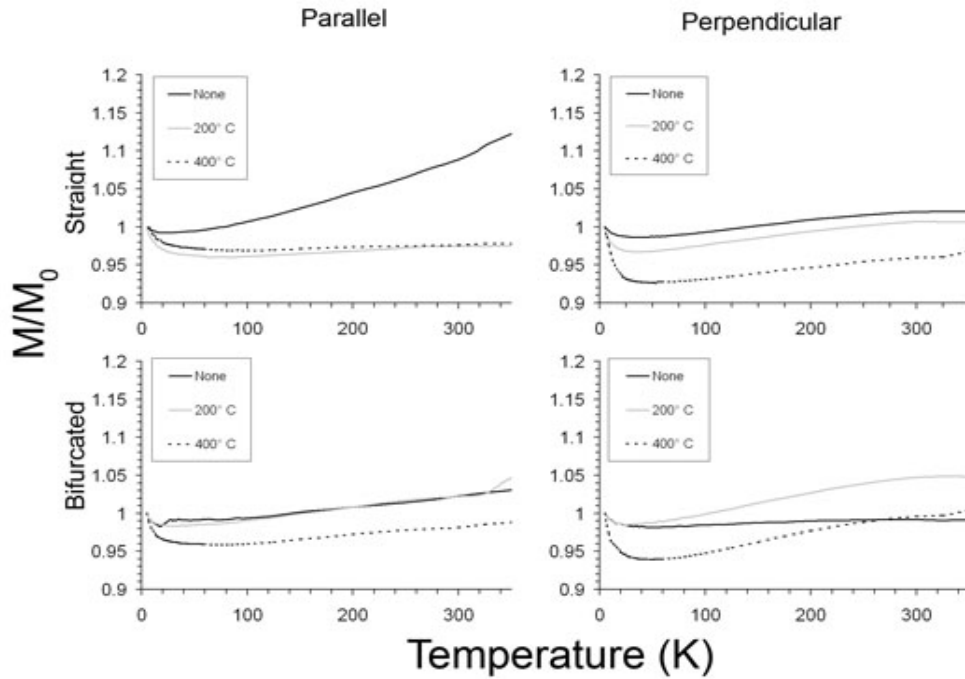


Figure 5.4: ZFC Moment vs. temperature for straight and bifurcated nanowires in parallel and perpendicular alignments. Samples were annealed at 200° C and 400° C for comparison. Applied field was 5 kOe.

Interestingly, we observed no evidence of superparamagnetism when comparing the ZFC and FC plots, which is typically revealed in a maximum corresponding to the blocking temperature. Such a peak is expected due to the previous explanation of lowered coercivities being caused by increased superparamagnetic interactions. However, we expect the ferromagnetism of the wires to dominate the magnetism of the sample, which could mask the appearance of a blocking peak. Moreover, the observed slight upturn the ZFC plots near low temperature can be partially attributed to previously superparamagnetic domains becoming ferromagnetic and, thus, contributing to the overall ferromagnetic moment.

Also, the magnetization vs. temperature dependence does not demonstrate the expected Bloch law behavior. In general, the magnetic moment of alumina (as measured in blank alumina templates) is several orders of magnitude lower than that of the

ferromagnetic wires. However, it does seem to contribute slightly to a paramagnetic upturn at lower temperatures. Moreover, this non-Bloch behavior could be due magneto-elastic effects, as previously discussed. The Al, upon which the template sits, by expanding and contracting due to the temperature change, could be altering the orientation of the wires in the field. The expansion and contraction of aluminum under temperature change is much greater than that of alumina. Thus, the expansion and contraction would cause a slight curling of the sample in the field, which would alter the orientation of the wires in the applied field. This could be the cause of the slight decrease in magnetic moment as the temperature decreases (see **Figure 5.4**).

Annealing may help to reduce the graininess of the deposited Co, forming structures that are more crystalline. For the straight nanowires, the magnetization of the as-deposited sample is seen to be significantly larger at higher temperatures. This is not the case for the bifurcated nanowires. This may be attributed to multi-phased nature of Co. Bulk Co is typically known to exist in hcp form at room temperature while the fcc phase is known to exist only at very high temperatures. However, in nanoscale forms of Co, particularly when prepared by means of electrodeposition, Co has been reported to exist in both forms, hcp and fcc, as previously discussed. It has been observed by Kroll et al. in [88], through X-ray photoelectron spectroscopy (XPS) and extended X-ray absorption fine structures (EXAFS) studies that in small Co nanoparticles, there is a decrease in hcp-Co in favor of fcc-Co. Hcp-Co is known to exhibit strong magnetocrystalline anisotropy in contrast with fcc-Co. This in turn reduces magnetocrystalline anisotropy in smaller Co nanowires – another indication of the strong shape anisotropy in our nanowire samples outweighing the effects of magnetocrystalline anisotropy. Interestingly, annealing the sample appears to reduce the magnetization of the nanowires, which may be indicative of a phase-stabilization

process achieved through the annealing process. Also, for the annealed samples the magnetization versus temperature exhibits a more typical Bloch law kind of behavior. This is also true for the bifurcated nanowires (both as-deposited and annealed samples) where the behavior is of the Bloch-law type. The smaller diameters of the mid-section of the wires possibly ensure a more single-phased fcc-type Co in such small dimension wires.

5.2.3 *PAni Composite Nanowires*

The fabrication of PAni nanotubes filled with metallic wires is carried out using the methods of Chapter 3. The acids used for the anodization process were 15% sulfuric and 3% oxalic acid. A range of voltages (5 – 60 V) were used. Typical anodization time is around 30 minutes. For the deposition of polyaniline, an AC voltage of 20 V and 250 Hz was applied. The total deposition time for PAni was three minutes. The produced tubes consistently showed diameters that were approximately 15% of the alumina pores. The applied voltages for deposition were in the range of 35-45 V and frequency of 250 Hz was used for deposition were based on the anodization acid used. Typical deposition time was approximately 4 minutes.

A Princeton Measurements Corp. Model 2900 AGM (Appendix B) was used to measure hysteresis loops for both magnetic fields perpendicular and parallel to the axis of the wires. Some typical curves are presented in **Figure 5.5**.

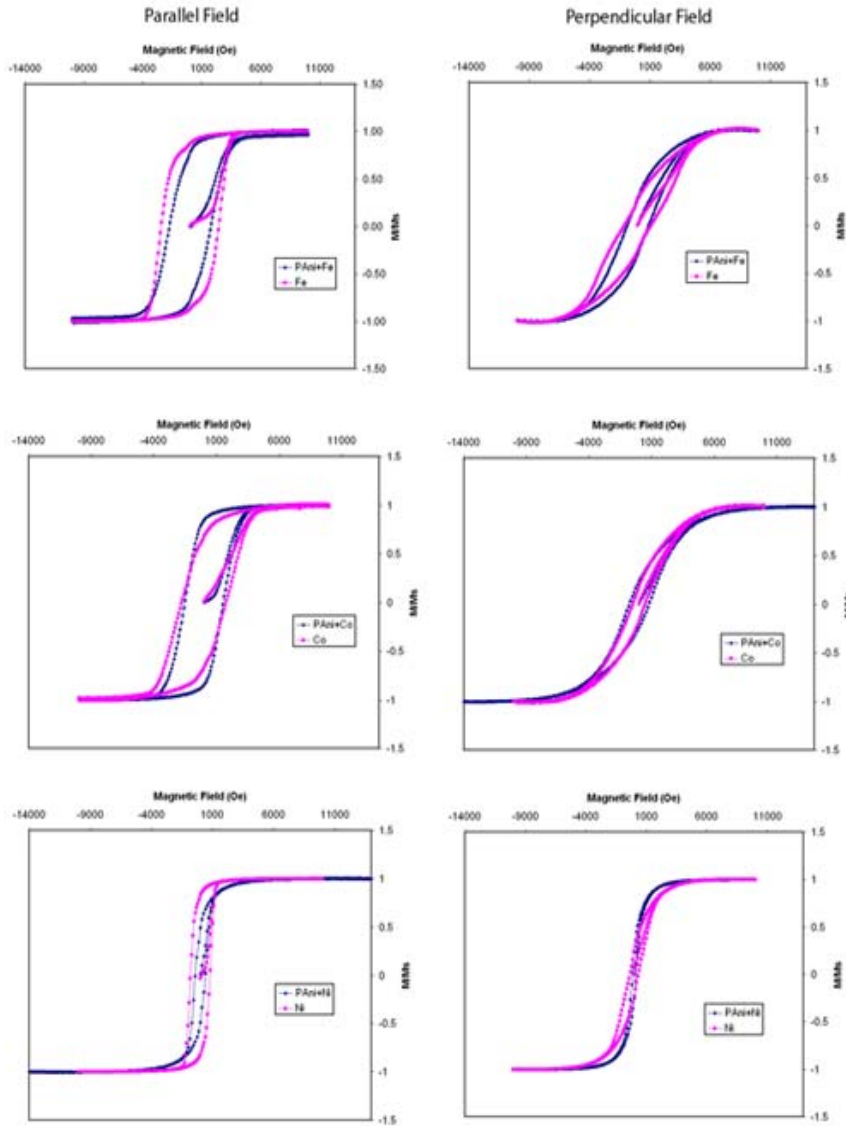
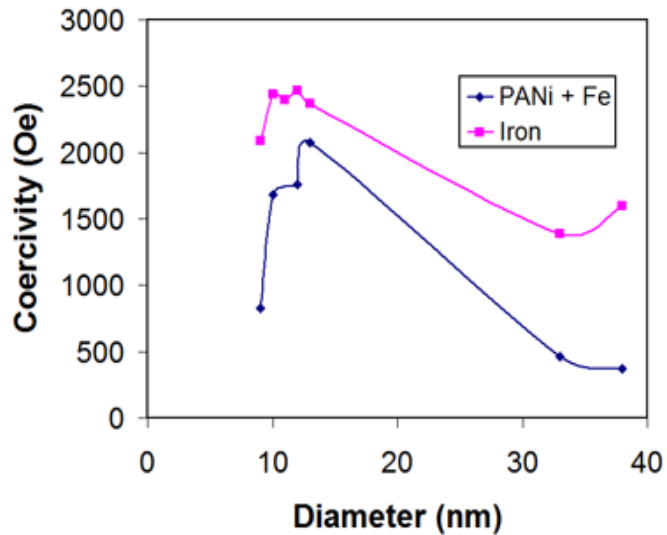


Figure 5.5: Room temperature hysteresis loops for filled PANi nanotubes as compared to nanowires for Fe, Co, and Ni. Diameters are approximately 11 nm, 12 nm, and 31 nm respectively. All show strong magnetic shape anisotropy, which indicates the presence of nanowires.

The coercivities for the filled PANi tubes for fields parallel to the axis of the nanowires were slightly lower than those of plain nanowires. Due to the large shape anisotropy observed in the hysteresis loops, we have a confirmation of the existence of nanowires in the PANi. If the metal formed a film, shape anisotropy would not exist. This method of confirmation does not account for the possible situation where the PANi fills only part of the pores and the ferromagnetic material completes the filling. However, by controlling

anodization time, thus controlling the length of the pores, we were able to find the approximate amount of time to fill the templates with PANi completely. One is then left with two possible scenarios for the wire deposition: 1) On top of the template in the form of a thin film or 2) inside the PANi in the form of wires. The first scenario did not occur, which is evidenced by the aforementioned strong magnetic shape anisotropy and the absence of a thin film in the SEM images.

Figure 5.6 displays graphs of coercivity vs. diameter for the nanostructures. There are several factors that can affect the measured coercivities.



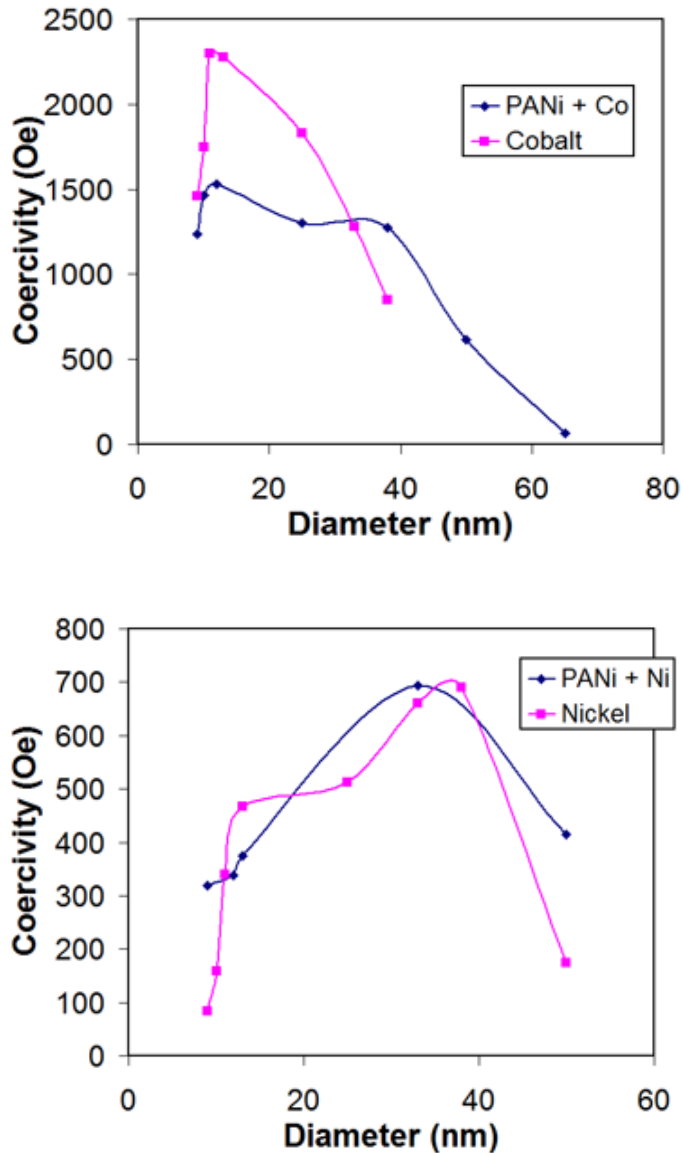


Figure 5.6: Coercivity vs. Diameter graphs for Fe, Co, and Ni filled PANi nanotubes as compared to Fe, Co, and Ni nanowires. The magnetic field is applied along the axis of the wire.

First, because the metal was being deposited inside PANi rather than inside the alumina, the diameters of the nanowires inside the PANi will be slightly smaller than nanowires deposited directly inside porous alumina. We measured the thickness of the PANi tube walls to be approximately 15% of the total pore radius by measuring the diameters of pores of several templates, filling the templates with PANi, and then re-measuring the

diameters of the pores. The two numbers were then subtracted from each other, yielding the thickness of the PANi nanotube. From this we learn that the wires deposited in PANi are 15% smaller in diameter than wires deposited directly in alumina. Second, defects in the walls of the deposited PANi nanotubes can cause blockages in the channels, making it more difficult for the deposited metal to form complete wires. Thus, instead of a complete wire, a chain of nanoparticles could fill the tube. This would lead to superparamagnetic effects reducing the measured coercivity of the composite structures. Thirdly, the PANi itself, as it is strongly diamagnetic, could interfere. From **Figure 5.6**, we see that the coercivity dependence on diameter for the composite curves is very similar to those for the coercivity dependence on diameter for the metal wires. However, the coercivities for the composite wires do appear to be slightly reduced, which is most likely due to the second suggested scenario.

Magnetic viscosity can be used to understand the intrawire interactions in the PANi composite structures and determine the superparamagnetic effects described above. The magnetic moments aligned in a saturating field are in equilibrium, but, when a demagnetizing field is applied, thermal fluctuations and the demagnetizing field cause the moments to overcome a stable energy barrier and change with time. The magnetic viscosity, $S(H)$, is a measure of how easily this change occurs. For samples that are long continuous wires, the magnetic interactions between domains will be strong causing a larger energy barrier. For samples that contain grainy, nanoparticle structures, which are superparamagnetic, magnetic interactions will be weaker, as superparamagnetic particles are quick to switch orientations at room temperature. So, the overall energy barrier for demagnetization will be lower. In this way, one can obtain an understanding of our PANi composite arrays and determine whether the wires inside them are continuous structures or non-continuous grains. **Figure 5.7** shows a graph of viscosity

vs. demagnetizing field for the Co-PAni structure as compared to Co nanowires and also the viscosity vs. demagnetizing field for the Co, Fe, and Ni containing PAni composite arrays.

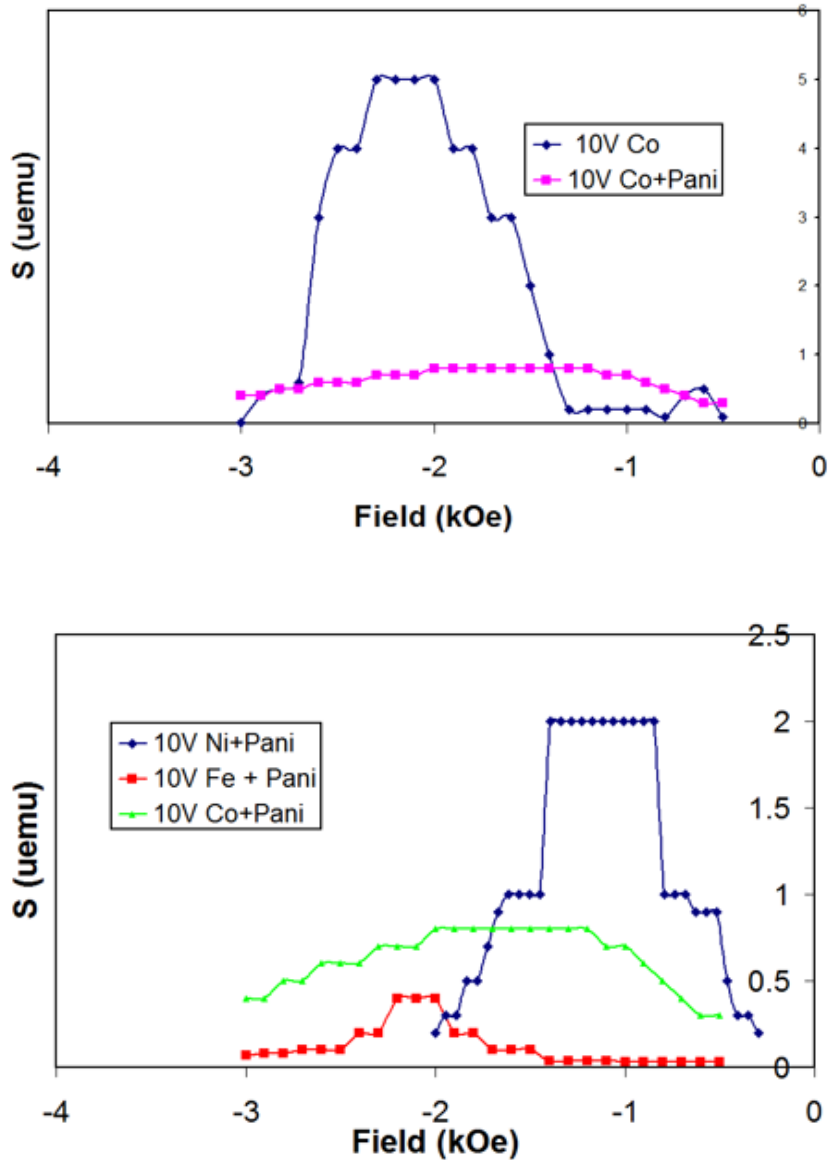


Figure 5.7: Magnetic viscosity vs. demagnetizing field for (upper) Co filled PAni nanotubes as compared to Co nanowires , and (lower) Co, Ni, and Fe filled PAni nanotubes.

We see that the composite structures are most probably non-continuous. Rather, they may be granular because the peaks appear to be broad and spread out. The broadness of

the peak indicates a rapid demagnetization. In consistence, the PAni composites have a viscosity much less than that of the nanowires.

In addition to intrawire interactions, we examine interwire interactions. A good way to measure how the PAni affects the magnetostatic interactions of the nanowires is to use the Henkel method explained above using the parameter α given in equation (5.7).

Figure 5.8 displays a plot of $\Delta M/M_r$ vs. H . α is proportional to the area under the curve of this plot.

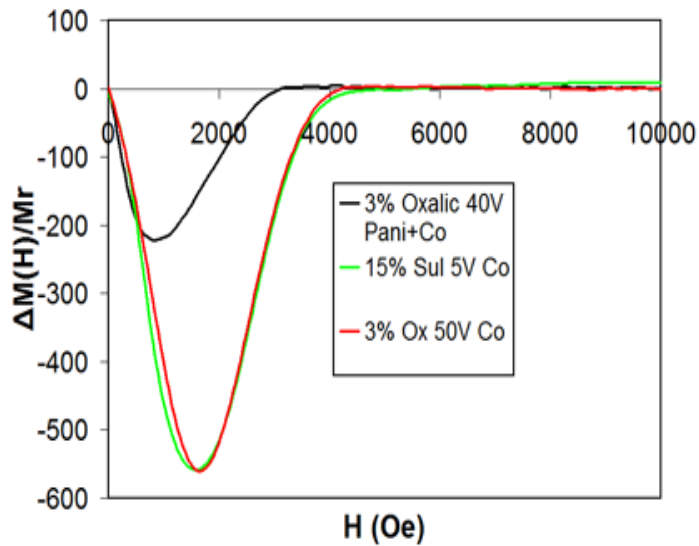


Figure 5.8: Graph showing interwire interactions for Co filled PAni nanotubes as compared to different diameters of Co nanowires. We see that PAni strongly shields the interwire interactions.

A large α represents large interwire interactions that is, large magnetostatic coupling between neighboring wires. The data are summarized in **Table 5.1**. We can clearly see that PAni greatly reduces the inter-wire magnetostatic interaction.

Table 5.1: Summary of α data

sample	$ \alpha $
40V Co	205
50V Co	224
5V Co	232
40V PAni+Co	71.4

For the various diameters of the PAni-composites studied here, the interwire spacing was approximately the same (about 2.5 times the radius). So the values of α are approximately the same. For the case of the PAni composite wires, (for which the PAni tube comprises approximately 15% of the wire diameter), the interwire interaction is less than half as large than that for nanowires deposited directly inside the templates. This appears to be inconsistent with the fact that a magnetic field for a dipole decreases like $1/r^3$. So, a 15% increase in interwire separation caused by the introduction of PAni would cause a field that was about 66% of what it was before the increase. However, we see a field that is only about 32% of what it was before the increase, or a field that decreases approximately like $1/r^8$. Therefore, the PAni not only shields the wires magnetostatically by increasing the distance between them, but also shields the wires, possibly, by reducing the magnitude of the overall dipole field itself.

By examining how temperature affects the observed magnetic characteristics, we can learn yet more about the interactions in the wires. For these measurements we used a Quantum Design MPMS SQUID Magnetometer. **Figure 5.9** shows the coercivity as a function of temperature for a PAni-Co composite and nanowire samples at a variety of diameters.

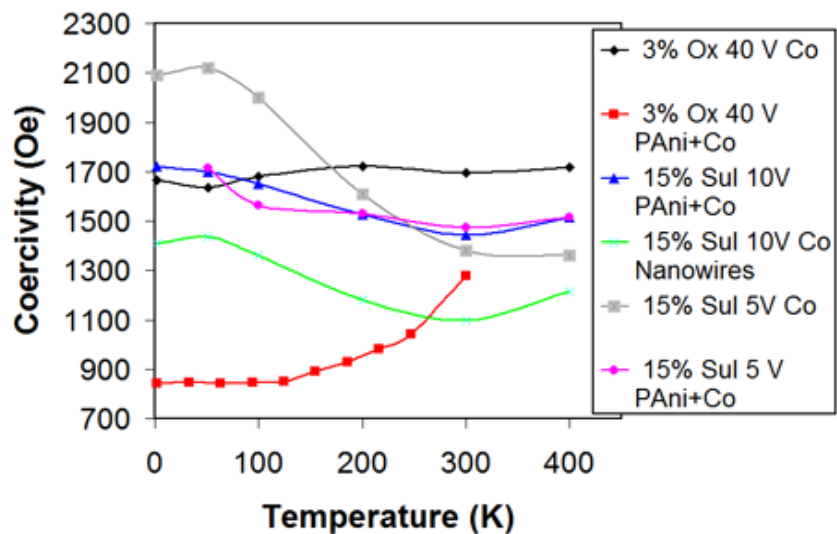


Figure 5.9: Coercivity vs. temperature for a variety of diameters of Co nanowires and Co filled PANi nanotubes.

We see that for the samples prepared by anodization in oxalic acid, that is with the largest diameter (~40 nm), they show either constant or decreased coercivity with decreasing temperature. However, for the smaller diameter composites, prepared by anodization in sulfuric acid, we see that the coercivity increases slightly as temperature decreases. This may be indicative of the presence of superparamagnetic components which contribute to the magnetization and hence the coercivity of the sample below the blocking temperature.

Figure 5.10 displays graphs of the magnetic moment vs. temperature for the same PANi-Co and Co samples as in **Figure 5.7**. **Figure 5.10(C)** and **5.10(D)** show the magnetization versus temperature plots under ZFC and FC conditions.

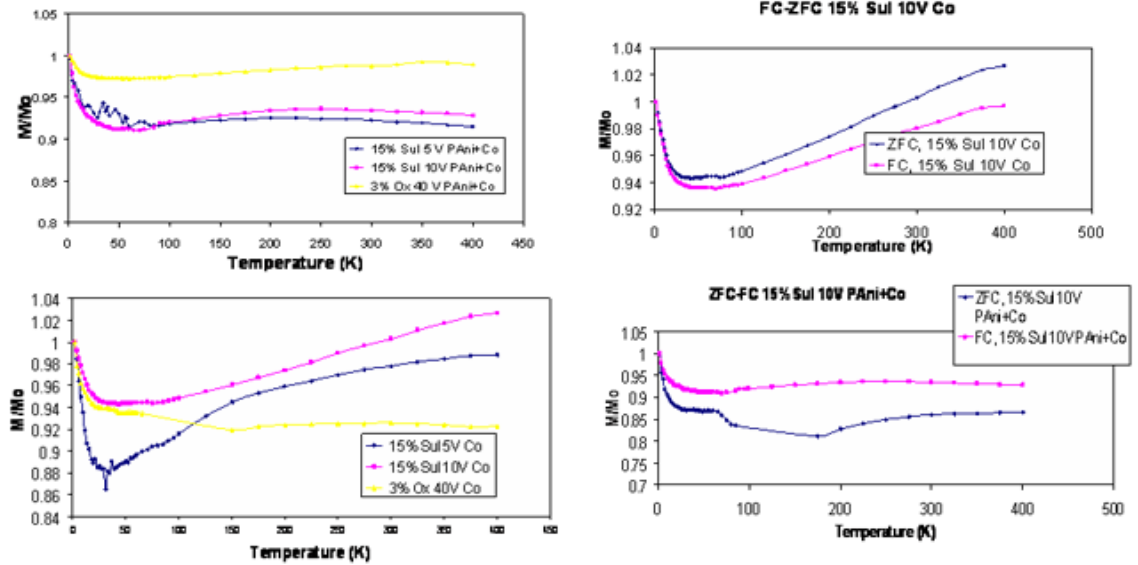


Figure 5.10: Moment vs. temperature for a magnetic field of 5000 Oe applied along the axis of the nanostructure for (starting top left and proceeding counter clockwise) (A) Field-Cooled Co filled PANi nanotubes of a variety of diameters, (B) Field-Cooled Co nanowires of a variety of diameters, (C) and (D) Field-Cooled and Zero-Field-Cooled Co filled PANi nanotubes as compared to Co nanowires.

No marked difference is observed in these two plots. Interestingly, we observe no evidence of superparamagnetism, which is typically revealed in a maximum corresponding to the blocking temperature. Also, the magnetization vs. temperature dependence does not demonstrate the expected Bloch law behavior. This could be due to any of the following reasons. First, magnetoelastic effects could play a role. The alumina template itself, by expanding and contracting due to the temperature change, could be altering the orientation of the long axis of some of the wires in the field. The observed behavior may also be attributed to the magnetic behavior of the alumina and the PANi itself. In general, the magnetic moment of alumina is several orders of magnitude lower than that of the ferromagnetic wires, however, it does seem to contribute slightly to a paramagnetic upturn at lower temperatures (as measured in blank alumina templates). PANi is a much better dielectric than alumina and, we see much more pronounced minima in the samples containing PANi. Moreover, recent studies of carbon nanotube

magnetism, which is a similar structure to the PANi nanotube, also show this pronounced dip [89]. The large dip and subsequent upturn is most probably a paramagnetic contribution due to the carbon, in our case arising from PANi.

We have shown that we can create metal-filled PANi nanotubes by a efficient and reliable three step anodization/electrodeposition process. In addition, our PANi-ferromagnet composite structures exhibit strong magnetic shape anisotropies, high magnetic shielding of interwire magnetostatic interactions, and an interesting composite dielectric-ferromagnet temperature dependence. We also find that the as-created wires have a granular structure, although they still exhibit large magnetic viscosities. In the future, it would be valuable to remedy this granular structure, perhaps by annealing, before applying them in devices.

5.3 Carbon Nanotube Magnetism

5.3.1 Theory

In general, carbon nanotubes are diamagnetic [89]. Recently, it was theoretically posited that H, O, or N impurities can induce ferromagnetism in carbon structures by analyzing such systems with density functional theory methods [90-92]. Here we discuss the theory of carbon nanotube magnetism.

There are two primary contributors to vacancy and molecule implantation magnetism in graphite nanostructures: H-complex and adatom magnetism. First, when hydrogen bonds to carbon in a vacancy it causes delocalization of the π electrons and orients itself outside of the localized graphene plane, which creates the magnetism termed H-vacancy complex magnetism [90, 91]. A vacancy in the graphene plane causes three carbon atoms to have dangling bonds. Two of those can bond to each other, creating a pentagon structure, although this causes great mechanical stress in that area of the tube. The third bond is left dangling. Hydrogen atoms can then saturate this

bond. The saturated bond can be oriented either parallel or perpendicular to the length of the nanotube and the same process can occur for zigzag and armchair CNTs. However, the perpendicular case has been found to be the most stable [91]. The parallel case for zigzag CNTs is depicted in **Figure 5.11**.

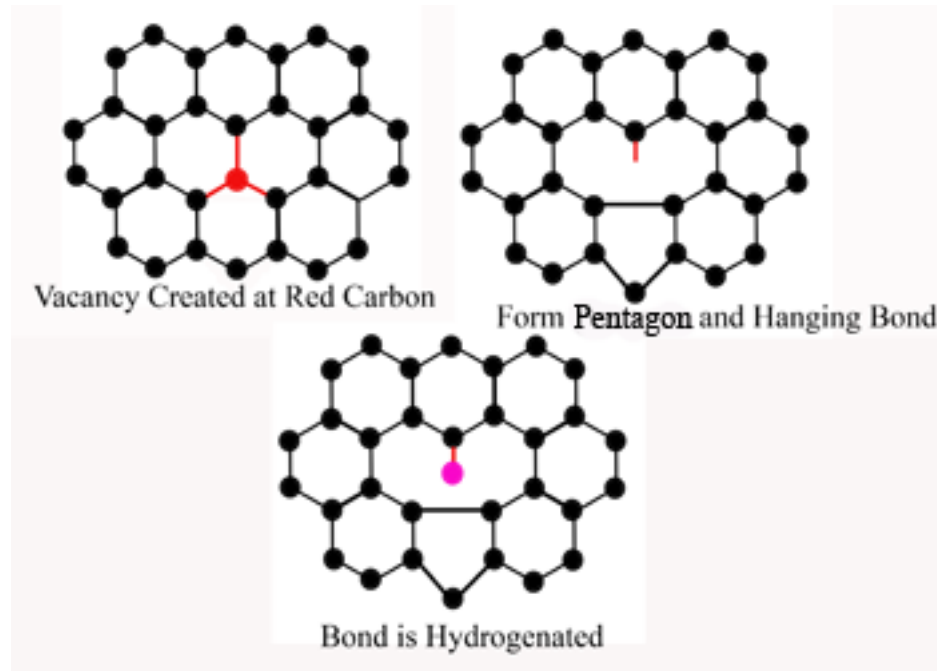


Figure 5.11: Demonstration of hydrogenation of a zigzag CNT in the parallel configuration. The top left diagram shows a red circle where the carbon vacancy will be. The top right picture shows the formation of a pentagon and the dangling carbon bond. The bottom picture shows the saturation of this bond with hydrogen (purple circle).

In a CNT without defects, all of the electrons are paired in π bonds, and the carbon atoms are sp^2 hybridized. However, in a CNT with a vacancy, when the vacancy is hydrogenated, it creates a new σ bond and leaves an unpaired π electron. In three dimensions, the saturating hydrogen atom is located outside and above the local graphene plane. However, this is a non-magnetic state for MWCNTs, most likely due to stabilization from other overlapping graphene sheets in the nanotube, as magnetism is predicted in a similar structure in flat monolayer graphene planes and in SWCNTs [90]. If a second hydrogen atom comes, it will bond to another side of the vacancy (in the

pentagon), but below the plane. This state has been calculated to be magnetic. However, a third hydrogen atom saturating the produced dangling bond will again result in no magnetism. Lehtinen, et al. in [90] have calculated the absorption energy of the second saturating hydrogen to be lower than the adsorption energies of the first and third saturating hydrogen. So, this magnetic state is rather stable even in the presence of other hydrogen atoms. It has been calculated that this delocalization produces a ferromagnetic moment of 0.9-1.2 μ_B [90, 91]. In addition, it is noted that a third saturating hydrogen is even less likely due to pinning and hindrance from the pre-existing saturating hydrogens. Therefore, the most likely state is the two hydrogen saturated magnetic state.

Second, in addition to the saturation of vacancies, some graphite magnetism has been attributed to hydrogen adatoms. The increased interlayer separation in ordered graphite and carbon nanotubes is a perfect size for hydrogen adsorption and the formation of interstitials and Frenkel pairs. However, it should be noted that many of these will most likely form covalent bonds in nearby vacancies unless they are hindered by the aforementioned pinning in already doubly saturated vacancies. Furthermore, Ma, et al. in [91] find that carbon adatom impurities on the surface of the nanotube can also result in magnetism if they are singly saturated due to the same delocalization that caused H-complex magnetism. But, the contribution to the overall magnetism from these adatoms strongly depends on the geometry of the CNT itself. A range of 0.45 -1 μ_B has been predicted [90, 91]. However, calculations have shown that the magnetic behavior will be dominated by H-complex vacancy induced magnetism [92].

Ordered graphite magnetism has been experimentally shown to occur in bulk HOPG [93-95]. Although ferromagnetism was experimentally shown to occur in irradiated graphite structures and predicted in carbon nanotubes, to the best of our

knowledge, it has never been experimentally observed in carbon nanotubes. In previous studies, in order to induce ferromagnetism by vacancy implantation, high energy irradiation (such as beam energies of 100 kV for N ion implantation reported in [94], or 2.25 MeV for proton irradiation reported in [95]) must be performed to make the necessary disorder. Such energies are not necessary for highly disordered carbon nanotubes due to the pre-existence of sufficient vacancies. Furthermore, it has been experimentally shown that dangling carbon bonds or vacancies in various graphite structures will bond to hydrogen, especially in carbon nanotubes, making such structures ideal for future applications in hydrogen storage [96, 97]. Even though carbon nanotube magnetism has not been demonstrated, there have been studies showing that hydrogen uptake in carbon nanotubes can occur [96, 97].

5.3.2 *Experimental Results*

MWCNTs are made using the methods of Chapter 3. For this study, we use pores that are approximately 65 nm in diameter. We make 4 different inner diameters as discussed in Chapter 3. The nanotubes are then removed from the templates by dissolving the alumina in 15% sulfuric acid heated to 100 °C, as will be discussed in Chapter 6. The acid is removed from the solution and replaced with 99.5% ethanol. The nanotubes are then dispersed in the solution in an ultrasonic bath for 3 seconds. TEM studies show that the tubes are polycrystalline and extremely disordered, discussed in Chapter 3.

Samples are made by depositing a drop of nanotube solution onto a Si/SiO₂ substrate and then heating the substrate slightly until the ethanol is evaporated off resulting in a well dispersed, sparse film of nanotubes on the Si/SiO₂. Therefore, the nanotubes were oriented randomly in the field. The chips are then annealed in a tube furnace containing equal parts Ar and H₂ at 800° C. For comparison, other chips were

also annealed in Ar only. Low temperature magnetic hysteresis loops were taken in a Quantum Design MPMS SQUID magnetometer and room temperature hysteresis loops were taken in a Princeton Measurements Corporation MicroMag AGM.

Figure 5.12(A) shows raw data for H₂/Ar annealed tubes, Ar only annealed tubes, and the Si/SiO₂ substrate alone. **Figure 5.12(B)** shows the data after the diamagnetic signal was subtracted out. It is clear that there is a rather strong ferromagnetism in the H₂/Ar annealed nanotubes that is not present in the substrate or in the samples annealed in Ar only. From this, we can conclude that the ferromagnetism is indeed due to the H rather than random impurities in the sample or substrate. However, the paramagnetism left after the diamagnetic background subtraction in the Ar only annealed samples and in the substrate, viewed in **Figure 5.12(B)**, can be attributed to impurities in the substrate material.

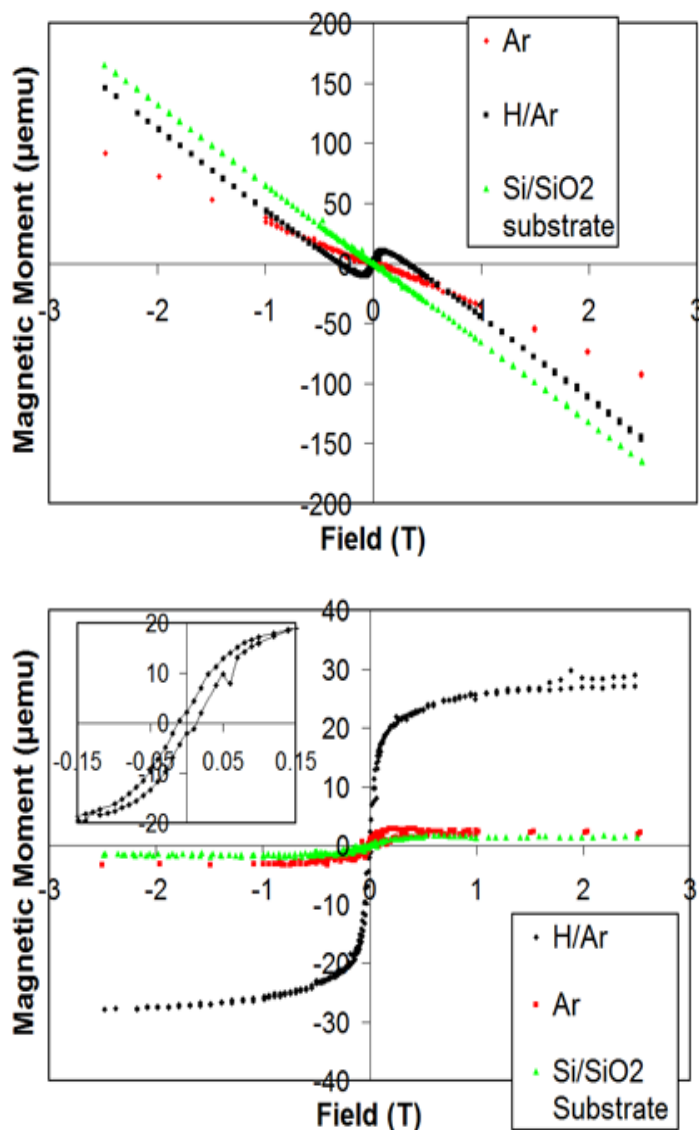


Figure 5.12: Hysteresis loops at 2 K for nanotubes annealed in H₂/Ar, Ar only, and the substrate material for (A) Raw data (B) with the diamagnetic part subtracted out. The inset shows the coercivity of the hydrogen annealed CNTs.

Great pains were taken to avoid contamination of the carbon samples themselves with ferromagnetic impurities. Moreover, as is well discussed in [93], a typically small concentration of ferromagnetic impurities, such as Fe or FeO₃, would not produce as great a saturation moment as we observed in our H₂ annealed samples. Furthermore, as magnetism did not exist in the same Ar only annealed samples, impurities cannot be the source of the observed magnetism.

Our experiments suggest a Curie temperature well above room temperature.

Figure 5.13 shows a graph of the magnetization vs. temperature.

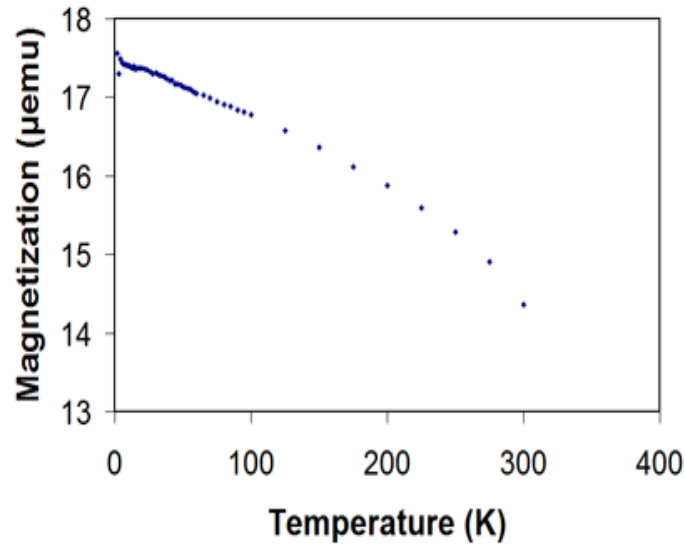


Figure 5.13: Moment as a function of temperature. A diamagnetic moment has been subtracted off. Field = 0.1 T. The plot was fit to the Curie-Weiss model to extrapolate a Curie temperature of ~1026 K.

By extrapolating our data using the Curie-Weiss law, we find a Curie temperature of 1026 K based on a Levenberg-Marquardt fitting algorithm using the fitting program EasyPlot. Using the Quantum Design SQUID MPMS oven insert (Appendix A), we also took magnetization data up to 775 K, however due to poor instrumentation design and unpreventable excessive noise, the results of this study were inconclusive and have not been included here. This measured Curie temperature may be larger than the temperature at which we would expect the nanotubes to expel the hydrogen [98, 99], thus, possibly eliminating the ferromagnetism altogether. The samples had a coercivity of 0.02 T at 2 K (found in the inset of **Figure 5.12**) and remained relatively constant as a function of temperature, as displayed in **Figure 5.13**. The slight decrease in moment with the increase of temperature is similar to that reported by previous studies of graphite magnetism (for instance, refer to [93]). At least part of this behavior can be

attributed to superparamagnetic impurities in the substrate becoming ferromagnetic below their blocking temperature. The consistency in magnetization may be attributed to the great strength of the C-H and C-C bonds, resulting in less thermal oscillations and the maintenance of the positions of the H-complex bonded hydrogen atoms out of plane as well as keeping C and H adatoms in position.

For all of these measurements, the nanotubes were oriented randomly in the field. However, we annealed and performed hysteresis measurements on some as-deposited aligned arrays to determine if there was any magnetic shape anisotropy. Normally for small enough diameter ferromagnetic nanowires, the easy axis is directed along the length of the wire. Therefore, by applying a field at a different angle, a different hysteresis pattern is observed, as discussed in the previous sections of this chapter. We determined that there is virtually no difference in magnetism as a function of field angle, thus no magnetic shape anisotropy. However, it is more likely that due to the random dispersion of saturated vacancies and adatoms, there is no easy axis for the nanotubes and the spontaneous orientation of dipoles in the sample is entirely random.

We try to determine the temperature at which the nanotubes become ferromagnetic. For these AGM measurements, we found that the magnetization of the sample holder contributed significantly to the overall magnetic measurement. Therefore, the magnetization of the sample holder was measured alone and taken as a background that was then subtracted from the data. **Table 5.2** provides a summary of room temperature magnetic measurements for different annealing temperatures.

Table 5.2: Summary of annealing results. All samples are made from 20 μL of the solution of the 60 min CVD nanotubes dried on Si/SiO₂. Samples are annealed in H/Ar for 2 hours.

Annealing Temperature (°C)	Magnetic Moment ($\mu\text{emu}/\text{ng}$)
un-annealed	0.00212 ± 0.0009
200	0.00278 ± 0.001
400	0.00187 ± 0.0008
500	0.00621 ± 0.003
600	0.0170 ± 0.006
700	0.0133 ± 0.005
800	0.0140 ± 0.006

The temperature necessary for making and breaking C-H bonds is estimated to be 600° C [96]. In consistence with this, we see in **Table 5.2** that for samples annealed at temperatures $\geq 600^\circ\text{C}$, magnetism is clearly present and the moment does not change much. For temperatures just below 600° C, there exists some ferromagnetic moment, but this falls off very quickly for temperatures well below 600° C. We see some very small residual magnetic moment for the unannealed and lower temperature annealed samples, which can be again attributed to impurities in the Si/SiO₂ substrate material, rather than in the nanotubes themselves. In any case, the much increased moment of the nanotubes annealed at temperatures $\geq 600^\circ\text{C}$ as compared to lower temperature annealed tubes again excludes the consideration of random impurities as a cause of the nanotube magnetism.

Using a Stanford Research Systems Model QCM200 Quantum Crystal Meter Scale (QCM), we are able to measure the concentration of our nanotube solution, thus we are able to measure the mass of the deposited nanotubes. Room temperature saturation magnetizations of the samples were found and divided by the mass of the sample. Again, the background magnetization of the sample holder is subtracted out. Nanotubes are found to have $0.0140 \pm 0.006 \mu\text{emu}/\text{ng}$ at room temperature. Our samples displayed a magnetization very similar to that of ferromagnetic graphite

prepared by N ion implantation in by the group of Talapatra, et al. in [94], where it was reported that samples had a magnetization of 0.0009-0.0115 $\mu\text{emu}/\text{ng}$ depending on dosage. Also, our magnetization measurements are on the same order as those measured by Esquinazi, et al. in [93], where oriented graphite films (HOPG and Kish graphite) were used.

As the inner diameter of the carbon nanotube increases, more of the volume of the nanotube is contained in the walls. Thus, we would expect that the magnetic moment would also increase due to a greater number C-H bonds being available. The disorder observed in our CNTs make them perfect for uptake of H. It follows that the extreme disorder in our CNTs allows for many such bonds. And, more individual C-H bonds would create a higher overall moment per carbon nanotube. **Figure 5.14** shows the magnetization as a function of inner diameter. Error in moment was determined by taking the standard deviation of 5 measurements. Error in mass was determined by taking the standard deviation of 10 QCM measurements. We can see that, as expected, as the magnetization increases approximately linearly.

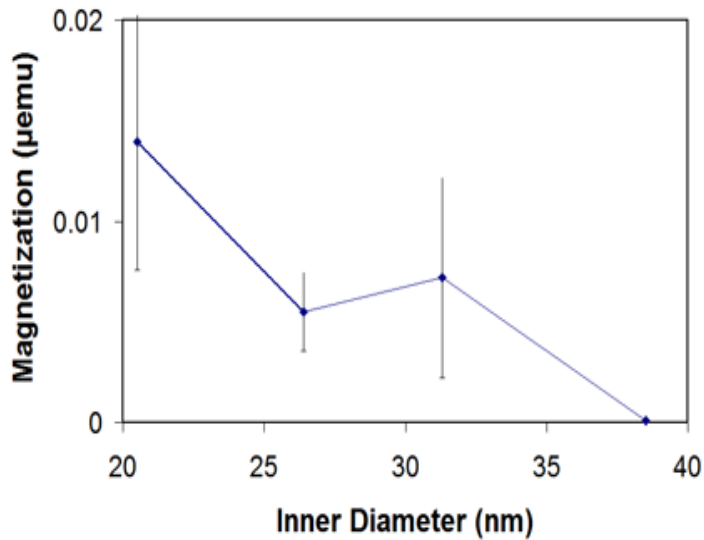


Figure 5.14: Moment/mass as a function of inner diameter. The magnetic moment increases somewhat linearly as a function of inner diameter.

Chapter 6: Fabrication of Nanoscale Devices From Nanotubes, Nanowires, and Graphene Flakes

6.1 Introduction

In order to perform electrical experiments with new nanoscale materials, one must have a reliable, highly repeatable, and simple method for connecting the nanostructures to macroscopic devices. This is no trivial task. There are many factors that one must consider including the properties of the substrate, how interacting with the nanostructure can change its properties, the expense of the method, the length of time required for production, *etc.* In the past it has been done using masking techniques, focused ion beam lithography (FIB), electron beam lithography (EBL), photolithography, or with the aid of nano- and micro-manipulation devices [100-102].

The basic steps of the process are as follows: First, the structures must be released from the porous alumina template and deposited on a substrate (in our case Si/SiO₂). However, nanostructure deposition can be done before or after the creation of electrical contacts. Electrical contacts must be connected to the structure that allows macroscopic device interfaces. This most often also includes some form of lithography and the deposition of material onto the substrate. Next, the devices must be cut out of the substrate and mounted onto chip holders. Finally, the device must be wired to the chip holder. Here, we discuss the various methods that we use to turn the materials fabricated in Chapter 3 into devices so that their unique properties can be measured, and we discuss the advantages and disadvantages of each method.

6.2 Preparation of Template Synthesized Materials

For nanowires, the alumina template is dissolved to release the nanostructures by immersing it in a 5% Phosphoric/5% chromic acid solution and heating to 100 °C for

about 6 hours. This creates a very thick, blackish-colored liquid containing the acid and the nanostructures. The remaining aluminum below the template is removed from the solution and discarded and the solution is centrifuged until the nanostructures settle at the bottom. The top few mL of solution is removed and replaced with de-ionized water. This process is repeated approximately 25 times, or until the majority of the acid has been removed from the solution. During this process, the solution will become more grayish in appearance (as opposed to the amber of the phosphoric/chromic acid solution) and clumps of nanostructures will begin to become visible.

For carbon nanotubes, although the 5% Phosphoric/5% Chromic acid solution releasing method works, it is too dirty. There is a chance that the CNTs will become filled with precipitating Cr metal, and therefore, it should not be used to release CNTs from the templates. Instead 15% Sulfuric acid is used. The template and acid are heated to approximately 100°C, where it is known that sulfuric acid is at its most potent [103]. The etching is allowed to proceed until the entire template is dissolved, which takes approximately 6 hours. It should also be noted that the centrifuge method works best on nanowires and does not work very efficiently on CNTs. In general CNTs form a very stable solution with the acid and do not easily separate out. The best method to get separation is to let the vial containing the solution sit overnight and repeat dilutions over the course of about a week and half. As the acid is slowly replaced by water, the CNTs begin to fall out much faster. Eventually, the CNTs will fall out of the solution in as little as a half hour. Then, the water can be replaced by 100% ethanol.

This new solution is centrifuged and the water is replaced by 100% ethanol. The use of 100% ethanol is essential in the process. The low boiling point of ethanol facilitates the easy deposition of the nanostructures onto a substrate later in the device fabrication process. Moreover, 100% ethanol is the only liquid that was tried in this

process that gave successful results. Other solvents tried were water, acetone, hexane, heptane, octane, and 70% ethanol. Water has a boiling point that is too high to facilitate easy deposition onto a substrate. And, its strong surface tension forces the nanostructures to cluster at the edges of a drop placed onto a substrate rather than be well dispersed throughout the drop. Acetone was far too volatile and evaporated far too quickly and violently during deposition of the solution onto a substrate. Hexane, heptane, and octane were also far too volatile. In addition, they did not mix sufficiently with the solution and separated from it entirely in some cases. 70% ethanol had the problem of being too impure. Impurities in the commonly available 70% ethanol included benzene, which actually can dissolve many of the nanostructures.

Next in the process, one must unclump and evenly disperse the nanostructures in the solution. To accomplish this, the solution is sonicated for about 3 seconds in an ultrasonic bath. However, care must be taken in during this process, as too much sonication can destroy them. For nanowires, it is difficult to visually determine when the solution has been dispersed adequately due to the small sizes of the clumps. It is best to sonicate for 3 seconds and then get visual confirmation of the clump sizes by SEM analysis. If the clumps are still too large, then sonicate again. Too much sonication of nanowires and the resulting solution will only contain particles that used to be wires. For CNTs, visual confirmation of adequate sonication is easier. Large, black clumps of CNTs, which easily fall out of the solution, will visually separate and the clearish solution will turn a dull gray color. The solution will now retain this gray color for several hours before the CNTs separate out again and form clumps. However, these new clumps are much more weakly bound and can easily be separated again by agitating the solution slightly rather than re-sonicating. If the CNTs are sonicated for too long, they will break into very small pieces, which do not easily avail themselves to electrical measurements.

The substrate that is used for the deposition of the nanostructures and as the platform for device fabrication is Si with a layer of insulating silicon dioxide on top. We use 480 nm of SiO₂ grown by wet oxidation in a tube furnace. In general, the growth of SiO₂ can be done with either wet or dry oxidation. In the case of dry oxidation, oxygen gas is used as the oxidant to form a very uniform oxide layer. However, this oxidation takes a very long time and is not practical for thick layers of oxide. Wet oxidation uses water vapor as the oxidant. Although it produces very thick oxides rather quickly, the uniformity of the oxide is not as good as in wet oxidation. In general, the growth times for the oxide is found using the Deal-Grove model of oxidation [104]. The rate of oxide growth is given by

$$\frac{dt_{ox}}{dt} = \frac{Hk_s P_g}{N_1 \left[1 + \frac{k_s}{h} + \frac{k_s t_{ox}}{D} \right]} \quad (6.1)$$

Here, t_{ox} is the oxide thickness, k_s is the chemical rate constant for the overall reaction, H is Henry's gas constant, P_g is the partial pressure of the oxygen in the furnace, N_1 is the oxygen flux at the interface divided by the number of molecules of oxygen per unit volume of SiO₂, D is the diffusivity, and $h = h_g / Hk_B T$, where h_g is the mass transport coefficient, k_B is Boltzmann's constant, and T is the temperature. The equation has the solution:

$$t_{ox}^2 = At_{ox} = B(t + \tau) \quad (6.2)$$

where,

$$\begin{aligned} A &= 2D \left(\frac{1}{k_s} + \frac{1}{h} \right), \\ B &= \frac{2DHP_g}{N_1}, \\ \tau &= \frac{t_0^2 + At_0}{B} \end{aligned} \quad (6.3)$$

with t_o =initial oxide thickness.

In the limit of thin oxides, this reduces to

$$t_{ox} \approx \frac{B}{A}(t + \tau) \quad (6.4)$$

And, in the limit of thick oxides, which is what we commonly have, we can approximate

$$t_{ox}^2 \approx B(t + \tau) \quad (6.5)$$

Therefore, if a series of oxides are grown in a furnace, the parameters A , B , and τ can be determined and the amount of time required for the growth of any given thickness of oxide can be determined. This applies to both wet and dry oxidation.

Prior to oxidation, an acid etch is performed to remove impurities from the Si wafers, which increases the quality of the oxide. First, the wafer is cleaned of native oxide by etching in 2:1 96% sulfuric acid: 30% hydrogen peroxide for 10 minutes. Then, impurity metals and any remaining native oxide are removed by etching in 50:1 49% hydrofluoric acid: water for 15 seconds. Finally, impurity organics are removed by etching in 6:1:1 water: 37% hydrochloric acid: 30% hydrogen peroxide. Once the oxide is grown, the wafer is diced into 10 x 10 mm chips to be used for devices.

Now, the nanostructure solution is ready to be deposited onto the Si/SiO₂ chips. A 10 x 10 mm Si/SiO₂ chip is placed on a hot plate set to 150°C and the ethanol/nanostructure solution is pipetted onto it. When the liquid evaporates, one is left with the nanostructures on the Si/SiO₂ chip. Due to the small size of the nanostructures and the uniform flatness of the oxide, the structures adhere solely by Van Der Waals forces. **Figure 6.1** shows a cobalt nanowire bundle grown by electrodeposition deposited onto the Si/SiO₂ substrate and CVD grown MWCNTs on the Si/SiO₂.

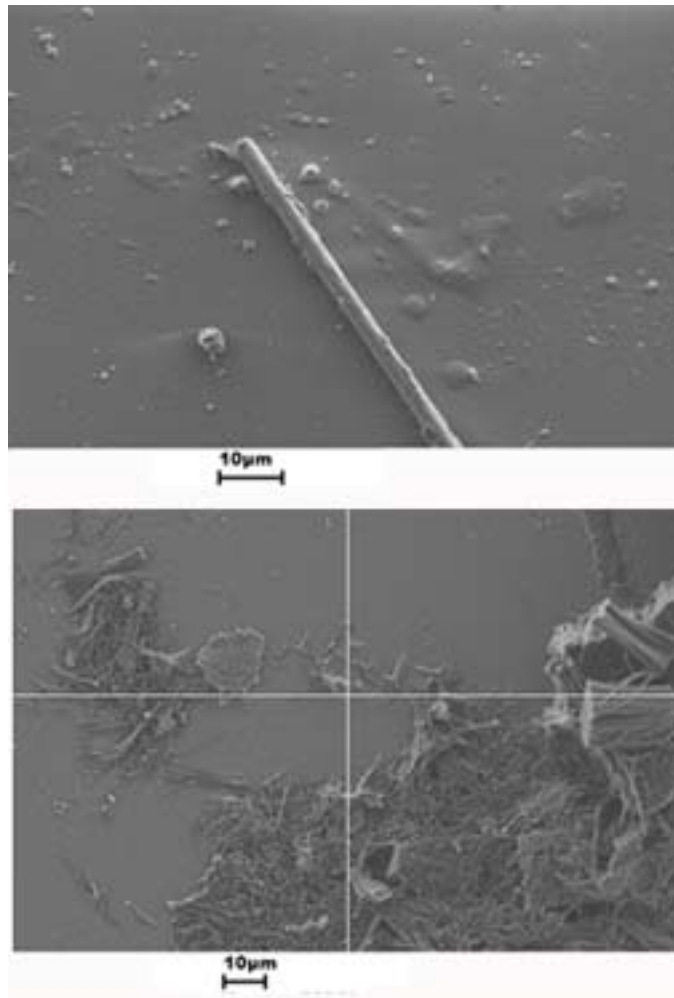


Figure 6.1: Bundle of cobalt nanowires released onto Si/SiO₂ (upper) and a carbon nanotube film released onto Si/SiO₂ (lower).

6.3 Preparation of Graphene Flakes

The deposition and identification of a single layer sheet of graphene on a Si/SiO₂ substrate depends entirely on the unique property of silicon dioxide to absorb light differently when it is a different thickness [105, 106]. In fact, the color of a silicon dioxide surface is so dependent on thickness, that one can guess the thickness within about 50 nm simply by looking at it with the naked eye. **Figure 6.2** displays a color chart as a function of thickness of silicon dioxide.

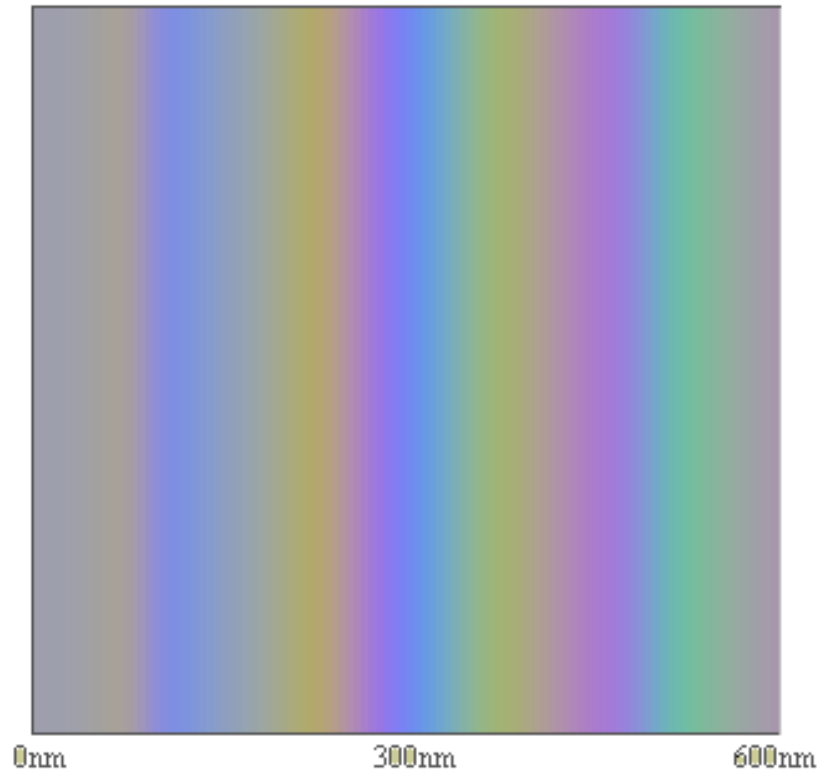


Figure 6.2: Graph of silicon dioxide color vs. thickness at 0 degree angle, or looking straight down onto the oxide [107]. The most used, first three, purple bands are shown: approximately 80-100 nm, 250-290 nm, and 410-490 nm.

It has been found that few-layer to monolayer graphene sheets will exhibit a type of optical interference with a purplish color of silicon dioxide. As we can see in **Figure 6.2**, there are many bands of purple in the spectrum of silicon dioxide. The first three bands are the most suitable for graphene because growing thick layers of oxide takes much longer times, and after the third band, the color begins to dull significantly. The first band is the smallest of the three at approximately 80-100 nm. However, this is the thinnest oxide that can be used for graphene experiments. The second band is the brightest of the three and is at approximately 250-290 nm. This is currently the most commonly used band for graphene device making. Finally, the third band is the widest of the three, second most luminous, and is at approximately 410-490 nm. Because it is

the widest band, it is the most easily obtained. One has greater room for error in thickness here.

To grow the oxide layer, as stated earlier, wet and dry oxidation are used. Dry oxidation is much slower than wet oxidation, but the quality and uniformity of the oxide layer is much greater. Dry oxidation is used to grow thicknesses in the first band. However, it takes far too long to grow thicknesses in the second and third bands, for which wet oxidation is used exclusively.

As stated earlier, the identification of mono-layer graphene is due to an optical interference with a purplish oxide. **Figure 6.3** shows a monolayer graphene sheet on 90 nm of oxide and shows a mono-layer graphene sheet on 480 nm of oxide.

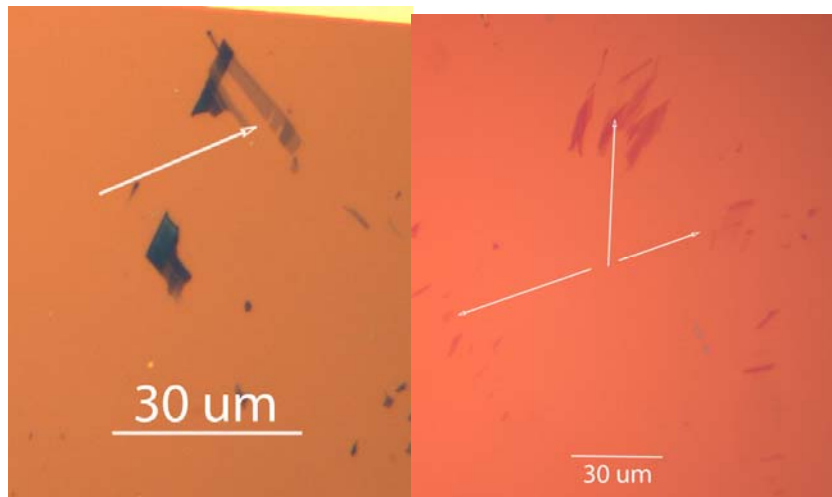




Figure 6.3: (top left) Optical image of monolayer graphene on 90 nm silicon dioxide. The arrow points to the monolayer. (top right) optical image of monolayer graphene on 480 nm silicon dioxide. The arrows point to the monolayers. (bottom) Optical image of a graphene monolayer on 285 nm of oxide.

We can see that graphene looks slightly different on different oxide thicknesses. This is because the 90nm oxide layer is duller and slightly more bluish than the deep purple of the 285 nm or 480 nm oxide layer. Therefore, it becomes obvious that if the oxide layers are not exactly correct, identification of graphene becomes impossible. In fact, once the color of the oxide switches to green, the graphene becomes invisible. The graphene can also be imaged using a scanning electron microscope (SEM). However, using an SEM, one can not distinguish between a monolayer and a multilayer. **Figure 6.4** displays an SEM image showing different graphene layers in a piece of graphite. Here we can see that it is not apparent how thick each layer is.

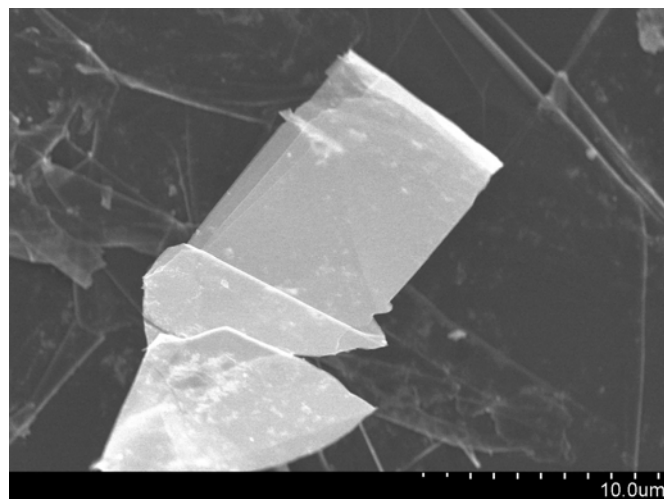


Figure 6.4: SEM image showing graphene layers. It is impossible to determine how thick each layer is.

It was shown in [106], and independently discovered by us, that, actually, 90 nm of oxide is the ideal layer thickness to observe graphene. We made this discovery based on visual trial and error. The group of Blake, et al. use a model based on the Fresnel law to show that this indeed has the greatest optical contrast [106].

However, this visual method may seem to lack some accuracy. Thicknesses of graphene layers can be determined more accurately with atomic force microscopy (AFM) [108]. But, it is difficult to locate a flake in this way, and if the flake is slightly folded or does not sit totally flat on the oxide surface, it can give false results. AFM is also rather time consuming. The most accurate way to determine the thickness of a graphene layer is to use Raman spectroscopy. This was first done by Ferrari, et al. in [109]. **Figure 6.5** displays some Raman spectra of our graphene flakes.

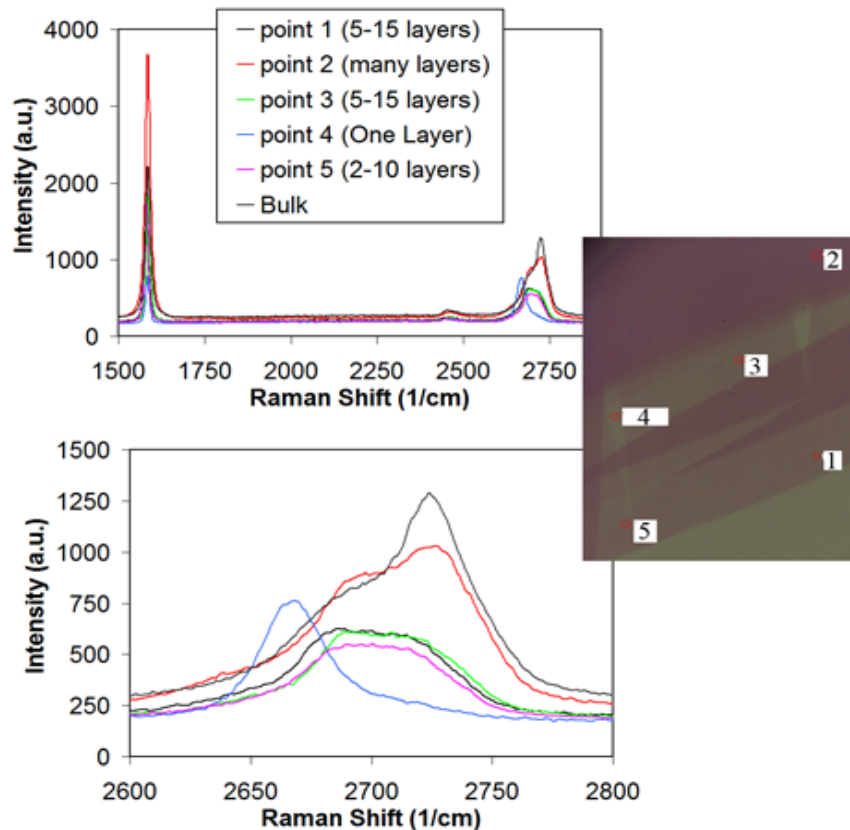


Figure 6.5: Raman spectroscopy of various points on a multiplayer sample of graphene (optical image shown). The bottom image is a close up of the secondary peaks.

In **Figure 6.5**, the identification of various layers was done using the analysis presented in [109]. In [109], they compared their Raman peaks to thicknesses given by AFM to ensure accuracy, and we compare our peaks to theirs. We can see that for bulk graphite (shown in gray) that the first peak is greater in magnitude than the second peak. For many layer graphene, the first peak is very tall, and the secondary peak begins to widen and shrink and develop a plateau-like feature. As the graphene layer get thinner, the first peak remains greater in magnitude, but the second peak continues to shrink and develop the plateau. Finally, for monolayer graphene, the first and second peak have approximately the same magnitude (or even the second peak has a greater magnitude) and the second peak loses the plateau feature and becomes slightly blue-shifted. In

truth, with some practice, the identification of graphene flakes can be done quite accurately with visual methods and then the identification can be supported by Raman spectroscopy.

The most common method of graphene production is by exfoliation, or micromechanical cleaving, from HOPG or its equivalent (for instance, natural graphite), performed by abrading the graphite on a SiO₂ surface to form thin randomly placed flakes of various sizes and shapes. While most flakes are composed of multiple sheets, some are monolayer graphene. First, a piece of clear scotch tape is rubbed, sticky side down, onto a block of HOPG. Then, the tape is lifted off, to reveal a thick carbon film on the sticky side. This film is cleaved by taking a second piece of scotch tape and rubbing it against the first piece. This is done several times. The pieces of tape are then rubbed onto the silicon dioxide surface. This must be done with care, because rubbing too hard will enable glue from the tape to stick to the silicon. This glue is difficult to remove and can be conductive. Van Der Waals forces enable thin graphene sheets on the edges of cracks in the graphite to adhere to the oxide surface. There are usually numerous multi-layered graphene sheets and pieces of graphite on the chip. Graphite will show up as opaque, while thinner multi-layered graphene sheets will be the same color as the substrate, but slightly darker (as previously demonstrated). The monolayers will be the most translucent of all the pieces. They are so translucent that they can barely be seen.

Aside from this method, there are other methods of making flakes. Recently, some groups have been successful in making graphene flakes out of decomposition of epitaxially grown SiC [110]. This technique produces much larger areas of graphene than exfoliation and is more adaptable to technological applications; however, the carrier mobilities in graphene films produced by mechanical exfoliation are usually higher than those produced by epitaxial growth. The cleavage method is the most common and gives

the best results. We attempted several other methods. In one method, we applied photoresist to a wafer and put the HOPG onto the photoresist. This left a thick graphene multiplayer in the photoresist. We then baked the wafer to solidify the photoresist and attempted to cleave the thick graphite layers with tape until there was no visible graphite left. Then, the wafer was placed in acetone to dissolve the photoresist. It was the hope that there would be monolayers remaining in the photoresist after repeated cleaving that would then float in the acetone. We attempted to capture these layers by dipping another wafer into the acetone. This method was entirely unsuccessful.

In another method, we attempted to use an electric field to pull layers off of bulk HOPG and position them onto a wafer. To do this, we placed bulk HOPG onto a chip and applied a large voltage to the bottom of the Si. We also attempted a dielectrophoretic method by first putting contacts on a wafer and applying an AC voltage between the contacts. These methods gave limited success. Very small flakes were occasionally found on the wafers. However, it is unclear whether the success was due to the methods or to random flakes coming off of the bulk HOPG by Van Der Waals forces. This method may, in fact, have a little promise as others are also attempting variations of it. In [111], Sidorov, et al. had some success in peeling monolayers from the bulk using a electrostatic field applied through an STM tip and in transferring monolayers from one point to another on a Si/SiO₂ chip using the same method.

To date, the largest graphene flakes are made by the micromechanical cleavage of HOPG and natural graphite by the company Graphene Industries, Ltd. They are routinely able to make flakes of about 500 μm^2 and have occasionally made flakes larger than 700 μm^2 [112]. However, it can take hundreds of attempts to produce flakes so large. We have been successful at making flakes that are approximately 500 μm^2 . In general, though, our average usable flake size is approximately 100-250 μm^2 .

6.4 Lithography

6.4.1 Photolithography

Photolithography is the fastest of the three lithographic methods used here. In a matter of seconds, hundreds of devices can be made. However, it is also the least accurate of the methods used here. The photolithographic aligner uses an optical microscope to position the lithographic pattern, and this highly limits the ability to place the pattern with pinpoint accuracy. In addition, the smallest feature size one can make is limited by the wavelength of the UV light source used for exposure. In theory, this limit is approximately 300 nm. However, in practice it is difficult to get features smaller than 1 μm to develop properly.

Photolithography is performed in an aligner. **Figure 6.6** shows the Quintel 4000-6 photolithography aligner.



Figure 6.6: Quintel 4000-6 photolithography aligner.

First, a lithography mask must be manufactured. In our case, this is done by creating a pattern in CAD in consultation with the Photronics Corporation, who manufactures the mask. The mask is made of glass with a layer of Cr covering one side. The pattern appears as holes in the Cr.

Next, the wafer on which the lithography is desired is coated with a UV light sensitive photoresist by spinning. When this photoresist is exposed to UV light, it changes its chemical makeup, allowing it to be chemically removed while leaving unexposed areas intact. We use the Shipley series 1800 photoresists. S1813 photoresist will create trenches of approximately 150 nm in height. S1818 photoresist will create trenches of approximately 200 nm in height. Once coated, the photoresist is stable for approximately 2 days, as long it is kept in a light-safe box, after which it is no longer effective. After spin coating at 4000 RPM for 45 seconds, the wafer with photoresist is baked at 115°C for 1 minute and 15 seconds. Next, the wafer is placed in the wafer loading area of the aligner and held down with a vacuum. The mask is placed Cr side down on the mask holding area of the aligner and held with a vacuum. The wafer is then pushed into direct contact with the mask. The dosage of UV exposure must be determined. If too little dosage is given, the pattern will not form completely. If too much exposure is given, the pattern will bleed and become distorted. We find that it is best to experiment with several dosages every time lithography is done. This allows one to adjust the procedure based on the cleanliness of the substrate and any changes to the equipment. In general, the cleaner the substrate, the lower the dose that is necessary. For a dirty substrate, a higher dose is needed to expose the photoresist around the impurity. This makes a difference for whether or not the nanostructures should be placed on the substrate before the lithography, allowing the lithography to place contacts on the nanotubes, or placing the nanostructures on the substrate after the contacts have been made, which allows for a better lithography but not as good contact. **Figure 6.7** shows optical images of some patterns made by photolithography.

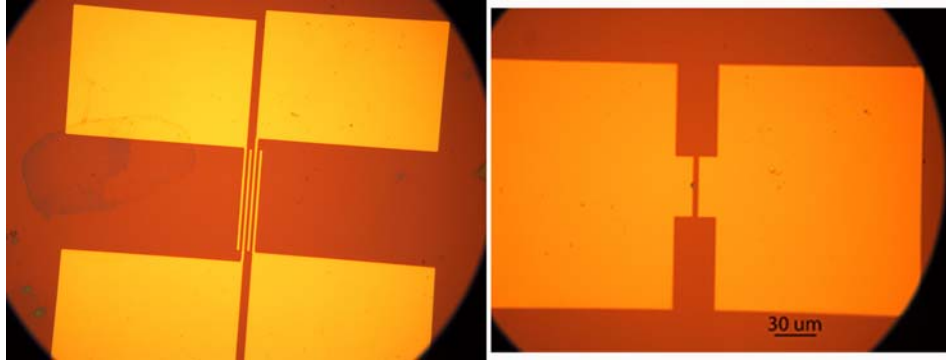


Figure 6.7: Patterns made by photolithography.

After exposure, the wafer is removed and is placed in a bath of MF-319 photo-developer for 40 seconds and is agitated. If too little development time is used, the exposed layer of photoresist will not lift out, making deposition nearly impossible. If too much development time is used, the pattern will overdevelop and fine features will bleed into one another. The MF-319 is then washed off with de-ionized water and the device is ready for deposition.

6.4.2 *Electron Beam Lithography*

Electron beam lithography (EBL) is more accurate than photolithography and it can make smaller features (sub 10 nm). However, it is also much more time consuming. Whereas in photolithography, a single mask can have hundreds of patterns that are all exposed simultaneously, EBL can only expose one pattern at a time. In addition, the amount of time it takes to expose each pattern can be extremely long, depending on the parameters chosen.

Like photolithography, the EBL process begins by coating a wafer with a photoresist. But, for EBL, an electron beam sensitive photoresist must be used. We use PMMA, which is the most commonly used EBL photoresist. PMMA A-950 is diluted by half with anisole, making a 3.5% PMMA solution. This is spun onto a silicon wafer at 5000 RPM for 1 minute, which creates a PMMA layer of approximately 150 nm. The

wafer is then baked at 180°C for 90 seconds to harden the PMMA. This PMMA layer remains stable for a rather long time, up to months, as long it is kept free from dirt and scratches. Next, a CAD program that interfaces with the EBL writing program, Nability, is created to draw the desired patterns. The wafer is placed in the SEM and the electron beam is blanked electromagnetically while the wafer is moved into position. Finally, the Nability program is set to run the CAD file.

There are many parameters to set while doing an EBL write. The success of a write is a function of the beam spot size (beam current), the beam accelerating voltage, the spot center-to-center distance, the raster line spacing, the dosage, and the raster pattern. Setting the parameters will largely depend on the size of the features in the pattern. Once tuned, the SEM column will send a circular shaped electron beam down to the wafer. This beam will raster, line by line, in the pattern described by the CAD file.

Figure 6.8 shows a drawing of a square pattern that has been exposed by an electron beam.

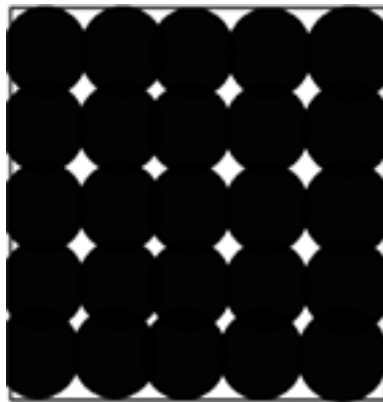


Figure 6.8: Square EBL raster pattern. The black dots represent the exposed area due to the electron beam.

The black spots in **Figure 6.8** represent the exposure from the electron beam. The spot size is determined by setting the beam current. Obviously, if the feature size is large and the spot size is small, it will take far too long to expose an area, or the area will be

underexposed. Likewise, if the spot size is large and the feature size is small, the feature will easily become overexposed. In general, we like to use a beam current of 400 pA for features larger than $25 \mu\text{m}^2$ and a beam current of 40 pA for features $<25 \mu\text{m}^2$. The beam accelerating voltage sets the amount of energy each electron in the beam has when hitting the sample. In general, we use the maximum allowed 30 kV on the Zeiss SUPRA 25 system. However, the greater the energy the electron has, the more unintended exposure of surrounding PMMA occurs. So, if making very fine features, it may be necessary to lower the accelerating voltage. The center-to-center distance determines the horizontal spacing between successive spots in the raster. As can be extrapolated from **Figure 6.8**, if this distance is too large, the resulting raster line will not be straight and the pattern will be underexposed. The smaller the center-to-center distance, the straighter the raster line becomes. However, if the center-to-center distance is too small, then some areas will be doubly exposed, which creates bleeding. Similarly, the line spacing determines the vertical distance between successive raster lines. The success of the write is affected in the same way as the center-to-center distance. If the line spacing is too large, there will be underexposure. If the line spacing is too small, there will be overexposure. In addition to overexposure, if the line spacing and center-to-center distance is not set properly it can result in undercutting. This is when the beam exposes more PMMA closer to the surface of the chip than is exposed higher up, giving trenches that have a profile like an inverted “V.” This is demonstrated in **Figure 6.9**.

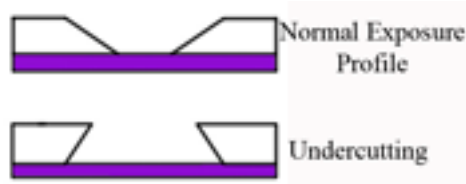


Figure 6.9: The normal exposure pattern is a V shape, although cold development can create a more ideal, vertical trench. If the sample is overexposed, there may be undercutting making an inverted V shape.

It is sometimes advantageous to change the raster pattern to prevent over exposure. One can tell the program to first do small features and then expand to larger features. Finally, the beam dosage must be set. This tells the program how long each spot is exposed to the electron beam. Obviously, if too much dosage is given, the pattern overexposes and bleeds, and, if too little is given, it is under exposed. Ultimately, tests must be run in order to determine the best parameters for each pattern. In general, though, for features larger than $25 \mu\text{m}^2$, we use a line spacing/center-to-center distance of $30 \text{ nm}/30 \text{ nm}$ and a beam dosage of 1.3 nC/cm . For features smaller than $25 \mu\text{m}^2$ we use a line spacing/center to center distance of $10 \text{ nm}/10 \text{ nm}$ and a beam dosage of 0.8 nC/cm . **Figure 6.10** shows an example of a dosage test.

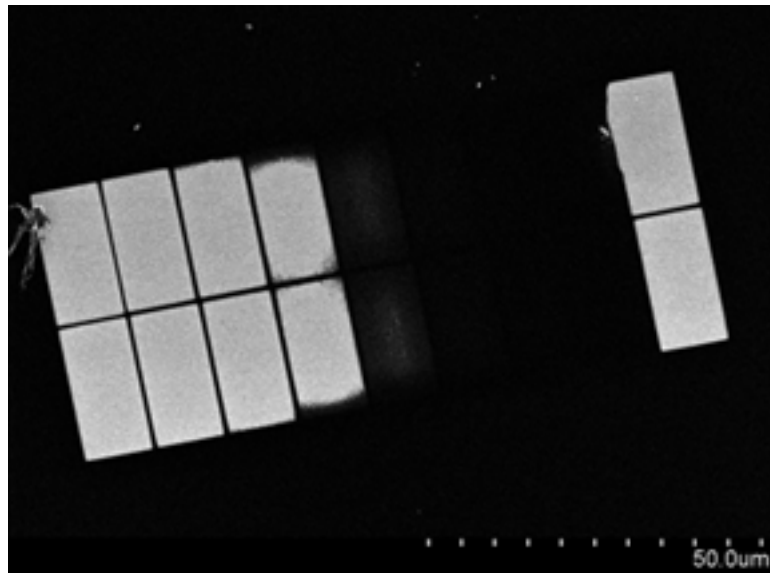


Figure 6.10: EBL dosage test. The patterns on the left exposed properly. The patterns in the middle require a higher dose.

Like in photolithography, patterns generally come out much better when the surface of the substrate is very clean. However, there is much more success, as compared to photolithography, with putting patterns onto already deposited nanostructures. But, putting EBL patterns on substrates containing nanostructures with

EBL presents its own set of problems. Primarily, because the electron beam must be blanked when not writing patterns, one cannot position the chip under the beam visually before writing a pattern. This requires one to very carefully position and map the features of the chip prior to performing the EBL and to very precisely calculate the vector movements to where the nanostructure on which one wishes to write a pattern lives. To accomplish this, it is necessary to put a grid onto the chip before depositing the nanostructures. This is usually done using photolithography. This grid will allow a reference point when locating a nanostructure for lithography.

As shown in **Figure 6.11**, very careful chip positioning is absolutely essential and the closeness of a nanostructure to a reference point is also very important.

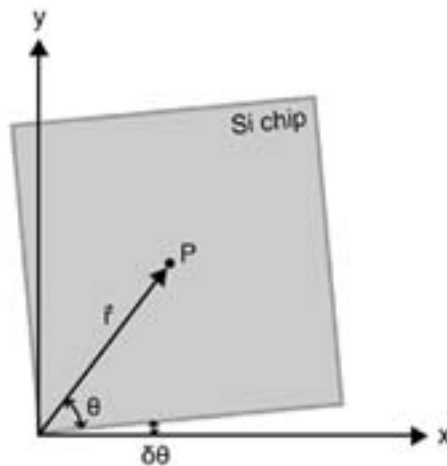


Figure 6.11: Diagram showing how a chip is positioned in the SEM before an EBL write. The reference point is taken to be the edge of the chip. Point P is the location of a desired nanostructure.

The chip will later be removed for an application of photoresist, so it is essential that the exact placement be repeatable. To be more precise, the rotation angle of the chip must be the same. Because the vector between the reference point and the nanostructure is a radial vector, a small deviation in the rotation angle can create a large error in placement of contacts at distances away from the corner, as movement vectors are calculated using

x - y plane vectors by the EBL program. A point P on the chip can be described in polar coordinates by (r, θ) . In the x - y frame of the SEM stage, there will be a small rotation $\delta\theta$ relative to the chip. When locating P in the x - y frame it is thus necessary to minimize $\delta\theta$ by manual rotations. This ensures that a coordinate (r, θ) in the x - y frame yields the point P . This is explained diagrammatically in **Figure 6.11**. Usually, $\delta\theta$ can be minimized to within an accuracy of the polar coordinate $y = r \sin(\delta\theta)$, at a distance of 10 mm, to ≤ 100 nm. Or, we can minimize the angle between the x -axis and the chip edge to be about $\leq 5.73 \times 10^{-4}$ degrees. So, the closer the nanostructure is to the reference point, the less error enters in movement. The coordinates of a reference point on chip are recorded, and the placements of the desired nanostructures are recorded. Then, by using simple vector subtraction, the nanostructure placement in reference to the corner is calculated. Also, there is a small error of stage movement in the SEM. This can be as small as 1 μm and as large as 10 μm , depending on when the SEM was last serviced. But, overall, if positioned properly, there is an approximately 60% success rate in placing a pattern on a nanostructure. **Figure 6.12** shows an angled SEM image of a pattern placed onto a carbon nanotube.

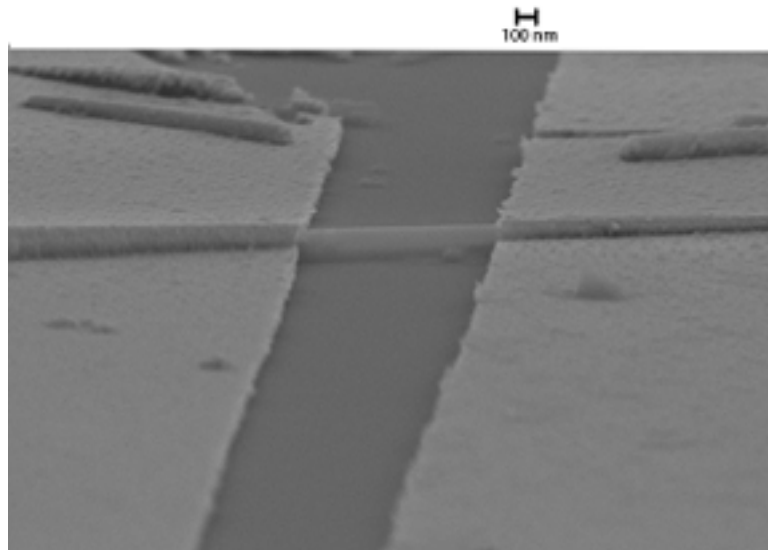


Figure 6.12: Angled SEM image of contacts placed onto a carbon nanotube by EBL.

After the write is over, the chip is removed from the SEM chamber and developed. For development, the chip is placed in a 3:1 mixture of MIBK: IPA for 70 seconds. This is followed by a rinse in IPA for 20 seconds and then a rinse in de-ionized water. For better results, the development can be done with the developers cooled to 5°C. PMMA is a polymer. As such, parts of a long molecular chain can be exposed by the electron beam while leaving other areas of a chain unexposed. Due to thermal energy that exists at room temperature, the unexposed area of the chain can be ripped out when the exposed area is developed, leaving lithographically defined trenches that are not completely vertical. However, by performing lower temperature development, the unexposed areas of the chain are frozen in place, which allows the development of only the exposed areas and results in much more vertical trenches.

To date, the only successful method of placing working electrical contacts on to graphene monolayers has been accomplished by EBL, even though other methods have been attempted (photolithography by [112], FIB by us). Because of the relatively large size of graphene flakes, movement error is not as much of a problem as with smaller

nanostructures like CNTs. But, graphene has the problem of rolling up and changing positions during spinning of photoresist. Approximately 90% of our graphene flakes become ruined during the spinning process. To limit this, we can anneal the flakes on the wafers on a hot plate at 180°C for a half hour prior to spinning and also ramp up to 5000 RPM very slowly while spinning. This has increased our sample viability to approximately 50% of the samples survive coating and spinning. This issue has also been noticed by other groups and they also share our success rates [112]. Also, it is incredibly difficult to see the graphene when mapping out the chip with the SEM prior to the EBL write. This makes positioning difficult. **Figure 6.13** shows graphene monolayers with contacts placed by EBL. The device on the right shows has a yellow outline where part of the monolayer rolled up during processing.

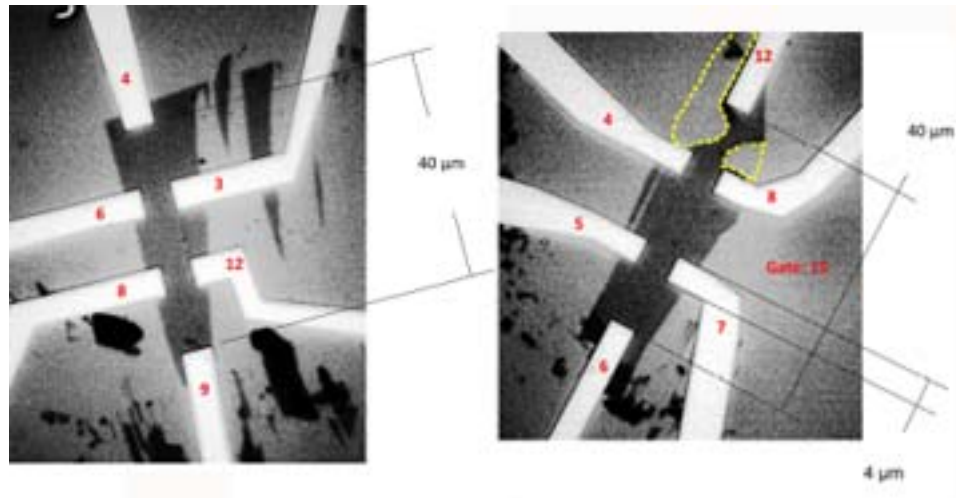


Figure 6.13: Graphene devices prepared by EBL. The yellow dotted lines on the right hand device show where the graphene has rolled up during processing.

6.4.3 Focused Ion Beam Lithography

Focused ion beam lithography (FIB) is the most precise and also the cleanest of the lithographic methods, as it uses no photoresists and one can look directly at the

sample with SEM while performing the lithography. But, it is also the slowest of the methods. It can take days and multiple sessions to completely write a pattern.

Figure 6.14 shows a diagram of the FIB chamber. In our case we use an FEI dual beam system.

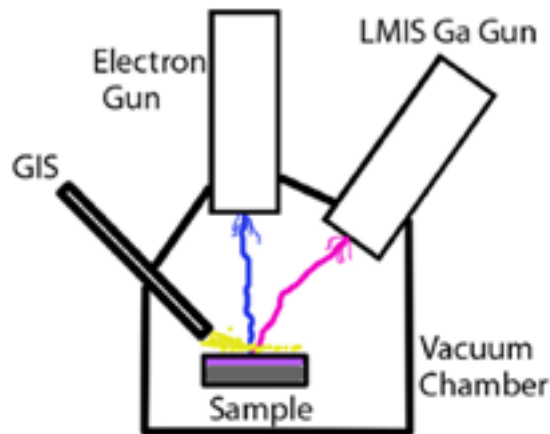


Figure 6.14: Schematic of the FIB system.

The sample is placed in the chamber and the desired area is located with the electron beam using SEM. The area is again viewed using a liquid metal ion source (LMIS) Ga gun by ion beam microscopy. The Ga ion gun is located at a 42 degree angle from the electron gun. So, the sample must be positioned at the eucentric height such that the ion beam and electron beam are focused on the same area of the chip. The gas insertion system (GIS) tube is lowered into the system and gas is spread over the surface of the sample. The gas contains the desired deposition constituents. This is usually W or Pt. The metal gases are either Methylcyclopentadienyl platinum trimethyl for Pt deposition or Tungsten Hexacarbonyl for W deposition. A pattern is then drawn onto the sample using a program supplied by FEI and the ion beam is allowed to raster inside the pattern. This decomposes the metal gas into the metal, which is deposited onto the

surface of the chip, and into some volatile components, which are swept away from the sample by the FIB scope vacuum.

As in EBL, the line spacing, center-to-center distance, and spot size must be determined. These all have the same effect in EBL. But, more importantly, the dosage and accelerating voltage must be determined very carefully. Because we are bombarding the sample with metallic ions, a dosage and voltage (energy) that is too great will harm the sample and actually etch into the substrate. During FIB there are two competing processes: sputtering and etching. Sputtering deposits metal onto the surface and etching knocks atoms away from the surface by bombardment. For a deposition to work properly the sputter rate must be larger than the etch rate. This can be done by setting an appropriate dosage and accelerating voltage.

In addition, deposition can also be accomplished by decomposing the GIS gases using the electron beam. This is good for delicate samples because it does much less damage than the ion beam, but the process is substantially slower. It can take 10 hours to deposit a $10 \times 10 \times 0.05 \mu\text{m}$ line as opposed to approximately 30 minutes for the same ion beam process. **Figure 6.15** shows devices made from FIB for graphene and CNTs.

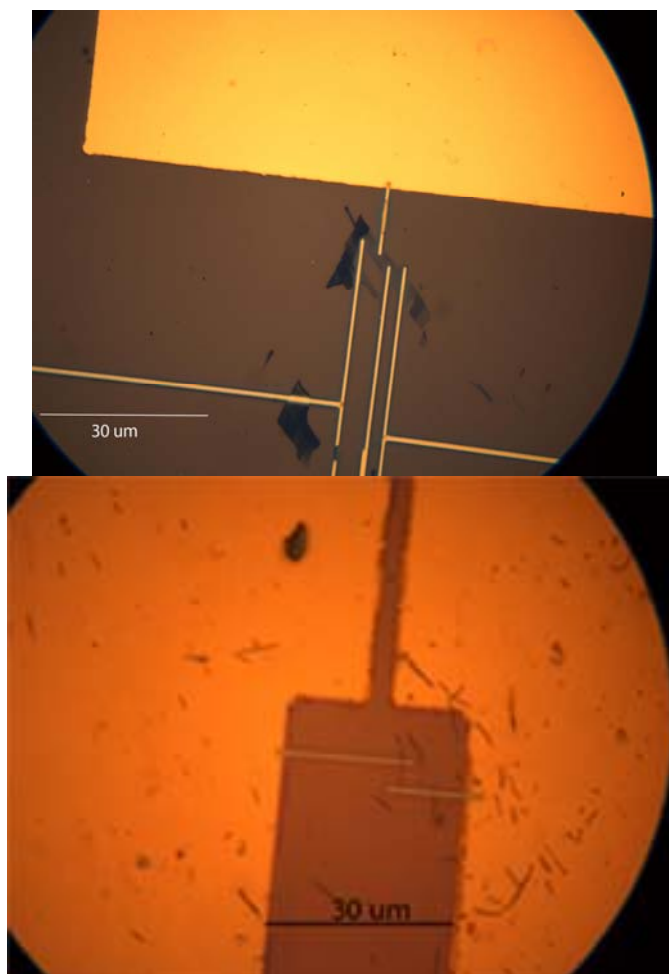


Figure 6.15: Photolithography/FIB devices with Pt wires. The upper image shows a graphene monolayer attached to photolithographically defined Cr/Au contact pads with FIB wires. The bottom image shows a carbon nanotube attached to photolithographically defined Cr/Au contact pads with FIB wires.

The FIB method is not without its flaws. Due to the deposited metal coming from a decomposed gas, it contains many impurities. This greatly reduces the conductivity of the wires. The resistivity of Pt and W wires has been quoted as 70-700 $\mu\Omega\text{-cm}$ and 150-225 $\mu\Omega\text{-cm}$, respectively [113]. This means that the resistance of a 100 μm long, 40 nm high, 1 μm wide wire is 17500 Ω at the worst quoted theoretical value. This increases significantly with length. If the resistivity is worse than the quoted value, this contact resistance can be a major hindrance to the ability to take good measurements with the

device. The contact resistance can, obviously, be decreased significantly by making the wires thicker and wider. However, it was noted in [114] that this is only good up until a certain height, quoted as 200 nm for W. And, this often takes way too long to be feasible. In practice, we found that the FIB drawn wires had resistances far too large to be of use in our experiments.

6.5 Plasma Etching

From **Figure 6.8**, it can be seen that due to the circular beam pattern, there can be certain areas of an exposed chip during an EBL write that are not as exposed as others. This can, after development, result in small dots of photoresist left on the chip, which will highly affect the ability of metal to adhere to the surface during a metal deposition. Likewise, with photolithography, there is always a small amount of photoresist related dirt that covers the bottom of the lithographically defined trenches that affects the adhesion of deposited metal. A way to remove this dirt is by plasma etching in a reactive ion etcher (RIE). This increases adhesion by 100%.

Figure 6.16 shows a picture of the South Bay Technologies RIE-2000.



Figure 6.16: South Bay Technologies RIE-2000 reactive ion etcher.

The RIE etcher allows the post-lithography cleaning of the samples to prepare them for metal deposition. To do this, the patterned chips are placed in the RIE. The RIE creates

plasma from a chosen gas and the sample is bombarded with ions for a set amount of time. For the etching of photoresist, which is organic, the best two gases to use are oxygen and argon. However, because oxygen reacts chemically with the organic photoresist, the etching rates are far too high to use for regular cleaning. In general, we require a slow, controllable etch rate to remove no more than 10 nm of photoresist from the surface of the chip. If too much resist is removed, the deposition of metals will not work properly. **Figure 6.17** shows etch rates for PMMA and S1813 for Ar etching, which is the preferred etching gas.

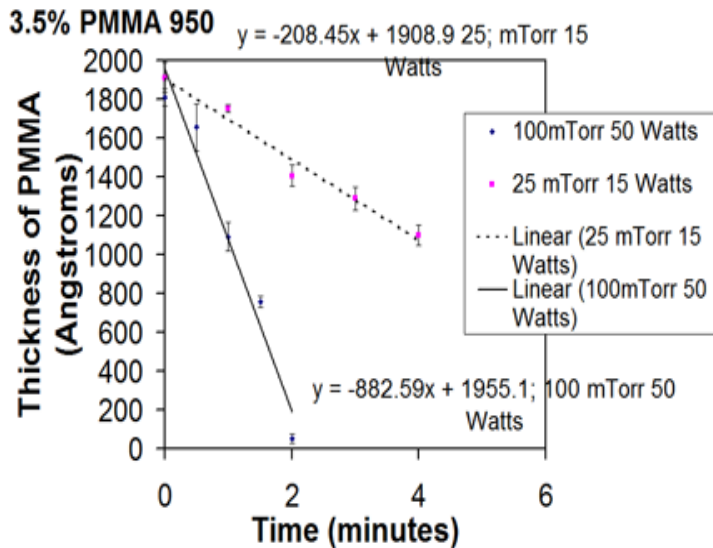
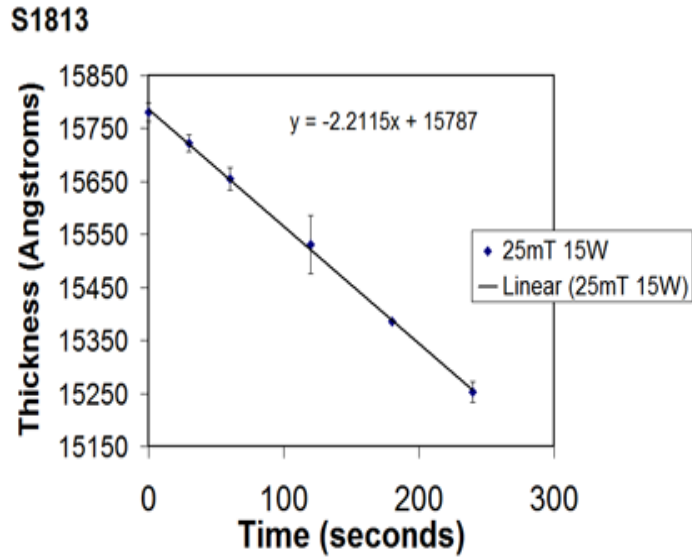


Figure 6.17: RIE calibrations for PMMA and S1813 photoresist. Thickness of photoresist was measured using a Nano-spec 200 microscope given the indices of refraction of the photoresists.

If there are nanostructures present on the sample during the etching, they will usually be unharmed because the coating of photoresist will protect them.

In addition to cleaning, oxygen plasma can be used to pattern graphene flakes into shapes for devices. **Figure 6.18** shows such a device that has been patterned.

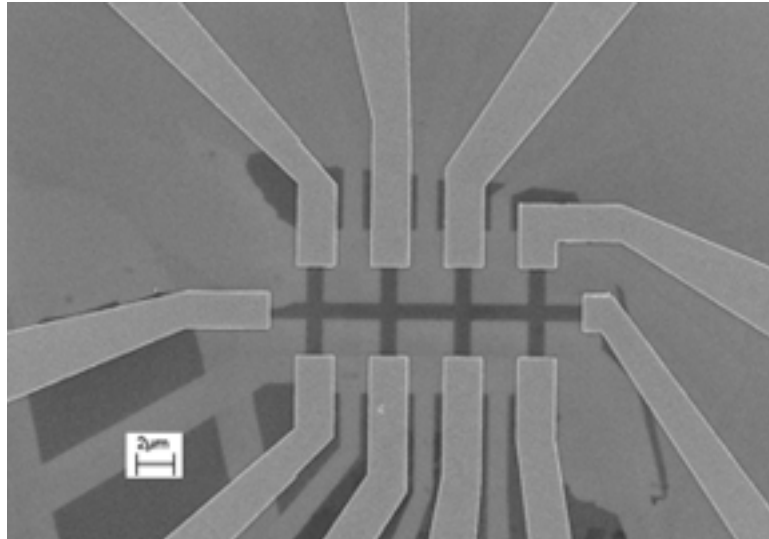


Figure 6.18: Graphene flake contacted by EBL defined contacts and patterned by oxygen plasma etching.

In order to make the patterned design, the chip is coated with a positive photoresist, or a photoresist that when exposed by the electron beam, stays in place while the photoresist around it washes off in acetone. This can be done with the photoresist NEB or by exposing S1800 series resists to a high dosage of the electron beam, which chars the pattern into the photoresist. The sample is then etched in oxygen plasma, which removes the graphene except for that under the mask pattern. The mask is then removed by chemical methods leaving a patterned graphene device.

6.6 Deposition Techniques

Deposition is an extremely important step in the device fabrication process. The correct metals must be chosen and if the process is done incorrectly, adhesion will be bad and the sample will have to be discarded, wasting hours of work. For a contact metal, the most commonly used are Pt, Au, W, and Al due to their good conductivities and their slowness to oxidize in air. But, most of these metals do not adhere well to silicon dioxide, which makes the use of a “sticking” metal necessary. A very small amount of a

sticking metal is deposited on the substrate prior to the contact metal deposition. The most commonly used sticking metals are Ti and Cr. However, because Ti and Cr oxidize quickly in air, the deposition of the contact metal and sticking metal must be done at the same time and under vacuum. For all of our devices, we use Cr as the sticking metal and Au as the contact metal due to their ease of procurement and the capabilities of the equipment. Usually, we use a Cr/Au ratio of approximately 5 nm/50 nm, but this can sometimes depend on the deposition method. We use three primary techniques for the deposition of metals into the lithographically defined patterns: sputtering, thermal evaporation, and electron beam evaporation. Here, each one is discussed along with its advantages and disadvantages. In addition we also discuss the post deposition lift-off of excess metal and remaining photoresist.

First, sputtering is a process where metal is deposited by plasma. **Figure 6.19** shows a diagram of the sputtering process. The substrate is placed in a vacuum chamber away from a target. The target is bombarded by argon plasma which knocks out individual metal ions from the target, which in turn deposit themselves on the substrate.

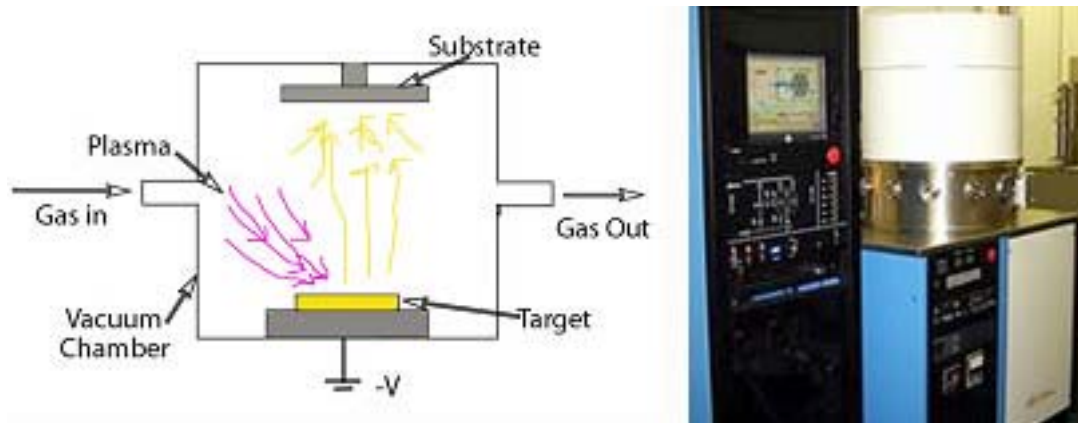


Figure 6.19: Schematic of the sputtering process and picture of the MRC 8667 sputtering system.

Because the deposition is done by plasma, one can perform a sputter-etch process prior to deposition. This has the advantage of making the RIE cleaning step of the fabrication process unnecessary. In fact, sputtering will give the best metal adhesion of all of the deposition methods.

However, sputtering has many major disadvantages. First, it is the most time consuming of the processes. It must be done at extremely low vacuum and it is therefore necessary to pump out the chamber for over 6 hours. In addition, because the deposition is done by plasma, the metal will deposit everywhere in the sample. Referring to **Figure 6.9**, one can see how this can become a problem if the lithographically defined trenches are not perfectly straight. The metal in the trenches will connect to the excess metal on the top of the chip, which makes lift-off very difficult. In general to perform lift-off on a sputtered chip, the sample must sit in acetone for about 4 days. After that, it needs to be sonicated or sprayed with an acetone-nitrogen brush to remove the extra metal. If one has pre-placed nanostructures on the chip with the contacts on top of the nanostructures, this lift-off will remove the nanostructures and ruin the devices. But, if this is not done, lift-off will not occur at all. **Figure 6.20** shows a sputtered pattern where lift-off did not occur.

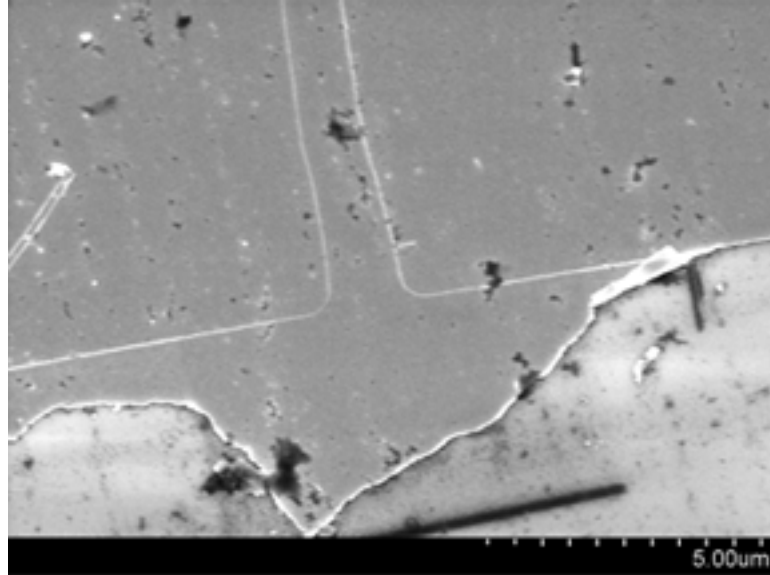


Figure 6.20: Device created by sputtering where lift off did not occur. One can see the gap between two deposited electrodes that remains covered in excess metal even after lift-off.

Also, due to the same lift-off problem, sputtering cannot resolve small features. Either lift-off will not occur, or the features will be ruined by excess sonicating or brushing. But, if the features on the chip are large and there are no nanostructures on it, then sputtering provides a very good way to produce large amounts of very well-adhering devices.

Unlike sputtering, thermal evaporation is a line of sight process. This means that metal is not deposited everywhere and only deposits in the line of sight from the source to the sample. So, lift-off occurs much more easily. Usually, lift-off will occur by placing the chip in acetone for about 10 minutes while heating the acetone slightly and agitating the sample. Some small amount of sonication or acetone-nitrogen brushing may be necessary. But, in general, it is a much gentler lift-off procedure.

The thermal evaporation set-up is pictured in **Figure 6.21**.

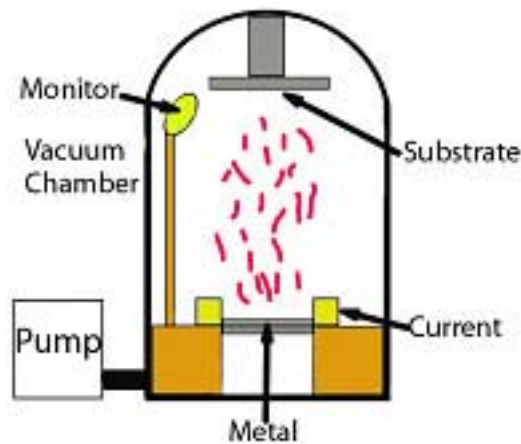


Figure 6.21: Schematic of a thermal evaporator and picture of the Sharon Vacuum custom thermal evaporation system.

The entire process is done at vacuum inside a bell jar. The sample is placed upside down above the source. The deposition metal sits on a tungsten boat in between two current contacts. A quartz crystal monitor is used to monitor the deposition. As current is applied to the metal, it heats up and melts, evaporating onto the substrate. Cr, however, has a very high melting point, and is not deposited by melting and evaporation. Rather, at low pressures, it will sublime and deposit onto the substrate. Cr has a boiling point of about 900 °C at a vapor pressure of 10^{-6} Torr, the common deposition pressure, compared to its usual melting point of 1907 °C [115]. For comparison, Au deposits at approximately 1064 °C [115].

The adhesion of thermally deposited metal is the worst of all the three methods. This is most likely because the vacuum pressure is the highest of all three and the metal particle size is the largest. Rather than deposit a smooth film of metal, thermal evaporation deposits chunks of nanometer to micron size particles. Also, thermal evaporation uses up a very large amount of material, making it very expensive to deposit gold. The entire bell jar is covered with the same amount of metal that is deposited on

the substrate. But, the thermal evaporation method is also very fast and is very well suited to trial and error fabrication.

The third, and usually the best, method of deposition is electron beam evaporation. Unlike sputtering, and like thermal evaporation, the deposition is line of sight. The particle size is also much smaller than in thermal evaporation, leading to a much smoother and more uniform deposited layer, which greatly enhances adhesion over thermal evaporation. But, plasma cleaning is still necessary to ensure proper adhesion. And, the source metal is heated very locally, which greatly saves in expense and wasted metal. **Figure 6.22** shows a drawing of a thermal evaporator.

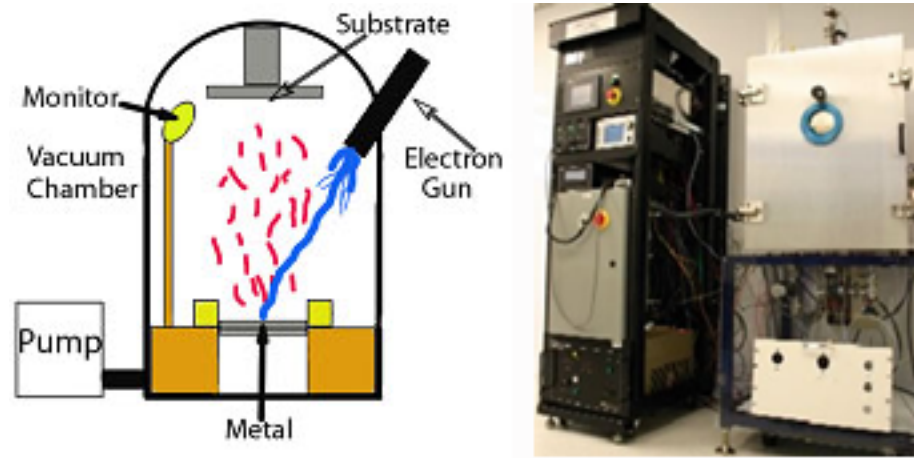


Figure 6.22: Schematic of an electron beam evaporator and picture of Kostas Center custom electron beam evaporation system.

The sample is placed upside down, directly above the source metal in the vacuum chamber. The chamber is pumped for approximately 30 minutes to a pressure of 10^{-7} Torr. The source metal sits in a graphite crucible surrounded by a water-cooled copper holder. This prevents the deposition of any impurities from elsewhere in the chamber. A high powered electron beam is used to locally melt and evaporate the metals onto the

substrate. Like in thermal evaporation, Cr is sublimated at a temperature lower than its melting point.

The lift off procedure for electron beam evaporation is by far the most gentle and easiest of all the deposition methods. The sample is simply placed in a bath of either acetone or 1165 (a common chemical developer) and simply agitated for several minutes. This is usually successful in removing all of the excess metal. But, sometimes, a 1 second sonication is necessary. However, this sonication must be done very carefully if nanostructures have been pre-placed onto the substrate so as to not remove them accidentally. **Figure 6.23** shows a device where Cr/Au contacts were placed on CNTs and the sonication ruined the device.

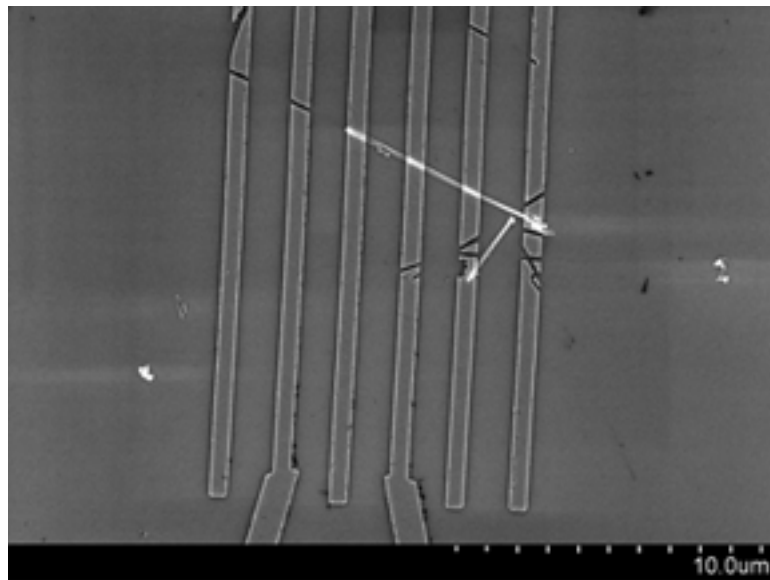


Figure 6.23: CNT device where sonication has destroyed part of the device. One can see that part of the nanotube has broken off, leaving holes in the contacts and other nearby nanotubes have become dislodged, leaving holes in the contacts and rendering the device useless for electrical measurements.

For all of the deposition methods, there is a limit in the amount of metal that can be deposited into the lithographically defined mask that is strongly related to the height of the mask before lift-off becomes impossible. For sputtering, the general rule is that

the height of deposited metal can be $\leq 1/3$ of the height of the mask. So, for a mask height of 150 nm, the most metal that can be deposited is 50 nm. For thermal evaporation and electron beam evaporation, the general rule is that the height of deposited metal can be $\leq 1/2$ of the height of the mask. So, for a mask height of 150 nm, the maximum height of metal that can be deposited is 75 nm. Although, in practice, most of the time, the most metal that is deposited in a mask is about 20 nm less than the maximum value to account for any errors in measurement. If the amount of deposited metal is just slightly higher than the maximum, lift-off will not occur properly and hours will have been wasted on a useless device.

6.7 Other Treatments

6.7.1 Lowering Contact Resistances of CNT Devices

Carbon nanotube devices often suffer from contact resistances that are far too large to enable electrical measurements. In our case, we measured the untreated two probe contact resistances to range from 1-100 M Ω . The primary cause of this high contact resistance is poor physical contact of the tube to the electrical contacts. In general, contact resistance is inversely proportional to area of physical contact as long as the physical contacts are large (so as to negate reflection as a cause). The more physical contact that the nanotube makes with the electrical contacts, the lower the contact resistance will be. There are two places where this comes into concern. First, an amorphous carbon layer on the outside of the tube prevents adequate contact with the polycrystalline walls of the nanotube (see **Figure 3.21**). Second, because our nanotubes are so large, relatively speaking (for most experiments, we use tubes that are about 65 nm in diameter rather than the more common sub-25 nm diameter tubes used in previous experiments), a default 50 nm layer of metal will not cover the entire tube and also metal deposition will not be deposited on the underside of the tube, making the

physical area of contact to the metal only a fraction of the surface area of the nanotube itself. There are many methods that one can use to lower these contact resistance. We discuss two such methods that have proven to be successful: electron beam soldering and pre-annealing.

The electron beam soldering method was pioneered by the group of Bachtold, et al. in [116]. They created CNT devices where they first fashioned electrical contacts on Si/SiO₂ and then placed a drop of CNT containing solution onto the contacts. When the liquid dried, the CNTs were randomly placed across the contacts. They chose suitable devices where only a couple of CNTs bridged the contacts. They noticed that by slowly scanning the CNTs locally at the point of physical contact to the electrical contacts they could drastically lower contact resistances by multiple orders of magnitude. They do not offer an explanation as to why the method works, except that they electron beam may be “soldering” the CNTs in place by slightly melting the metal around the tube and reforming it in more closely contacting way. However, the exact reason for the method’s success is more likely due to a combination of this “soldering” and also beam introduced defects into the tube. When a high powered electron beam hits a CNT, it causes defects in the graphene layers. These defects at the area of contact would increase the surface area of the CNT and thus increase the area of contact and lower the contact resistance.

Figure 6.24 shows 2-probe V-I curves of a carbon nanotube before and after electron beam soldering.

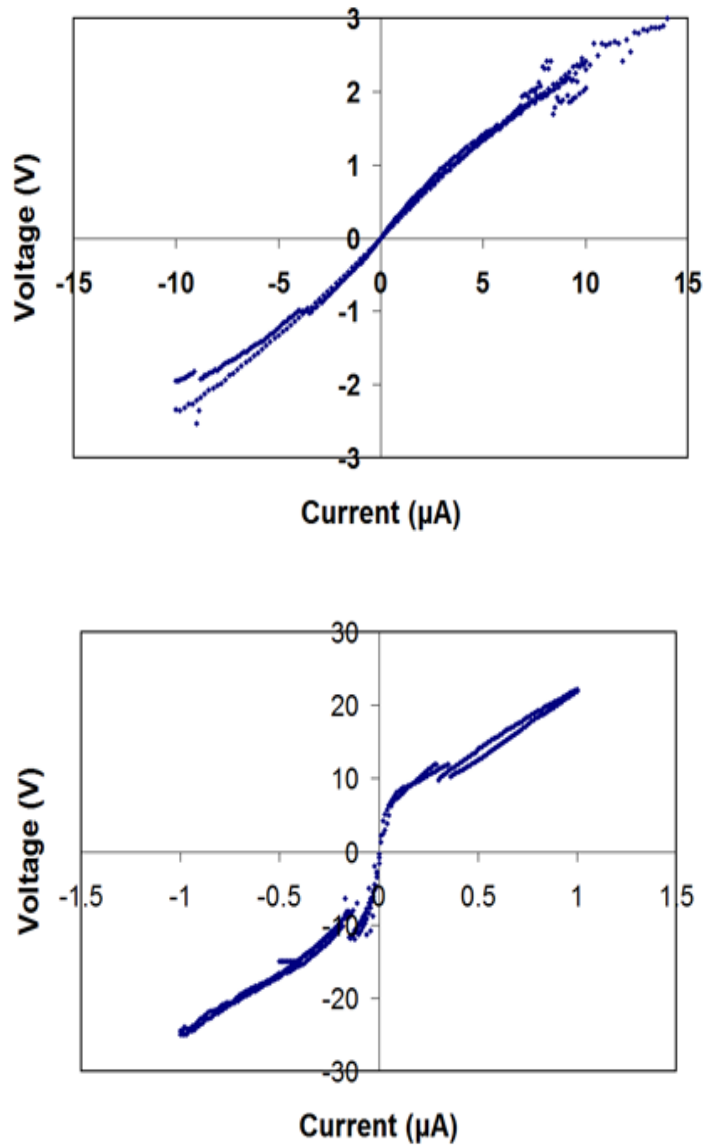


Figure 6.24: (upper) V-I curve of a CNT device before electron beam soldering. The contact resistance is approximately 4 MΩ. (lower) V-I curve of a CNT device after electron beam soldering 700 pA for 10 minutes. The contact resistance is 40 kΩ. For both graphs the current was up, then down, then up again.

We can see from **Figure 6.24** that electron beam soldering lowered the contact resistance by about 3 orders of magnitude. However, our success rates were quite low.

Despite the high success rate of Bachtold, et al., [117], we were only successful about 5%

of the time. And, the method is quite time consuming, as it requires constant monitoring of the SEM while soldering.

A better method for lowering contact resistance, and the method that we chose to use for the experiments in this thesis is the pre-annealing method. It has been found that annealing can lower the contact resistances of carbon nanotubes [118]. Although the exact mechanism for this is still unknown, it most likely has to do with the removal of the amorphous outer layer of the nanotube, which would enable direct physical contact between the electron transporting walls of the nanotube with the electrical contacts. However, if high annealing temperatures are used (>1100 °C), increased conductivity can be due to enhanced graphitization and ordering in the CNT.

To perform this method, CNTs are placed onto the substrate prior to lithography. In the past, researchers have primarily used rapid thermal annealing to anneal then anneal the nanotubes on the substrate [119]. However, we found that this is not necessary and that ordinary annealing also has the same effect. The nanotubes must be annealed in an oxygenless environment. We tried two such environments: first with H_2/Ar and second, with Ar alone. Annealing was done at 800 °C for 2 hours at 100 mTorr. Below this temperature, we did not find any enhanced conductivity. **Figure 6.25** shows V-I curves for un-annealed and annealed CNT devices. For the un-annealed device, the nanotubes were placed on the substrate prior to lithography as well.

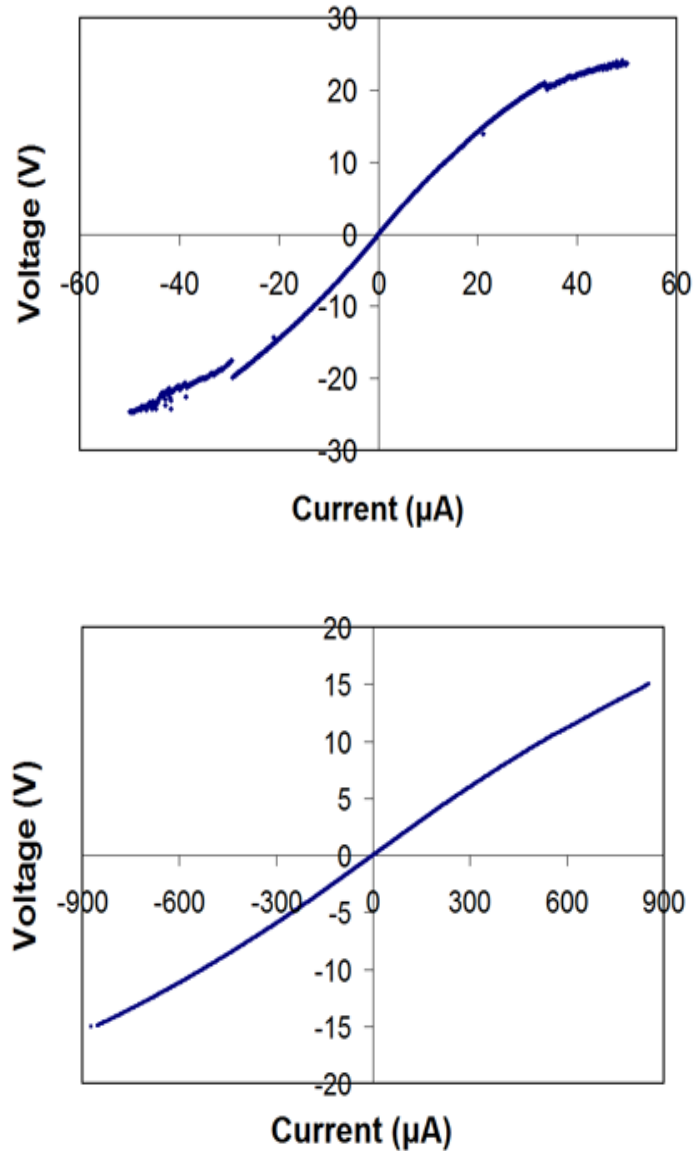


Figure 6.25: (upper) V-I curve for un-annealed CNT device. The contact resistance is approximately $1\text{ M}\Omega$. (lower) V-I curve for an annealed CNT device. The contact resistance is approximately $10\text{ k}\Omega$.

As seen in **Figure 6.25**, annealing also lowers contact resistances by approximately 3 orders of magnitude. However, because it does not induce defects, the V-I curve is much more stable. After annealing, the samples have lowered contact resistances indefinitely. In addition, annealing at $800\text{ }^\circ\text{C}$ has a negligible effect on the crystal structure of the carbon nanotube. **Figure 6.26** shows TEM images of the walls of nanotubes after

annealing. We can see that there is no difference at all, with all of the nanotubes remaining polycrystalline, and increased graphitization does not occur.

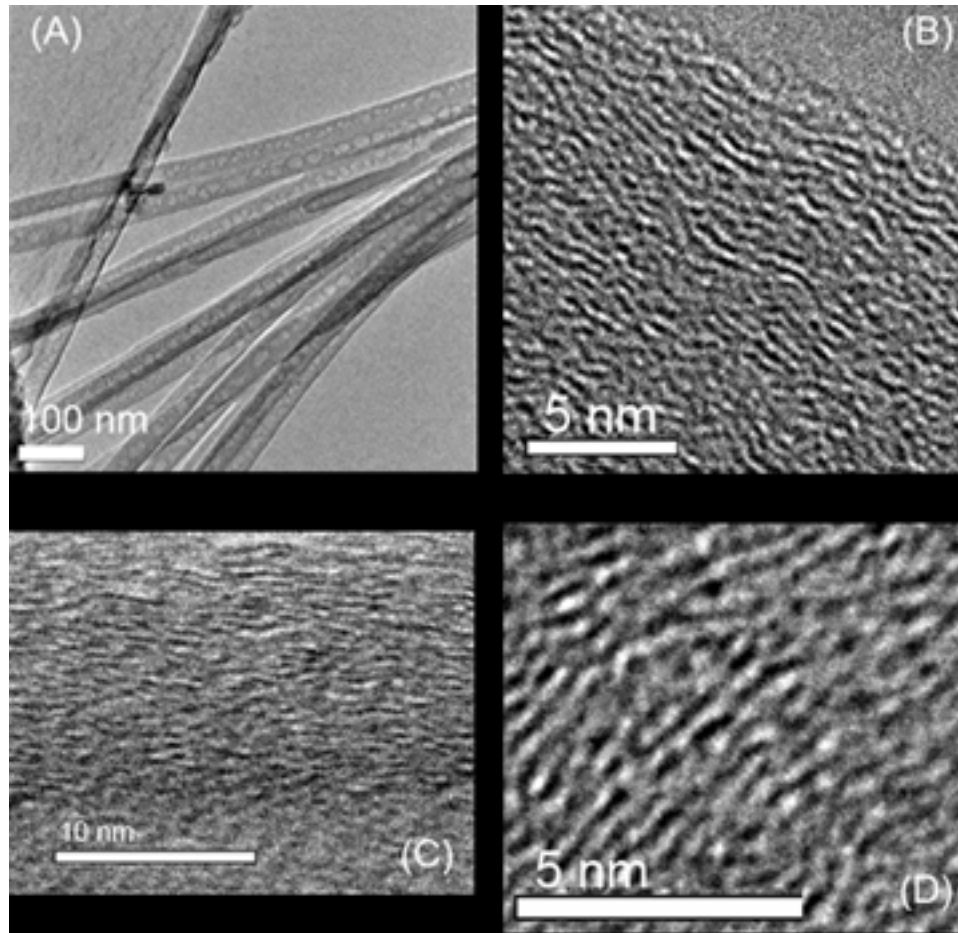


Figure 6.26: TEM images of nanotubes A) A bundle of tubes B) the walls of unannealed tubes, C) the walls of tubes annealed in H₂/Ar at 800 °C for 2 hours, and D) the walls of tubes annealed in Ar only at 800 °C for 2 hours. For all annealed images, CNTs were annealed on top of TEM grids.

6.7.2 Dielectrophoresis

When placing CNTs on top of pre-made electrical contacts, one relies solely on chance for getting them positioned between contacts. However, there is a method that allows for the sure positioning of the CNTs between the contacts: dielectrophoresis [120]. To perform this method, an AC voltage is applied between the two contacts where one wishes to align the carbon nanotubes. A drop of nanotubes in solution is placed on

the contacts while the AC voltage is applied. The AC voltage creates an AC electric field. This induces a torque on the carbon nanotubes given by

$$T = \frac{\pi r^2 l}{2} \varepsilon_1 \frac{(\varepsilon_2 - \varepsilon_1)^2}{[\varepsilon_1 + (\varepsilon_2 - \varepsilon_1)L_{\parallel}](\varepsilon_2 - \varepsilon_1)} E^2 \sin 2\theta. \quad (6.6)$$

Here, L_{\parallel} is a depolarization factor, ε_1 and ε_2 are the dielectric constants of the CNTs and the solution solvent, r and l are the radius and length of the CNT, E is the electric field, and θ is the from the CNT to the electric field. The force applied to the CNT, given by the cross product of the dipole moment of the CNT and the electric field is given by:

$$\mathbf{F} = \frac{\pi r^2 l}{2} \left[\frac{(\varepsilon_2 - \varepsilon_1)}{1 + \left(\frac{\varepsilon_2 - \varepsilon_1}{\varepsilon_1} \right)} \right] \nabla E^2. \quad (6.7)$$

This torque and force align and deposit the nanotubes between the contacts. When the liquid evaporates, one is left with a well aligned CNT device. The amount of CNTs that deposit between the contacts can be controlled by changing the strength of the electric field, or, by changing the magnitude and frequency of the applied AC voltage. Also increasing the amount of time increases the amount of deposited, aligned CNTs. **Figure 6.27** gives an example of this aligned deposition.

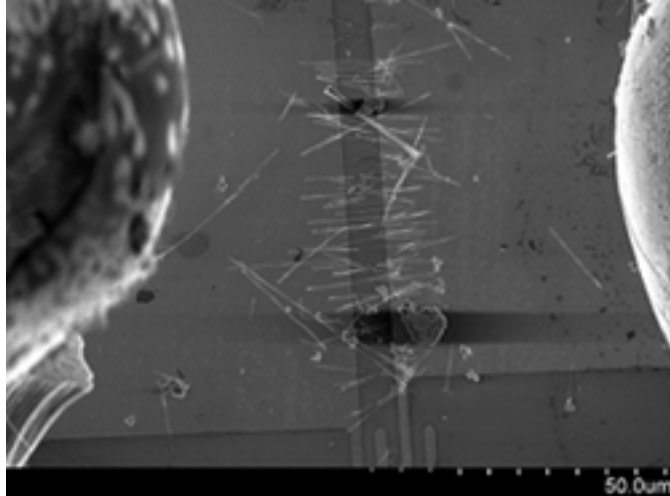


Figure 6.27: Carbon nanotubes deposited and aligned between two contacts by the dielectrophoresis method. An AC voltage of 10 V peak to peak and 100 kHz was applied for 1 minute.

6.7.3 Graphene annealing

Before measuring from graphene devices, it is necessary to anneal them in order to clean them of adsorbed water molecules from the air [108]. Without annealing, the electronic properties of the device will not display regular and smooth characteristics. The preferred method of annealing is in H_2/Ar atmosphere. However, the annealing must be done immediately before the device is used in an experiment because of the speed in which graphene adsorbs water molecules. H_2 annealing at high enough temperatures can ruin the electrical contacts of the device, rendering it useless. So, the correct annealing conditions must be determined. We chose to fix the H_2/Ar to a 1:1 mixture and the annealing pressure at 100 mT due to ease of use. **Figure 6.28** shows the results of testing to find a suitable annealing temperature.

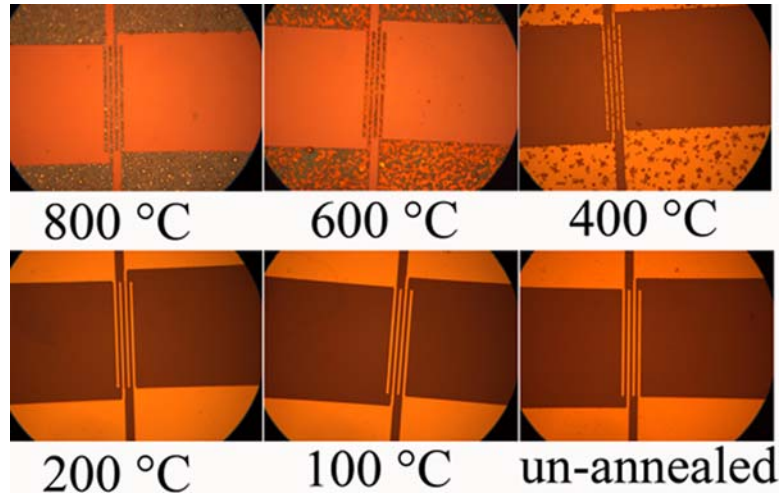


Figure 6.28: H₂/Ar annealing tests at various temperatures to find a suitable temperature for graphene annealing. Patterns were made by photolithography and annealed in 1:1 H₂/Ar for 1 hour at 100 mTorr.

From **Figure 6.28**, we can see that the highest annealing temperature that did not destroy the test pattern was 200 °C. This is the temperature that we use for our graphene annealing.

6.7.4 Wire Bonding

Wire bonding is a very important part of the fabrication process. As the very last step in device fabrication, it is essential that it be done carefully and properly so as not to destroy a device at the last moment. There are several methods of wire bonding, but we use only hybrid ball binding. The MEI 1204B hybrid ball bonder is pictured in **Figure 6.29**.

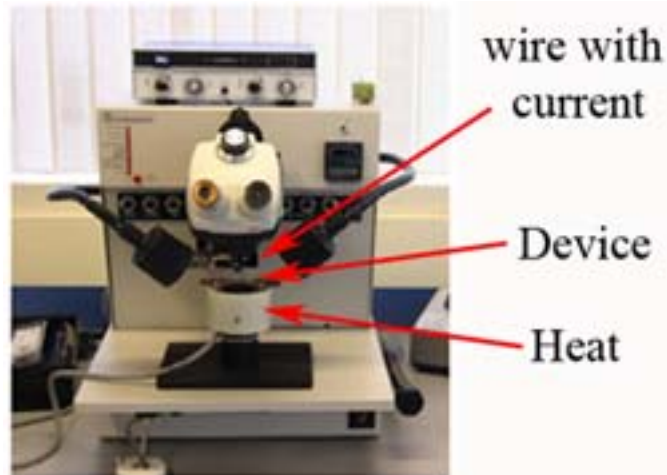


Figure 6.29: MEI 1204B hybrid ball bonder.

The device is first mounted on a chip holder using conductive silver paint. Then it is placed in the sample holder of the ball bonder. This sample holder heats the device from the bottom to soften the contacts. A hollow micro-probe is threaded with gold wire. Looking through an optical stereoscope, the tip of the gold wire, which forms a ball, is placed in physical contact with the electrical contacts on the device. A small current is passed through the wire for a set amount of time to melt the wire. When the current stops, the wire is soldered to the contact. **Figure 6.30** shows the successful bonding of a CNT device.

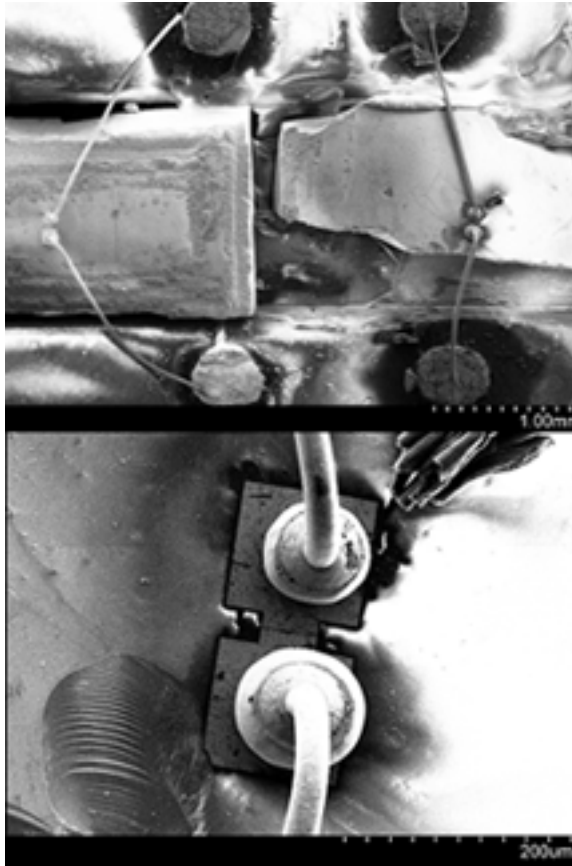


Figure 6.30: SEM images of the successful bonding of a CNT device fabricated by electron beam lithography and electron beam evaporation of Cr/Au. The upper image shows the wire bonding to contacts on the edge of the chip holder. The bottom image shows a close up image.

The minimum size that the wire bonder can successfully bond is approximately $75 \mu\text{m}^2$. For gold contact pads we use a bottom heat of $60 \text{ }^\circ\text{C}$. Wire bonding requires much practice and skill. But, ultimately, success depends on the quality of the adhesion between the deposited metal and the substrate. If the adhesion is bad, the contact pads will easily rip off, ruining the device, as is demonstrated in **Figure 6.31**.

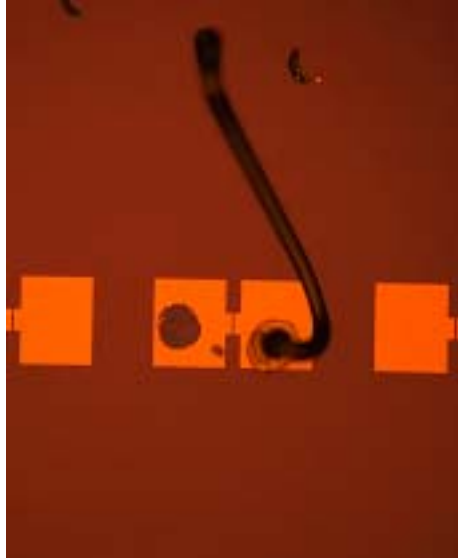


Figure 6.31: Optical image of unsuccessful wire bonding due to poor adhesion. The device was created by photolithography followed by thermal evaporation of Cr/Au. We can see one contact has been completely destroyed. The other contact has a hanging bonded gold wire.

Chapter 7: Transport Properties of Template Synthesized Carbon Nanotubes

7.1 Introduction

Carbon nanotube systems have been idealized as true one-dimensional systems. In one dimension, the normal bulk physics describing conductivity does not work very well. This can be seen from a simple demonstration using Ohm's law: $R=\rho L/A$. For a hypothetical nanotube of dimensions, $d=10$ nm and $L=10$ μ m, and taking the resistivity of carbon, the resistance should, by Ohm's law, be 5 M Ω . However, in actuality, we find the resistance to range from about 4-100 k Ω in experiments. In addition, for extremely well ordered nanotubes, it has been found that the resistance does not change much as a function of length. How can this be? The answer is that the system is one-dimensional and normal three dimensional and bulk methods, such as Ohm's law or Fermi liquid theory (on the quantum scale), do not apply.

In fact, normal three dimensional Fermi Liquid theory breaks down entirely in one dimension. One can visualize this by considering quasiparticles interacting in three dimensions. A very dilute electron gas in three dimensions will have very few quasiparticle-quasiparticle interactions, which is the normal Fermi liquid [121]. Now if we consider the quasiparticles in a two-dimensional box, the number of interactions increases significantly due to the loss of the third degree of freedom. Finally, if the quasiparticles are constricted to only move in one dimension, then every movement will result in the movement of all of the other quasiparticles and the system becomes strongly correlated. Or, because perturbation theory fails to work in one dimension, which is a requirement to maintain the 1:1 correspondence between excitons and quasiparticles, Fermi liquid theory cannot apply. Known as the Peierls instability, a degenerate

perturbation causes a splitting of the electron states at the Fermi surface [122].

Mathematically, this can be seen by calculating the Green's function for an electron:

$$G(k, \omega) = \frac{1}{\varepsilon_0(k) - \omega - \Sigma(k, \omega)}, \quad (7.1)$$

Where, $\Sigma(k, \omega)$ is the self energy (found using the Tomonga-Luttinger Hamiltonian)

and $\varepsilon_0(k)$ is the bare dispersion. For a normal Fermi Liquid this has 1 pole, but now, in 1 dimension, has 2 poles. This means there are two solutions giving the single particle excitation energy [123].

The conductance of a 1-dimensional system is quantized in units of $2e^2/h$, a result first found by R. Landauer and studied, notably, by M. Buttiker. [124-128]. Systems that obey such a quantized conductance are termed ballistic conductors. Landauer originally formulated his result by considering transmission of electrons across a hypothetical 1-dimensional system from electron reservoirs without the convenience of modern low dimensional (bosonization) formalism. He considered two reflectionless contacts, each acting as an electron reservoir of potentials μ_1 and μ_2 , bridged by a single 1-dimensional ballistic conductor. The current that passes from one reservoir to the other, based on transmitted electrons having some energy E with $\mu_2 < E < \mu_1$, is related to the transmission probability of an electron for a given applied bias. The current is given by

$$I = \frac{e}{L} \sum_{k,j} \frac{1}{\hbar} \frac{\partial E_j}{\partial k} \left[f(E_j - \mu_1) - f(E_j - \mu_2) \right]. \quad (7.2)$$

Here, each state of wave number k belongs to a transverse mode of energy E , f is the Fermi function, and L is the length of the conductor. Converting the sum over k to an integral, performing the sum over j , multiplying by 2 for spin, and including a function, $M(E)$, that contains the number of modes, or channels, above a cut-off energy E , we get

$$I = \frac{2e}{h} \int_{-\infty}^{\infty} [f(E - \mu_1) - f(E - \mu_2)] M(E) dE . \quad (7.3)$$

Finally, performing the calculation,

$$I = \frac{2e^2}{h} M \frac{(\mu_1 - \mu_2)}{e} = \frac{2e^2}{h} MV , \quad (7.4)$$

with V being the voltage. This results in Landauer's formula for the conductance of the tube given by,

$$G = \frac{2e^2}{h} MT , \quad (7.5)$$

where, M is the number of transverse modes and T is the transmission probability. Also, it defines the quantum of conductance to be $G_o = 2e^2/h$. It should be noted that for an ideal ballistic conductor, the transmission coefficient is 1 and all of the resistance is contained entirely in the contacts. However, in practice, it has been found that conductances are indeed multiples of G_o [129].

However, the result is also very nicely derived using the one-dimensional Hamiltonian picture due to J. M. Luttinger [130], for which the one dimensional Fermi liquid is named Luttinger liquid. The following derivation is due to Voit and Schultz, et al. in [131, 132], but there is also a very nice derivation by T. Giamarchi in [121]. The non-interacting Tomonaga-Luttinger Hamiltonian for a one dimensional system is given by

$$H = \sum_{k;r=R,L} v_F (\varepsilon_r k - k_F) c_{r,k}^\dagger c_{r,k} . \quad (7.6)$$

Here, ε_r is 1 for $r=R$ (right going particles) and -1 for $r=L$ (left going particles). $c_{r,k}$ are the fermion raising and lowering operators. We note that density fluctuations are just a superposition of particle-hole excitations:

$$\rho^\dagger(q) = \sum_k c^\dagger_{k+q} c_k. \quad (7.7)$$

By treating the electron (fermion) operators as a paired particle of spin 1 (boson), the operators ρ can be rewritten in terms of boson raising and lowering operators. This rather elegant solution is called bosonization. After bosonization the Hamiltonian can then be written in terms of the new raising and lowering operator fields as:

$$H = \frac{1}{2\pi} \int dx u K (\pi \Pi(x))^2 + \frac{u}{K} (\nabla \varphi(x))^2. \quad (7.8)$$

Here, $u=v_F$ for non-interacting fermions, and has the dimensions of velocity, and K is a dimensionless parameter. The interaction of the fermions is described by adding a term H_{ext} in the Hamiltonian, given by:

$$H_{ext} = -e \int dx \hat{\rho}(x) \varphi(x, t). \quad (7.9)$$

Here, φ is the same boson field and ρ is the spin wave function. We need to calculate the linear response with a slowly varying external field. The probability density current is then given by

$$j(x, t) = -\frac{e^2}{\hbar} \int_{-\infty}^0 dt' \int dx' D_{jp}(x-x', t-t') \varphi(x', t'). \quad (7.10)$$

Here, D_{jp} , the retarded current density correlation function is

$$\begin{aligned} D_{jp}(x, t) &= -i\Theta(t) \langle [j(x, t), \rho(0, 0)] \rangle \\ &= -\frac{u_\rho K_\rho}{\pi} \Theta(t) (\delta'(x - u_\rho t) + \delta'(x + u_\rho t)) \end{aligned} \quad (7.11)$$

for spin $1/2$ electrons. Here u_ρ is the same variable with dimensions of velocity and K_ρ is the dimensionless constant. If we adiabatically switch on a potential of frequency ω and wave number q , then the total conductivity is calculated from the previous equation to be:

$$\sigma(q, \omega) = \frac{4e^2}{\hbar} u_\rho K_\rho \frac{i(\omega + i0^+)}{(\omega + i0^+) - u_\rho^2 q^2}. \quad (7.12)$$

The real part is then

$$\text{Re } \sigma(0, \omega) = \frac{2e^2}{\hbar} u_\rho K_\rho \delta(\omega). \quad (7.13)$$

Likewise, if there is a static field over part of the sample, we calculate the current to be:

$$j = \frac{2e^2}{\hbar} K_\rho U. \quad (7.14)$$

where U is the applied tension. This gives a conductivity of

$$G = \frac{2e^2}{\hbar} K_\rho. \quad (7.15)$$

For the non-interacting case, $K_\rho=1$, which is Landauer's quantum of conductance. The value of K_ρ increases as the number of interactions increase, thus has the same role as the transmission coefficient T . Another interesting result of the Luttinger Hamiltonian is spin and charge density wave separation (a physical meaning of the two quasiparticle excitation energy solutions), which has also been shown to occur experimentally [133].

However, the previous discussion was primarily for the case of the idealized carbon nanotube system that is free of defects and has walls that continue along the entirety of the system. In reality, most carbon nanotubes have defects, and their dimensionality can be described by the three important lengths of the system, the mean free path ($l=v_F t_m$), the phase relaxation length ($L_\phi=v_F t_\phi$), and the Fermi wavelength, λ_F [67]. $t_{m,\phi}$ are the momentum relaxation and phase relaxation times, respectively. If $L_\phi < l < L$, then the situation is one of classical conduction. If $l < L_\phi < L$, then we are in the localized electron regime. Here, when $L_\phi < L_c$, the coherence length, the system is weakly localized. If $L_\phi > L_c$, the system is strongly localized. Finally, if $l > L_\phi > L$, the conductor is

ballistic. SWCNTs are almost always ballistic conductors. MWCNTs are sometimes ballistic conductors, but oftentimes fall into the weak localization regime.

From TEM images of our MWCNTs (in Section 3.2.2), we can see that they are highly disordered. The very short walls mean that the mean free path is very short (~5 nm) as compared to the total length of the conductor between the contacts (3 μm). Therefore, we would expect them to be a localized electron system exhibiting, in particular, Anderson localization. This type of system occurs because the presence of many scatterers causes reflections, thus causing the transmission probability to become very small and the conductor transitions and approaches the behavior of a perfect insulator [134].

Very little work has been done previously on disordered carbon nanotubes. However, some transport studies were carried out on disordered CVD synthesized carbon nanotubes similar to ours, notably, by the group of Tarkiainen, et al., who found the transport behavior to be dominated by behavior indicative of 2-dimensional weak localization theory, but with system lengths close to the strong localization limit [135, 136]. In doing their experiments, they found the magnetoconductance to follow[137]:

$$G(B) - G(0) = \frac{N_v w_{eff}}{L} \frac{e^2}{\pi h} \left[\Psi \left(\frac{1}{2} + \frac{l_B^2}{4L_\phi} \right) + \ln \left(\frac{4L_\phi^2}{l_B^2} \right) \right] \quad (7.16)$$

Here, $l_B^2 = \hbar/eB$, N_v is the number of separate valleys on the Fermi surface, L is the length of the nanotube across the junction, w_{eff} is the effective width of the nanotube, and Ψ is the digamma function. They fit their magnetoresistance data to this weak localization formula and used the fitting parameters to calculate the various lengths of the system to show that it is indeed weakly localized. **Figure 7.1** shows a theoretical plot of this curve using the parameters given in [136], which shows the negative magnetoresistance characteristic of weak localization. The plot was made using the program MathCAD.

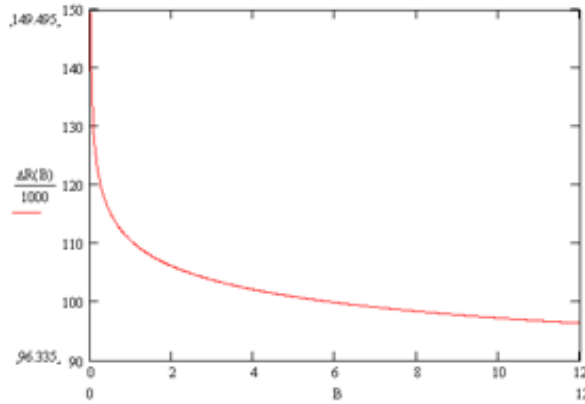


Figure 7.1: Theoretical plot of weak localization magnetoresistance.

However, the discussions in their two papers are somewhat contradictory. As in their first paper [135], they compared their results to strong tunneling single electron transistor models and their results contain many of the hallmarks of a Luttinger liquid and a ballistic conductor rather than a weakly localized system. But, they also note that in their second paper [136], they oxidize their nanotubes in air prior to performing electrical experiments, which, as we note in Chapter 6, may irrevocably damage the nanotubes, and thus make them lose the physical characteristics of carbon nanotubes. It is interesting, though, that they also note that after this oxidation, no damage is visible under AFM imaging. Based on our own experience, we determine this finding to be highly contentious. Moreover, they use a method of catalytic decomposition when fabricating their nanotubes by CVD. This creates the incredibly likely scenario that the catalyst, which in their case is Co, remains in the nanotubes. There are no predictions as to what affect random ferromagnetic-metallic impurities will have on the transport properties of the nanotubes. However, it is likely that large impurities such as this would cause a great deal of scattering, thus artificially lowering the order of the nanotube. Ultimately, it shows that the current research on disordered carbon nanotubes is highly lacking.

7.2 Room Temperature V-I Sweeps and Contact Resistances

As discussed in Chapter 6, devices are made by depositing a drop of nanotube solution onto a Si/SiO₂ substrate and then heating the substrate slightly until the ethanol is evaporated off, resulting in a well-dispersed, sparse film of nanotubes on the Si/SiO₂. The chips are then annealed in a tube furnace containing equal parts Ar and H₂ at 800° C. For comparison, other chips were also annealed in Ar only. The contact resistance is defined as $R_c = (R_{2p} - R_{4p})/2$. R_{2p} and R_{4p} are the 2- and 4-probe resistances, respectively. Likewise, here, unannealed devices gave contact resistances of 1-100 MΩ, while those that were annealed gave contact resistances of 1-6 kΩ. In general, we found the contact resistance to be less than about 30% of the average measured 2-probe resistance. Lower annealing temperatures were attempted. However, they did not successfully lower the contact resistances. This low contact resistance allows us to successfully measure the CNTs using a 2-probe device set up, which is far easier to fabricate than a 4-probe device. A 4-probe device made by photolithography is shown in **Figure 7.2**.

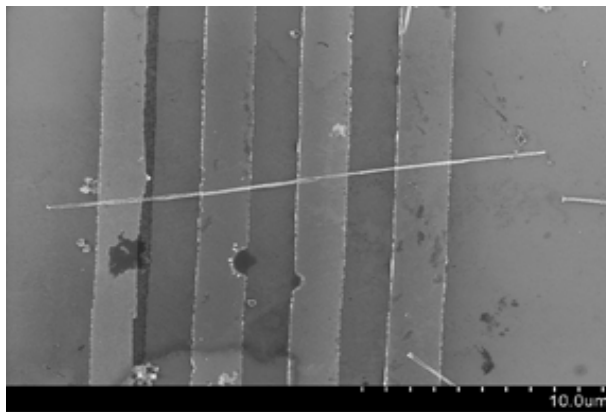


Figure 7.2: A 4-probe carbon nanotube device.

For this study, 2-probe devices are made by photolithography. The gap between electrodes is approximately 3 μm. Cr/Au contacts of 5/60 nm are deposited in an electron beam evaporator. The photolithography method makes many devices

simultaneously on a single chip. So, suitable devices must be chosen from these. We choose devices where only a few nanotubes bridge the gap between contacts. **Figure 7.3** displays an SEM image of one such device.

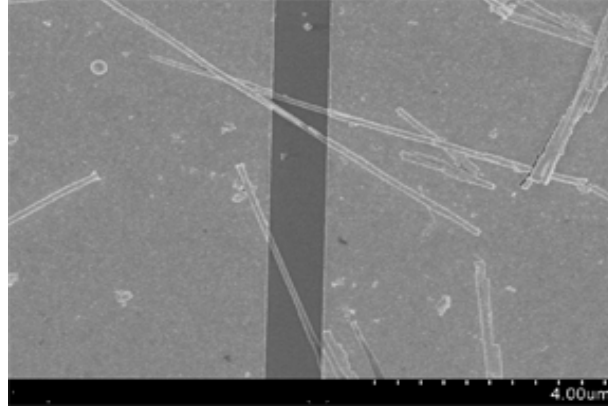


Figure 7.3: SEM image of a 2-probe CNT device of the kind used in the experiments.

To test the contact resistances we use a Wentworth Labs model 6000 micromanipulator probe test station with Signatone SE-10T 30 micron tungsten probe tips. **Table 7.1** shows an example of a contact resistance test for a typical 4-probe CNT device made by CVD for 60 minutes and the method described above.

Table 7.1: Example of a contact resistance test for a typical 60 minute CVD CNT 4-probe device.

Probe Number	current (A): 1 μ A		units in table are Volts	
4	x	X	x	x
3	x	X	x	0.03
2	x	X	0.0164	0.0215
1	x	0.0221	0.0278	0.0223
Probe Number	1	2	3	4

average R_{2p} (Ω)	23350
R_{4p} (Ω)	9950
R_c (Ω)	6700

Although we chose devices for which only a few nanotubes bridged the gap between electrical contacts, it is apparent that the current only flows across the nanotube

or bundle of nanotubes that have the lowest resistance. We found that by electrically burning out a low resistance nanotube on the device with a too-high applied voltage, another higher resistance nanotube would then take over conduction of current. This is displayed in the graph of **Figure 7.4** for a 75 minute CVD 2-probe device.

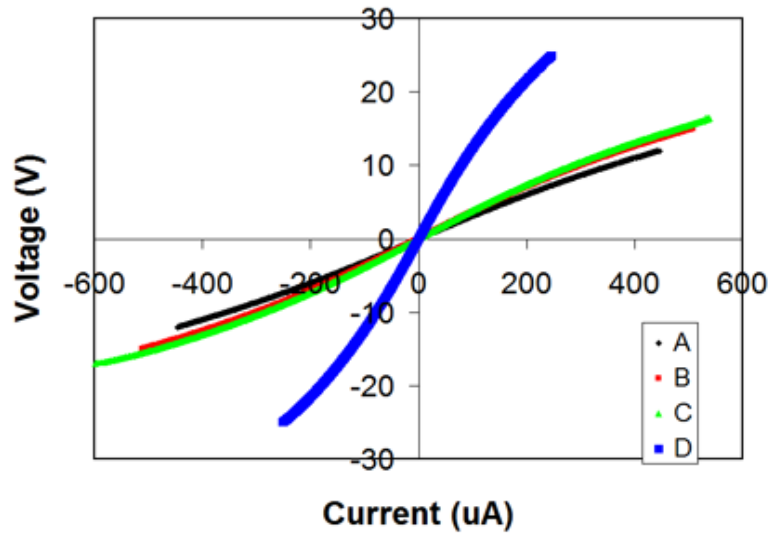


Figure 7.4: Voltage vs. Current for a 75 minute CVD device for which a great applied voltage broke the first nanotube and another nanotube began to conduct.

We can see in **Figure 7.4** that at first, the resistance is low when the current is going through one nanotube (measurement A). As we increase the applied voltage (measurements B and C), the nanotube eventually burns out. Applying a voltage above this breakdown voltage, results in conduction through a more resistive tube in the device (measurement D). Eventually, this nanotube will also break as the voltage is increased. We found that some nanotubes could pass huge current densities, sometimes passing currents on the order of mA before burning out. This means the nanotubes are capable of current densities $>10^5$ A/cm², which is consistent with previous results, but not quite as high as in very well ordered nanotubes which can reach densities $>10^8$ A/cm² [138].

7.3 Luttinger Liquids

7.3.1 Theory of Transport in Luttinger Liquids

The previously discussed strongly correlated electron system of a Luttinger liquid results in a power law dependence of the density of states on the energy. It has been found that this situation leads to a differential conductance, $G=dI/dV$, given by [100, 139-141]

$$G(V, T) = AT^\alpha \left| \Gamma(z) \right|^2 \cosh\left(\frac{x}{2}\right) \otimes \frac{1}{4k_B T} \operatorname{sech}^2\left(\frac{E - eV}{2k_B T}\right), \quad (7.17)$$

where,

$$\begin{aligned} z &= 1 + \alpha/2 + ix/2\pi \\ x &= \eta eV / k_B T \end{aligned} \quad (7.18)$$

Γ is the gamma function and T is the temperature. Performing the convolution operation (\otimes) due to thermal broadening of the electrical leads, this can be written as,

$$G_{LL}(V, T) = AT^\alpha \left| \Gamma\left(z + \frac{1}{2}\right) \right|^2 \sinh\left(\frac{x}{2}\right) \left[\frac{1}{2} \coth\left(\frac{x}{2}\right) - \frac{1}{\pi} \operatorname{Im} \Psi\left(z + \frac{1}{2}\right) \right]. \quad (7.19)$$

Thus, the model has 3 parameters: α , η , A . A is simply a constant. η has the physical meaning of accounting for voltage division of the nanotube at the electrical contacts. It should be 0.5 for two contacts, i.e. tunnel barriers. α is discussed below, as are tunnel barriers. There are two limits to this equation that produce the familiar Luttinger-type scaling relationships:

$$\begin{aligned} G(T) &\propto T^\alpha & eV \ll k_B T \\ \frac{dI}{dV} &\propto V^\alpha & eV \gg k_B T \end{aligned} \quad (7.20)$$

The value of the exponential scaling factor α strongly depends on the type of electron tunneling in the device. There are two cases [100]:

$$\begin{aligned}\alpha_{end} &= \frac{1}{4N} \left(\frac{1}{g} - 1 \right) \\ \alpha_{bulk} &= \frac{1}{8N} \left(\frac{1}{g} + g - 2 \right)\end{aligned}\tag{7.21}$$

Here, N refers to the number of layers, or conducting channels, and g is the so-called Luttinger interaction parameter that measures the strength of the interaction between electrons. First, it is important to note where in the system the Luttinger liquid is located. For the ideal case, as discussed before, the nanotube itself will have no resistance and the transmission probability for an electron to get from one side to the other will be 1. The resistance is contained at the points of contact between the nanotube and the electrical contact. This is also where the Luttinger liquid will reside. So, the first case is that an electron tunnels from the contact into the Luttinger liquid from the end (α_{end}), in the direction that points along the length of the nanotube, in which case the interaction is stronger because the electrons can only respond by moving in one direction. And, the second case is that an electron tunnels from the contact into the Luttinger Liquid from the side (α_{bulk}), at some angle from the length of the nanotube, in which case the electrons can respond by moving in two directions. In any case, for a strongly correlated system such as this, we expect $g < 1$. For $g=1$, we would have the case of a non-interacting Fermi Liquid. For the case of $g < 1$, we would have very strong repulsive electron-electron interactions and the material would become localized. Based on this, we can make a theoretical prediction for α . Graugnard, et al. predict a range of 0.2-0.6 [139]. Bockrath, et al. have predicted that $\alpha_{end}=0.65$ and $\alpha_{bulk}=0.24$ [100].

7.3.2 *Experimental Results*

To perform the experiments testing our samples for Luttinger liquid behavior, we place the sample in a variable temperature cryostat made by Cryo Industries of America, Inc. (Coolpower 4.2Lab) (See Appendix C), controlled by a LakeShore model 340 temperature controller. The cryostat is capable of cooling the sample to about 5 or 6 K. The sample sits in a chip holder that contains a number of electrical leads. Data is taken using an acquisition VI written in LabVIEW. Current is applied using the Keithely model 6220 current source. Voltage is collected using a Keithely model 2182A nanovoltmeter. Temperature is read directly from the analog outputs of the LakeShore temperature controller fed into a Hewlett Packard Model HP34401A voltmeter.

We measure the resistance of our samples as a function of temperature. **Figure 7.5** shows the resistance vs. temperature of the hydrogen annealed nanotubes. The behavior is as is expected, as it decreases like T^α and is consistent with previous studies. The behavior seems to be independent of inner diameter and is consistent across different samples. We made several batches of devices, and the behavior was consistent across all devices made at different times. We see that the curve is punctuated by a “knee” at approximately 14 K. After this knee, the resistance increases dramatically. If we could go to lower temperatures (< 4 K), we would expect the resistance to eventually saturate [67].

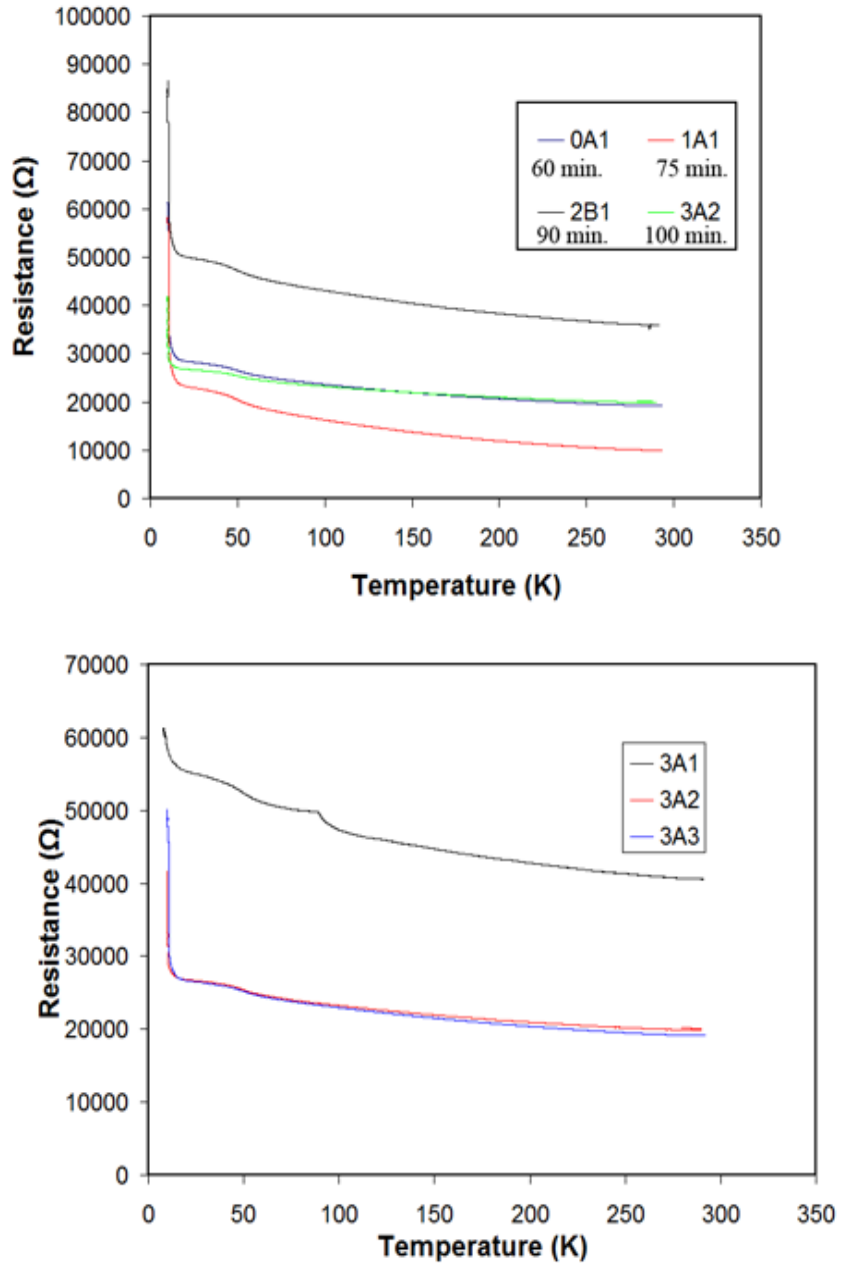


Figure 7.5: Hydrogen annealed CNTs. The upper figure shows 1 typical sample for each inner diameter given by the CVD time. The lower figure shows 3 different 100 min. CVD samples.

Figure 7.6 shows a similar diagram for CNT devices annealed in Ar only. The same T^{α} behavior persists and the knee observed for H_2 annealed devices is also still visible.

However, for Ar annealed device, the knee appears to be much smaller. We can offer

only a qualitative discussion for the reasons for this knee. Some previous studies show the presence of this knee and some show a more smoothly increasing curve. At first, we thought it was related to some phase transition in the sample. However, as we shall soon see, the position of the knee, which is consistently at about 13 or 14 K is independent of all other observed behaviors in the nanotube. It could possibly be from instrumental error due to the rate of cooling of the sample and the cryostat. The sample sits in the bottom of the cryostat, while the cold head is on the top of the cryostat. This creates a temperature differential between the sample area at the bottom and the top of the cryostat. We found that that the cryostat cools slowly at first and then cooling speeds up due to the development of a steeper differential (about 100 K at the maximum differential as measured from a thermometer near the sample and a thermometer near the cold head). If the sample is not given enough time to cool down to a certain temperature before the measurement is made, it may result in a temperature reading from the thermometer that is not quite the true temperature of the sample. Eventually, as the bottom of the cryostat begins to cool very quickly, the thermometer will become greatly out-of-sync with the true temperature of the sample. When the cryostat reaches its base temperature, the temperature differential gets smaller and eventually the top and bottom of the cryostat reach thermal equilibrium. Then, the true sample temperature catches up to the temperature of the cryostat. This out-of-sync phase would cause the resistance to artificially blow up suddenly rather than smoothly as we would expect. We made every attempt to ensure good thermal contact between the sample (Si/SiO₂ on top of a gold coated ceramic chip bed), the sample holder (plastic), and the copper cold finger. However, due to the vastly different thermal conductivities of the various elements involved and the nature of the equipment, it may not have been enough to eliminate this error.

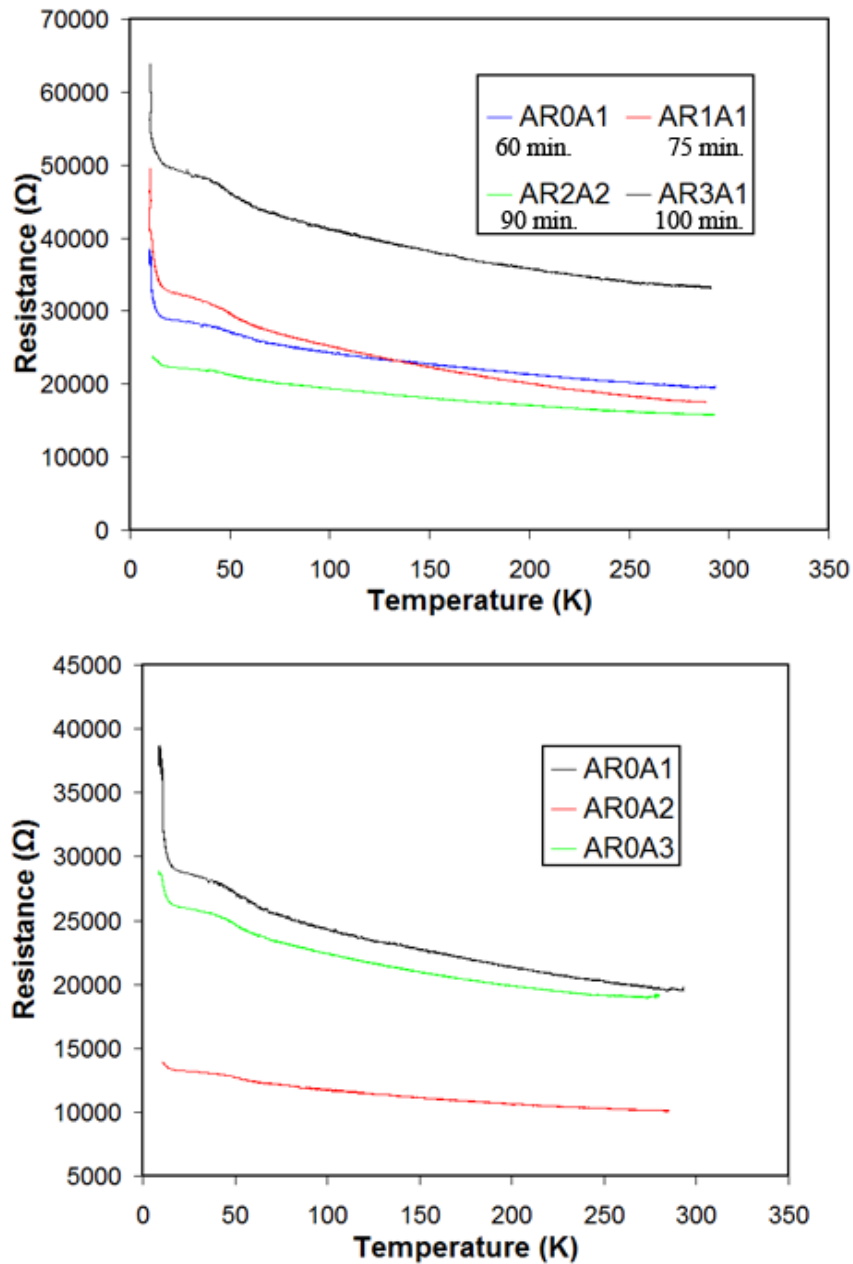


Figure 7.6: Argon annealed CNTs. The upper figure shows 1 typical sample for each inner diameter given by the CVD time. The lower figure shows 3 different 60 min. CVD samples.

Luttinger liquid theory predicts near ohmic behavior near room temperature, but the development of a singularity in the conductance curve as the temperature decreases. This singularity, at low enough temperatures, will eventually become a conductance gap.

Figure 7.7 shows an example of temperature dependent conductance curves for a hydrogen annealed sample and for an argon annealed sample.

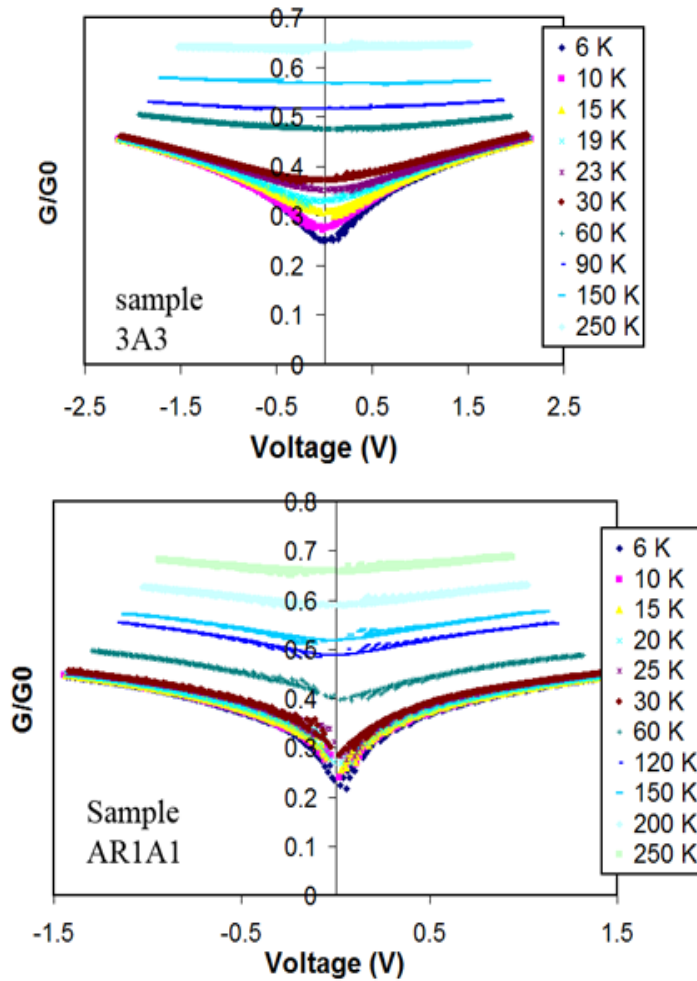


Figure 7.7: Conductance vs. Voltage curves as a function of temperature showing the formation of a singularity indicative of Luttinger liquid behavior for (upper figure) a 100 min. CVD hydrogen annealed device and (lower image) a 75 min. argon annealed device.

We can see from the **Figure 7.7**, that, indeed, our samples show the formation of the predicted conductance gap. And, the behavior also approaches ohmic behavior at higher temperatures. All of the samples tested (several of each CVD time) showed this behavior. There appears to be no dependence on the inner diameter and the depth of the conductance singularity or the temperature at which the sample becomes ohmic. The

behavior persisted for both Ar and H₂ annealed devices. **Figure 7.8** shows a close up graph of the singularity for a 60 min. CVD hydrogen annealed device.

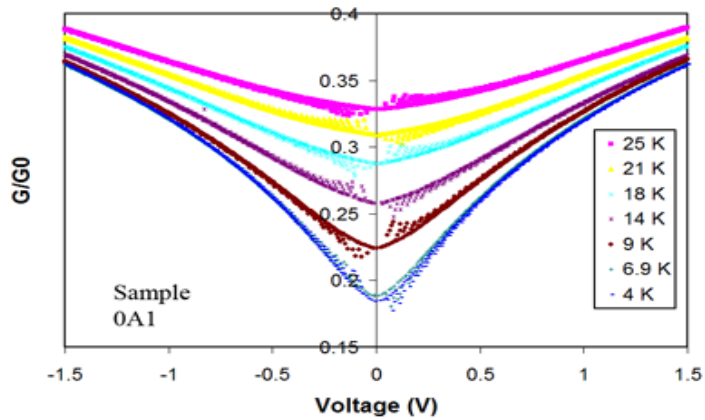


Figure 7.8: Close up of the conductance singularity for a 60 min. CVD hydrogen annealed device.

Another prediction of the Luttinger model, taken from equation (7.19) is that a graph of $G(V,T)/G_0/T^\alpha$ vs. $eV/k_B T$ should show that the data collapses into a universal curve. We performed this analysis, and the results for an Ar annealed sample and a H₂ annealed sample are displayed in **Figure 7.9**. The data was fit to equation (7.19) using Mathematica by varying the parameters A , α , and η to the lowest temperature data set.

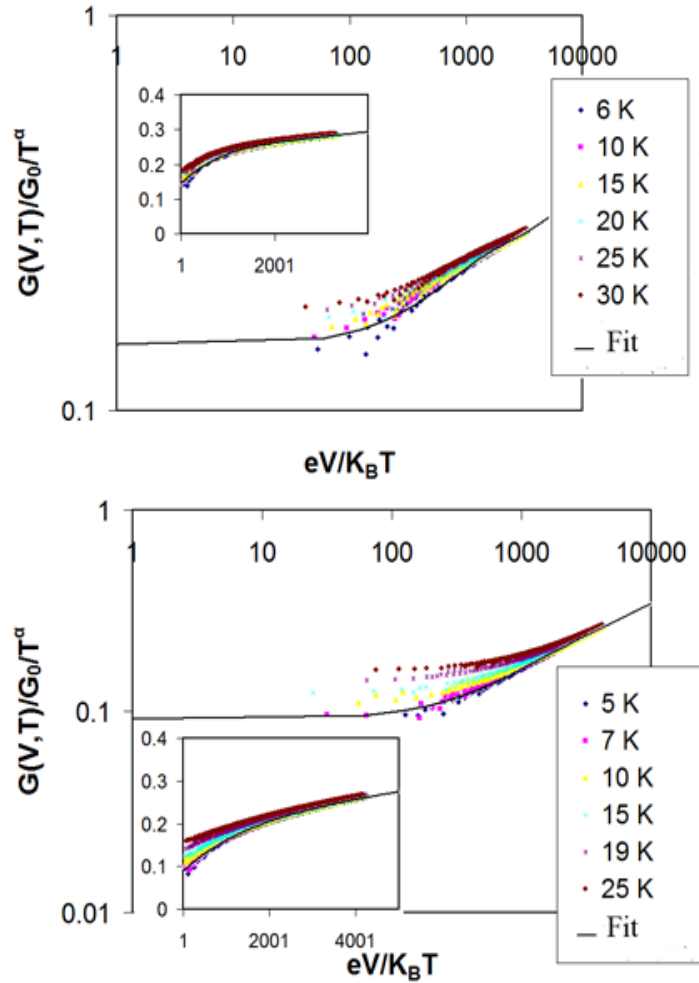


Figure 7.9: Luttinger scaling plots fit with Mathematica. The large plots are log-log and the insets are not logarithmic. The upper graph is for an argon annealed device and the lower is for a hydrogen annealed device. For both devices, the CNTs were deposited for 75 minutes.

From **Figure 7.9**, we see that the Luttinger model does provide a rather good fit for the data. However, there are some deviations from the predicted universal curve. This was noticed by others performing a similar analysis on carbon nanotubes as well [100, 139].

Table 7.2 summarizes our fitting data for a variety of devices. Meas. α refers to the value taken from a least squares fit of the conductance vs. temperature curve. Scaled α refers to the value taken from the Luttinger scaling fit, as in **Figure 7.9**.

Table 7.2: Luttinger parameters for a variety of samples.

Sample	Annealing	CVD Time	Meas. α	Scaled α	Scaled η	A
0A1	H ₂ /Ar	60	0.283	0.833	0.00718	0.286
1A1	H ₂ /Ar	75	0.420	0.683	0.00871	0.227
2B1	H ₂ /Ar	90	0.171	0.768	1.694	0.0546
3A3	H ₂ /Ar	100	0.221	0.784	0.00454	0.407
AR0A2	Ar	60	0.119	0.843	3.439	0.229
AR1A1	Ar	75	0.277	0.821	0.0222	0.311
AR2A1	Ar	90	0.158	0.846	1.29	0.142
AR3A1	Ar	100	0.168	0.847	0.0192	0.276

From **Table 7.2**, we see that, the values of α are indeed close to the predicted values for the two cases of α_{end} and α_{bulk} . However, we see a significant deviation for the measured and scaled values. This is most likely due to the above possible instrumental error signified by the appearance of the knee feature in the conductance vs. temperature data. Therefore, the scaled value is most likely the best measured value. Although we expect both cases of end and bulk tunneling to occur, from the scaled value, we can determine that the majority of tunneling is end tunneling. However, our values of scaled α are slightly higher than the predicted value for end tunneling. This can be attributed to the disorder in the CNTs. Based on our scaled α , the Luttinger parameter, g , is estimated to be approaching the limit of what can be considered “less than 1” before it becomes “much, much less than 1”. As g decreases, it corresponds to increasing strength of electron-electron interactions. Therefore, our material can be judged to be just barely a Luttinger liquid and almost in the localized electron region of mesoscopic systems.

We also note that the value of η is widely varying with some values above the predicted value and some well below the predicted value. This can be attributed to the coupling of the electrical contacts to the nanotube. In the case of very strong coupling (or very low contact resistance), the value of η becomes significantly less than the predicted value. Our results are a testament to the superiority of our contact resistance

lowering method. In the case of weaker coupling (found only in a few samples), the value of η can increase. However, for us, it does not increase too much. This is entirely consistent with our measured range of contact resistances for our devices.

7.4 Magnetoresistance

7.4.1 Theory

There are many competing theories to explain the observed magnetoresistance in carbon nanotubes. In a normal Luttinger liquid with spin, it is expected that the application of a magnetic field will break spin rotation invariance (while maintaining spin-charge separation), adding a new term to the Hamiltonian of the form of [121]

$$H_m = -\frac{g_l \mu_B B}{2} \int dx [\rho_\uparrow - \rho_\downarrow] = \frac{g_l \mu_B B}{2} \int dx \frac{1}{\pi} \nabla \phi_\sigma(x), \quad (7.22)$$

where, g_l is the gyrometric ratio, B is the magnetic field and the far right hand side is the result after bosonization. Thus, we see that a magnetic field will introduce spin anisotropy into the system. Or, in the ideal case of a perfectly transmitting (perhaps paramagnetic) 1-dimensional wire bridging the two contacts, a magnetic field will result in 1-dimensional spin polarized transport [121].

In the past, measurements on ordered carbon nanotubes that have proven to be Luttinger liquids at low temperatures have produced negative magnetoresistance when the field is perpendicular to the nanotube [142] and positive magnetoresistance when the field is aligned parallel to the nanotube [143]. But, this phenomenon has been found to be independent of weak localization, but rather a flux dependence of the density of states and is termed a field orientation dependent metal-insulator transition [142].

As discussed earlier, weak localization or Anderson localization predicts negative magnetoresistance for a sufficiently disordered nanotube. It also predicts the appearance of universal conductance fluctuations. Both of these phenomena have been

seen in very well ordered carbon nanotubes [144]. These data suggest that the magnetotransport behavior, even for very well ordered nanotubes, is dominated by localization in the nanotube rather than the Luttinger liquid. This further indicates that the number of scatters and interactions effectively increases when the field is turned on and the transmission coefficient of the tube is no longer even close to the hypothetical ideal. Or, turning on the magnetic field effectively destroys the Luttinger liquid in carbon nanotubes. However, in order for localization to be implicated in a transition, the temperature must be sufficiently cold. In most previous studies, negative magnetoresistance disappeared for sample above about 5 K (for ordered tubes), and universal conductance fluctuations were only observed in millikelvin environments [67]. For the disordered nanotubes of Tarkiainen, et al., negative magnetoresistance persisted up to about 50 K [136]. But as discussed, their results could be due to impurity scattering from residual ferromagnetic or superparamagnetic catalyst nanoparticles.

In fact, due to the many strong effects a magnetic field is expected to have on a nanotube, including the opening of a band gap, a field-driven metal-insulator transition has been predicted [145]. Anderson localization caused metal-insulator transitions in well ordered carbon nanotubes have been studied [143, 146, 147]. Roche and Saito showed theoretically that a magnetic field leads to an total density of states at the Fermi level that oscillates between metallic and semiconducting [147]. The oscillation of the total density of states is a function of $\nu=L/2\pi l$, where $l = \sqrt{\hbar c / eB}$, the magnetic length. Fujiwara, et al. demonstrated this oscillatory type of metal-insulator transition [146]. For low fields (<1 T), the behavior was metallic. For fields between 1 and 7 T, the behavior was insulating. For fields >7 T, the behavior was again metallic. However, for this Anderson type transition, the CNT conductance behavior was similar and

indistinguishable until temperatures below about 10 K were reached, which, as discussed earlier, is expected for observation of localization effects.

However, our carbon nanotubes are unique in that, as discussed in Chapter 5, we made them ferromagnetic (as opposed to the usual diamagnetic nanotube) by annealing them in H_2 . In the case of a ferromagnetic carbon nanotube, the Luttinger formalism fails. This is because, by definition, a Luttinger liquid is paramagnetic [122]. So, the transport behavior is effectively a different type of system entirely, which is caused by turning on a magnetic field that is slowly changing, thus acting on the ferromagnet carbon nanotube. The transport behavior of the ferromagnet in the tube would dominate the effects of the Luttinger liquid just like the previously studied cases where the diamagnet in the nanotube dominates the Luttinger liquid [67, 148]. We would then expect to characterize the magnetoresistance behavior by other methods related to low-dimensional ferromagnets.

Recently, work on carbon coated Co nanowires by the group of Brand, et al., building on the work of S. Friedrichowski, et al. and A. Carl, et al., has shown that the dominant effect in these structures is not localization, and no Anderson transition was found [149-151]. It has been hypothesized in such ferromagnetic structures that upon application of an external magnetic field, magnetic induction in the sample, which would create an internal magnetic field, would then destroy the phase coherence of any backscattered electron waves, resulting in an Anderson transition [152]. Or, it has also been hypothesized that the application of a magnetic field could cause a type of screening of the Coulomb interaction of interacting electrons due to diffuse scattering [153]. Such internal screening has been calculated to easily overcome Luttinger liquid behavior [154]. Both this localization and these enhanced electron-electron interactions can lead to negative magnetoresistance. But, Brand, et al. showed that, in fact, the

magnetoresistance of carbon coated Co nanowires was entirely dominated by anisotropic magnetoresistance effects and some enhanced 2-dimensional electron-electron interaction at fields greater than 1 T [149]. In addition, it has been noted that another scattering mechanism exhibited by a ferromagnetic metal will be due to electron-magnon interactions in an applied field [155]. This has been shown to lead to negative magnetoresistance in amorphous ferromagnetic structures [155].

Work has been done on ferromagnetic nanowires and results have shown the behavior to be dominated mainly by anisotropic magnetoresistance (AMR) [156-161]. It would, therefore, make sense that we should see some similarities between the magnetoresistance behavior of ferromagnetic nanowires and our ferromagnetic CNTs. For a normal ferromagnet the magnetoresistance ratio given by Kohler's rule is generalized by

$$\frac{\Delta\rho}{\rho} \propto a\left(\frac{H}{\rho}\right)^2 + b\left(\frac{M}{\rho}\right)^2, \quad (7.23)$$

where, ρ is the resistivity, H is the applied field, M is the magnetization and a and b are proportionality constants [162]. The second term gives the AMR contribution. For low fields, the magnetization is not yet saturated, so the magnetoresistance ratio has a field varying contribution from the second term. However, once a saturating field is reached, the first term dominates and the MR ratio goes like H^2 . Likewise, we would expect to see a direct correlation between the $M(H)$ hysteresis loop, and the MR ratio curve.

Saito, et al. note, in passing, that a viable cause of negative magnetoresistance above 4 K is due to behavior predicted by the Bright model [67]. Interestingly, this path was contemplated by us before we discovered the note by Saito, et al. This model was formulated by A.A. Bright almost 30 years ago when contemplating negative magnetoresistance in different types of carbon fibers and filaments from the amorphous

to the highly graphitized [163]. In it, Bright suggests that negative magnetoresistance is the result of formation of Landau levels at the Fermi energy which increases the density of states and the current path due to disorder in the structure of the conductor. Bright makes four assumptions in his model. First, the band structure and density of states is 2-dimensional. Second, there is a shallow ($E_a \sim -10^{-2}$ eV) acceptor concentration, N_a , due to defects. Third, there are collision and thermal broadened Landau levels, which also takes into account defects and disorder. And, fourth, there is an extra density of states, N_o , in the ground state Landau level to account for the effects of 3-dimensional overlap in the graphene layers. Taking into account these considerations, Bright adjusts the 2-dimensional density of states of graphene to read:

$$g(E) = \frac{AB\lambda}{\sqrt{\pi}} \left[\left(1 + \frac{N_o}{AB} \right) \exp(-\lambda^2 E^2) \right] + \sum_{n=1}^{\infty} \left\{ \frac{\exp[-\lambda^2 (E - E_N)^2]}{1 + \exp[-\lambda^2 (E + E_N)^2]} \right\}. \quad (7.24)$$

Here, there are four parameters to be fit by the data: N_o , N_a , E_a and μ (carrier mobility), which is contained in the width of each Landau level λ :

$$\frac{1}{\lambda} = \frac{1}{\sqrt{2}} \sqrt{(\hbar/\tau)^2 + (k_B T)^2}, \quad (7.25)$$

with, $\tau = \mu m^*/e$, and m^* = the average effective mass. A is a parameter that includes the magnetic field. The electron and hole concentrations are:

$$n, p = \int_0^{\infty} \frac{g(E) dE}{1 + \exp[(E - E_F)/k_B T]}. \quad (7.26)$$

The Fermi energy must be determined by the self-consistent neutrality condition given by:

$$p = n + \frac{N_a}{1 + \exp[(E_a - E_F)/k_B T]}. \quad (7.27)$$

It is assumed that the application of the electric field does not affect the effective mass and the scattering method, or the mobility. The resistivity is then found to be:

$$\rho(B) = \frac{1 + \mu^2 B^2}{(n + p)e\mu \left[1 + \mu^2 B^2 (p - n)^2 / (p + n)^2 \right]}. \quad (7.28)$$

In general practice, the quantity that is required for analysis is $\Delta\rho/\rho = (\rho(B) - \rho(0))/\rho(0)$, also known as the MR ratio. Thus, we calculate the MR ratio for a couple of situations. There are two important limits to equation (7.28). First, if $n \ll p$, then the hole concentration is proportional to the density of states and we get:

$$\frac{\Delta\rho}{\rho} \sim -157\mu^4 B^2 \quad (7.29)$$

Here, values for the parameters were taken from [98]. This is the physical case of a very disordered nanotube. In the second case, $|p - n| \ll p + n$. In this case, we get

$$\frac{\Delta\rho}{\rho} \sim \left(\frac{n_0 + p_0}{n + p} - 1 \right) + \frac{n_0 + p_0}{n + p} \mu^2 B^2. \quad (7.30)$$

This is the case of a very well ordered nanotube. Here the $\mu^2 B^2$ term dominates in high fields. So, the magnetoresistance approaches that of a regular metallic conductor, for which $\Delta\rho/\rho = \mu^2 B^2$.

The Bright Model was very well applied by Endo, et al. in [99]. There they found that carbon fibers, that were for the most part turbostratic (amorphous), displayed negative magnetoresistance. If they annealed the carbon fibers, they continued to display negative magnetoresistance up to approximately 1100°C, after which they began to show positive magnetoresistance. All of the experimental data curves fit the Bright model excellently. Effectively, below 1100°C, the fibers were extremely disordered with the number of holes far greater than the number of electrons and greatly increased

electron-electron interactions. Above this temperature, the fibers began to graphitize and order themselves into interwoven graphene sheets. At this point, the nanotubes began to conduct in a more metallic way, as the number electron-electron interactions decreased.

7.4.2 *Hysteretic Magnetoresistance*

For magnetoresistance measurements, we use a 2 terminal DC set-up. We tried an AC set-up, but the low signal-to-noise ratio did not necessitate it, and we switched to the less complicated DC set-up. Magnetoresistance measurements were taken using a Cryogenic, Ltd. 14 Tesla superconducting magnet system with a room temperature bore (see Appendix C). The variable temperature cryostat used for the Luttinger liquid measurements earlier was placed in the magnet so that the device sat in the center of the field with the field perpendicular to the area of the device and the nanotube itself. Data is taken the same way as before, but now the magnetic field is also read directly from the analogue outputs of the magnet fed into a Hewlett Packard model HP34401A voltmeter.

Figure 7.10 displays the observed hysteretic magnetoresistance for a typical nanotube device annealed in H₂/Ar and compares it to the magnetoresistance observed for a device annealed in Ar only. For all graphs, we measure the MR ratio. **Figure 7.11** shows the hysteresis as a function of the sweeping rate of the field. The hysteresis is most apparent when the field is swept in an increasing direction. However, there is a slight, but still noticeable, difference between the magnetoresistances at different sweeping rates taken with a decreasing field sweep. This behavior was highly reproducible, occurring in all devices tested. Three separate batches of devices were made at different times and the same behavior persisted.

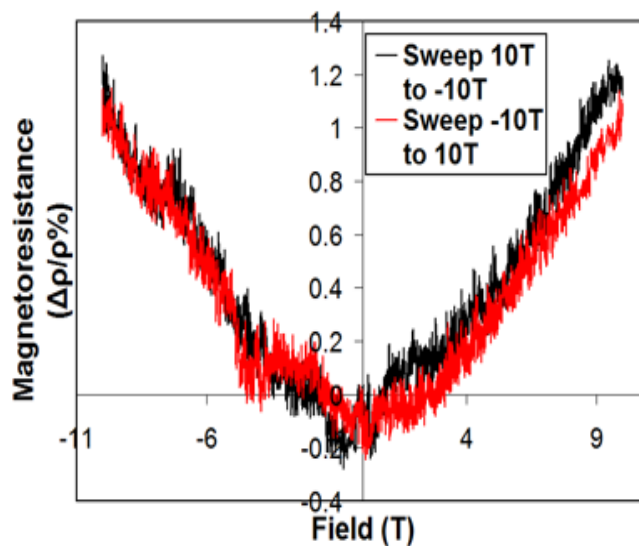
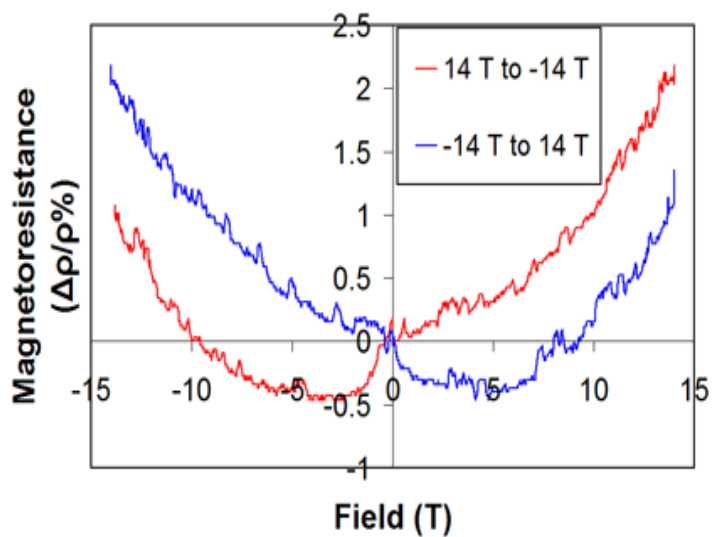


Figure 7.10: Hysteretic magnetoresistance observed (upper) in a 60 min. CVD hydrogen annealed nanotube device, and not observed (lower) in a 60 min. CVD Ar annealed device.

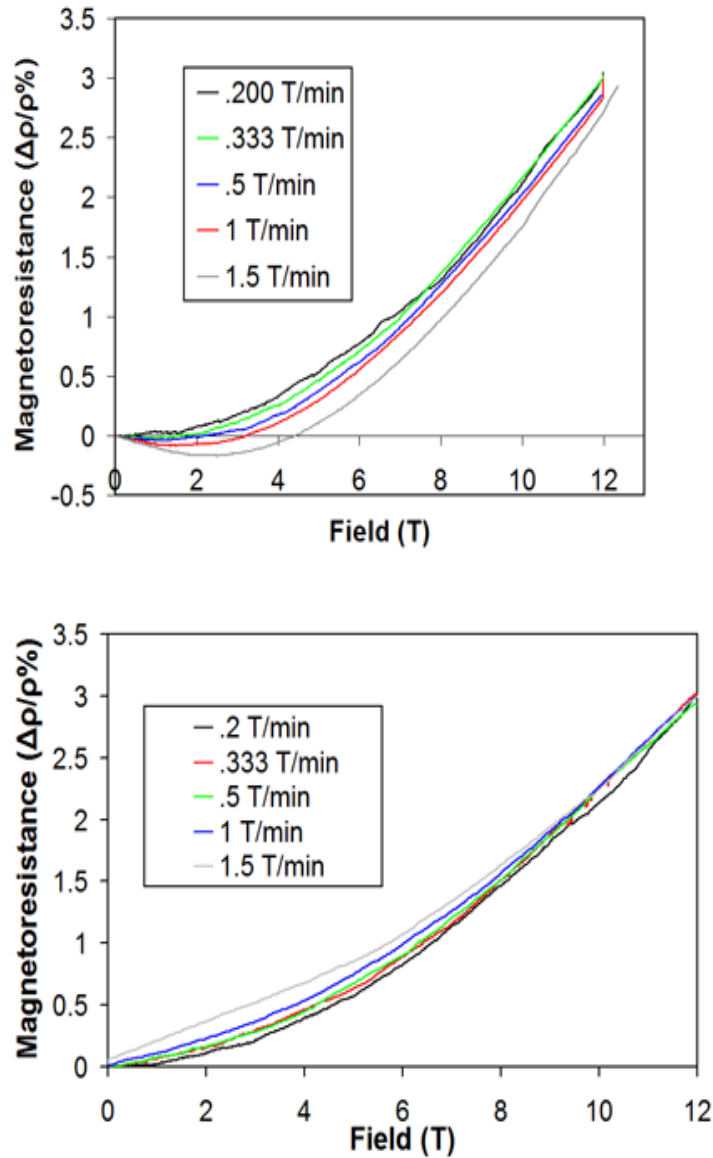


Figure 7.11: Graphs showing the rate dependence of the magnetoresistance at 6 K, (upper) field sweeping from 0 to 12 T, and (lower) field sweeping from 12 to 0 T.

The data sets taken with the magnetic field sweeping up and sweeping down were fit using least squares analysis. The two least squares fit equations were subtracted and the result was plotted as a function of magnetic field in **Figure 7.12**.

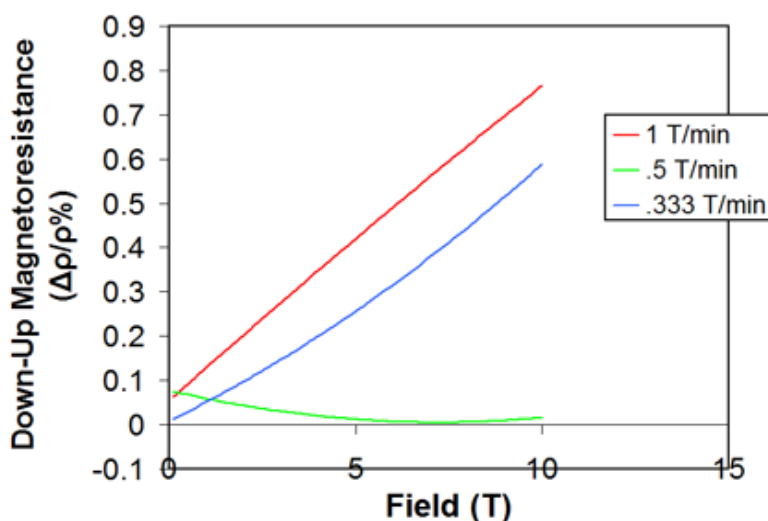
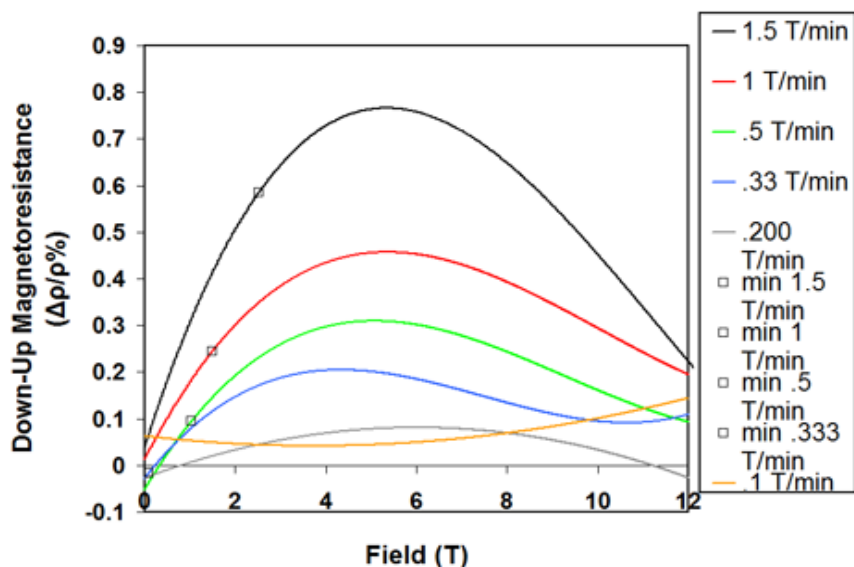


Figure 7.12: Graph showing the sweeping up magnetoresistance minus the sweeping down magnetoresistance (upper) for H₂/Ar annealed CNTs at 6 K. The squares show the position of the minimum of the magnetoresistance when sweeping up in field. All data was taken at 6 K. (lower) Ar only annealed CNTs at 6 K.

We can see from this that the difference between the sweeping down and sweeping up lines is very great for fast sweeping rates and almost disappears for rates ≤ 0.200 T/min.

The squares on the lines in **Figure 7.12** show the minimum of the sweeping up line. For

comparison, the same analysis was also done on Ar only annealed CNT devices and is also displayed in **Figure 7.12**. Here we see absolutely no dependence on sweep rate.

The strong rate dependence of the hysteresis for the ferromagnetic H₂/Ar annealed CNTs can be attributed to large magnetic viscosity effects, nucleation, and magnetization reversal like those normally found in ferromagnetic metallic nanowires, as discussed earlier. As discussed in Chapter 5, for a single energy barrier, there is an activation volume involved the magnetic reversal process. There is also a certain amount of time required for nucleation and a saturation magnetization to decay in an applied field, called the relaxation time. For faster sweeping rates, there is not enough time for the relaxation to occur, resulting in a stronger minimum. The observed minimum then disappears for sweeping rates that are slow enough to allow this decay to occur. With further analysis, we can find the relaxation time constant for spins to decay in the new field. If we take the deviation of the magnetoresistance at a rate and the magnetoresistance at the smallest rate at a certain field value and plot it as a function of the amount of time it takes to sweep to that field value, we can get a graph of the relaxation of the spins in the field. This is found in **Figure 7.13**. Each curve can then be fit to an exponential decay and the time constant can be determined from this fit. We fit the curves with EasyPlot and take the average and standard deviation of the time constants to measure a relaxation constant of $\langle\tau\rangle=4.2\pm 1.5$ minutes.

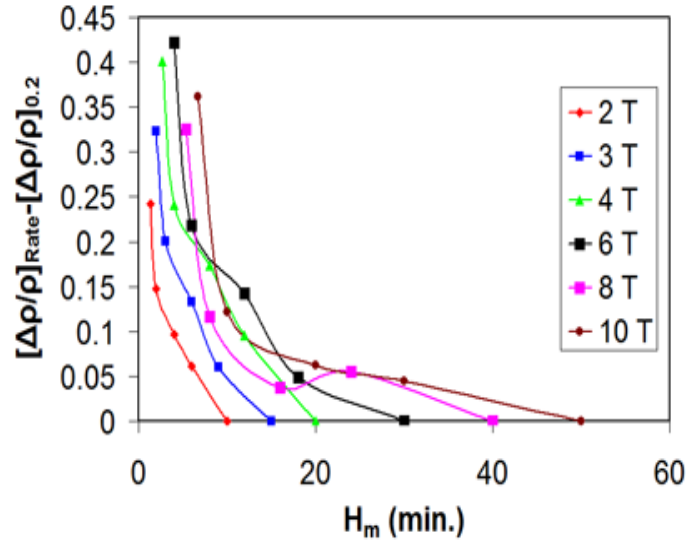


Figure 7.13: A graph of the deviations between the magnetoresistance at a certain field and the slowest sweeping rate magnetoresistance vs. the time it takes to sweep to that field. This shows an exponential decay which can be fit to give the relaxation time constant.

In addition, we attribute the observed hysteresis to anisotropic magnetoresistance (AMR), as discussed earlier. For low fields, the magnetization is not yet saturated, so the MR ratio has a field varying contribution from the second term. However, once a saturating field is reached, the first term dominates and the MR ratio goes like H^2 . Likewise, we would expect to see a direct correlation between the $M(H)$ hysteresis loop (**Figure 5.12**), and the MR ratio curve (**Figure 7.10**). Indeed, for the $M(H)$ hysteresis loop, we see saturation at approximately 2 T, and for the MR ratio curve we see the H^2 term begin to dominate at approximately 2 T. For a normal ferromagnetic nanowire, we would, of course, also expect the magnetoresistance, or more specifically, the switching field and magnetization to depend strongly on the angle between the current and the applied field. However, due to the absence of magnetic shape anisotropy, we have no intuition as to what we would see for these ferromagnetic nanotubes. Unfortunately, due to equipment limitations, we cannot perform this experiment.

7.4.3 Temperature Dependent Magnetoresistance

Figure 7.14 displays a graph of the temperature dependent magnetoresistance for a hydrogen annealed and an argon annealed device.

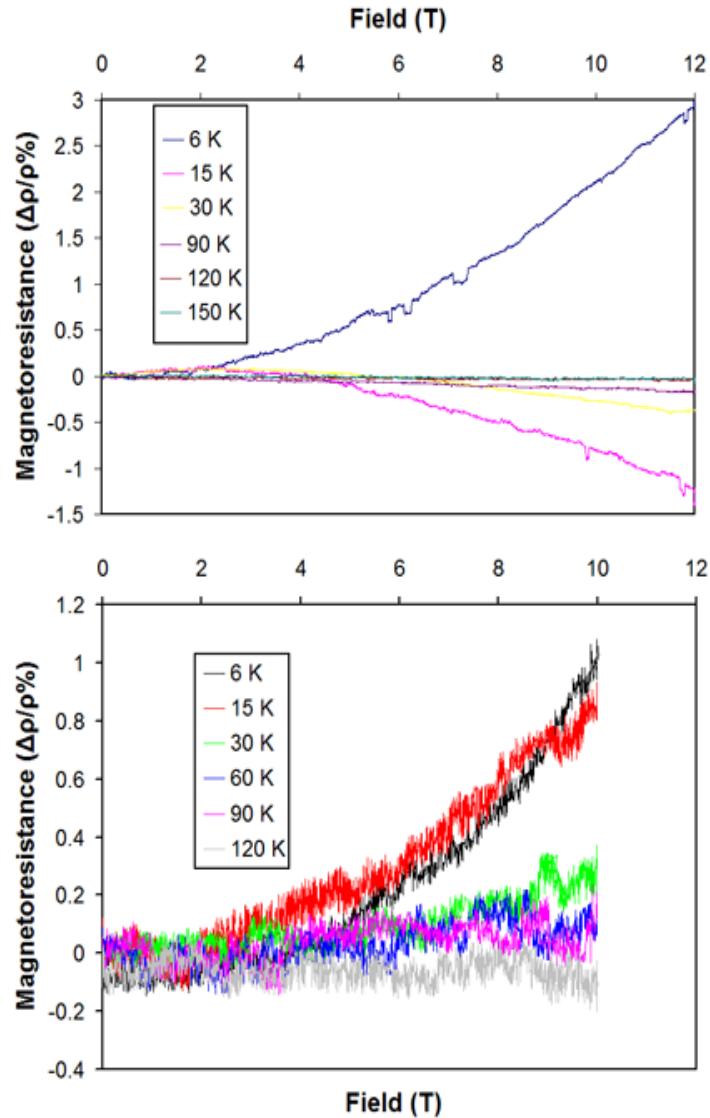


Figure 7.14: Temperature dependent magnetoresistance for a 60 min. CVD device for (upper) H_2 annealing and (lower) Ar annealing.

Many interesting things are happening in **Figure 7.14**. First, we note that there is a positive to negative magnetoresistance transition that occurs in the hydrogen annealed sample and not in the argon annealed sample. This behavior was consistent in all

devices tested. The temperature at which the hydrogen annealed sample began to show negative magnetoresistance does not seem dependent on inner diameter. Transition temperatures ranged from approximately 13-40 K (thus, they were independent of the observed knee in the resistance vs. temperature curves). Furthermore, the Ar only annealed samples never showed this transition and always displayed positive magnetoresistance. In addition, the Ar only devices show much more noise even though the MR ratio shows an increase as a function of field that is approximately the same as in the hydrogen annealed case.

Based on the discussion in Sections 7.1, 7.3.1, and 7.4.1, we attribute this behavior to magnetic field induced increased electron-electron interactions (and the introduction of scattering due to electron-magnon interactions) that lead to a Bright model transition in the hydrogen annealed devices. At low temperatures, and in the absence of a magnetic field, the device behaves like a Luttinger liquid, but only barely, as the disorder in the sample produces many electron-electron interactions that almost make it a 2-dimensional system. However, upon application of a magnetic field, the number of interactions increases significantly, especially at fields higher than 1 T. This is evident in **Figure 7.14**, as all of the interesting behavior happens well above 1 T, and for low fields, it is effectively a straight line. However, despite increased interactions, at low temperatures the device behaves like a metal. As the temperature increases, thermal fluctuations introduce even more disorder into the system. Eventually, the magnetoresistance transitions from the more ordered case to the disordered case and becomes negative. In the case of a non-magnetic Ar annealed device, switching on a magnetic field will not increase the number of electron-electron interactions much. Therefore, the device remains metallic, and, as the temperature increases, thermal fluctuations cause the cause the mobility to decrease gradually. But, because there are

not the same added electron interaction effects due to the absence of ferromagnetism, there is never a transition. So, there are at least two additional sources of scattering available in the hydrogen annealed nanotubes that are not present in the argon only annealed nanotubes. We can rule out Luttinger liquid behavior as a cause because the field will destroy the quantum critical state of the Luttinger liquid. We can also rule out weak localization as a cause because 1) weak localization is expected to be unobservable if ferromagnetism is present [149] and 2) the curve does not fit the shape of the weak localization magnetoresistance very well (**Figure 7.1**).

In addition, we performed some measurements with an applied gate voltage. If the behavior was due to an Anderson (or Mott-Hubbard, for that matter) transition, we would expect the behavior of a gate voltage sweep to be different before and after the transition. For a metal, we expect Coulomb blockade behavior leading to low temperature oscillations of a well-defined period [100]. For a semiconductor, we would expect the appearance of a minimum corresponding to the carrier minimum. However, we found that the behavior was roughly the same everywhere, showing un-reproducible fluctuations. So, the device is most likely a metal, with us unable to reach temperatures low enough to observe well defined oscillations. This means that this is not a metal-insulator or metal-semiconductor type of transition. In addition, due to the disorder of our samples, as compared to other carbon nanotubes, it would make sense that they would behave more like the carbon fibers previously described by the Bright model. **Figure 7.15** shows the mobilities that were calculated as fitting parameters for the Bright model calculated using equations (7.29) and (7.30). The magnetoresistance curves were fit using least squares analysis. The mobilities are very similar for both Ar and H₂ devices. However, we see the mobility of the hydrogen devices fall of a bit more

quickly at lower temperatures, which is a graphical representation of the Bright transition from order to disorder.

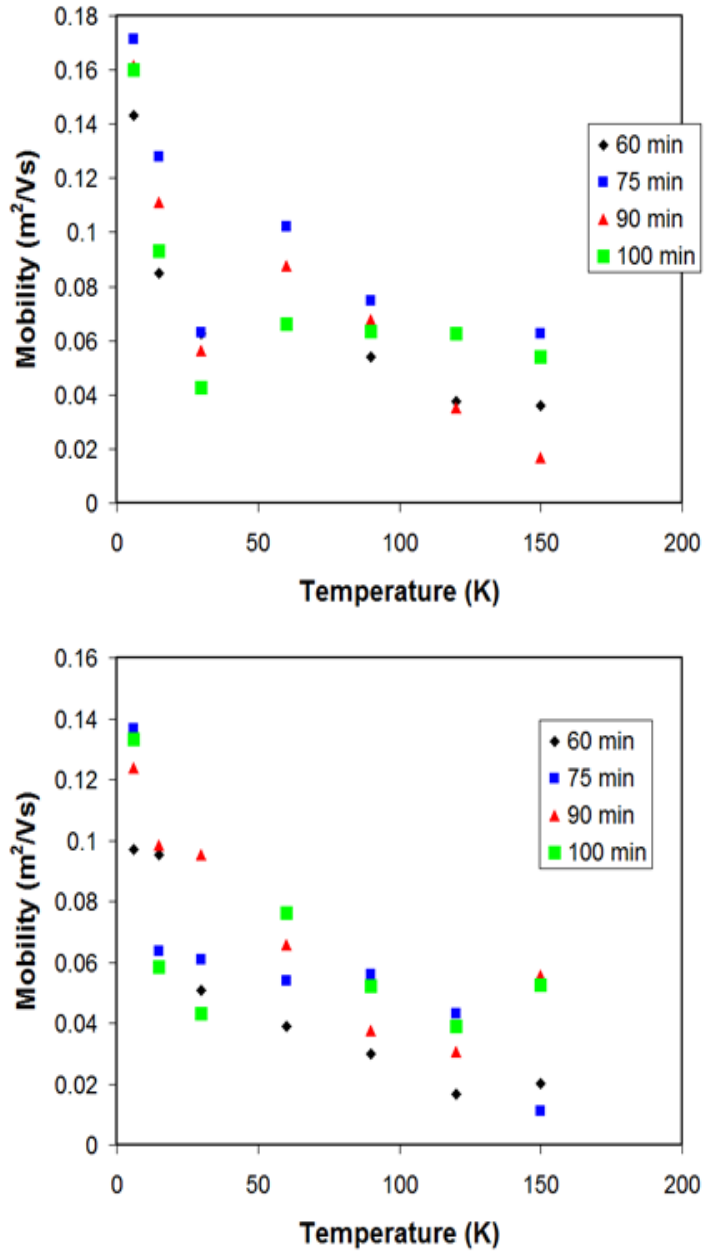


Figure 7.15: Mobilities calculated as parameters of the Bright model for (upper) Hydrogen annealed CNT devices and (lower) Argon only annealed devices.

Chapter 8: Transport Properties of Graphene

8.1 Introduction and Theory

If one unrolls a carbon nanotube, one will be left with graphene sheets held together by Van Der Waals forces. It is interesting, then, that graphene should have such different properties from carbon nanotubes. These unusual properties arise from the linear dispersion relation of graphene's band structure $E(k) \sim k$, from which it follows that carriers in graphene behave as 2-dimensional relativistic, massless chiral Dirac fermions (a combination impossible in 3-dimensional particle physics) and have many fascinating properties unique both to condensed matter and particle physics.

The Hamiltonian of carriers in monolayer graphene is given by

$$H = \hbar v_F \begin{pmatrix} 0 & k_x - ik_y \\ k_x + ik_y & 0 \end{pmatrix} = \hbar v_F \vec{\sigma} \cdot \vec{k}, \quad (8.1)$$

Where, v_F is the Fermi velocity and $k_{x,y}$ is the quasiparticle momentum and, unlike other condensed matter systems, is linear instead of quadratic in k ($E = \hbar v_F k$) [164, 165]. The σ matrices arise from the fact that there are two atoms per unit cell in the graphene crystal, and thus act as a pseudospin variable (unrelated to the intrinsic electron spin, which must be treated separately) [164]. The band structure of graphene is made up of two different sublattices that intersect at $E=0$, which also corresponds to an overlap of the conductance and valence bands in the Brillouin zone, resulting in a conical shaped energy spectrum [166]. Pseudospin is a direct result of the contributions of electronic states near $E=0$ contributing to different sub-lattices requiring the use of spinors in the wavefunction [164, 167]. This Hamiltonian describes a massless chiral fermion propagating with a constant Fermi velocity v_F ($= 1 \times 10^8$ cm/sec, $1/300$ the speed of light) independent of the energy of the particle. This is a truly relativistic system with the

speed of light replaced by v_F . Chirality (the projection of the momentum operator on the spin matrix) is preserved for both electrons and holes (which are the particle-antiparticle pairs predicted by the relativistic Dirac formalism) [164]. This creates a situation remarkably analogous to that found in relativistic Dirac relativistic quantum electrodynamics, and the Hamiltonian describes a 2-dimensional analogue of the massless Dirac neutrino. In fact, extremely high mobilities of 15,000-77,000 cm²/Vs at room temperature and almost 200,000 cm²/Vs for graphene sheets recently suspended between contacts have been observed [164, 168].

These unusual properties lead to an integer quantum Hall conductivity of $\sigma_{xy} = \pm 4e^2/h(N+1/2)$ [164, 169]. Here, the factor of 4 is due to particles and holes and their double degeneracy. This anomalous shift of $1/2$ (unlike the QHE effect observed in any other material) arises from a Landau level ground state degeneracy at zero energy shared by both particles and holes and unique to graphene [164]. The fractional quantum hall effect has also been predicted, but never observed [170, 171]. The fact that all carriers, regardless of energy, travel with speed $v_F = 1 \times 10^8$ cm/sec (extremely high for carriers in condensed matter systems) also suggests that graphene devices could operate at very high frequencies, perhaps into the Terahertz range. However, in order for this to be realized, the fundamental properties of graphene must be known in greater depth.

To date, graphene has been experimentally studied only in magnetic fields perpendicular to the graphene plane, the standard geometry for observation of the QHE. Keeping in line with the rest of graphene's properties, the magnetoresistance has also been found to behave very anomalously. Interestingly, weak localization does not occur at all in graphene near the Dirac point and graphene is always metallic [172]. And, away from the Dirac point, its occurrence was random and sample dependent [164]. Although

it is not quite understood why this happens, it could be due to the destruction of time-reversal symmetry due to strain and warping of the graphene sheet [164].

Parallel fields affect only spins of 2-dimensional carriers, and therefore any response to a parallel field is associated with spin properties. In zero magnetic field, graphene is a gapless semiconductor with two Fermi points (valleys) in the Brillouin zone (as discussed above). An applied parallel magnetic field breaks the symmetry of the system and pushes spin bands for spin up and spin down electrons and holes in opposite directions. The electron and hole states then experience an attractive Coulomb interaction, which leads to an instability and transforms the system into a gapped insulator with extended Fermi surfaces for electrons and holes of opposite spin. Under these conditions, exciton condensation due to the attraction between electron and holes has been theoretically predicted [173] but not experimentally observed.

However, a major problem with graphene is that the devices made from it are extremely fragile. They have a huge susceptibility to damage by electrostatic discharge. And, graphene sheets appear to be very brittle as heating and cooling too quickly can destroy them as well. Too make matters worse, due to the great ability of graphene to adsorb molecules from the air, devices must be cleaned by annealing and then kept at vacuum at all times. Too much exposure to air will cause adsorption, resulting in transport behavior that is far from ideal. In particular, the minimum of conductivity (corresponding to a minimum in carrier density) will shift dramatically in unclean samples and the QHE may not be distinguishable from the background noise. In fact, if the graphene is not rather clean, increased electron-electron interactions can cause it to lose its conductance quantization ($\sigma=4e^2/h$) completely [174]. If this occurs, one must remove the sample from the instrument and risk damage by electrostatic discharge.

Figure 8.1 shows an example of a device destroyed by electrostatic discharge and too-fast heating and cooling.

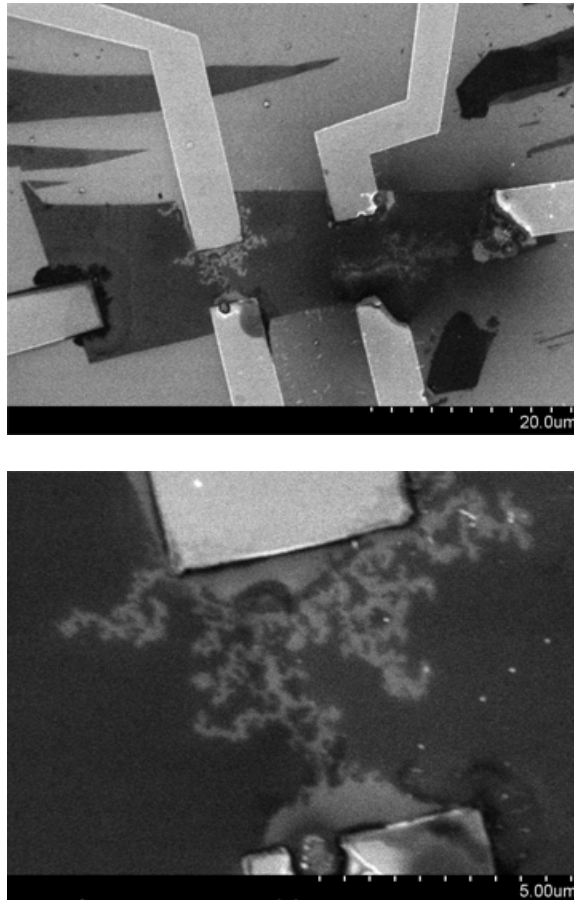


Figure 8.1: SEM images of a graphene device destroyed by electrostatic discharge and too rapid heating and cooling. The upper image shows damaged gold contacts and cuts in the graphene monolayer. The lower image shows a close up of one of the areas between contacts where the graphene was destroyed.

For these reasons, we had a terribly difficult time extracting data from our samples. Of the approximately 10 devices that we worked with, only 2 produced good data. And, because it can take weeks to fabricate a device, this low success rate is very frustrating. We found that even when extraordinary precautions are taken to protect the devices (using static-free tweezers, bench-top air ionizers, humidity controlled lab rooms, transporting the sample only on rainy days, and grounding out the experimenter

and every piece of equipment) the device may break before any data is even measured. However, the devices that did work, continued to do so until they were removed from the apparatus for a necessary wire bonding change or re-annealing, thus exposing them to electrostatic discharge damage. Theoretically, a good device that is left in position can continue to work for months without failure [175]. Unfortunately, due to instrumental considerations, we were never able to realize this. Despite our difficulties, here we examine the temperature dependence of the QHE in graphene. We also examine some of the parallel field transport behavior.

8.2 Temperature Dependence of the Quantum Hall Effect

For the measurements that follow (Sections 8.2 and 8.3), devices were made by the methods described in Chapter 6 with the collaboration of Graphene Industries, Ltd. (located in Manchester, UK). For ultra-low temperature data, we use an Oxford Instruments, Ltd. Kelvinox dilution refrigerator. For variable temperatures from approximately 5K-room temperature, we use the same Cryogenics, Ltd. superconducting magnet system and Cryo-Industries of America variable temperature insert used in Chapter 7 (see Appendix C). A voltage gate is made by bonding the chip holder bed, which has been metalized with gold, to one of pins on the chip holder. High purity silver paint is used to glue the device into the chip holder to ensure conductivity between the bed and the silicon device substrate. To take data we use a 4-probe AC set up. An AC current is supplied from a lock-in (SRS Model SR810) at a low frequency (1-5 Hz). The current is converted to voltage and placed across the source and drain contacts. Voltage data from the two voltage probe contacts are placed into a pre-amplifier (SRS Model SR570) and filtered. The result is fed back into the lock-in. A voltmeter (HP34401A) takes the voltage data point from the lock in. Gate voltages are applied using Keithley Model 236 source-measure unit. Values of temperature are recorded by reading the

analog voltage output from a voltmeter (Hewlett Packard model HP34401A) directly from the LakeShore model 340 temperature controller. Magnetic field is recorded by reading the analog voltage output from the magnet from a Hewlett Packard model HP34401A voltmeter.

Besides noticing that the QHE survives up to room temperature in graphene [176], little has been done to study the temperature dependence graphene devices. A notable exception, however, is the theoretical work of L.A. Falkovsky, who performed a theoretical study of the effects of defects on carrier transport as a function of temperature [177]. **Figure 8.2** shows the temperature dependence of the resistance of graphene. We can see that the resistance decreases slightly as a function of temperature. This is most likely the result of decreased phonon interactions at lower temperatures. This is expected for a good ballistic conductor, such as graphene [139]. Moreover, these results are supported by the Falkovsky, who predicts the same behavior, including the rather quick drop in resistance at lower temperatures for clean graphene samples [177]. Interestingly, though, this is the opposite of the behavior found in similarly ballistic carbon nanotubes in Chapter 7 (which we have explained is due to the status of the nanotube as a Luttinger liquid, which results in the Luttinger scaling of the conductance as T^α).

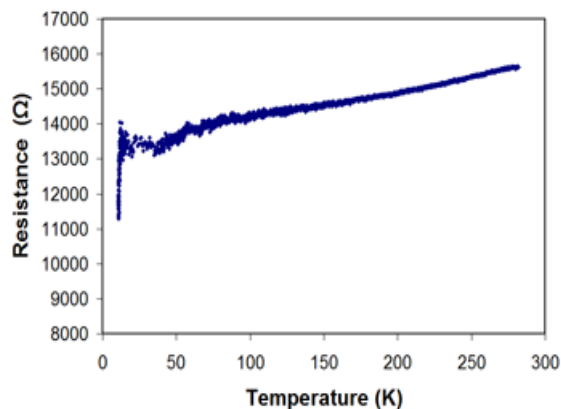


Figure 8.2: Temperature dependence of the resistance of graphene.

Figure 8.3 shows an example of the QHE in one of our graphene devices at ultra-low temperature and at 9 T. The carrier minimum is shifted to the left of zero gate voltage (to approximately -7.8 V) due to defects in the graphene lattice and adsorbed molecules on the surface. The presence of randomly charged impurities can create scattering that leads to this asymmetry in electron and hole states [178]. However, experimentally, very few graphene samples have a carrier minimum at zero (most likely due to the presence of impurities between the graphene sheet and the substrate that cannot be removed by annealing), and this sample is determined to be quite clean and defect free.

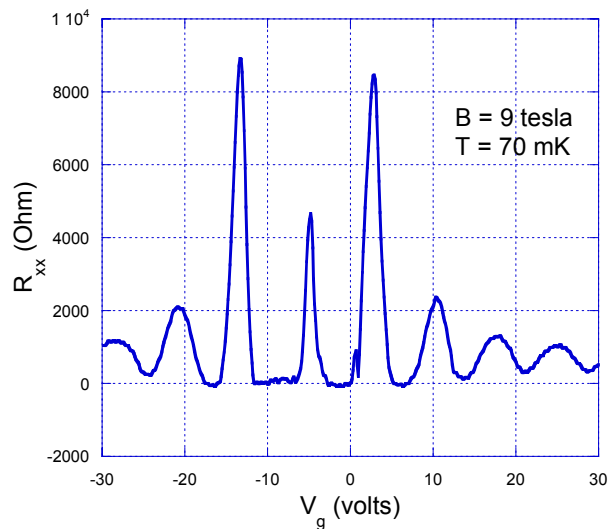


Figure 8.3: R_{xx} as a function of the back-gate voltage in one of our samples taken in a dilution refrigerator. The peak is shifted from zero due to impurities.

Figure 8.4 displays a graph of the Shubnikov-de Haas oscillations (SdHO) in a graphene sample. We find maximums at approximately 4, 6, 8, and 11 T, corresponding to integer values of the Landau filling factor ν . This is in contrast to a normal metal where it is expected that integer values of ν occur at minima [165]. It has been found

that the SdHO are strongly dependent on temperature at high carrier densities, and will decay more rapidly as the temperature increases [165].

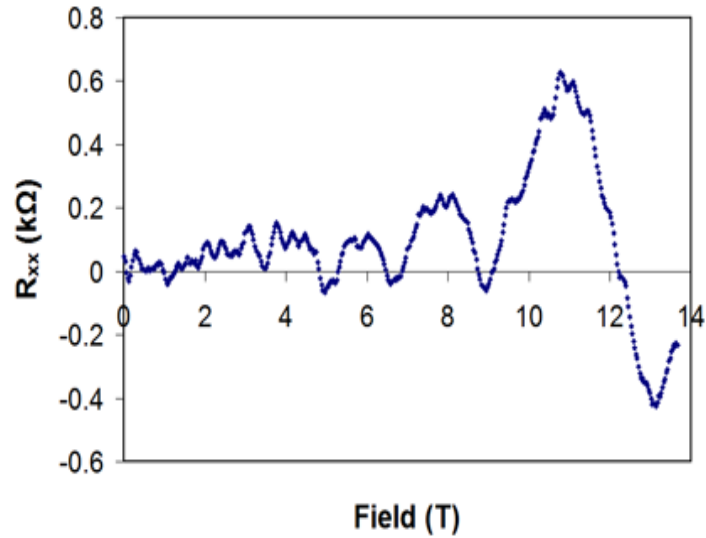


Figure 8.4: SdHO at $V_g = -10$ V at 6 K.

We are interested in learning more about the affect of temperature on the QHE in the graphene sample. **Figure 8.5** displays the QHE for a graphene sample as a function of temperature. We can see that, as predicted, the QHE survives up to room temperature. Moreover, the oscillations begin to decay very quickly at higher temperatures.

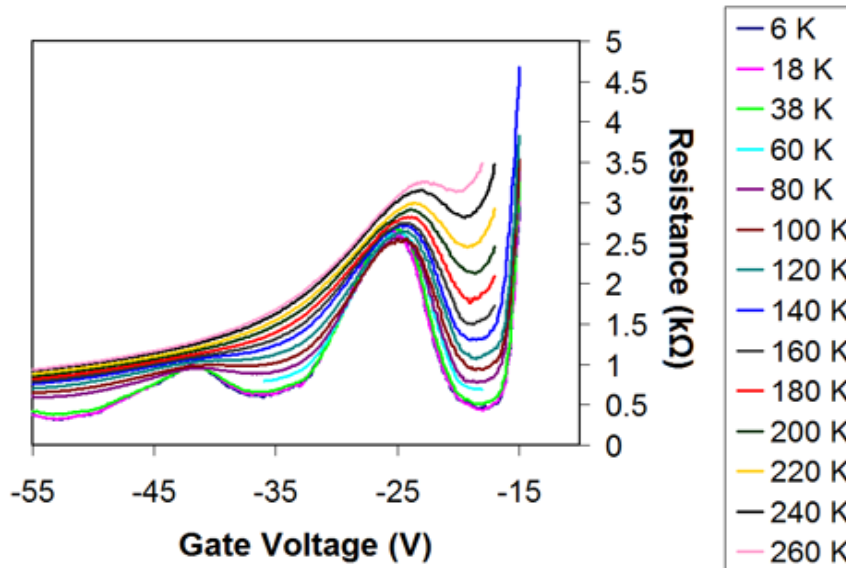


Figure 8.5: Temperature dependence of the QHE in graphene.

To quantify the affect of temperature, we examine the secondary Hall peak, pictured in **Figure 8.5**. We take the derivative of the curve and measure the resultant peak to peak width, ΔV_g . This is plotted as a function of temperature in **Figure 8.6**.

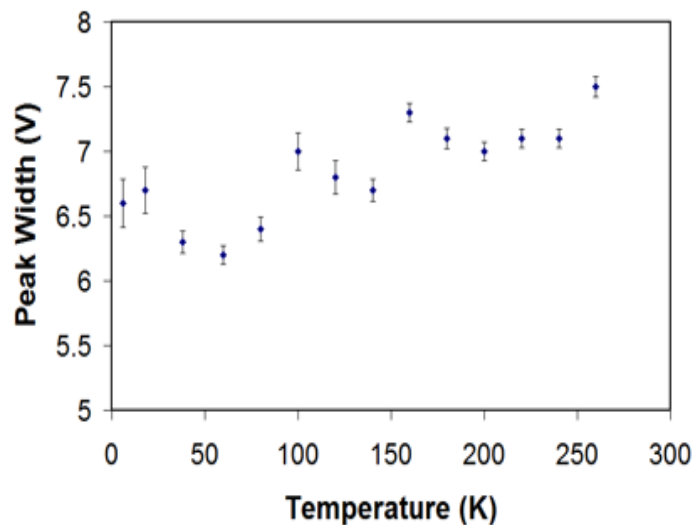


Figure 8.6: Temperature dependence of the width of hall peak. The width slowly increases as the temperature increases.

We can see that the width of the peak indeed increases slowly, and quite linearly as a function of temperature. Here, the error bars are calculated by taking the average standard deviation of the derivative points after that curve has been smoothed by averaging.

8.3 Parallel Field

Figure 8.7 shows the dependence of resistance on gate voltage for different magnetic fields applied parallel to the graphene plane. **Figure 8.8** shows the resistance as a function of applied parallel magnetic field for several different gate voltage values.

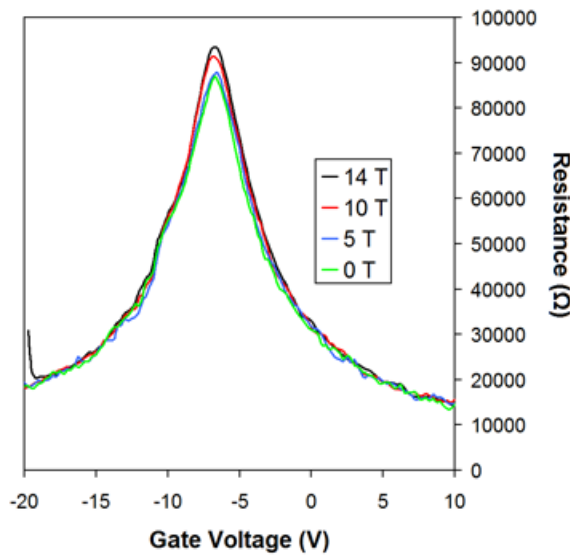


Figure 8.7: Gate voltage sweep for graphene in a parallel field at 5 K. The ordering of the curves in the magnetic field is consistent with the theory that says that a parallel field will cause the graphene to become increasingly more insulating.

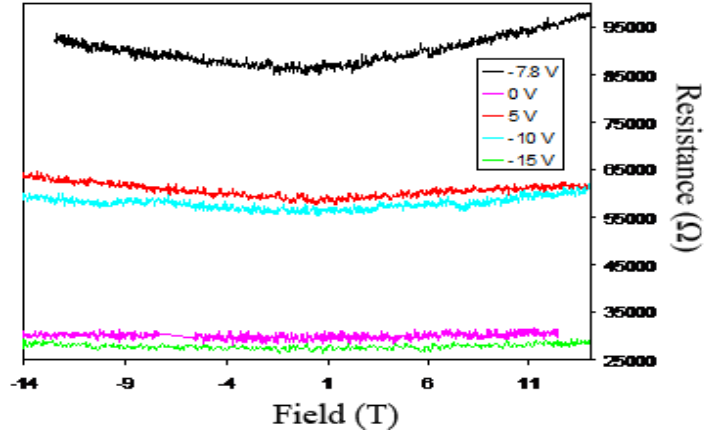


Figure 8.8: Resistance vs. field at various gate voltages for a graphene sample in a parallel magnetic field at 5 K.

Our results are consistent with the theory developed by Aleiner, et al. [173]. Although we do not see the predicted metal-insulator transition, we see positive magnetoresistance at the place where the gate voltage gives a peak in resistance (approximately -7.8 V, for this device). We also see that as the magnetic field is increased, the height of the resistance peak increases. When the field is applied, the graphene begins to become more insulating. This result can be attributed to the predicted interactions, because for free electrons (as we expect in a 2-dimensional non-interacting gas of electrons in graphene), we would expect the opposite behavior, whereby a field would create a Fermi surface for particles and holes of opposite spin [179]. However, the theory predicts that thermal fluctuations can cause a lot of noise in the sample. We will need to significantly lower the temperature in order to eliminate this noise and see the predicted transition.

Chapter 9: Conclusion

9.1 Restatement of Major Results

We have shown through a systematic study of porous alumina formation that the current models do not accurately describe the process because they all assume that oxidation and dissolution occur with the same weight. The pH of the solution clearly does not factor into the process in the way the models assume. However, by studying the formation of nanonoodles, we have learned that dissolution will occur if the sample is allowed to anodize for long times, at high temperatures, under severe electric conditions, or when the acid's ability to etch is enhanced. This should be taken into account in the models by adding a weighting factor that includes these variables to the dissolution part of the equation. Furthermore, we have shown that the models also do not accurately depict the stability formation of the pores. Although they do not at all describe the 2-dimensional stability, possibly by overlooking the proper affects of pH and acid type, they fail to consider the 3-dimensional stability, which manifests itself in the formation of dendrite structures in the alumina. We have shown under what conditions these dendrites form and what implications they have on the physical models. We have also shown that by systematically altering the voltage during anodization we can create branched and bifurcated porous structures.

Next, we have shown that porous alumina templates are ideal for synthesizing a variety of nanowires and nanotubes by utilizing the templates as a scaffold. Nanowires can be synthesized by chemical self-assembly using AC electrodeposition. The ideal conditions for nanowire synthesis occur in the center of a deposition rate vs. frequency curve. Here, the current does not oscillate too much and can still penetrate the barrier layer. Moreover, we have shown that the pH of the deposition solution must be kept in a

certain range in order for deposition to occur. We have demonstrated our unique three step process for the fabrication of PANi composite nanowires. We have also shown that carbon nanotubes can be synthesized in the porous alumina without catalyst by CVD. Depending on the time of CVD, the inner diameter of the nanotubes can be changed.

We have shown that alumina/metal arrays have a valuable application as negative index of refraction metamaterials. The two predicted SPRs have been observed, and we expect negative refraction to occur.

The magnetic properties of our template synthesized structures have been studied. We have shown that magnetism can be a powerful tool in understanding the structure and make-up of nanostructures by examining the magnetic properties of bifurcated Co nanowires and PANi composites. By measuring the various magnetic properties, we have learned more about how the magnetic interactions between the constituent parts of the nanowire and between each nanowire and its neighbors contribute to the overall magnetic behavior of the array. We are also the first to experimentally demonstrate carbon nanotube magnetism. We show that H-complex and C and H adatom magnetism can occur easily in our nanotubes, which are more disordered than other nanotubes synthesized by different methods. Due to the great disorder of our CNTs, H induced magnetism can be created by simply annealing the carbon nanotubes in a tube furnace at temperatures >600 °C. We show that this magnetism falls off greatly for annealing temperatures below 600 °C. We also show that the magnetism is stable at room temperature, exhibits no shape anisotropy, has a Curie temperature higher than the expected temperature of increased graphitization, and is dependent on the inner diameter of the nanotube.

We have described the process by which a template synthesized nanostructure can be prepared for device applications. We have described how to remove

nanostructures from the templates and place them in solutions that can then be deposited on Si/SiO₂ grown by wet or dry oxidation. We have described methods of electrical contact fabrication including electron beam lithography, FIB, and photolithography. Metals can then be deposited onto the substrates using the described deposition methods. We have discussed the various pros and cons of each method. In addition, we have discussed methods for better orienting and improving the contact resistances of nanotube devices including dielectrophoresis and electron beam soldering. However, we have shown that the best method of improving contact resistances is by annealing, which also creates the magnetism previously discussed. Furthermore, we have shown how to fabricate graphene devices out of bulk HOPG. We have shown how to exploit the destructive optical interference of graphene with the purple substrate to locate monolayer graphene and then to confirm this result with Raman spectroscopy. We have shown how to clean the devices with hydrogen annealing.

We have studied the transport and magnetotransport properties of our unique ferromagnetic carbon nanotubes and compared the result to similarly disordered unferromagnetic nanotubes. We have shown that at low temperatures and in the absence of magnetic field, they conduct ballistically and behave as Luttinger liquids, but are just barely Luttinger liquids, owing to a small interaction parameter, g . By switching on a magnetic field, we have shown that the Luttinger liquid is destroyed. This also results in the appearance of increased electron-electron and electron-magnon interactions that are not concurrent in non-magnetic nanotubes. This greatly increased disorder leads to a Bright transition as a function of temperature in the ferromagnetic nanotubes that does not occur in the non-magnetic nanotubes because they lack these increased scattering pathways. In addition, we find that the application of magnetic field results in a field sweeping rate dependent hysteretic magnetoresistance for the ferromagnetic nanotubes.

We have shown that the rate dependence can be explained by magneto-viscosity effects and nucleation. And, we have shown that the hysteresis can be explained by anisotropic magnetoresistance.

Finally, we have performed some measurements in graphene devices. We have shown that the QHE survives up to room temperature and that the peak width increases somewhat linearly as a function of temperature. We have also shown that the ordering of the resistance peaks of graphene in a parallel field supports the prediction of a field driven metal-insulator transition.

9.2 Outlook for Future Work

There is a great amount of work that is left to be done on these topics in the future. Now that we have discovered that the current theoretical models of porous alumina formation do not accurately describe the growth and stability of porous alumina and we have suggested how they can be altered, it is necessary that a new theoretical model be created. Furthermore, there is a vast quantity of literature, both theoretical and experimental on the formation of dendrites in different types of materials. It would be of great interest to see if any of these models and results can describe the dendrite growth process in alumina and how they can then be applied to the overall porous alumina growth process. Also, now that we have created the new material of nanonoodles, it would be interesting to find an application for them. As alumina is such a good dielectric, it would be of interest to measure the capacitive properties of the nanonoodles.

There is still much to be learned about the PANi composite structures. Unfortunately, we were unable to release them from the templates and measure their transport properties. We found that all acids that are capable of dissolving the template also destroy the PANi. We also tried releasing them in basic solutions. However, this

was also unsuccessful. The electrodeposition process of the PANi structures can also be fine tuned. It is apparent that at some deposition voltages and concentrations of aniline, the resulting deposited structures are of a much more squiggly nature. Sometimes the deposited structures are very straight. There also appears to be a situation in which, rather than tubes, the PANi forms a mask in the shape of the template over top of the template itself. In addition, we have not yet found an application for the PANi structures. We had the idea, however, to try to fashion a coaxial nanocable. Undoped PANi is very insulating. It could act as a sheath separating two conductors, both electrodeposited. Or, the PANi can be doped, in which case it will conduct electricity quite well. It is unclear how this doping could be accomplished. Perhaps by introducing impurities to the deposition solution itself. Moreover, it would be of interest to experiment with the great capacitive properties of the PANi nanotubes. We noticed that during SEM imaging, there was a huge amount of charging, even greater than that of alumina. All of these considerations need to be experimented on in depth.

Although we have shown that alumina/metal composites display the necessary conditions for negative refraction, it remains to show this phenomenon. To do this, one can easily create lenses out of the composite arrays and place them over a diffraction grating or other pattern. It needs to be demonstrated that these lenses do indeed focus the light by negative refraction. Moreover, by experimenting with post-processing of the filled templates, it may be possible to narrow the SPR. We assume that the reason why we see such wide peaks is due to non-uniformity and granularization in the deposited wires. It may help to anneal the arrays under pressure to form a more uniform, clean sample.

In addition to demonstrating negative refraction, there is great amount of optical work that can be done. Over the course of our alumina experiments, we noticed that as

the pore diameter increases, the color of the template become more yellow-gold. For very large diameter pores, the color is a very deep gold. This can be explored both theoretically and experimentally. In addition, we began some optical experiments on the carbon nanotube arrays. We found that the reflection was dominated by noise, most likely due to the aluminum backing and alumina. We did preliminary measurements on nanotubes of a variety of diameters. It would be of interest to remove the aluminum backing and reattempt the experiments for possible applications to negative index materials.

Due to the newness of ferromagnetic carbon nanotubes, there is much that can still be done. Although we performed some experiments to describe the affect of electron-electron interactions, there is still much that can be done to help differentiate the types of interactions in the nanotubes in an applied field. And, the lack of observation of any shape anisotropy, even though we found AMR, is intriguing. This effect needs to be explored by changing the angle at which the field is applied. In addition, it would be of interest to perform ultra-low temperature experiments in a dilution refrigerator to see if any weak localization effects can be observed and if the resistance as a function of temperatures saturates or continues to increase exponentially. And, much work can be done on the Argon only disordered carbon nanotubes. It would be of interest to go to higher magnetic field and lower temperature to see if localization can indeed cause the predicted metal-insulator transition that has yet to be observed in nanotubes. Moreover, it would be interesting to try to remove some of the defects in the nanotubes by higher temperature annealing and see how this affects the transport behavior.

The fact that the nanotubes can easily uptake hydrogen has great potential in application. Experiments can be done where the nanotube can be annealed in hydrogen

to become magnetic, then annealed in argon. Does it then return to its non-magnetic state? How many times can it be magnetized without a loss in magnitude of magnetic moment? Does the moment decay slightly each time? These structures can then be used as hydrogen storage cells for the generation of electricity generation. It is possible that the entire cell could be a closed system whereby the nanotubes sit in a hydrogen atmosphere. Heating once would cause uptake of hydrogen, heating again would cause the dispelling of hydrogen. This could act as the cycle of an engine. It would also be of interest to see if any other elements can also be intercalated or bonded to the nanotubes by annealing. Perhaps nitrogen will cause the same effects as hydrogen. Or, perhaps the heated nanotubes will uptake carbon dioxide and have applications as carbon dioxide scrubbers.

Finally, the experiments herein on graphene are hardly complete. However, due to the immense difficulty in getting working, robust devices, it is of immediate necessity to develop methods for creating devices that are faster and easier to fabricate and more hardy. It is also of interest to develop ways to make bigger graphene flakes more systematically. We attempted to apply the process of dielectrophoresis to graphene exfoliation, but were met with limited results. It did produce flakes, but they were small. However, perhaps this electro-mechanical cleaving can be tailored to better produce more uniform flakes. And, we have not yet shown the predicted metal-insulator transition and fully explored the affect of parallel magnetic field.

Appendix A: The Quantum Designs SQUID MPMS Oven

The following is a brief guide for the operation and use of the Quantum Designs SQUID MPMS Oven. **Figure A1** displays a picture of the SQUID.



Figure A1: The Quantum Designs MPMS SQUID. The left box is the SQUID and the right box is the controller unit.

Figure A2 displays a picture of the oven. The oven is inserted into the sample space of the SQUID following the step by step instructions in the SQUID manual. However, one must take care to make sure the upper limit of the temperature sweep is reset to the upper limit of the oven. The default upper temperature limit of the SQUID is 400 K, however, now that the oven has been inserted, it should be changed to 800 K. If this is not done, a temperature sweep above 400 K will result in an error.



Figure A2: The top end of the oven and the bottom end of the transport rod.

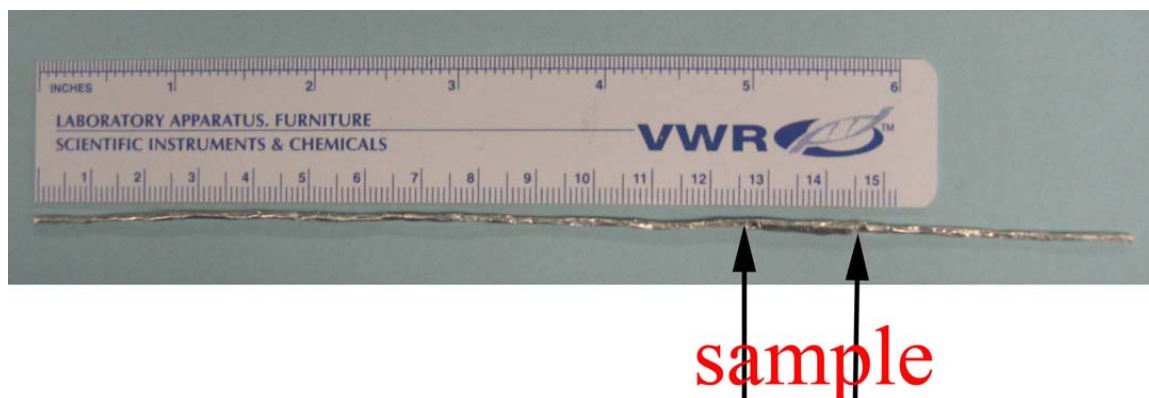


Figure A3: A picture of an aluminum sample holder. Displayed is a holder that is the ideal size for measurements.

The space available for a sample holder in the oven is quite small (about 0.25 cm in diameter), so great care must be taken to fashion a sample holder that is small enough to fit and still has enough structural integrity to hold up to some bending. There can be very little friction between the sample holder and the walls of the oven in order to receive accurate results due to the oscillation involved in an RSO measurement. **Figure A3** shows an example of a sample holder. A sample holder is made from high purity aluminum foil. The foil is cut into a strip approximately 0.9 cm in width. The sample is positioned and placed in the foil. The foil is then folded in half and around the sample. The foil is folded in half and pressed together another two times. A pair of tweezers is then used to squeeze the holder into a circular shape. The entire length of the sample holder should not be more than 19.25 cm. If the holder is too long, the holder carrier in the SQUID transport will not reach its necessary position and the sample holder itself

will bottom out on the oven insert. If one suspects that the holder is too long and is bottoming out, one can perform a full DC scan (not in RSO mode). If the holder has bottomed out, the scan will show a flat line and part of a centering peak. A small hole should be drilled at about 0.25 cm from the top. The sample center should be located at about 13.5 cm. This accounts for the addition of the oven to the transport column, which adds a small amount of length to the normal column resulting in the need to make the sample/transport rod longer. The holder is then inserted into the hollow end of the transport rod. A piece of wire is threaded through the hole drilled in the transport rod, going through the hole drilled in the sample holder, and then out the other side of the transport rod. The wire is then twisted one layer thick around the end of the transport rod until the sample holder is secure. The end of the transport rod has been machine shaved down to account for the thickness of the wire.

We found that the background noise measurement of the empty oven was on order of 10^{-7} emu. The background noise measurement of the sample holder is on the order of 10^{-6} emu. So, in general, the background is small compared to the signal of any strongly magnetic samples.

The advantages to this method are 1) The sample holder is quickly and easily made, 2) Because it is high purity aluminum foil, the background noise is small, and 3) The sample is contained in an enclosed space, which prevents contamination of the oven space if there is any evaporation during heating.

Appendix B: Princeton Measurements Corporation MicroMag AGM

The following is a short step-by-step guide to operating the Princeton Measurements Corporation MicroMag Model 2900 AGM. **Figure B1** displays a picture of the AGM.



Figure B1: Picture of the MicroMag AGM.

1. Turn on water cooler.
2. Turn on Magnet Power Supply
3. Turn on Magnet Controller
4. Open "MicroMag AGM" software
5. A screen will pop up asking you to "Abort" or "Continue". Click "Continue"
6. The software has two boxes. The box on the right contains measured values. The box on the left contains values to set. See the manual for specific options.
7. In the left box, click the "0.000" next to "Applied Field." A box will pop up. Click the box next to the box that says "Magnet Power Supply". Click "Off" to switch the Magnet on. You will hear a pop from the AGM.

8. Before taking any measurements, the AGM must be calibrated. It must also be calibrated when switching probes.
9. To calibrate, take the calibration sample out of the box and place it on the desired probe with a SMALL amount of grease.

IMPORTANT: The probes are very fragile. Any small wrong movement will break them. Rough handling of their shafts will damage their ability to measure properly. WHEN THE PROBES ARE IN USE, FOCUS ALL ATTENTION ON THEM. NEVER LEAVE THE PROBES OUT OF THE BOX WHEN NOT USING THEM. ALWAYS USE THE PROBE MOUNTING PLATFORM TO MOUNT YOUR SAMPLE.

10. Carefully place the probe in the AGM.
11. Pull out the switch on the front of the probe holder. Pull it with a quick jerk to release the probe isolator.

IMPORTANT: DO NOT PULL THE PROBE ISOLATOR OUT. USE THE SWITCH WITH A QUICK JERKING MOTION.

12. While holding the probe holder at the "elbow," release the z axis lock switch.
13. Lower the sample until it is lined up in the center of the field coils. Note that the z-axis adjustor does not work very well, so it is best to line the sample up by eye.
14. In the software click "autofunctions" in the toolbar. A box will pop up.
15. click "initial autotune"
16. When the autotune is done, the program will ask if you want to keep the values it measures. Yes you do.
17. now click "incremental autotune"
18. Again accept the measured values and close the autotune box.
19. Go to the "applied field" box again. Enter a centering field here, usually 5000 Oe.

Close the box. The applied field should register in the measurement box on the right in the software.

20. Go to the "tools" menu in the toolbar. Click "optimize." A box will pop up containing a blue bar and a sensitivity adjustment.
21. Adjust the sensitivity until the bar does not fluctuate rapidly.
22. Center the sample in the x-plane using the side adjust knob. Minimize the magnitude of the blue bar. Click "tare" to reset the measuring arrows.
23. Center the sample in the y-plane using the rear adjust knob. Maximize the magnitude of the blue bar.
24. Check by eye that the sample is centered and the software is correct. If the sample is very far out of the center, the software often behaves oddly.
25. Go back to the autofunctions menu and do another incremental autotune and accept the changes.
26. Go to the toolbar and select "Measurements," "Direct Moment vs. Field," and "Hysteresis Loop."
27. A box will pop up asking for parameters for the hysteresis loop. For the calibration, it is not necessary to demagnetize the sample. Also, a maximum field of 5000 Oe is fine.
28. Click execute to run the hysteresis loop.
29. When it is finished, a paramagnetic graph will be displayed. First adjust the slope by going to "tools," "adjust slope (automatic)," and a box will pop up. keep the 70% default setting. click "ok."
30. Now calibrate by going to "tools" and selecting "calibrate." Type in 77.61E-3. Push enter. The AGM is now calibrated.
31. To remove the probe, hold the probe holder at the "elbow." Unlock the z-axis switch. Raise the probe out of the coils. Push in the probe isolator. CAREFULLY remove the

probe and place it back on the probe mounting platform.

32. Remove the calibration sample and place it back in the box.

33. Put your sample on the probe. More grease may not be necessary.

34. Repeat steps 10 through 29 for hysteresis loops with minor modifications. Now you may want to demagnetize for ferromagnetic samples and apply a field of more than 5000 Oe or less for centering. You can save the graphs after taking them. The data files can be opened using excel on other computers.

35. For other measurements, repeat steps 10 through 25 and then refer to the manual.

36. When measurements are complete, clean the probes with ethanol or IPA. Make sure they are back in their box and the box is locked securely.

37. To turn off the AGM, close the software. Turn off the magnet power supply and the magnet controller.

38. Turn off the cooling water.

39. Put the plastic cover back on the AGM.

Appendix C: Cryogenics, Ltd. Cryo-free Magnet System with Cryo Industries Variable Temperature Insert

The following is a brief guide to operating the Cryogenics, Ltd. cryo-free superconducting magnet system and Cryo Industries Variable Temperature Insert. The complete system is pictured in **Figure C1**.

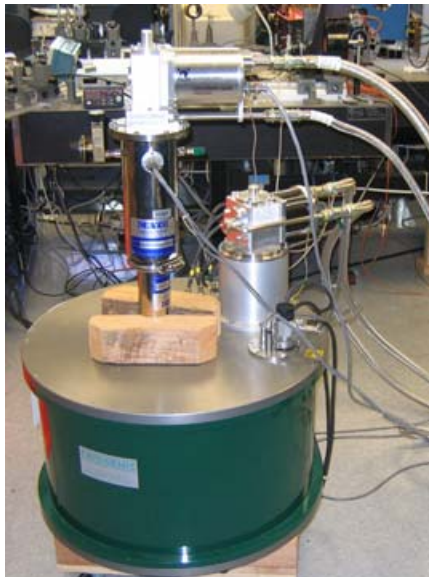


Figure C1: The magnet system. The variable temperature insert is inserted into the magnet.

Running the magnet has many quirks. First, we found a slight leak either in the compressor lines or the cold head, but it has not been precisely located. However, this leak does not manifest itself while the compressor is running and is only visible at higher temperatures. The compressor pressure should be set to a static pressure of 1.6 MPa, which give a dynamic pressure of approximately 2.2 MPa. If the pressure is below 1.6 MPa, the compressor motor will not start the cooling cycle. If there is not enough pressure in the compressor at low temperature, the magnetic will heat slightly as a function of time. Therefore, the daily base temperatures of the magnet must be tracked

to prevent a quench. So, while this leak is in existence, the compressor must be filled with high purity helium each time before the compressor is switched on. Moreover, it should be noted that if the cooling supply to the compressor has not been switched on, the motor will overheat and the compressor will automatically shut off (the same is true for the cryostat compressor).

Degradation of the equipment over time has led us to make some manual changes to the hardware and software. First, a burn-out of the switch heater controller card (located in the back of the magnet controller) has required us to attach an external power supply to act as a switch heater. This is placed in the circuit in the feed-back loop that measures the temperatures of the various thermometers (the green box). The voltage to the switch heater should be in the range of 1.5-2.2 V. The switch heater should be turned on before sweeping field and turned off when in persistent mode or in zero field. Another important degradation that requires some procedure change has occurred, most likely, in the current leads to the magnet. The nominal maximum safe field sweeping rate is 1.5 T/min for fields up to 10 T, 1.0 T/min for fields up to 12 T, and 0.5 T/min for fields up to 14 T. However, we have noticed that this creates excessive heating of the magnetic and protective shields and stages resulting in either a quench or the imminent danger of a quench. If the switch heater is applying 1.5-2.2 V, then the switch temperature should not exceed about 17 K. However, heating due to induction caused by current lead degradation causes the switch to heat up significantly more, sometimes above 50 K. If this is happening, the sweep rate is too high and needs to be turned down. In general, the new maximum sweep rate should be between 0.5-1 T/min for fields up to 8T, 0.5 T/min for fields up to 12 T, and then 0.333 T/min or less for fields up to 14 T. In addition, the magnetic controller will stop a field sweep and return to 0 field if there is danger of a quench, but not all the time. The magnet must be monitored

to be sure to prevent a quench. A normal base temperature for the inner magnet shield is approximately 3.2 K. There is danger of a quench if the inner magnet shield shows a temperature above about 6.5 K. The shields will heat slightly during field sweeping, but if the temperature gets to this point, the sweep should be aborted and the magnetic should be allowed to cool before continuing.

The Cryo Industries of America CoolPower Lab4.2 is pictured in **Figure C2**.

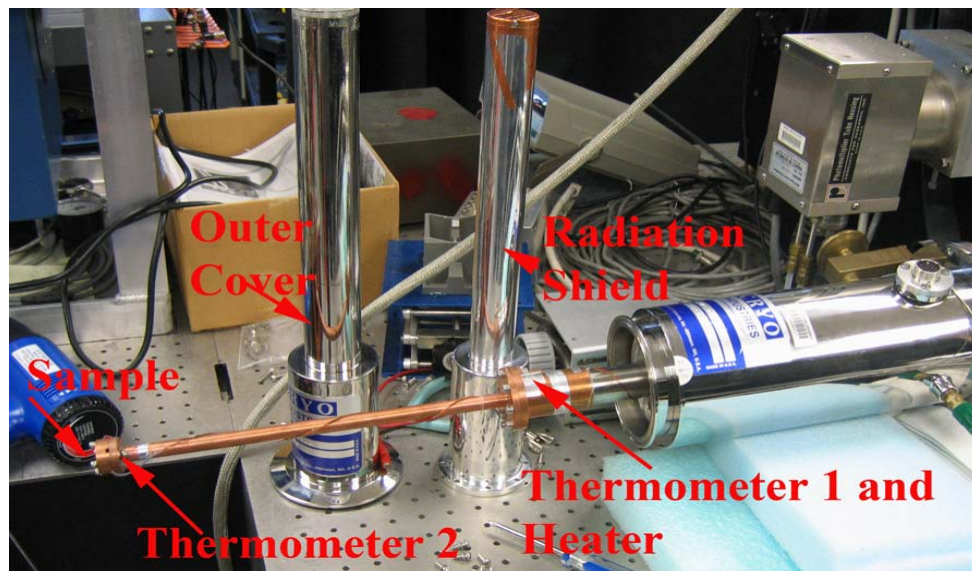


Figure C2: Cryo Industries of America CoolPower Lab4.2 cryostat. The positions of the 2 thermometers on the copper cold finger have been marked along with the sample position and the shield components.

The electrical connections are made with resistance wire having a resistance of approximately $2 \Omega/\text{ft}$. There are two GaAlAs temperature sensors in the cryostat. One is located at the top of the cryostat and one is located on the bottom next to the sample. For an accurate temperature reading, good thermal contact between the thermometers and the copper cold finger must be assured. In addition, the 16 pin chip holder is plastic and good thermal contact must be made between it and the cryostat and the chip that it holds and the cryostat. Sometimes, it is good to use a little bit of In wire to ensure good thermal contact. There are several holes drilled in the radiation shield, which must be

covered by copper or aluminum tape prior to performing an experiment. Once assembled and ready, the cryostat must be pumped out to a pressure lower than 2×10^{-5} mbar. However, there is a slight leak in the cryostat at the place of connection to the temperature controller. Therefore, the cryostat must be re-evacuated approximately every 8 hours to prevent condensation on the inside of the cryostat. When it needs to be pumped, condensation will build up on the outside of the cryostat and the temperature will be impossible control. To re-evacuate, it is best to warm the cryostat to above liquid nitrogen temperature ($\sim 70\text{K}$) and then pump down with the condenser in stand-by.

It takes approximately 3 hours to cool the cryostat to base temperature ($\sim 5\text{ K}$). However, with the condenser motor in “cool-down” or “run” it will never reach base due to noise from the cold head. When the cryostat temperature reaches approximately 10K , the controller should be placed in “run.” Then, when the temperature reaches approximately 6 K , the controller should be placed in “stand-by,” which will result in cooling to base temperature. One should make sure that the set point on the LakeShore controller is set to either 0 K , or the heater is off during cool down. The temperature can be read from the controller’s analogue outputs in the form of a voltage. The conversion from voltage to temperature can be set by following the instructions in the LakeShore temperature controller manual. Currently, it is set so that $0\text{ K}=0\text{ V}$ and $500\text{ K}=5\text{ V}$. It should be noted that there is a 2 K temperature difference between the upper and lower thermometers. The upper thermometer should be read as the most accurate thermometer, as it was replaced and calibrated during summer 2008. However, the lower thermometer gives the closest temperature to the actual sample temperature due to its proximity to the sample. We adjust for this instrumental error by subtracting 2 K from the lower thermometer.

In order to best operate the cryostat, the relationship between these thermometers must be very well understood. As discussed in Chapter 7, there is a formation of a great temperature differential during cooling. This differential cannot be altered by slowing the rate of cooling and is inherent in the design of the cryostat. However, when sweeping the temperature up and setting a warming temperature, changing the rate of sweeping can help improve the results. The temperature controller allows one to specify a sweeping rate or simple tell the controller to sweep as fast as possible (all outlined in the LakeShore manual). There are three resistors that can be used to heat the sample. The heater is located at the top of the cryostat close to the first thermometer. By specifying the resistance, one may use many different heating powers. However, we found that the best one to use in almost every circumstance was the default power on the highest resistor, which is 20 W. In general, it takes more than 5 hours for the cryostat to heat up to room temperature in order to change or remove a sample. We found that although setting the heater to warm to room temperature will warm the sample space up temporarily, it quickly cools back down again and does not speed warming of the overall cryostat much. But, the use of a small amount of exchange gas, such as He, can create thermal contact between the room air and the inner cryostat chambers and speed warming.

Bibliography

1. Friedman, A.L., D. Brittain, and L. Menon, *Roles of pH and Acid Type in the Anodic Growth of Porous Alumina*. J. Chem. Phys., 2007. **127**: p. 154717.
2. Friedman, A.L. and L. Menon, *Dendritic-Pattern Formation in Anodic Aluminum Oxide Templates*. J. Appl. Phys., 2007. **101**: p. 084310.
3. Friedman, A.L., et al., *High-Aspect Ratio Nano-Noodles of Alumina and Titania*. J. Nanosci. Nanotech., 2008. **8**: p. 1.
4. Menon, L., et al., *Synthesis of Materials Using Self-Assembled Nanotemplates*, in *The Encyclopedia of Nanotechnology*. 2009.
5. Friedman, A.L., *One-Dimensional Nanocomposite Materials Based on Semiconductor/Metal Nanowires and Carbon Nanotubes*. From Nanowires To Quantum Dots, ed. D. Aurongzeb. 2009: Research Signpost.
6. Friedman, A.L. and L. Menon, *Optimal Parameters for Synthesis of Magnetic Nanowires in Porous Alumina Templates*. J. Elec. Soc., 2007. **154**: p. E68.
7. Menon, L., et al., *Negative Index Metamaterials Based on Metal-Dielectric Nanocomposites for Imaging Applications*. Appl. Phys. Lett., 2008. **93**: p. 123117.
8. Friedman, A.L., D. Brittain, and L. Menon, *Magnetostatic Interactions in Ferromagnet-Polyaniline Composite Structures*. Submitted to International Journal of Nanomaterials, 2008.
9. Friedman, A.L., et al., *Ferromagnetism in Hydrogenated Multiwalled Carbon Nanotubes*. Submitted to Phys. Rev. Lett., 2008.
10. Silverberg, J., A.L. Friedman, and L. Menon, *Growth and Magnetic Properties of Polycrystalline Self-Assembled Bifurcated Co Nanowires*. Accepted by Journal of Nanomaterials, 2008.
11. Friedman, A.L., J. Silverberg, and L. Menon, *Preparing and Applying Electrical Contacts to Template Synthesized Carbon Nanotubes and Nanowires*. From Nanowires to Quantum Dots, ed. D. Aurongzeb. 2009: Research Signpost.
12. Friedman, A.L., et al., *Bright Transition in Hydrogenated Multiwalled Carbon Nanotubes*. Manuscript in Preparation.
13. Thompson, G.E., et al., *Nucleation and Growth of Porous Anodic Films on Aluminum*. Nature, 1978. **272**: p. 433-435.
14. Thompson, G.E. and G.C. Wood, *Porous Anodic Film Formation on Aluminum*. Nature, 1981. **290**: p. 230-232.

15. Keller, F., M.S. Hunter, and D.L. Robinson, *Structural Features of Anodic Oxide Films on Aluminum*. J. Electrochem. Soc., 1953. **100**: p. 411-419.
16. O'Sullivan, J.P. and G.C. Wood, *The Morphology and Mechanism of Formation of Porous Anodic Films on Aluminum*. Proceedings of the Royal Society of London: A: Mathematical and Physical Sciences, 1970. **317**(1531): p. 511-543.
17. Parkhutik, V.P. and V.I. Shershulsky, *Theoretical Modeling of Porous Oxide Growth on Aluminum*. J. Phys. D: Appl. Phys., 1992. **25**: p. 1258-1263.
18. Singh, G.K., A.A. Golovin, and I.S. Aranson, *Formation of Self-Organized Nanoscale Porous Structures in Anodic Aluminum Oxide*. Phys. Rev. B, 2006. **73**: p. 205422.
19. Singh, G.K., et al., *Formation of Nanoscale Pore Arrays During Anodization of Aluminum*. Europhys. Lett. , 2005. **70**(6): p. 836-842.
20. Thamida, S.K. and H.-C. Chang, *Nanoscale Pore Formation Dynamics During Aluminum Anodization*. Chaos, 2002. **12**(1): p. 240.
21. Wu, Z., C. Richter, and L. Menon, *A Study of Anodization Process During Pore Formation in Nanoporous Alumina Templates*. J. Elec. Soc., 2007. **154**(1): p. E8-E12.
22. Kanakala, R., et al., *Modeling of Porous Alumina Template Formation Under Constant Current Conditions*. J. Elec. Soc., 2005. **152**(1): p. J1-J5.
23. Singaraju, P., et al., *Model for Porous Alumina Template Formation: Constant Voltage Anodization*. Eur. Phys. J.: Appl. Phys., 2006.
24. Parkhutik, V.P., et al., *Study of Aluminum Anodization in Sulfuric And Chromic Acid Solutions-Kinetics of Growth and Composition of Oxides*. Electrochimica Acta, 1989. **35**(6): p. 955-960.
25. Parkhutik, V.P., V.T. Belov, and M.A. Chernyckh, *Study of Aluminum Anodizations in Sulfuric and Chromic Acid Solutions-Oxide Morphology and Structure*. Electrochimica Acta, 1990. **35**(6): p. 961-966.
26. Parkhutik, V.P. and V.I. Shershulskii, *The Modeling of DC Conductivity of Thin Disordered Dielectrics*. J. Phys. D: Appl. Phys., 1986. **19**: p. 623-641.
27. Asoh, H., et al., *Conditions for Fabrication of Ideally Ordered Anodic Porous Alumina Using Pretextured Al*. J. Elec. Soc., 2001. **148**(4): p. B152-B156.
28. Ono, S., et al., *Controlling Factor of Self-Ordering of Anodic Porous Alumina*. J. Elec. Soc., 2004. **151**(8): p. B473-B478.

29. Chu, S.Z., et al., *Large-Scale Fabrication of Ordered Nanoporous Alumina Films with Arbitrary Pore Intervals by Critical-Potential Anodization*. J. Electrochem. Soc., 2006. **153**: p. B384.
30. Galenko, P.K., M.D. Krivilyov, and S.V. Buzilov, *Bifurcations in a Sidebranch Surface of a Free-Growing Dendrite*. Phys. Rev. E, 1997. **55**(1): p. 611.
31. Meng, G., et al., *Controlled Fabrication of Hierarchically Branched Nanopores, Nanotubes, and Nanowires*. Proc. Natl. Acc. Sci., 2005. **102**: p. 7074.
32. Alper, M., *Electrodeposition of Multilayered Nanostructures*, in *Nanostructured Magnetic Materials and Their Applications*, D. Shi, et al., Editors. 2002, Springer: New York. p. 111-128.
33. Bard, A.J. and L.R. Faulkner, *Electrochemical Methods*. 1980, New York: John Wiley and Sons, Inc.
34. Paunovic, M. and M. Schlesinger, *Fundamentals of Electrochemical Deposition*. 1988, New York: John Wiley and Sons, Inc.
35. Fodor, P.S., G.M. Tsoi, and L.E. Wenger, *Fabrication and Characterization of $Co_{1-x}Fe_x$ Alloy Nanowires*. J. Appl. Phys., 2002. **91**(10): p. 8186-8188.
36. Wang, J.-B., et al., *Structure and Magnetic Study of $Fe_{1-x}Ni_x$ ($0 < x \leq 0.32$) Alloy Nanowire Arrays*. J. Phys. D: Appl. Phys., 2001. **34**: p. 3442-3446.
37. Ji, G., et al., *Structural and Magnetic Properties of Electrochemically Assembled Ni-Pb/ Al_2O_3 Nanostructures*. Solid State Communications, 2005. **136**(97-101).
38. Xu, H.-B., et al., *Fabrication of Organic Copper Phthalocyanine Nanowire Arrays Via a Simple AAO Template-Based Electrophoretic Deposition*. Chemical Physics Letters, 2005. **412**: p. 294-298.
39. Gultepe, E., et al., *High-Throughput Assembly of Nanoelements in Nanoporous Alumina Templates*. Appl. Phys. Lett., 2007. **90**: p. 163119.
40. Liu, K., C.L. Chien, and P.C. Searson, *Finite-size effects in bismuth nanowires*. Phys. Rev. B, 1998. **58**(22): p. R14 681-684.
41. Liu, K., et al., *Structural and magneto-transport properties of electrodeposited bismuth nanowires*. Appl. Phys. Lett., 1998. **73**(10): p. 1436-1438.
42. Wang, X.F., et al., *Fabrication and temperature dependence of the resistance of single-crystalline Bi nanowires*. J. Appl. Phys., 2001. **89**(7): p. 3847-3851.
43. Wang, X.F., et al., *Ordered single-crystalline Bi nanowire arrays embedded in nanochannels of anodic alumina membranes*. J. Phys. D: Appl. Phys., 2001. **34**: p. 418-421.

44. Routkevitch, D., et al., *Nonlithographic Nano-Wire Arrays: Fabrication, Physics, and Device Applications*. IEEE Transactions on Electron Devices, 1996. **43**(10): p. 1646-1658.
45. Zheng, M., et al., *Magnetic Properties of Ni Nanowires in Self-Assembled Arrays*. Phys. Rev. B, 2000. **62**(18): p. 282-286.
46. Bao, X., F. Li, and R.M. Metzger, *Synthesis and magnetic properties of electrodeposited metal particles on anodic alumite film*. J. Appl. Phys., 1996. **79**(8): p. 4866.
47. Benfield, R.E., et al., *Structure of Metal Nanowires in Nanoporous Alumina Membranes Studied by EXAFS and X-ray Diffraction*. Eur. Phys. J. D., 2001. **16** p. 399-402.
48. Min, J.H., et al., *Substrate Effect on Microstructure and Magnetic Properties of Electrodeposited Co Nanowire Arrays*. J. Appl. Phys., 2006. **99**(08Q510).
49. Xu, J. and Y. Xu, *Fabrication of Amorphous Co and CoP Nanometer Array With Different Shapes in Alumina Template by AC Electrodeposition*. Materials Letters, 2006. **60**: p. 2069-2072.
50. Huang, Y.H., H. Okumura, and G.C. Hadjipanayis, *CoPt and FePt nanowires by electrodeposition*. J. Appl. Phys., 2002. **91**(10): p. 6869-6871.
51. Li, W., et al., *The Magneto-Optical Properties of Annealed Co₉₆Pt₄ Nanowire Arrays*. J. Appl. Phys., 2005. **97**(104396).
52. Zhang, J., et al., *Composition-Dependent Structural and Magnetic Properties of Co_{1-x}Pt_x (0.09<=x<=0.86) Nanowire Arrays*. J. Appl. Phys., 2006. **99**(08Q502).
53. Wan, D., et al., *Fabrication of the Ordered FeS₂ (pyrite) Nanowire Arrays in Anodic Aluminum Oxide*. Materials Science and Engineering B, 2005. **122**: p. 156-159.
54. Luo, H., et al., *Prussian Blue Nanowires Fabricated by Electrodeposition in Porous Anodic Aluminum Oxide*. J. Electrochem. Soc., 2004. **151**(9): p. C567-C570.
55. Zhou, P.H. and D.S. Xue, *Finite-Size Effect on Magnetic Properties in Prussian Blue Nanowire Arrays*. J. Appl. Phys., 2004. **96**(1): p. 610-614.
56. Zhou, P., et al., *Preparation and Characterization of Highly Ordered Vanadium-Iron Cyanide Molecular Magnet Nanowire Arrays*. Nanotechnology, 2004. **15**: p. 27-31.
57. Yun, M., et al., *Nanowire Growth for Sensor Arrays*. Nanofabrication Technologies, 2003.

58. Cao, H., et al., *An Array of Iron Nanowires Encapsulated in Polyaniline Nanotubules and its Magnetic Behavior*. J. Mater. Chem., 2001. **11**: p. 958-960.
59. Cao, H., et al., *Template Synthesis and Magnetic Behavior of an Array of Cobalt Nanowires Encapsulated in Polyaniline Nanotubules*. Adv. Mater. , 2001. **13**(2): p. 121-123.
60. Cao, H., et al., *Template Synthesis and Magnetic Behavior of an Array of Cobalt Nanowires Encapsulated in Polyaniline Nanotubules*. Adv. Mater., 2001. **13**(2): p. 121.
61. Cao, H., et al., *An Array of Iron Nanowires Encapsulated in Polyaniline Nanotubules and its Magnetic Behavior*. J. Mater. Chem., 2001. **11**: p. 958.
62. Gupta, V. and N. Miura, *Electrochemically Deposited Polyaniline Nanowire's Network*. Elec. Sol. St. Lett., 2005. **8**(12): p. A630-A632.
63. Cao, H., et al., *Array of Nickel Nanowires Enveloped in Polyaniline Nanotubules and its Magnetic Behavior*. Appl. Phys. Lett., 2001. **78**: p. 1592.
64. Gao, M., et al., *Aligned Coaxial Nanowires of Carbon Nanotubes Sheathed with Conducting Polymers*. Angew. Chem. Int. Ed., 2000. **39**: p. 3664.
65. Chen, A., H. Wang, and X. Li, *One-Step Process to Fabricate Ag-polypyrrole Coaxial Nanocables*. Chem. Comm., 2005: p. 1863.
66. Parthasarathy, R.V. and C.R. Martin, *Template-Synthesized Polyaniline Microtubules*. Chem. Mater., 1994. **6**: p. 1627.
67. Saito, R., G. Dresselhaus, and M.S. Dresselhaus, *Physical Properties of Carbon Nanotubes*. 1998, Singapore: Imperial College Press.
68. Bouhelier, A., et al., *Surface Plasmon Characteristics of Tunable Photoluminescence in Single Gold Nanorods*. Phys. Rev. Lett., 2005. **95**: p. 267405.
69. Mcmillan, B.G., et al., *Transverse and Longitudinal Surface Plasmon Resonances of a Hexagonal Array of Gold Nanorods Embedded in an Alumina Matrix*. J. Appl. Phys., 2005. **86**: p. 211912.
70. Mock, J.J., et al., *Composite Plasmon Resonant Nanowires*. Nanolett., 2002. **2**(5): p. 465-469.
71. Lu, W.T. and S. Sridhar, *Superlens Imaging Theory for Anisotropic Nanostructured Metamaterials with Broadband All-Angle Negative Refraction*. Phys. Rev. B, 2008. **77**: p. 233101.
72. Hornyak, G.L., et al., *Dynamical Maxwell-Garnett Optical Modeling of Nanogold-Porous Alumina Composites: MIE and Kappa Influence on Absorption Maxima*. Nanostruct. Mater., 1997. **9**(575-578).

73. Valmalette, J.-C., J. Dutta, and H. Hofmann, *Dynamical Maxwell-Garnett Optical Modeling of Nanogold-Porous Oxide Composites: Mie and Kappa Influence on Absorption Maxima*. *Nanostruct. Mater.*, 1997. **9**: p. 575.
74. Aspenes, D.E., *Local-Field Effects and Effective-Medium Theory: Microscopic Prospective*. *Am. J. Phys.*, 1982. **50**: p. 704.
75. Bohren, C.F. and D.R. Huffman, *Absorption and Scattering of Light by Small Particles*. 1983, New York: Wiley.
76. Schider, G., et al., *Optical Properties of Ag and Au Nanowire Gratings*. *J. Appl. Phys.*, 2001. **90**(8): p. 3825.
77. Yu, Y.-Y., et al., *Gold Nanorods: Electrochemical Synthesis and Optical Properties*. *J. Phys. Chem. B*, 1997. **101**(34): p. 6661.
78. Kumar, A., et al., *Competition Between Shape Anisotropy and Magnetoelastic Anisotropy in Ni Nanowires Electrodeposited Within Alumina Templates*. *Phys. Rev. B*, 2006. **73**(064421).
79. Fodor, P.S., G.M. Tsoi, and L.E. Wenger, *Modeling of Hysteresis and Magnetization Curves for Hexagonally Ordered Electrodeposited Nanowires*. *J. Appl. Phys.*, 2003. **93**(10): p. 7438.
80. Vazquez, M., et al., *Modeling Hysteresis of Interacting Nanowire Arrays*. *Physica B*, 2004. **343**: p. 395-402.
81. Zeng, H., et al., *Structure and Magnetic Properties of Ferromagnetic Nanowires in Self-Assembled Arrays*. *Phys. Rev. B*, 2002. **65**: p. 134426.
82. Bergmann, G., et al., *Frustrated Magnetization in Co Nanowires: Competition Between Crystal Anisotropy and Demagnetization Energy*. *Phys. Rev. B*, 2008. **77**: p. 054415.
83. Zheng, M., et al., *Magnetic Properties of Ni Nanowires in Self-Assembled Arrays*. *Phys. Rev. B*, 200. **62**(18): p. 62.
84. Zeng, H., et al., *Magnetic Properties of Self-Assembled Co Nanowires of Varying Length and Diameter*. *J. Appl. Phys.*, 2000. **87**(9): p. 4718.
85. Sellmyer, D.J., M. Zheng, and R. Skomski, *Magnetism of Fe, Co, and Ni Nanowires in Self-Assembled Arrays*. *J. Phys.: Condens. Matter*, 2001. **13**: p. R433-R460.
86. Menon, L., et al., *Size Dependence of the Magnetic Properties of Electrochemically Self-Assembled Fe Quantum Dots*. *J. Elec. Mater.*, 2000. **29**(5): p. 510.

87. Heydon, G.P., et al., *Magnetic Properties of Electrodeposited Nanowires*. J. Phys. D: Appl. Phys., 1997. **30**: p. 1083-1093.
88. Kroll, M., et al., *Magnetic Properties of Ferromagnetic Nanowires Embedded in Nanoporous Alumina Membranes*. J. Magn. Magn. Mater., 2002. **249**: p. 241.
89. Likodimos, V., et al., *Magnetic and Electronic Properties of Multiwall Carbon Nanotubes*. Phys. Rev. B, 2003. **68**: p. 045417.
90. Lehtinen, P.O., et al., *Irradiation-Induced Magnetism in Graphite: A Density Functional Study*. Phys. Rev. Lett., 2004. **93**(18): p. 187202.
91. Ma, Y., et al., *Hydrogen-Induced Magnetism in Carbon Nanotubes*. Phys. Rev. B, 2005. **72**: p. 085451.
92. Zhang, Y., et al., *First-Principles Study of Defect-Induced Magnetism in Carbon*. Phys. Rev. Lett., 2007. **99**: p. 107201.
93. Esquinazi, P., et al., *Ferromagnetism in Oriented Graphite Samples*. Phys. Rev. B, 2002. **66**: p. 024429.
94. Talapatra, S., et al., *Irradiation-Induced Magnetism in Carbon Nanotubes*. Phys. Rev. Lett., 2005. **95**: p. 097201.
95. Esquinazi, P., et al., Phys. Rev. Lett., 2003. **91**: p. 227201.
96. Li, X., et al., *Hydrogen Uptake by Graphitized Multi-walled Carbon Nanotubes Under Moderate Pressure and at Room Temperature*. Carbon, 2001. **39**: p. 2077-2088.
97. Nikitin, A., et al., *Hydrogenation of Single-Walled Carbon Nanotubes*. Phys. Rev. Lett., 2005. **95**: p. 225507.
98. Dresselhaus, M.S., et al., *Graphite Fibers and Filaments*. 1988, New York: Springer.
99. Endo, M., Y. Hishiyama, and T. Koyama, *Magnetoresistance Effect in Graphitizing Carbon Fibres Prepared by Benzene Decomposition*. J. Phys. D: Appl. Phys., 1982. **15**: p. 353.
100. Bockrath, M., et al., *Luttinger-liquid Behavior in Carbon Nanotubes*. Nature, 1999. **397**: p. 598.
101. Pablo, P.J.d., et al., *A Simple, Reliable Technique for Making Electrical Contact to Multiwalled Carbon Nanotubes*. Appl. Phys. Lett., 1999. **74**(2): p. 323-325.
102. Xiang, B., et al., *Electrical Transport of Individual Multi-wall Carbon Nanotubes*. Mater. Lett., 2006. **60**: p. 754-756.
103. The Kostas Center for Nanofabrication at Northeastern University.

104. Campbell, S.A., *The Science and Engineering of Microelectronic Fabrication* 2ed. 2001, New York: Oxford University Press.
105. Roddaro, S., et al., *The Optical Visibility of Graphene: Interference Colors of Ultrathin Graphite on SiO₂*. *Nanolett.*, 2007. **7**: p. 2707.
106. Blake, P., et al., *Making Graphene Visible*. *Appl. Phys. Lett.*, 2007. **91**: p. 063124.
107. http://www.ee.byu.edu/cleanroom/color_chart.phtml. [cited.
108. Ishigami, M., et al., *Atomic Structure of Graphene on SiO₂*. *Nanolett.*, 2007. **7**(6): p. 1643-1648.
109. Ferrari, A.C., et al., *Raman Spectrum of Graphene and Graphene Layers*. *Phys. Rev. Lett.*, 2006. **97**: p. 187401.
110. *Private conversation with Paul Campbell of the Navy Research Labs*. August 2008.
111. Sidorov, A.N., et al., *Electrostatic Deposition of Graphene*. *Nanotech.*, 2007. **18**(135301).
112. *Private conversation with Peter Blake of Graphene Industries, Ltd. and the University of Manchester*. March 2008.
113. Stevie, F.A., D.P. Griffiths, and P.E. Russell, *Focused Ion Beam Gases for Deposition and Enhanced Etch*. Introduction to Focused Ion Beams, ed. L.A. Giannuzzi and F.A. Stevie. 2005, New York: Springer.
114. Wei, B.Q., R. Vajtai, and P.M. Ajayan, *Reliability and Current Carrying Capacity of Carbon Nanotubes*. *Appl. Phys. Lett.*, 2001. **79**: p. 1172.
115. Hill, R.J., *Physical Vapor Deposition*. 1986: Temescal.
116. Bachtold, A., et al., *Contacting Carbon Nanotubes Selectively with Low-Ohmic Contacts for Four Probe Electric Measurements*. *Appl. Phys. Lett.*, 1998. **73**(2): p. 274.
117. *Private conversation with Adrian Bachtold of the Centro de Investigacion en Nanociencia y Nanotecnologia in Barcelona, Spain*. July 2007.
118. Jin, R., et al., *The Effect of Annealing on the Electrical and Thermal Transport Properties of Macroscopic Bundles of Long Multi-wall Carbon Nanotubes*. *Physica B*, 2007. **388**: p. 326.
119. Lee, J.-O., et al., *Formation of Low-Resistance Ohmic Contacts Between Carbon Nanotube and Metal Electrodes by a Rapid Thermal Annealing Method*. *J. Phys. D: Appl. Phys.*, 200. **33**: p. 1953-1956.

120. Li, J., Q. Zhang, and Q. Zhu, *Manipulation of Carbon Nanotubes Using AC Dielectrophoresis*. Appl. Phys. Lett., 2005. **86**: p. 153116.
121. Giamarchi, T., *Quantum Physics in One Dimension*. 2004, Oxford: Clarendon Press.
122. Voit, J., *A Brief Introduction to Luttinger Liquids*. arXiv:cond-mat/0005114v1, 2000.
123. Voit, J., *One-Dimensional Fermi Liquids*. arXiv:cond-mat/9510014v1, 2006.
124. Landauer, R., *Spatial Variation of Currents and Fields Due to Localized Scatterers in Metallic Conduction*. IBM Journal, 1957: p. 223-231.
125. Stone, A.D. and A. Szafer, *What is Measured When You Measure a Resistance--The Landauer Formula Revisited*. IBM J. Res. Develop., 1988. **32**(3): p. 384-413.
126. Buttiker, M., *Coherent and Sequential Tunneling in Series Barriers*. IBM J. Res. Develop., 1988. **32**(1): p. 63-75.
127. Imry, Y. and R. Landauer, *Conductance Viewed as Transmission*. Rev. Mod. Phys., 1999. **71**(2): p. S306-S312.
128. Buttiker, M. and R. Landauer, *Traversal Time for Tunneling*. IBM J. Res. Develop., 1986. **30**(5): p. 451-454.
129. Urbina, A., et al., *Quantum Conductance Steps in Solutions of Multiwalled Carbon Nanotubes*. Phys. Rev. Lett., 2003. **90**(10): p. 106603.
130. Luttinger, J.M., *An Exactly Soluble Model of a Many-Fermion System*. J. Math. Phys., 1963. **4**(9): p. 1154-1162.
131. Schulz, H.J., G. Cuniberti, and P. Pieri, *Fermi Liquids and Luttinger Liquids*. arXiv:cond-mat/9807366 v2, 1998.
132. Voit, J., *One-Dimensional Fermi Liquids*. Rep. Prog. Phys., 1995. **58**: p. 977.
133. Auslaender, O.M., et al., *Spin-Charge Separation and Localization in One Dimension*. Science, 2005. **308**(5718): p. 88-92.
134. Mott, N., *Metal-Insulator Transitions*. 1990, New York: Taylor and Francis.
135. Tarkiainen, R., et al., *Transport in Disordered Carbon Nanotubes*. Physica E, 2003. **18**: p. 206.
136. Tarkiainen, R., et al., *Transport in Strongly Disordered Multiwalled Carbon Nanotubes*. Phys. Rev. B, 2004. **69**: p. 033402.
137. Lee, P.A. and T.V. Ramakrishnan, *Disordered Electronic Systems*. Rev. Mod. Phys., 1985. **57**(287).

138. Wei, B.Q., R. Vajtai, and P.M. Ajayan, *Reliability and Current Carrying Capacity of Carbon Nanotubes*. Appl. Phys. Lett., 2001. **79**(8): p. 1172-1174.
139. Graugnard, E., et al., *Temperature Dependence of the Conductance of Multiwalled Carbon Nanotubes*. Phys. Rev. B, 2001. **64**: p. 125407.
140. Fisher, M.P.A. and A.T. Dorsey, *Dissipative Quantum Tunneling in a Biased Double-Well System at Finite Temperatures*. Phys. Rev. Lett., 1985. **54**(15): p. 1609-1612.
141. Grabert, H. and U. Weiss, *Quantum Tunneling Rates for Asymmetric Double-Well Systems with Ohmic Dissipation*. Phys. Rev. Lett., 1985. **54**: p. 1605-1608.
142. Roche, S. and R. Saito, *Magnetoresistance of Carbon Nanotubes: From Molecular to Mesoscopic Fingerprints*. Phys. Rev. Lett., 2001. **87**(24): p. 246803.
143. Fujiwara, A., K. Tomiyama, and H. Suematsu, *Quantum Interference of Electrons in Multiwall Carbon Nanotubes*. Phys. Rev. B, 1999. **60**(19): p. 13492-13496.
144. Langer, L., et al., *Quantum Transport in a Multiwalled Carbon Nanotube*. Phys. Rev. Lett., 1996. **76**: p. 479-482.
145. Lu, J.P., *Novel Magnetic Properties of Carbon Nanotubes*. Phys. Rev. Lett., 1995. **74**(7): p. 1123-1126.
146. Fujiwara, A., et al., *Magnetotransport of Carbon Nanotubes: Magnetic-Field-Induced Metal-Insulator Transition*. Physica B, 2001. **298**: p. 541-545.
147. Roche, S. and R. Saito, *Effects of Magnetic Field and Disorder on the Electronic Properties of Carbon Nanotubes*. Phys. Rev. B, 1999. **59**(7): p. 5242-5246.
148. Langer, L., et al., *Quantum Transport in a Multiwalled Carbon Nanotube*. Phys. Rev. Lett., 1996. **76**: p. 489.
149. Brands, M., et al., *Electron-Electron Interaction in Carbon Coated Ferromagnetic Nanowires*. Phys. Rev. B, 2005. **72**: p. 085457.
150. Carl, A., G. Dumpich, and D. Hallfarth, *Antilocalization and Electron-Electron Interaction in Thin Granular Palladium-Carbon Mixture Films*. Phys. Rev. B, 1989. **39**(5): p. 3015-3020.
151. Friedrichowski, S. and G. Dumpich, *One and Two Dimensional Quantum Transport in Thin Gold Wires*. Phys. Rev. B, 1998. **58**(15): p. 9689-9692.
152. Abrahams, E., et al., *Scaling Theory of Localization: Absence of Quantum Diffusion in Two Dimensions*. Phys. Rev. Lett., 1979. **42**(10): p. 673-676.

153. Altshuler, B.L., A.G. Aronov, and P.A. Lee, *Interaction Effects in Disordered Fermi Systems in Two Dimensions*. Phys. Rev. Lett., 1980. **44**(19): p. 1288-1291.
154. Egger, R., *Luttinger Liquid Behavior in Multiwall Carbon Nanotubes*. Phys. Rev. Lett., 1999. **83**(26): p. 5547-5550.
155. Bergmann, G., *Magnetoresistance of Amorphous Ferromagnetic Metals*. Phys. Rev. B, 1977. **15**(3): p. 1514-1518.
156. Wegrowe, J.-E., et al., *Magnetoresistance of Ferromagnetic Nanowires*. Phys. Rev. Lett., 1999. **82**(18): p. 3681.
157. Han, D.S., et al., Appl. Phys. Lett., 2005. **86**: p. 03506.
158. Wunderlich, J., et al., Phys. Rev. Lett., 2006. **97**: p. 077201.
159. Kelly, D., et al., *Spin-polarized Current-induced Magnetization Reversal in Single Nanowires*. Phys. Rev. B, 2003. **68**: p. 134425.
160. Oliveira, A.B., S.M. Rezende, and A. Azevedo, *Magnetization Reversal in Permalloy Ferromagnetic Nanowires Investigated with Magnetoresistance Measurements*. Phys. Rev. B, 2008. **78**: p. 024423.
161. Leven, B. and G. Dumpich, *Resistance Behavior and Magnetization Reversal Analysis of Individual Co Nanowires*. Phys. Rev. B, 2005. **71**: p. 064411.
162. O'Handley, R.C., *Modern Magnetic Materials*. 2000, New York: Wiley.
163. Bright, A.A., *Negative Magnetoresistance of Pregraphitic Carbons*. Phys. Rev. B, 1979. **20**(12): p. 5142.
164. Geim, A.K. and K.S. Novoselov, *The Rise of Graphene*. Nature Materials, 2007. **6**: p. 183-191.
165. Novoselov, K.S., et al., *Two-Dimensional Gas of Massless Dirac Fermions in Graphene*. Nature, 2005. **438**: p. 197.
166. Geim, A.K. and A.H. MacDonald, *Graphene: Exploring Carbon Flatland*. Physics Today, 2007: p. 35-41.
167. Nomura, K. and A.H. Macdonald, *Quantum Transport of Massless Dirac Fermions*. Phys. rev. Lett., 2007. **98**: p. 076602.
168. Du, X., et al., *Approaching Ballistic Transport in Suspended Graphene*. Nature Nanotechnology, 2008. **3**: p. 491-495.
169. Nomura, K. and A.H. MacDonald, *Quantum Hall Ferromagnetism in Graphene*. Phys. Rev. Lett., 2006. **96**: p. 256602.

170. Toke, C., et al., *Fractional Quantum Hall Effect in Graphene*. Phys. Rev. B, 2006. **74**(235417).
171. Apalkov, V.M. and T. Chakraborty, *Fractional Quantum Hall States of Dirac Electrons in Graphene*. Phys. Rev. Lett., 2006. **97**: p. 126801.
172. Abanin, D.A., et al., *Dissipative Quantum Hall Effect in Graphene Near the Dirac Point*. Phys. Rev. Lett., 2007. **98**: p. 196806.
173. Aleiner, I.L., D.E. Kharzeev, and A.M. Tsvelik, *Spontaneous Symmetry Breakings in Graphene Subjected to In-Plane Magnetic Field*. arxiv:cond-mat/0611251.
174. Mishchenko, E.G., *Effect of Electron-Electron Interactions on the Conductivity of Clean Graphene*. Phys. Rev. Lett., 2007. **98**: p. 216801.
175. *Private conversation of Andrei Geim of the University of Manchester*. March, 2008.
176. Novoselov, K.S., et al., *Room-Temperature Quantum Hall Effect in Graphene*. Science, 2007. **315**: p. 1379.
177. Falkovsky, L.A., *Unusual Field and Temperature Dependence of the Hall Effect in Graphene*. Phys. Rev. B, 2007. **75**: p. 033409.
178. Hwang, E.H., S. Adam, and S.D. Sarma, *Carrier Transport in Two-Dimensional Graphene Layers*. Phys. Rev. Lett., 2007. **98**: p. 186806.
179. *Private conversation with Alexei Tsvelik and Dmitri Kharzeev of Brookhaven National Labs*. October 2008.